UNIVERSITÀ DEGLI STUDI DI TRIESTE

XXVI CICLO DEL DOTTORATO DI RICERCA IN FISICA

Matter under Extreme Transient conditions investigated with Free Electron Laser radiation at FERMI

Settore scientifico-disciplinare: FIS/03

DOTTORANDA:

Erika Giangrisostomi

COORDINATORE:

Paolo Camerini

SUPERVISORE:

Claudio Masciovecchio

ANNO ACCADEMICO 2013/2014

If you can't fly, then run;
if you can't run, then walk;
if you can't walk, then crawl;
but - whatever you do -
you have to keep moving forward.

Martin Luther King, Jr.

A te, occhi blu...

Riassunto

Sottoposti ad impulsi luminosi ultra-intensi ed ultra-brevi, i materiali solidi sono temporaneamente portati ad altissime temperature e pressioni.
Generare tali stati in controllate condizioni di laboratorio ed investigarne le proprietà fisiche con una risoluzione temporale adeguata a seguirne la rapida evoluzione è stato un obiettivo primario degli esperimenti di tipo "pump-and-probe" facenti uso dei laser ottici al femtosecondo ed elevate potenze di picco che sono divenuti di crescentemente diffusa disponibilità nel corso degli scorsi tre decenni.
Operativi soltanto da pochi anni, i laser ad elettroni liberi (FEL) uniscono - alle desiderate proprietà di alta brillanza, breve durata temporale e coerenza propri di questi laser - l'energia variabile fin negli intervalli spettrali dell'estremo ultravioletto (EUV) e dei raggi X che è tipica delle sorgenti di sincrotrone, offrendo in tal modo una serie di vantaggi sia per quanto riguarda la generazione che la caratterizzazione dei suddetti stati.

Questa tesi descrive gli sforzi che sono stati intrapresi verso il consolidamento di una nuova piattaforma sperimentale per lo studio della materia in condizioni estreme e transienti presso la linea di luce TIMEX del laser ad elettroni liberi FERMI in funzione a Trieste e discute la raggiunta comprensione di un certo numero di indagini pionieristiche.

Stati esotici istantaneamente raggiunti da campioni metallici in seguito ad eccitazione FEL sono caratterizzati attraverso misure a singolo impulso delle loro riflettanza ed assorbanza EUV.
In particolare, diamo la prima dimostrazione di spettroscopia di assorbimento EUV vicino soglia ad alte densità energetiche e con risoluzione temporale inferiore ai 100 fs. La combinazione di queste caratteristiche è disponibile solamente presso sorgenti FEL, ma rende FERMI unico qualora, in aggiunta, si consideri che qui si presenta senza bisogno di monocromatizzazione grazie alla natura "seeded" che rende gli impulsi rilasciati quasi Fourier-transform limited in larghezza di banda.

Viene riportata la dipendenza dalla fluenza di irraggiamento dell' assorbanza e della riflettanza transienti del Ti per selezionate lunghezze d'onda sulla soglia $M_{2,3}$ di assorbimento e vicino alla frequenza di plasma, rispettivamente. Essa rivela una

modificazione ultraveloce della struttura elettronica compatibile con uno scenario in cui un singolo impulso FEL, entro la sua durata di circa 100 fs, trasforma il titanio a temperatura ambiente in un gas caldo di elettroni liberi coesistente in condizioni altamente fuori dall'equilibrio con un reticolo freddo di ioni. Si propone una prospettiva interpretativa che, basata su semplificati ma ragionevoli modelli simil-Drude, permette di ricavare informazioni sulla temperatura e sulla densità elettronica medie e sullo stato di carica medio del plasma denso generato.
Sono presentate misure di trasmissione di impulsi ultra-veloci e ad alta densità di energia su un campione di Al ad alcune energie fotoniche tra la frequenza di plasma e la soglia di assorbimento $L_{2,3}$. Queste evidenziano per la prima volta un andamento non-monotonico della trasmissione EUV in funzione della fluenza, che giudichiamo interpretabile nell'ambito di un modello a tre canali come risultante da un effetto di saturazione congiunto ad una variazione della sezione d'urto d'assorbimento dovuta al riscaldamento elettronico.
Si mostra come condizioni di ancora più elevata fluenza inducono una trasparenza quasi completa in un campione Al-Mg-Al sull'intero intervallo di energie a cavallo della soglia di assorbimento $L_{2,3}$ dell'Mg. Viene formulato un modello analitico che, tentativamente, permette di dedurre dai dati una stima per l'energia di prima ionizzazione dell'Mg in condizioni di plasma denso.

Le risposte di campioni isolanti e semiconduttori ad eccitazioni FEL e laser - dall'iniziale fase di non-equilibrio, attraverso le successive dinamiche di rilassamento, alle possibili trasformazioni di fase - sono esplorate attraverso misure pump-and-probe.
In questo caso, gli impulsi FEL sono sfruttati in combinazione con impulsi dallo stesso laser infrarosso che funge da iniziatore del processo di emissione FEL, il che assicura una naturale sincronizzazione tra le due sorgenti di radiazione, una caratteristica - di nuovo - esclusiva dei FEL seeded.

Misure di riflettività ottica transiente su campioni di Si_3N_4 pompati dal FEL sono offerte come dimostrazione della capacità ad oggi imbattuta di FERMI di offrire una coppia di impulsi laser / FEL praticamente liberi da jitter. Sono discussi i risultati di uno studio sistematico della risposta ottica di questo materiale all'irraggiamento FEL a diverse lunghezze d'onda ed intensità di pump, diverse polarizzazioni di probe, diversi spessori del campione e diversi tipi di substrato, sia in riflessione che in trasmissione simultaneamente. Essi conducono a riconoscere il ruolo giocato da effetti di interferenza a causa delle differenti lunghezze di penetrazione tra impulsi EUV FEL ed infrarossi.
Le trasmissioni EUV transienti collezionate per il Ge alla sua soglia $M_{4,5}$ in una configurazione laser pump / FEL probe e per il Si alla sua soglia $L_{2,3}$ in una configurazione FEL pump / FEL probe restituiscono una visione risolta sia in tempo

che in energia del fenomeno di fusione dei semiconduttori indotto da impulsi al femtosecondo. Mostriamo come sia possibile seguire le dinamiche di eccitazione e diseccitazione della popolazione elettronica nella banda di valenza attraverso dati sotto soglia di assorbimento e come possiamo invece inferire informazioni di dinamica strutturale da dati sulla soglia di assorbimento, negli quali riteniamo di riconoscere l'impronta della chiusura parziale della band gap associata alla transizione verso uno stato liquido di aumentato carattere metallico.

Contents

Introduction

Subject to high-intensity ultra-short light pulses, solid materials are driven into short-living states of extremely high temperatures and pressures.
Creating such unique states under controlled laboratory conditions and addressing their physical properties with an adequate time resolution to follow their fast-evolving dynamics has been a primary objective of pump-probe studies employing the high-peak-power [1] femtosecond optical lasers that have become of increasingly widespread availability during the last three decades.
Since few years, free electron lasers (FELs) have come into this play: fourth-generation synchrotron sources which add - to the desired properties of high brilliance, short time duration and coherence - a tunable energy in the extreme ultraviolet (EUV) and X-ray spectral ranges, thus offering a number of advantages on both the fronts of pumping and probing with respect to visible light pulses.

The frequency of the latter being lower than typical plasma frequencies, their propagation is limited to a skin layer where steep intensity gradients develop that result in a ponderomotive force responsible, at high intensities, for the generation of directed beams of suprathermal electrons - in turn sources of secondary X-ray radiation - by means of various collitionless processes such as the anomalous skin effect, vacuum heating or $\vec{j}$ x $\vec{B}$ heating [1]. Yet higher intensities ($> 10^{19}$ W/cm^2) would instead be required for the electron density excited by EUV or X-ray light pulses to become overcritical [2]. Therefore - at the currently attainable intensities - the aforementioned processes do not play a role, so that an understanding of the fundamental mechanisms of strong laser-matter interaction can be more directly addressed, and, moreover, deeper penetration depths into highly ionized dense matter are reached, so that the photon energy is deposited more homogeneously within the target bulk and ballistic and diffusive transport need not to be invoked for a

[1] High peak powers usually means exceeding gigawatt levels. To have an idea, consider that a 100 fs -long pulse of 1 mJ energy already results in a 10 GW peak power, which yields a pulse intensity of the order of 10^{16} W/cm^2 upon focusing to a spot of 10 μm linear dimensions.

[2] A plasma is called overdense if its density n_e exceeds the critical density n_c, the latter being defined by the condition that the plasma frequency $\omega_p = \sqrt{\frac{e^2 n_e}{\epsilon_0 m_e}}$ equals the laser frequency ω_L.

time-dependent evaluation of the excitation volume.
Furthermore, EUV photon energies are those at which photoionization (i.e. bound-free electronic transitions) starts to take over against inverse bremsstrahlung (i.e. free-free electronic transitions), that instead governs the absorption cross-section at smaller photon energies. This circumstance then makes it possible to exploit the capabilities of core-level spectroscopies to probe - with their well-recognized elemental, chemical and magnetic state selectivity - the electronic and atomic structure and dynamics of materials under excitation strengths and at time resolutions which have been hitherto inaccessible to synchrotron radiation studies.

The TIMEX project of an end-station installed at the free electron laser FERMI in Trieste for ultrafast TIme-resolved studies of Matter under EXtreme and metastable conditions stemmed from the intent of exploring this asset of cutting-edge technology and concepts. Within it, my PhD work developed, that has accompanied the growth of the TIMEX beamline from its setting up, through the various commissioning activities, up to the present mature status.

In this thesis, I will describe the efforts that have been undertaken towards the establishment of a new experimental ground for the study of matter under extreme transient conditions at FERMI and discuss our understanding of a number of seminal investigations.
Various topics will be touched, ranging from the spectroscopic diagnosis of the free electron temperature and density and the modeling of saturation effects in dense non-equilibrium plasmas from FEL-excited metals, to the study of the temporal evolution of the optical properties of insulators under EUV-pumping, to the time and energy -resolved tracking of the ultrafast electron dynamics of laser-induced melting in semiconductors.

0.1 Background concepts

0.1.1 From optical lasers and laser-based X-ray sources, synchrotrons and synchrotron-based slicing sources to free electron lasers

Just as its acronym says, a laser provides “light amplification by stimulated emission of radiation”. Operated for the first time by Maiman in 1960, it basically consists of a gain medium where, once its atoms are brought into an excited state by an external source of energy, photons of suited frequency stimulate electronic transitions from the excited back into the ground state with consequent emission of additional photons of the same frequency, direction and phase, thus leading to an amplification of the input intensity with back and forth bouncing of the light

between two opposite mirrors [2].

Laser radiation therefore boasts the key property of coherence, both spatial (or transverse) - i.e. phase correlation between light waves at different points in space at all instants of time - and temporal (or longitudinal) - i.e. phase correlation between light waves at different instants of time at a certain point in space. The former characteristic is what permits a laser beam to stay collimated for very long distances and to achieve tiny spot sizes when properly focused. The latter characteristic goes together with monochromaticity - a tradeoff of the kind $\tau_c \, \Delta\nu \sim 1$ existing between the coherence time τ_c and the bandwidth $\Delta\nu$ - which renders laser radiation well-suited for spectroscopic studies.
Coherence is at the heart of the countless instruments and methods that rely on interferometry, there comprised imaging techniques [3]. In conjunction with brightness - other key property of laser radiation -, coherence is also essential for nonlinear optics, being meant by this term all those processes that result from the n-order response of the sample polarization to the applied electric field and provide the base for as many experimental techniques [4].

By switching on and off the lasing emission, a same accumulated energy E may be released concentrated in pulses of some duration τ at some repetition rate $1/T$. Such pulsed mode of operation enormously enriches the range of possible applications for laser light under two interconnected aspects.
The first aspect has to do with the potentialities of a short pulse duration. Much like a stroboscope that freezes the motion of objects moving at the speed of its flashes, the shorter a laser pulse is, the more temporal resolution one has to look at ultrafast events. When this is combined with a pump-probe approach in which a first intense pulse (the pump) is responsible for some excitation and a second weaker pulse (the probe) interrogates the excited system at increasing temporal delays from the excitation, insights can be gained on the dynamics of fundamental physical, chemical and biological processes, that mainly have in the attosecond to microsecond ranges their native timescales [5].
The second aspect has to do with the potentialities of a high pulse intensity. Since the single pulse power $P_{peak} = E/\tau$ equals the average power $P_{avg} = E/T$ divided by the pulse duration and by the repetition rate, by either shortening the pulse duration or lowering the repetition rate, higher and higher intensities may be reached. This possibility opens the door to a vast class of investigations in the increasingly growing field of high-energy density (HED) physics, wherein externally supplied energy densities are treated that compare to or exceed the energy density at standard conditions of the material under study [3] [6].

[3] In strictly conventional terms, the attribute "high" applies to energy densities beyond 10^{11} J/m^3 - the binding energy of a hydrogen molecule - or, equivalently, to pressures beyond 1 Mbar - a million times the atmospheric pressure!

Among the existing methods, the one that allows to generate pulses with the shortest time duration is modelocking [7], so named because it relies on the interference between different longitudinal modes of the laser cavity which have been somehow "locked" to a same phase. Longitudinal modes are those waves for which the resonator length L exactly equals a multiple of the half-wavelength $n\lambda/2$, the only that get amplified by successive reflections through the cavity mirrors. Establishing a phase relation between the longitudinal modes is, indeed, equivalent to reinforcing an intensity maximum at the expenses of the rest so as to concentrate all of the energy in a single pulse (Fig. 1).

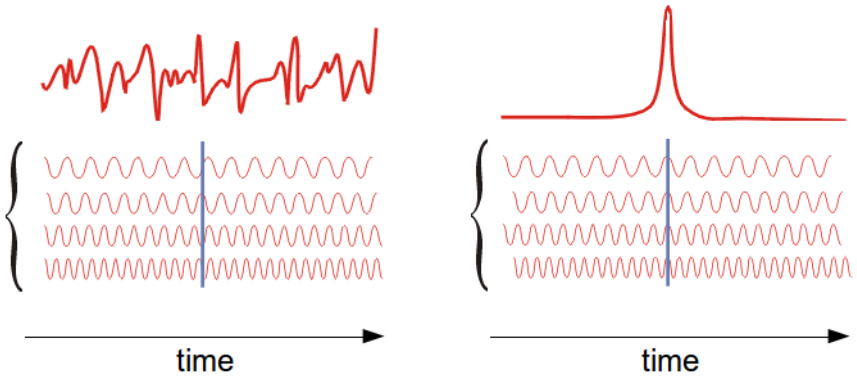

Figure 1: Generally, the longitudinal modes of a laser oscillate independently from one another giving rise to a noisy output intensity. In mode-locked operation, instead, they are forced to oscillate in phase, thus giving rise to a pulsed emission. Taken from Ref. [8].

A way to realize mode-locking makes use of an acousto-optic modulator (AOM) imparting to the laser light an amplitude modulation at a frequency synchronized to the cavity round-trip time in such a way that, from each mode, in-phase sidebands are driven which corresponds to its two adjacent modes. The shorter the circulating pulses become, the faster the loss modulation should be.
Since going below few tens of picoseconds is beyond the reach of the fastest electronic signal generators, one has to resort to passive mode-locking, a class of techniques where it is the radiation itself to generate an automatically synchronized modulation by means of a nonlinear device. One possibility is to exploit a saturable absorber, a material (typically a liquid organic dye) that displays decreasing light absorption with increasing light intensity and can, therefore, selectively amplify randomly generated high-intensity spikes. Another possibility is to exploit the self-focusing effect, where the high-intensity light from the beam center is focused more tightly than the low-intensity light for the beam tails, which can thus be suppressed by properly arranging an aperture in the laser cavity.

Following the uncertainty principle, a pulse of short duration τ inevitably possesses a wide bandwidth of the order $1/\tau$. It is easily demonstrable that, if we consider a train of such pulses phase-locked together, the corresponding spectrum preserves an envelope of width $1/\tau$ but also acquires a sinusoidal modulation with a period given by the inverse of the time interval T between two consecutive pulses, which is in turn defined by the round-trip time $2L/c$ (Fig. 2).

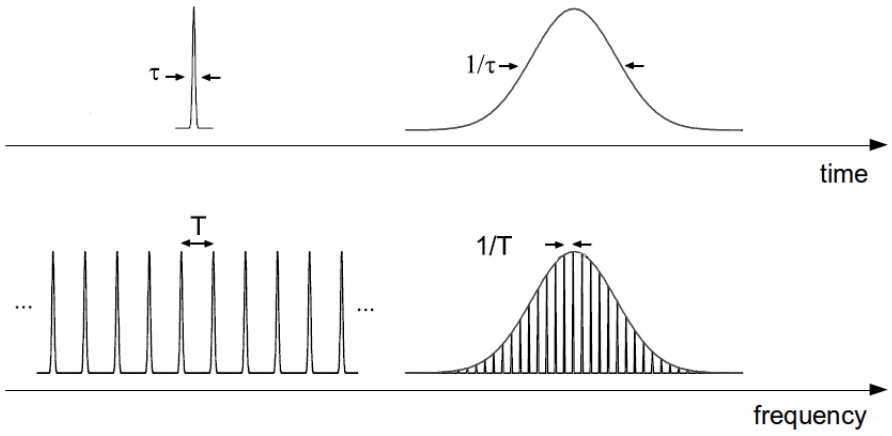

Figure 2: An infinite train of pulses, each of duration τ and separated from the next by a time interval T, has a spectrum of infinitely narrow frequencies spaced by $1/T$.

If we denote by τ and $\Delta\nu$ the full-width at half-maximum (FWHM) values of the pulse duration and bandwidth respectively, the relationship $\tau\,\Delta\nu \gtrsim K$ holds.
K is a number that uniquely depends on the pulse shape, the latter being in turn determined by the precise amplitudes and phases of the longitudinal modes. The minimum of K is attained for Gaussian pulses, in which case its value equals 0.44. When the above relationship is valid with the equality sign, one speaks of a transform-limited or unchirped pulse. For such condition to be satisfied, appropriate strategies have to be adopted to compensate for the temporal broadening of the pulse that possibly occurs when self phase modulation (SPM) - the variation of the phase with time due a variation of the refractive index with intensity for high intensities - combines with group velocity dispersion (GVD) - the variation of the group velocity with frequency.
The last parameter to be discussed, the most crucial one - actually - in determining the pulse duration, is the bandwidth. The latter grows with the number of phase-locked longitudinal modes, the ultimate limit being dictated by the gain bandwidth of the laser medium, which is peculiar to the atomic energetic levels involved in the lasing emission. To the present knowledge, the laser medium with the broadest tuning range is titanium-doped sapphire (Ti^{3+}:Al_2O_3), capable of operation over

the large interval of near-infrared wavelengths from ~ 660 to ~ 1180 nm [4]. A typical commercially available titanium-doped sapphire oscillator may deliver about 100 fs long pulses at a repetition rate around 80 MHz with an average output power in the order of several hundreds of mW, resulting in a pulse energy of several nJ and a peak power of several tens of kW.
While sufficient in many cases, for other applications such peak powers need to be raised - which is for sure the case if one wants to meet the goals of HED studies. This is possible, at the expense of a lower repetition rate, by using a regenerative amplifier: a single pulse from the oscillator is injected in a new resonator through an electro-optic switch, it there undergoes many round trips getting amplified by the gain medium (which is again a pumped Ti:Sapphire crystal) and it is finally released thanks to another electro-optic switch. Available fluences could not exceed 10^{14} W/cm^2 due to optical damage until the technique of chirped pulse amplification (CPA) was discovered by Mourou in 1985 [9]. Thanks to it, amplifications up to a factor 10^6 or greater without damage risks for the amplifier optics are achievable by including a pulse stretcher before the amplification stage to temporally elongate the pulse by means of dispersive optics and a pulse compressor after the amplification stage to recover the original pulse duration. Standard-performance chirped-pulse amplifiers can generate pulses with a typical average power of 5 W that, at a typical repetition rate of 1 kHz, correspond to a pulse energy of 5 mJ. Given a 100 fs pulse duration, this leads to a peak power of 50 GW and, considering an indicative focal area of 100 μm^2, to peak fluences of $5 \cdot 10^{16}$ W/cm^2. With advanced design compression setups, pulse durations down to below ≈ 5 fs are within reach of Kerr-lens mode-locked Ti:Sapphire lasers.

Attaining the same performances with EUV and X-ray light would be extremely desirable. Actually, even shorter pulses are in principle obtainable with this radiation, whose cycle periods are shorter than the about 2-3 fs cycle periods of near-infrared radiation. The difficulty, however, stands in the lack of materials with analogue properties to titanium-doped sapphire over that spectral region.
Downconvertion from optical to X-ray wavelengths via n-th order harmonic generation would be hopeless in the framework of "classical" non-linear optics, wherein the efficiency of harmonic generation rapidly decreases with increasing n order, scaling like the probability of having one high energy photon emitted as a result of the absorption of n low energy photons.

However, a new scenario emerges at ultra-high intensities, when the laser fields become comparable with the electric fields experienced by bound electrons inside atoms: $E_{las} \sim E_{at} \sim \dfrac{e}{4\pi\,\epsilon_0\,r_B^2} \sim 5 \cdot 10^{11}$ V/m, roughly corresponding to

[4] Consider, for comparison, that a helium-neon laser only operates in an interval of about 0.002 nm around 633 nm.

$\sqrt{\frac{\epsilon_0}{\mu_0}}|E_{at}|^2 \sim 10^{16}$ W/cm^2 [5]. Under these conditions, the standard perturbative regime of non-linear optics gives way to the so-called strong field regime, characterized by a negligible contribution to the induced polarization from bound electrons in favor of a dominant contribution from the electrons that have escaped the atomic Coulomb field through tunneling ionization [10]. The acceleration of those electrons by the laser electric field and their recombination with the parent ions upon reversal of the field direction half a period later are the key mechanisms leading to the release of high-energy photons in what is named high-order harmonic generation (HHG).

HHG from rare gases at moderate laser intensities of about 10^{13} W/cm^2 was first discovered by McPherson *et al.* in 1987 [11]. The emission spectra are observed to be made up of the only odd multiples of the laser frequency and to exhibit an initial decrease in intensity at low orders, then followed by a long plateau terminated by a sudden cutoff. Such features are explained by the three-step model proposed by Corkum in 1993 [12] to which we have already hinted: the superposition of the linearly polarized laser field around a maximum of the optical cycle to the atomic Coulomb field allows the continuum part of an electron wave function to tunnel; it then moves away from the atomic core and, half an optical cycle after, comes back; at recollision, it interferes with the bound part of the electron wave function giving rise to emission of a high energy wave packet (Fig. 3). Since one such pulse is emitted at every cycle of the driving femtosecond laser, a train of chirped attosecond XUV pulses is emitted for every incoming pulse.

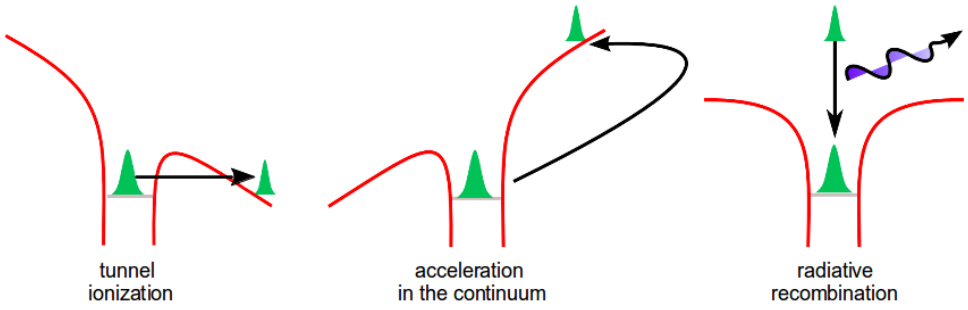

Figure 3: Schematic of the three-step model for the HHG process.
Taken from Ref. [13].

A classical calculation of the maximum energy that the ionized electron can gain in the laser field yields the cut-off of the harmonic plateau: $E_{max} = I_p + 3.17U_p$ where I_p is the ionization potential and U_p is the ponderomotive energy describing the average oscillation energy acquired by a free electron in the laser field:

[5] Whereas second harmonic generation, for example, was firstly demonstrated in 1961 using a ruby laser with an intensity of about 10^7 W/cm^2.

$U_p = \frac{e^2}{2\, m_e\, \epsilon_0\, c\, \omega^2} I$ with ω_L angular frequency of the laser radiation and I its intensity. Achieving higher harmonics would require higher intensities, which is however not possible since beyond 10^{15} W/cm^2 strong ionization of the gas, poor phase matching conditions and a deflecting action of the magnetic field on the returning electron prevent HHG at all. It is therefore believed that HHG from gases cannot be pushed beyond the state-of-the-art production of photons at about 100 eV energies in pulses with down to 80 as durations and few nJ intensities.

Much of the current efforts are directed toward an understanding of high-order harmonic generation from plasma mirrors. Actually, the very first observation of high-order harmonics - reported by Carman *et al.* in 1981 [14] - involved the interaction of laser light at 10.6 μm wavelength and more than 10^{15} W/cm^2 intensity with a solid target. Quéré *et al.* [15] claim the existence of two mechanisms, each prevailing in one of the two intensity regimes $a_0 \lesssim 1$ and $a_0 > 1$ ($a_0 = \frac{e\, E}{m_e\, c\, \omega_L}$ denoting the normalized vector potential) to which they refer as, respectively, coherent wake emission (CWE) and relativistic oscillating mirror (ROM).
CWE qualitatively works as depicted in Fig. 4: during one optical cycle, electrons are dragged out into the vacuum for up to several tens of nm and then back into the plasma where, as soon as they encounter a region with local density higher than the critical density $n_c = \frac{\epsilon_0 m_e}{e^2}\omega_L^2$, screened by the plasma, they escape the laser field (bringing away the acquired energy in what is known as Brunel absorption). When faster electrons join slower electrons, a bunch is formed which travels across the plasma at very high speed impulsively exciting plasma oscillations in its wake. In a kind of time-reversed resonant absorption, these oscillations emit one attosecond pulse of radiation per optical cycle whose energy content, dictated by the local plasma frequencies found in the density gradient, falls in the XUV.
At higher - relativistic - intensities (i.e. above 10^{18} W/cm^2 for 800 nm radiation), yet other processes are invoked as sources of high-order harmonics, like the mentioned ROM mechanism that, originally proposed by Bulanov *et al.* [17] and supported among other others by Quéré *et al.*, contrasts with the view of Baeva *et al.* [18].
We quit here a discussion that, although very fascinating and attracting a fast growing community [6], would bring us far away from our original scope of presenting the state-of-the-art techniques for the generation of short intense high-photon

[6] Worldwide, countless gigawatt- and terawatt-class lasers already exist, many petawatt-class lasers are now in either operation or development, and even an exawatt laser facility has been proposed, the European-founded "Extreme Light Infrastructure". Numerous and profound motivations prompt their spread, including for example the development of compact high-energy particle sources based on laser-plasma wakefield acceleration or the futuristic idea of reaching electric fields high enough to lead the formation of electron-positron pairs from vacuum!

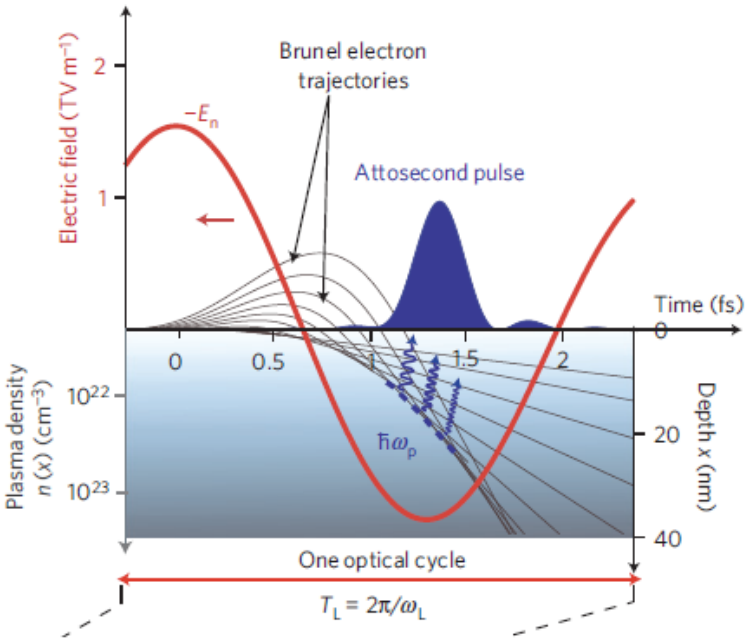

Figure 4: Sketch of the charge dynamics at the plasma surface responsible for the CWE process.
Taken from: [16]

energy pulses.

Leaving the world of lasers, there is another direction one would naturally look into at this purpose, and it points towards the world of synchrotrons.
Synchrotron radiation is produced whenever charged particles are radially accelerated. After its first observation in 1947, it was exploited parasitically at colliders designed for particle physics experiments (first generation sources) until recognition of its potentialities for materials sciences studies lead from the mid-70's to the construction of dedicated storage rings (second generation sources). Later on, installation of straight sections hosting wigglers and undulators magnetic structures in alternation with bending magnets in the curved sections of these machines made them evolve to a third generation optimized for an increased brightness [19] (Fig. 5).
The two main characteristics that led synchrotron radiation to be welcomed as revolutionary among scientists from a variety of disciplines are exactly its high brightness - namely, the large number of photons emitted per second and per unit source area into an unit solid angle - and its wide energy tunability - i.e., the broad spectrum extending with continuity between the far infrared and the hard X-rays. Other attractive properties are the high degree of polarization and the partial degree of coherence. Lastly, it is characterized by a pulsed time structure with typical

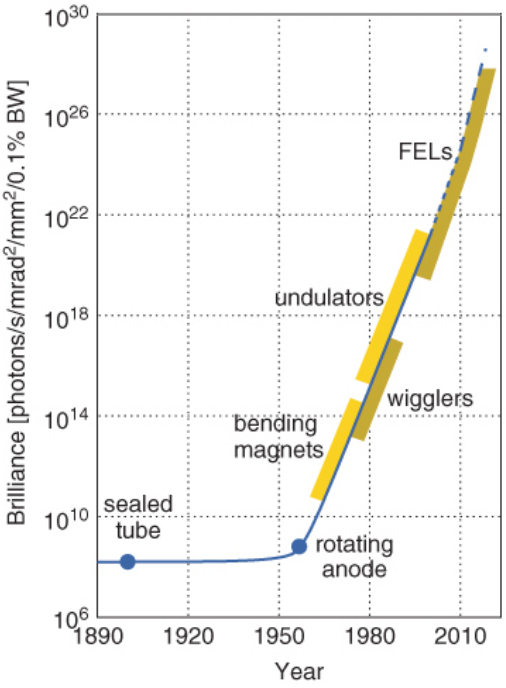

Figure 5: Increase in average brilliance achieved by synchrotrons as compared to laboratory X-ray sources.
Credits: P. Willmott.

pulse durations of tens to hundreds ps and typical pulse repetition rates of tens to hundreds ns. The latter descends from the temporal length and mutual separation of the bunches in which electrons are grouped, as dictated by the radio frequency cavity that has to give them back the energy lost due to synchrotron emission during a round trip in the storage ring.

When time resolution is needed, one possibility is to exploit time-gating detectors. Even the best streak cameras, however, cannot reach less than few ps time resolutions.
To beat this limitation, the method of femtoslicing has been proposed by Zholents *et al.* in 1996 [20] and is today implemented at a few storage rings worldwide. Fig. 6 provides a schematic illustration of its underlying idea: an intense femtosecond laser pulse is co-propagated with the electron bunch in an undulator inducing a modulation in the energy of a short slice of this bunch; electrons within the energy modulated slice will then follow slightly different paths through a dipole magnet and, in a second insertion device, they will emit short pulses of synchrotron radiation that will be easily separable from the regular beam; the process repeats at each laser pulse with a recirculated electron bunch.

Intrinsically synchronized to an external source of short intense laser pulses, the resulting short X-ray pulses are - unfortunately - not intense themselves, typical

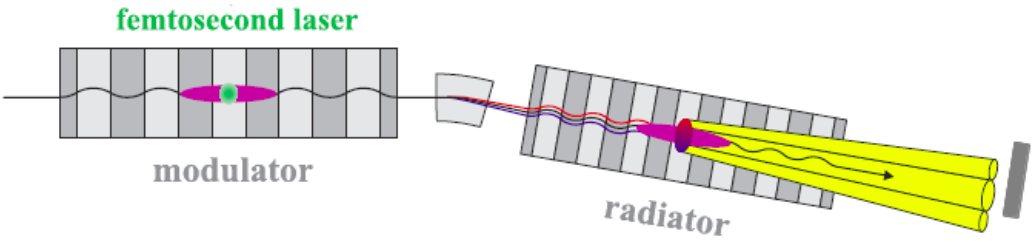

Figure 6: Principle of femtosecond slicing in storage rings.
Taken from Ref. [21].

average fluxes being in the order of 10^4-10^5 photons per second. Therefore, while their high temporal stability and extended energy range may be profitably exploited to probe fast dynamical processes, they cannot provide any significant excitation densities. Actually, the brightness at third-generation synchrotrons is still not yet sufficient for them to play a role in the generation of those extreme states of matter that we have instead seen to be within reach of modern optical lasers.
The brightness at third-generation synchrotrons is a joint outcome of the high flux and the small source size, the last being in turn determined by the combination of the small dimensions and divergence of the electron beam with the small angular distribution of the radiation itself. In recent years, intense optimization efforts have culminated in storage ring designs that honestly leave little space for further upgrades. Therefore, if looking for a significant advance in this respect, one needs to turn to radically different approaches.

Firstly proposed by Madey as long ago as 1971, one such approach aims at obtaining from accelerated electrons a true laser action by promoting synchronous, cooperative - i.e. stimulated, rather than spontaneous - synchrotron emission. These so-called free-electron lasers (FEL) - yielding peak brightnesses more than nine orders of magnitude higher than third-generation synchrotrons, full coherence and sub-100 fs pulse lengths - are already since few years an exciting reality.
All the experiments that will be discussed in this thesis made use of this extraordinary source, whose operating principles will be detailed in chapter .

0.1.2 Isochoric laser heating for the study of warm dense matter and its non-equilibrium precursor states

Trivially enough, the interaction of light with matter is regulated by the properties of light and by the properties of matter.
The first relevant factor is the energy of the photon as compared with the energy and the occupation of the electronic states in the material. EUV to hard X-ray

photons match well with the energies of core electrons; photoionization then occurs wherein a photon is absorbed and an electron is ejected from that core state. Photons whose energy is lower than the material ionization energies, like for visible radiation, are absorbed by free electrons during electron-ion collisions, a process known as inverse bremsstrahlung.
In the presence of photo-excited electrons, the target is turned into a plasma. Depending on its density, this plasma may display a collisional - at low (undercritial) plasma densities - or collective - at high (overcritical) plasma densities - behavior. In the latter case, the absorption of light is a highly non-linear process dominated by rather complex relativistic effects that also drive the generation of fast electrons, protons, neutrons and high-energy photons. As the critical plasma density scales with the square of the light frequency, the overdense regime is much less easier to reach for X-ray photons than for visible photons.

Even restricting our attention to the underdense regime, we have a poor knowledge of what happens at high irradiation intensities.
If the electrons get hot, the electron-ion collision frequency will change and, with it, the cross-section for inverse bremsstrahlung will also change. But how? Solid-state and plasma theories predict opposite trends for the dependence of the electron-ion collision frequency on the electronic temperature [22] and we are exactly studying a solid-state system which is turning into a plasma.
Our interpretation of core level spectroscopy experiments with synchrotron radiation is based on a weak field theory of photoionization. When will it break down and what should we expect to observe then? If multiple core-holes are simultaneously present in an atom its properties will be drastically changed and so its interaction with light. Can we hope to induce stimulated emission of X-rays [23]? These are just some of the questions that one may want to address.

Soon after the irradiation process, the photo-excited electrons have a kinetic energy which depends on the photon energy minus the energy needed to free them. This energy is redistributed among all other electrons via particle collisions within the successive tens to hundreds of fs. Only at this point, the electrons attain back a Fermi-Dirac energy distribution function and the concept of electronic temperature can be again applied.
Which exotic properties matter displays by that moment is something that still eludes our comprehension but that most probably has a relevant impact on how the successive de-excitation steps develop.
On slightly longer timescales, electron-phonon collisions transfer part of the electron energy to the lattice that heats until eventually reaching a common temperature with the electrons.
In metals subject to femtosecond laser irradiation, this process is commonly de-

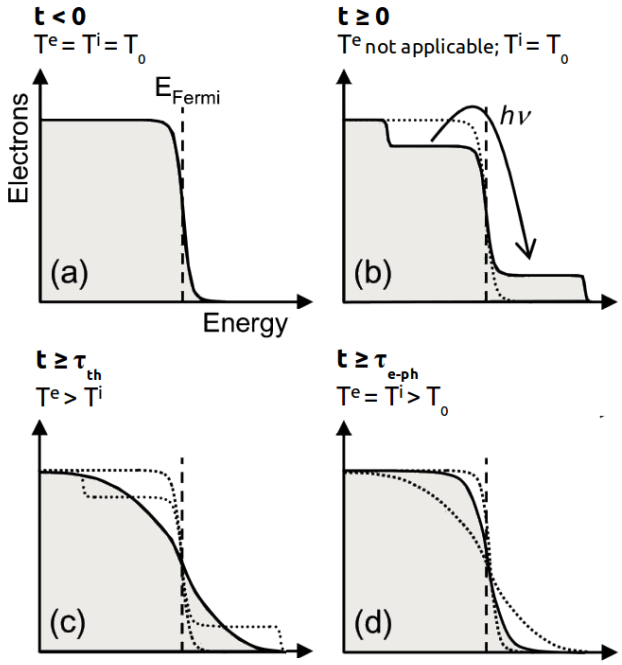

Figure 7: Femtosecond laser excitation creates a non-thermal electron distribution. The electrons first thermalise within them via electron-electron scattering and then equilibrate with the surrounding lattice via electronphonon coupling resulting again in the typical FermiDirac distribution.

scribed by the so-called two-temperature model, a system of two coupled equations depicting the energy exchange between the electrons and the lattice as driven by their temperature difference and a material-dependent electron-phonon coupling parameter [24]. At high excitations, however, such electron-phonon coupling parameter may no longer be constant but rather acquire a dependence on the electronic temperature; the same is true for the heat capacities [25] that enter those equations.

Since hydrodynamic expansion only occurs after some tens of ps from the incoming pulse, the whole process of excitation, equilibration and cooling is an isochoric one, i.e. the system initially retains the density of the starting solid. Therefore, when the irradiation intensity is high enough that, upon electron-phonon equilibration, the target reaches temperatures between 1 and 100 eV, we end up a region of density-temperature phase diagram which is known as warm dense matter (WDM). WDM is too hot to be described by condensed matter theories since, as the thermal energy becomes comparable to the Fermi energy, energy levels shift and broaden and more and more of them have to be included in a description of the system properties. At the same time, however, WDM is too dense to be described by plasma theories since, as the Coulomb energy becomes comparable to the thermal

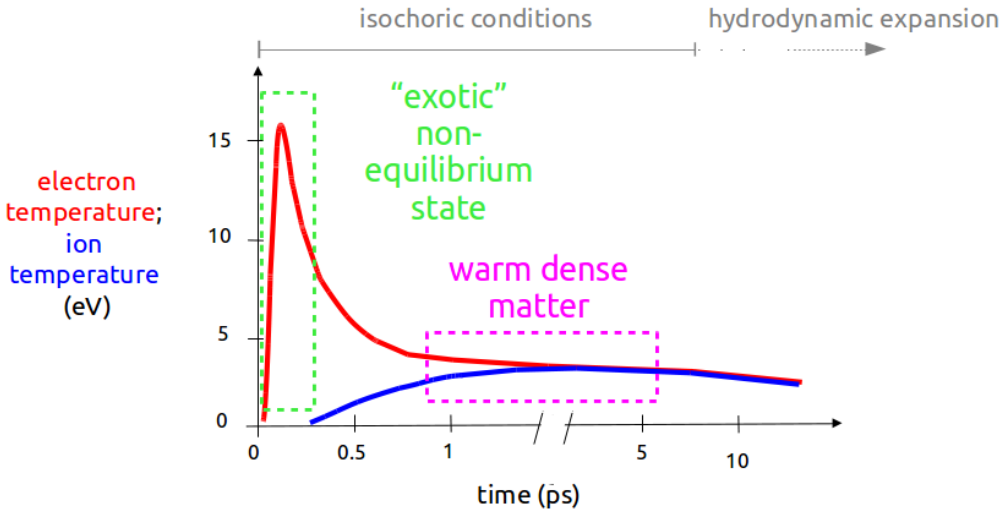

Figure 8: Typical response to ultrafast excitation: the target is quickly brought into a non-equilibrium state of hot electrons and yet cold ions, which evolves on a few ps timescale into an equilibrated warm dense matter state.
Credits: F. Bencivenga.

energy, particle correlations can no longer be ignored, nor the influence from the specific ionic structure.
Isochoric laser heating at FEL sources has the potential of shedding light on a state of matter that as much challenges current theories, as it is important to model astrophysically relevant bodies as well novel schemes for inertial confinement fusion.

0.2 Thesis structure

The outline of the dissertation is as follows.

- In chapter 1, I will explain the general working principle of a free electron laser, highlight the advantages of the seeding operation mode over the one based on self-amplified spontaneous emission and offer an overview of the main strategies to implement it. I will then enter the specific case of the FERMI FEL source, providing a comprehensive presentation of the facility that has been the playground for all the experiments reported in this thesis. With chapter 2, I will go through a description of the TIMEX beamline: from its optical and mechanical layout to the various FEL radiation diagnostic tools, from the control and acquisition infrastructure to the reduction of data.

- Explorative FEL self-transmission and self-reflection experiments in which a same pulse is acted as both a pump with its rising front and a probe with its

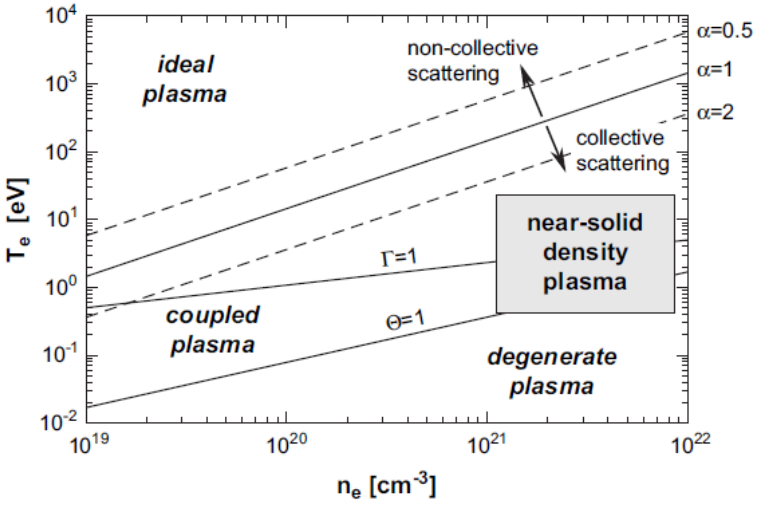

Figure 9: Exemplifying temperature / density phase diagram highlighting the region of near-solid density plasmas. Γ denotes the coupling parameter, i.e. the ratio of the interatomic potential energy to the thermal energy; Θ denotes the degeneracy parameter, i.e. the ration of the thermal energy to the Fermi energy. Taken from Ref. [26].

trailing front will be the object of chapter 3.
In particular, I will report about single-shot measurements on Ti samples aimed at determining the variation with irradiation intensity of the FEL absorption at the $M_{2,3}$ edge and of the FEL reflectivity in the vicinity of the plasma frequency.
I will also report about single-shot transmission experiments carried out on Al and Mg samples as a function of increasing FEL fluence at different wavelengths both below and above absorption resonances with the purpose of examining possible saturation effects.

- With chapters 4-5, a more proper way to handle time-resolved experiments will be introduced: a pump-and-probe approach - rendered possible at FERMI with the recent installation of an external user laser - in which either a FEL pulse acts as a pump and an optical laser pulse acts as a probe or the viceversa.
  To start with, I will present measurements of transient optical reflectivity on FEL-pumped Si_3N_4 samples that - routinely used as cross-correlators for readily adjusting the temporal superposition between FEL and laser pulses and characterizing their relative timing jitter - are also of great interest in themselves as they open a window onto the scarcely explored ultrafast electron dynamics following femtosecond EUV excitation of dielectrics.
  Next, I will discuss the results of an experiment conceived to study the laser-

induced melting transition in Ge from the novel perspective offered by time-resolved EUV absorption spectroscopy at the $M_{4,5}$ edge.
Lastly, in chapter 6 I will talk about an experiment performed on Si with similar purposes but under yet another scheme where - with the final availability of the splitting and delay line of FERMI - a double-color FEL emission has been exploited as a pump as well as as a delayed probe tuned at the $L_{2,3}$ absorption edge.

0.3 Author contributions

The work presented in this thesis makes part of a collective effort to address a topic which is as much fascinating as it is challenging, all the more so that it relies on the exploitation of experimental techniques at their infancy. With the "we" appearing all throughout the manuscript, I intend to acknowledge the contribution of the people that are or have been involved in the TIMEX project, with the awareness that, if I got the chance to bet my Ph.D. on it, it is also thanks to who conceived it and spent for its practical realization.
That said, this manuscript is not intended as a compilation of all works undertaken by the TIMEX collaboration, as much as it does not report on all the activities I afforded during my doctoral studies. Rather, it is build up on those subjects of primary concern to the TIMEX scientific program that have seen myself as an essential contributor.
People who have played a primary role in either the conception of an experiment or in the analysis of its results are time-by-time explicitly mentioned in the text.

Part I

First part

Chapter 1

The FERMI free electron laser

1.1 Free electron lasers

Free electron lasers are, at present, the most successful technology in offering a combination of the properties of high intensity, short pulse duration and coherence typical of a laser with the property of tunability across a broad spectral range extending up to the hard X-rays typical of a synchrotron.
Like in a synchrotron, the source are accelerated free electrons emitting synchrotron radiation at their passage with relativistic speeds through the magnetic field generated by an undulator. Like in a laser, light intensity grows up because coherent emission is stimulated that leads to amplification by interferential effects. What gets amplified at the detriment of the electrons' kinetic energy is an electromagnetic field co-propagating with the electron beam, that can be either the spontaneous undulator emission - in which case we have a so-called self-amplified spontaneous emission FEL - or an external signal - in which case we have a so-called seeded FEL.
Let us take a closer look to the mechanism of production of free electron laser radiation.

1.1.1 Operating principles

Consider a planar undulator magnet of period λ_u producing a magnetic field oriented in the vertical y direction whose strength varies sinusoidally along the longitudinal z direction: $\vec{B} = B_y(z) = B_0\, cos(k_u z)$, with $k_u = 2\pi/\lambda_u$. An electron entering the undulator with relativistic velocity directed along z will wiggle in the transverse x direction emitting synchrotron radiation at each curve (Fig. 1.1). Integration of the Lorentz equation $\gamma m\vec{a} = -e\vec{v}\times\vec{B}$, once introduced the undulator

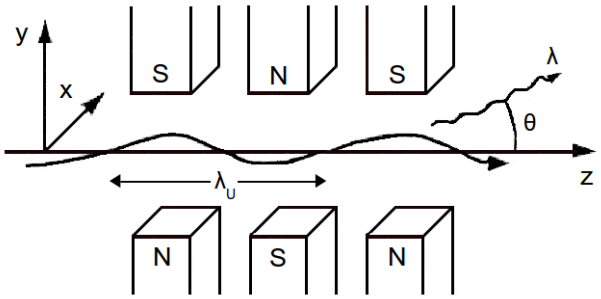

Figure 1.1: Spontaneous radiation emission by an electron wiggling in a planar undulator.

parameter $K = \dfrac{e\,B_0}{m\,c\,k_u}$, gives - to first order in x and to second order in z:

$$\begin{cases} v_x = \dfrac{c\,K}{\gamma}\sin(k_u z) \\ v_z = c\sqrt{\beta^2 - \dfrac{v_x^2}{c^2}} \simeq c\left[1 - \dfrac{1}{2\gamma^2}\left(1 + \dfrac{K^2}{2}\right) + \dfrac{K^2\,cos(2k_u z)}{4\gamma^2}\right] \end{cases}$$

Passing to the coordinate system that moves at the electron average longitudinal velocity $\langle v_z\rangle = c\,\langle\beta\rangle$, the Lorentz transformations $t' = \langle\gamma\rangle\left(t - \langle\beta\,\rangle\dfrac{z}{c}\right)$ and $z' = \langle\gamma\rangle\,(z - \langle\beta\rangle\,c\,t)$ yield:

$$\begin{cases} x'(t') = -\dfrac{c\,K}{\gamma\,\omega_u}cos(\omega' t') \\ z'(t') = \dfrac{c\,K^2}{8\gamma^2\,\omega_u}sin(2\omega' t') \end{cases},$$

which show that the electron performs a transverse oscillation at the harmonic frequency $\omega' = \gamma\,\omega_u$, together with a faster longitudinal oscillation that - at this stage - we neglect (it will be responsible for second harmonic emission).
The electron will then emit dipole radiation at the frequency ω' that, in the laboratory reference frame, will appear Doppler shifted as $\omega_r = \omega'\langle\gamma\rangle(1 - \langle\beta\rangle\cos\theta)$, being θ the angle formed with the z axis.
Within the approximations $\langle\gamma\rangle \simeq \gamma$, $\langle\beta\rangle \simeq 1 - \dfrac{1}{2\gamma^2}\left(1 + \dfrac{K^2}{2}\right)$ and $\cos\theta \simeq 1 - \dfrac{\theta^2}{2}$, one therefore ends up with the following expression for the peak wavelength of the spontaneous undulator emission:

$$\lambda_r = \frac{\lambda_u}{2\gamma^2}\left(1 + \frac{K^2}{2} + \gamma^2\theta^2\right) \tag{1.1}$$

Regarding its bandwidth, one can provide an estimate by considering that, in an undulator made of N_u periods, each electron radiates a wave with an electric field hav-

ing the same number of cycles: $E_r(t) = \begin{cases} E_0\, e^{i\,\omega_r\,t} & \text{for } -T/2 < t < T/2 \\ 0 & \text{otherwise} \end{cases}$, where $T \simeq \dfrac{N_u\,\lambda_r}{c}$. Squaring its Fourier transform $A(\omega) = \dfrac{1}{\sqrt{2\pi}} \displaystyle\int_{-\infty}^{\infty} E_r(t)\, e^{-i\,\omega\,t} dt = \dfrac{2E_0}{\sqrt{2\pi}} \dfrac{sin(\Delta\omega\, T/2)}{\Delta\omega}$ thus results in a spectral intensity $I(\omega) \propto \left(\frac{\sin\xi}{\xi}\right)^2$, where $\xi = \dfrac{\Delta\omega\, T}{2} = \pi\, N_u \left(\dfrac{\omega - \omega_r}{\omega_r}\right)$, which is indeed centered at the frequency ω_r and has a bandwidth of about $1/N_u$.

Now consider a light wave propagating along the same direction as the electron beam and polarized in the x direction: $\vec{E_l} = E_x(z,t) = E_0\, cos(k_l\, z - \omega_l\, t + \psi_0)$. The change of the electron energy in its presence is given by $\dfrac{dW}{dt} = -e\,\vec{v}\cdot\vec{E}$, that is: $\dfrac{d(\gamma\, m\, c^2)}{dt} = -\dfrac{e\, c\, K\, E_0}{2\gamma} \left\{\sin\left[(k_l + k_u)\, z - \omega_l\, t + \psi_0\right] - \sin\left[(k_l - k_u)\, z - \omega_l\, t + \psi_0\right]\right\}$. Neglecting the second term - that, quickly varying, cancels out - and introducing the ponderomotive phase $\psi = (k_l + k_u)z - \omega_l\, t + \psi_0$, the resulting equation

$$\frac{dW}{dt} = -\frac{e\, c\, K\, E_0}{2\gamma} \sin\psi \tag{1.2}$$

shows that the energy exchange rate depends on the phase of the electrons in the ponderomotive potential exerted by both the undulator and the radiation fields: electrons with a phase between $-\pi$ and 0 gain energy from the electromagnetic wave, so their trajectories are less bent and they move to the head of the packet while electrons with a phase between 0 and π release energy to the electromagnetic wave, so their trajectories are more bent and they move to the tail of the packet. For a continuous energy transfer to occur, the relative phase between the electrons and the light must stay constant, a condition - $\dfrac{d\psi}{dt} = (k_r + k_u)\langle v_z\rangle - k_r\, c = 0$ - which comes up as equivalent to require $\lambda_r = \dfrac{\lambda_u}{2\gamma^2}\left(1 + \dfrac{K^2}{2}\right)$, i.e. that the light wavelength be the same as the one characterizing the spontaneous undulator radiation in the forward direction. Indeed, the spontaneous undulator radiation is the one satisfying the requirement that the light advances the electrons by one wavelength at each undulator period, that is: $\lambda_r = c\left[\lambda_u \left(\dfrac{1}{c} - \dfrac{1}{\langle v_z\rangle}\right)\right]$, whence - once again - Eq. [1.1]. Allowing for an energy variation relative to the resonance wavelength - $\eta = \dfrac{\gamma - \gamma_r}{\gamma_r}$ - results in a variation of the ponderomotive phase. Actually,

$\frac{d\psi}{dt} = (k_l + k_u)\langle v_z \rangle - k_l\, c$ - when inserting the resonance condition for k_l - returns

$$\frac{d\psi}{dt} = 2\, k_u\, c\, \eta. \tag{1.3}$$

Eq.s [1.2] and [1.3] - which put together give $\frac{d^2\psi}{dt^2} + \Omega^2 \sin\psi = 0$ with $\Omega^2 = \frac{e\, E_0\, K\, k_u}{m}$ - are known as the pendulum equations of a low gain FEL, so-called because fully equivalent to the second-order differential equation describing the motion of a mechanical pendulum. The resulting electron trajectories in the (ψ, η) phase space - namely, the curves of constant Hamiltonian

$$H(\psi, \eta) = k_u\, c\, \eta^2 + \frac{e\, E_0 K}{2\, m\, c\, \gamma_r^2}(1 - \cos\psi)$$

- are shown in Fig. 1.2, with close orbits corresponding to small-amplitude harmonic oscillations and open orbits corresponding to complete rotations in the pendulum analogy. Note that the ponderomotive phase is in one-to-one relationship with

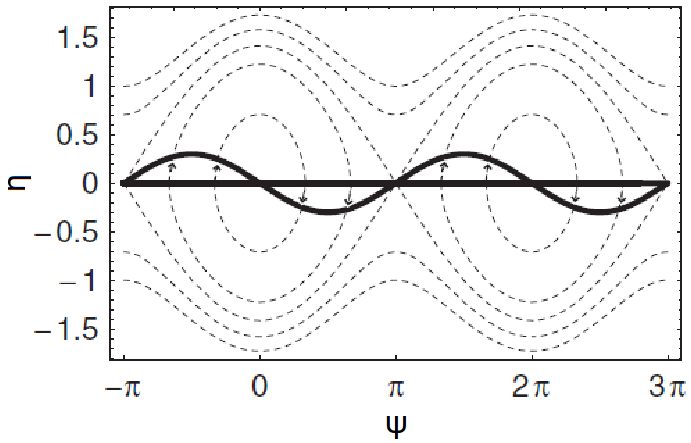

Figure 1.2: Electron motion in the longitudinal phase space: an initial distribution of the electron beam on a straight line changes into a distribution on a sinusoidal line, implying that the energy and the density of the electron beam are modulated, i.e. micro-bunched.
Taken from Ref. [27].

the electron longitudinal coordinate inside the bunch. In fact: if, for a reference electron exchanging no energy with the light, it is

$$z_r(t) = \langle v_z \rangle t \text{ and } \psi_r(t) = (k_l + k_u)\langle v_z \rangle t - w_l\, t - \tfrac{\pi}{2},$$

then, for an arbitrary electron with longitudinal internal bunch coordinate ζ, it is

$$z_r(t) = \langle v_z \rangle t + \zeta(t) \text{ and } \psi_r(t) = (k_l + k_u)\,[\langle v_z \rangle t + \zeta(t)] - w_l\, t - \tfrac{\pi}{2}\,,$$

from which $\psi_0 = (k_l + k_u)\,\zeta_0 - \dfrac{\pi}{2}$ or $\zeta_0 = \dfrac{\psi_0 + \frac{\pi}{2}}{k_l + k_u} \simeq \left(\psi_0 + \dfrac{\pi}{2}\right) \dfrac{\lambda_l}{2\pi}$.
The pendulum equations hence describe the combined evolution of the longitudinal density and relative energy deviation of the electrons under the Lorentz force due to the undulator magnetic field and the light wave electric field, whose amplitude has been so far assumed constant.

One should consider - however - that, whereas normally the total power of the emitted radiation depends linearly on the number of electrons in a bunch because each of them emits with an uncorrelated phase, once micro-bunching has set in, all electrons within a bunch radiates in phase resulting in a total emitted power that depends quadratically on their number. In turn, the more intense the electromagnetic wave gets, the more the electrons tend to bunch (Fig. 1.3), thus giving rise to a positive feedback loop. The constraint of a constant amplitude light wave must be - evidently - abandoned if one wish to describe a high-gain FEL process. Rather, self-consistent treatment is required of the development of the electron bunching together with the growth of the radiation field driven by the transverse electron current density $\vec{j}$ as described by the wave equation

$$\left[\vec{\nabla}^2 - \frac{1}{c^2}\frac{\partial^2}{\partial t^2}\right] \vec{E} = \mu_0 \frac{\partial \vec{j}}{\partial t} + \frac{1}{\epsilon_0}\vec{\nabla}\rho \tag{1.4}$$

as well as with the evolution of the space charge field associated to the longitudinal electron charge density ρ as evaluable through the Maxwell equation

$$\vec{\nabla} \cdot \vec{E} = \frac{\rho}{\epsilon_0}. \tag{1.5}$$

Due to the large number of electrons, one is faced with a many-body problem without analytical solution.
Following Ref. [28] - of whose reasoning we will only outline the main steps and results - a normalized particle distribution function may be introduced

$$F(\psi, \eta, z) = \Re\left\{\tilde{F}(\psi, \eta, z)\right\} = F_0(\eta) + \Re\left\{\tilde{F}_1(\eta, z) \cdot e^{i\psi}\right\}$$

in terms of which, with $\delta \ll 1$ such that $F_0(\eta)$ vanishes identically for all $|\eta| \geq \delta$,

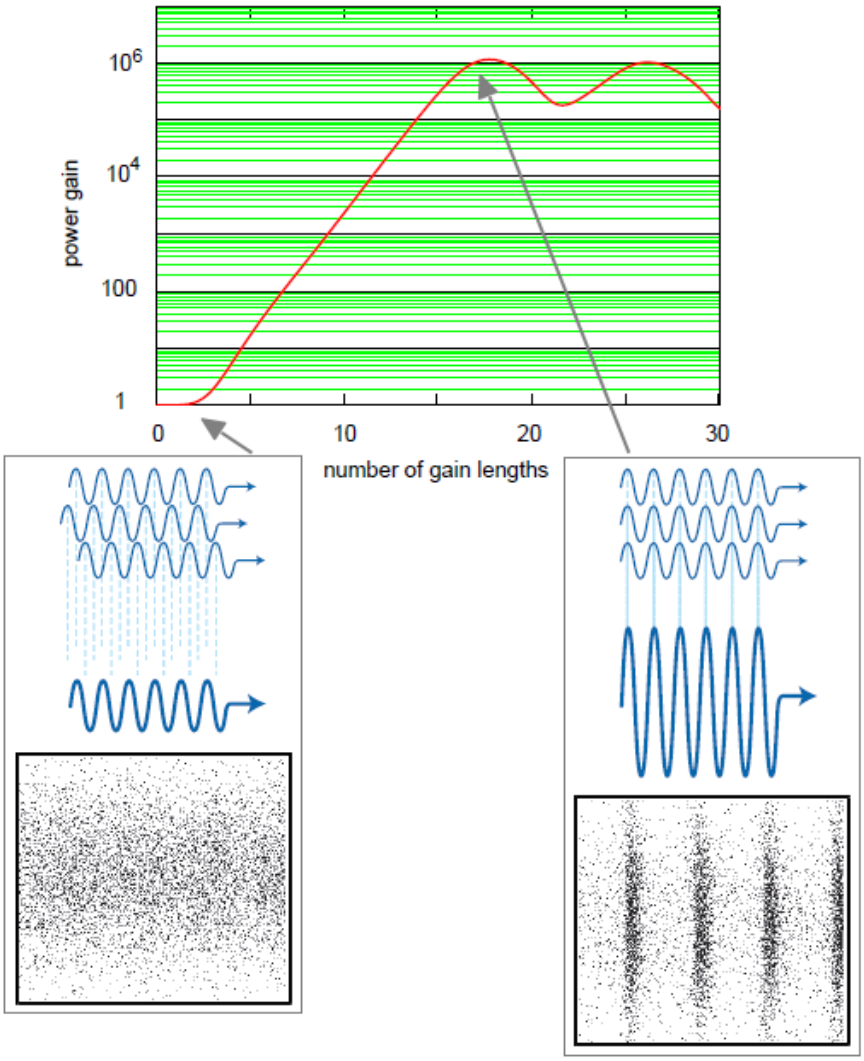

Figure 1.3: Interaction between the electrons and a co-propagating light wave (like their own emitted radiation) triggers the formation of micro-bunched electrons, that emit in phase leading to a progressive amplification of the light wave along the undulator. $P_{in} = E_{in}^2$ and L_G^0 are defined as explained in the main text (soon after Eq. 1.7).
Credits: P. Schmüser (adaptation from figures in Ref. [28]).

the charge and current densities are respectively expressed as

$$\tilde{\rho}_1(z) = \rho_0 \int_{-\delta}^{\delta} \tilde{F}_1(\eta, z) d\eta \text{ and } \tilde{j}_1(z) = j_0 \int_{-\delta}^{\delta} \tilde{F}_1(\eta, z) d\eta.$$

By virtue of Liouville's theorem stating the conservation of the space space volume

occupied by an ensemble of particles along their trajectory, F obeys a generalized continuity equation - known as the Vlasov equation

$$\frac{dF}{dz} = \frac{\partial F}{\partial z} + \frac{\partial F}{\partial \psi}\frac{d\psi}{dz} + \frac{\partial F}{\partial \eta}\frac{d\eta}{dz} = 0$$

- that, within the assumption $\left|\tilde{F}_1(\eta, z)\right| \ll |F_0(\eta)|$ of small density modulations, inserting the pendulum equations (Eq.s [1.2] and [1.3]) and the equations for the light wave and space charge fields (Eq.s [1.4] and [1.5] with proper approximations), can be shown to lead to a third-order differential equation for the electric field amplitude of the light wave solely:

$$\frac{d^3\tilde{E}_x(z)}{dz^3} + 4ik_u\eta\frac{d^2\tilde{E}_x(z)}{dz^2} + \left(k_p^2 - 4k_u^2\eta^2\right)\frac{d\tilde{E}_x(z)}{dz} - i\Gamma^3\tilde{E}_x(z) = 0, \tag{1.6}$$

where the space charge parameter k_p and the gain parameter Γ appear, defined - respectively - as:

$$k_p = \sqrt{\frac{2k_u\mu_0 n_e e^2 c}{\gamma_r m_e \omega_l}} \text{ and } \Gamma = \left[\frac{\mu_0\hat{K}^2 e^2 k_u n_e}{4\gamma_r^3 m_e}\right]^{1/3},$$

being $\hat{K}$ the undulator parameter modified to account for the electrons' longitudinal oscillations.
Eq. [1.6] can be solved analytically by choice of a trial function $E_x(z) = A\, e^{\alpha z}$. Assuming a mono-energetic beam ($W = W_r$) and neglecting space charge forces ($k_p = 0$, acceptable in cases of low electron density n_e or large electron energy γ_r), it reduces to $\frac{d^3\tilde{E}_x(z)}{dz^3} - i\Gamma^3\tilde{E}_x(z) = 0$, whose solution is easily seen to read:

$$\tilde{E}_x(z) = \frac{E_{in}}{3}\left\{e^{\left(i+\sqrt{3}\right)\frac{\Gamma z}{2}} + e^{\left(i-\sqrt{3}\right)\frac{\Gamma z}{2}} + e^{-i\,\Gamma\, z}\right\},$$

i.e. a light field that, at sufficiently large undulator distances, is dominated by the exponential growing term:

$$\left|\tilde{E}_x(z)\right| \approx \frac{E_{in}}{3}e^{\frac{\sqrt{3}}{2}\Gamma\, z} \equiv \frac{E_{in}}{3}e^{\frac{z}{2L_G^0}} \tag{1.7}$$

Above, E_{in} denotes the intensity of the light wave at $z = 0$, while $L_G^0 = \frac{1}{\sqrt{3}\Gamma}$ is the power gain length, a lower limit for what represents the distance over which the power increases by a factor e in real cases - that have to confront with the effects of energy spread, angular divergence and transverse beam size of the electron beam,

with diffraction effects of the light wave, as well as more subtle mechanisms (e.g. quantum recoil or quantum diffusion) (Ref. [27]).
As the electrons lose energy to the light, their relative phase continuously changes until - eventually - the direction of the energy exchange reverses and saturation of the FEL amplification takes place. In this regime, the radiation power stands at a value approximately equal to $\rho\, P_e$, where P_e is the electron beam power and $\rho = \dfrac{\Gamma}{2k_u} = \dfrac{1}{2\sqrt{3}\, k_u L_G^0}$ is the so-called dimensionless Pierce parameter.
Importantly, the latter quantity - which typically assumes values in the 10^{-3} range for soft X-ray FELs and of few 10^{-4} for hard X-ray FELs - turns out to be a measure, not only of the saturation power, but also of the bandwidth at saturation that, therefore, qualifies as very narrow.

1.1.2 Main schemes

An FEL can work in one of the basic configurations depicted in Fig. 1.4 and briefly analyzed in the following.

Oscillator FEL

In a so-called oscillator FEL (Fig. 1.4, panel a), spontaneous undulator emission - trapped in an optical cavity - is amplified by successive interactions with a re-circulated electron beam.

The fact that high-gain amplification need not to be reached within a single pass relaxes the otherwise stringent demands on the electron beam qualities, rendering the oscillator scheme exploitable at existing storage rings - that typically provide electrons of lower current, with larger energy spread, but at a higher repetition rate and with better stability. This possibility makes it the preferred approach in those wavelength regions where good quality mirrors are available, which means - unfortunately - only above 170 nm.

SASE FEL

In a so-called SASE FEL (Fig. 1.4, panel b), spontaneous undulator emission is amplified during a single passage of an electron beam through an undulator chain.

Such a layout potentially gives complete wavelength tunability, as it exclusively relies on the fact that any random electron distribution has a shot noise spectrum that provides a non-null density modulation (what is named the bunching factor) at every wavelength.
Very high peak powers may be reached, provided one disposes of a low emittance injector (where emittance stays for the electron beam transverse phase space area,

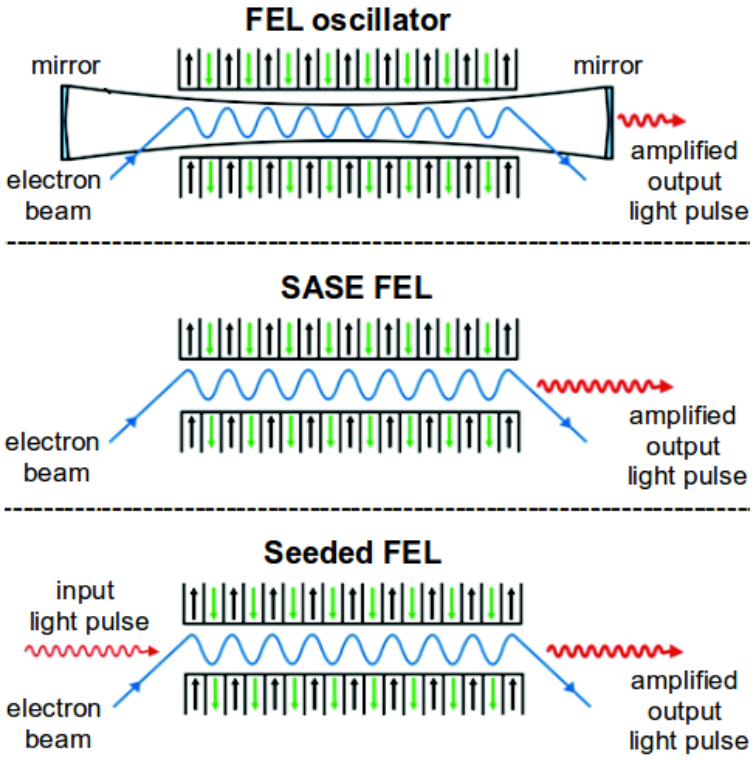

Figure 1.4: Main FEL configurations.
Credits: S. Milton.

i.e. size times divergence) and a long enough undulator section - not without repeated correcting manipulations on the electron beam all along its path. The tight requirements on the electron beam also comprise its duration, that must fit the desired duration of the FEL pulse - a purpose for which bunch compressors are mandatory.

A serious drawback of this scheme, however, is that it lacks control over the spectral and temporal properties of the radiation, which reflect in their randomness the stochastic nature of the startup process.

Indeed, each electron can only interact with the radiation generated by the electrons that are ahead of it by certainly no more than the total slippage $N_u\lambda_r$. Even more stringently, the interaction is limited - at all practical effects - to a distance within the electron bunch equal to the electron / radiation slippage over one gain length, a quantity which is known as the cooperation length: $l_c = \lambda_r L_g^0/\lambda_u = \lambda/(4\pi\rho)$. Therefore, toward the end stage of amplification, a correlation is established which smooths the random changes in the phase and amplitude of the emitted light waves from an initial scale on the order of λ_r to a final scale on the order of l_c. Despite

this cleaning effect, the output FEL pulses cannot be fully coherent because, the bunch length τ typically being much longer than the cooperation length, a number $M = \tau/(2\pi l_c)$ of uncorrelated spikes (the so-called longitudinal modes) originates from each electron bunch (Fig. 1.5). Within a single spike, the intensity has a

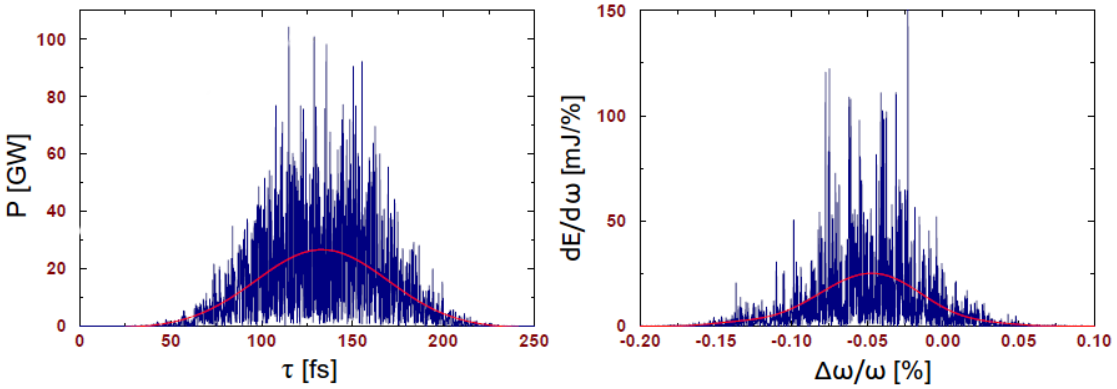

Figure 1.5: Typical temporal (*left*) and spectral (*right*) distributions of a single radiation pulse from a SASE FEL. Smooth lines show averaged profiles.
Taken from Ref. [29].

negative exponential distribution whereas, within a single pulse made by many such spikes, the intensity follows a Gamma distribution with a root mean square (rms) relative fluctuation of $1/\sqrt{M}$ (Fig. 1.6). It follows that the bandwidth -

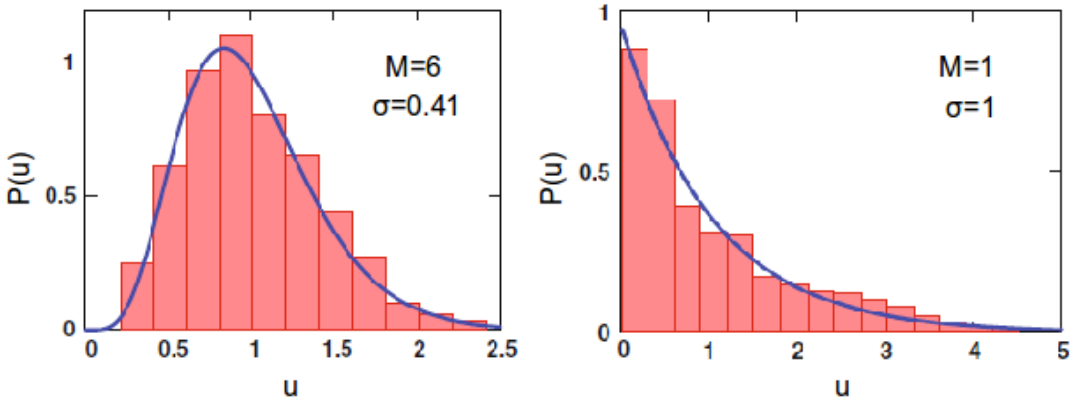

Figure 1.6: Normalized distributions of the energy of two SASE pulses containing a different number of spikes. In the second case (*right*), where a single longitudinal mode is selected by means of a monochromator, shot-to-shot fluctuations grow to 100%.
Taken from Ref. [28].

inversely proportional to the coherence time - is much larger than the Fourier-transform limited value for that pulse duration would be.

Seeded FEL

In a so-called seeded FEL (Fig. 1.4, panel c), by interaction with electrons passing through an undulator chain, an external "seed" laser is amplified.

External seeding brings several improvements over the SASE operation mode. First of all, the central wavelength, bandwidth, intensity and duration of the output FEL pulses are controllable to a larger extent and possess a higher degree of shot-to-shot stability.
Full coherence is achieved, the longitudinal coherence being inherited from that of the seed laser. Together with it, one gets an improved brilliance and Fourier-transform limited pulses, i.e. characterized by a time-bandwidth product which is the smallest allowed by the uncertainty principle (Fig. 1.7).
Additionally, such a scheme allows for a reduction of the overall undulator length needed to achieve saturation and provides a laser source automatically synchronized to the FEL radiation.
Of course, a seeding source capable of wide tunability would be desirable in order to preserve such an important characteristic of FEL light. This constitutes - however - a major problem, especially toward short wavelengths. In this regard, all the efforts that are currently being done in the direction of providing laser radiation at shorter than ultraviolet (UV) wavelengths prove useful. So, for example, high harmonic generation in noble gases up to now represents the most promising seed source above 30 nm.

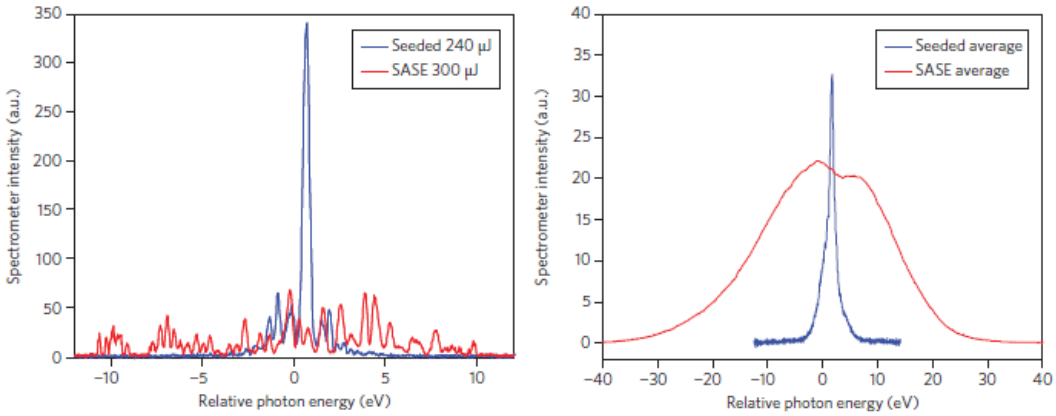

Figure 1.7: Single-shot (*left*) and averaged (*right*) FEL spectra in SASE mode (*red*) and self-seeded mode (*blue*). The fwhm single-shot seeded bandwidth is 0.4 eV, whereas the SASE fwhm bandwidth is $\sim$ 20 eV. Vertical scales have the same arbitrary units.
Taken from Ref. [30].

1.1.3 Seeding methods

Increasing efforts are being devoted to design alternative seeding schemes for covering those wavelength regimes where no sources are available for direct seeding. A short list of the proposed/implemented ideas is here below provided.

Self-seeding

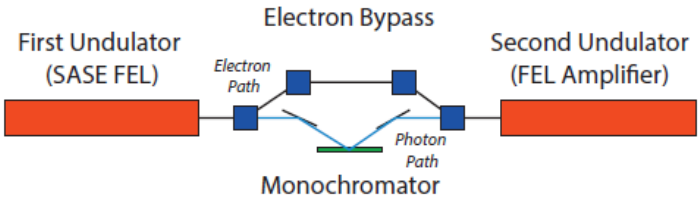

Figure 1.8: Schematic layout of a self-seeding configuration.
Taken from Ref. [31].

Not yet saturated SASE radiation produced in a first undulator chain and later filtered to a narrow bandwidth with a monochromator provides the seed source for a second undulator chain where it gets amplified up to the saturation level in the interaction with the electron beam that, after the exit of the first undulator, has traversed a dispersive bypass to have its micro-bunching smeared out.
Very short wavelengths may be reached with this configuration, but an undulator system almost twice as long as a single-stage is required and no synchronized external signal is available.

In another variant - the regenerative amplifier FEL (RAFEL) - the SASE radiation is spectrally filtered as above, but then brought back at the beginning of the same undulator where it propagates together with a second electron bunch. The same scheme is repeated with further electron bunches until exponential amplification of the monochromated FEL light is reached.
The convenience obviously lies in the reduced length of the undulator section. On the other hand, however, electron packets highly uniform in both energy and space need to be provided in order to have a good quality of the output pulses guaranteed.

High-gain harmonic generation (HGHG)

Interaction of an electron beam with a seed laser in a first short undulator (referred to as the modulator) produces an energy modulation, which is converted into a density modulation at a higher harmonic of the seed frequency as the electron beam passes through a magnetic chicane. Radiation is thus generated by the so-bunched electrons and amplified until saturation in a second undulator (referred to as the

radiator), that is set at resonance with the high harmonic frequency. The process can be better visualized with the help of Fig. 1.9 depicting the evolution of the electron longitudinal phase space during FEL generation.
The main advantage of this scheme is that the properties of the output FEL pulses mirror those of the high-quality seed laser, as discussed above.
Unfortunately, a single HGHG stage does not allow to reach high frequency multiplication factors - primarily because, the higher is the harmonic number (n), the larger the energy modulation amplitude must be (approximately n times the slice energy spread). The consequent substantial deterioration of the beam properties then contrasts with the general requirement that the energy spread be smaller for shorter wavelengths.
Thus, for example, the generation of FEL light in the X-rays using an UV seed laser resorts to a cascaded HGHG scheme, where the output of the radiator from one stage provides the seed signal for the modulator of the following stage. In the latter configuration - which undoubtedly represents a remarkable design complication - the problem of beam deterioration may be circumvented by feeding each cascading stage with a fresh portion of the electron bunch.

Echo-enable harmonic generation (EEHG)

A HGHG stage comprising one modulator seeded by a laser of frequency ω_2, one dispersive section and one radiator is preceded by a stage comprising one modulator seeded by a laser of frequency ω_1 and one dispersive section so that, at the exit of the second chicane, the beam displays a longitudinal modulation with wavenumber $k = nk_1 + mk_2$, being n and m two integers. The strength of the first chicane is 1-2 orders of magnitude larger than that of the second one in order to give rise to several well-separated energy bands at a same longitudinal position. This allows for the generation and amplification of high harmonics when the following HGHG stage converts to a density modulation the energy modulation of each band. The electron longitudinal phase space as it evolves through the main steps of an EEHG process is shown in Fig. 1.10.
A major advantage of EEHG over HGHG is the higher up-conversion efficiency obtainable with a small increase in the slice energy spread. In fact, while in HGHG the bunching factor exponentially decreases with the harmonic number, in EEHG the bunching factor of a specific harmonic number can be intentionally maximized. Moreover, extremely short (< 10 fs) FEL pulses may be generated by regulating the superposition between the two lasers.

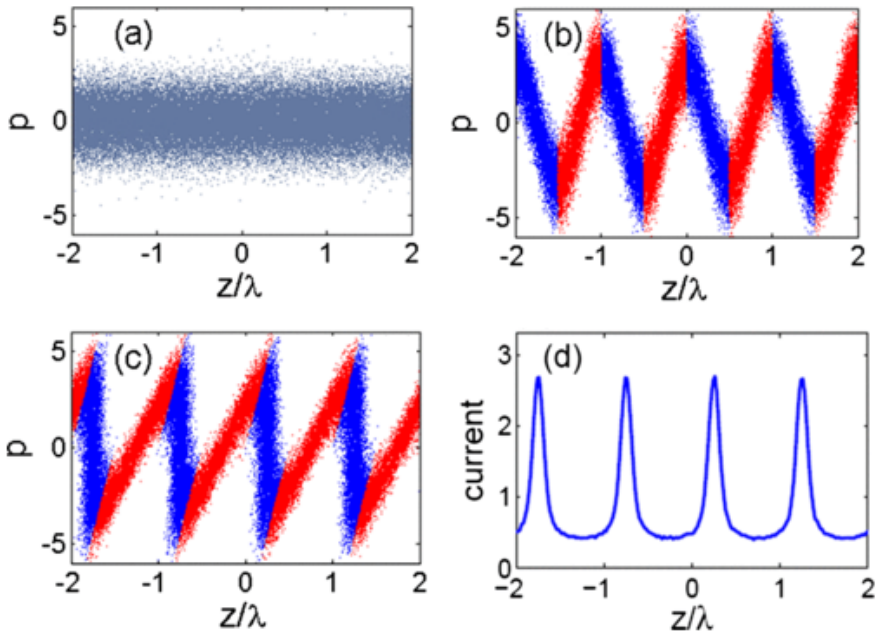

Figure 1.9: Evolution of the electron longitudinal phase space in a HGHG scheme from before the modulator (*a*) to after the modulator (*b*) and to after the chicane (*c*), and density distribution after the chicane normalized to the initial beam current (*d*). The horizontal axis is the beam longitudinal position normalized to the laser wavelength and the vertical axis is the particles energy deviation with respect to the reference particle normalized to the rms slice energy spread of the beam. The energy modulation is 3 times larger than the beam energy spread.
Taken from Ref. [32].

Additional methods

To conclude, we only hint at two other methods that provide seeding by electron beam manipulation, like HGHG and EEHG, but, contrarily to these, do not use any laser source, being rather relatively simply implementable in a SASE configuration.

- The method suggested by Emma *et al.* [33] foresees to place a thin film with a narrow vertical slot at the center of a magnetic chicane, where the electron beam is tilted at a large angle relative to the longitudinal axis. In this way, Coulomb scattering will increase the emittance of all electrons, exception made for those of a central thin slice that - unspoiled - will be the only ones to reach full power saturation.
  So-produced FEL pulses feature full coherence and durations as short as 1 fs or less, at the expenses - however - of a lower power.

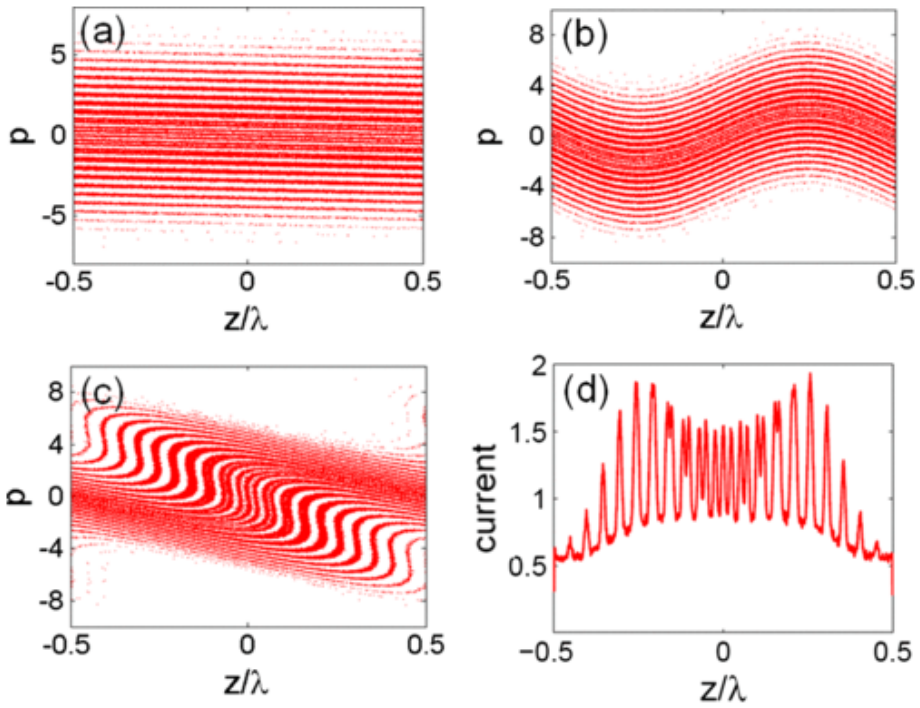

Figure 1.10: Evolution of the longitudinal phase space in a EEHG scheme: (*a*) after the first strong chicane, (*b*) after the second modulator, (*c*) after the second weak chicane; (*d*) density distribution after the second chicane.
Taken from Ref. [32].

- Another way of isolating the spikes of a SASE FEL - proposed by Saldin *et al.* [34] - simultaneously exploits a chirped electron beam and a tapered undulator, i.e. a linear variation of the energy along the beam longitudinal coordinate, which is compensated with a proper variation of the peak magnetic field along the beam propagation axis.
  Ultra-short pulses can thus be obtained, with a narrow spectrum and even a high pulse energy, as recently demonstrated in Ref. [35].

1.2 FERMI@Elettra

The work presented in this thesis has been conducted at FERMI, the free electron laser facility located in Trieste close to the synchrotron facility Elettra.

FERMI is a seeded source of FEL photons in the extreme ultraviolet and soft X-ray spectral ranges. It comprises two separate lines: FEL-1 that - based on a single stage of high gain harmonic generation - covers wavelengths between 100 and 20 nm (12 to 62 eV) roughly yielding 10^{14} photons per sub-100 fs pulse at 100 nm, and FEL-2 that - based on a double stage HGHG cascade in the "fresh bunch" injection mode - covers wavelengths between 20 and 4 nm (62 to 310 eV) roughly yielding 10^{13} photons per sub-100 fs pulse at 10 nm [36].
A detailed list of planned and so far achieved values for the most important machine parameters of both FEL-1 and FEL-2 is given in Tables 1.1 and 1.2 [37].

Lasing from FEL-1 was firstly observed in December 2010. Commissioning activities and optimization studies went on until, in December 2012, the facility opened to the first external users. Meanwhile, development of FEL-2 was started, leading to lasing of the first stage in May 2012 and of the second stage in the October of the same year. With an energy upgrade of the LINAC, in March 2013, demonstration of the capability of FERMI to operate at wavelengths as short as 4 nm was finally given [38].
Three end-stations are fully operative at the time of writing: TIMEX, that will be the object of the next chapter; DiProI, a beamline dedicated to DIffraction and PROjection Imaging; and LDM, a beamline dedicated to Low Density Matter (atoms, molecules and clusters in the gas phase). Three further end-stations are under construction: MagneDYN, a beamline for ultra-fast magnetodynamical studies; TeraFERMI, a beamline that will exploit the electron beam in the main beam dump to generate femtosecond, high intensity, broadband THz pulses; and finally - in a more advanced state of development - TIMER, an end-station thought for TIME-Resolved spectroscopy of mesoscopic dynamics in condensed matter (basically, an instrument for FEL-based four wave mixing experiments) that, together with TIMEX, makes part of the Elastic and Inelastic Scattering (EIS) beamline. In July 2014, using a semplified setup arranged at DiProI, a proof of principle for the kind of challenging experiments that TIMER intends to pursuit has been given [39] thanks to the joint efforts of the EIS and DiProI teams. // As visible from the aerial view of Fig. 1.11, the whole facility is hosted in three main buildings: the linear accelerator (LINAC) tunnel, the undulator hall and the experimental hall. Their main components are sketched in Fig.s 1.12, 1.14 and 1.17, respectively and described in the following sections.

FEL-1 PARAMETERS	*project goals*		*so far acheived*	
Electron beam Energy	1.2	GeV	1 - 1.5	GeV
Bunch Charge	800	pC	500 - 800	pC
Peak Current	850	A	300 - 800	A
Bunch Length (fwhm)	700	fs	600 - 1300	fs
Norm. Emittance (slice)	0.8 - 1.2	mm·mrad	1.2 - 1.5	mm·mrad (estimated)
Energy Spread (slice)	150 - 250	keV	100 - 200	keV
Wavelength	100 - 20	nm	100 - 20 (**)	nm
Photon energy	12 - 62	eV	12 - 62	eV
Tunability	continuous		continuous (**)	
Pulse Length (fwhm)	30 - 100	fs	30 - 100	fs (estimated)
Bandwidth ΔE (rms)	$\sim$ 20 - 40	meV	22 @32 nm	meV
Relative bandwidth ΔE/E (rms)	$\sim 5 \cdot 10^{-4}$		$2.5 \cdot 10^{-4}$ @32 nm	
Bandwidth fluctuations (rms)	-		$\sim$ 3% @32 nm	
Polarization	variable		LO/LC/RC	
Repetition Rate	10 - 50	Hz	10	Hz
Energy/pulse	>100	μJ	20 - 100 (*)	μJ
Peak Power	1 - 5	GW	0.2 - 1 (*)	GW (estimateed)
Photons per pulse	10^{14} @100nm		$\sim 10^{13}$ @32 nm	
FEL mode	TEM00		TEM00	
Power Fluctuation	$\sim$ 25%		-	
Central Wavelength Fluctuation	within bandwidth		$\sim$ 1.1	meV
Output Transverse Position Fluctuation	50	μm	-	
Pointing Fluctuation	<5	μrad	-	
Output Spot Size (fwhm@waist)	290	μm	-	
Divergence (rms)	50 @40nm	μrad	-	

Table 1.1: Machine parameters for FEL-1.
(*) Depending on wavelength. Up to two times higher by relaxing spectral purity.
(**) Tuning range continuous in selected regions, depending on seed laser.
Taken from Ref. [37].

FEL-2 PARAMETERS	*project goals*		*so far acheived*	
Wavelength	20 - 4	nm	14.4 - 4 (*)	nm
Photon energy	62 - 310	eV	86.1 - 310 (*)	eV
Pulse Length	<100	fs	-	
Bandwidth	$\sim$ 20 - 40	meV	0.1 @10.8nm	eV
Polarization	variable		Variable	
Repetition Rate	50	Hz	10	Hz
Peak Power	$\sim$ 1	GW	-	
Photons per pulse	$1 \cdot 10^{13}$ @10nm		$3 \cdot 10^{12}$ @10.8nm	
			$3 \cdot 10^{11}$ @6.5nm	
			$2 \cdot 10^{10}$ @4nm	
Power Fluctuation	>50 %		20% @10.8 nm	
Central Wavelength Fluctuation	within bandwidth		$\sim$ 3 @10.8 nm	
Output Transverse Position Fluctuation	50	μm	-	
Pointing Fluctuation	<5	μrad	-	
Output Spot Size (fwhm@waist)	140	μm	-	
Divergence (rms)	15 @10nm	μrad	-	

Table 1.2: Machine parameters for FEL-2.
(*) Integer harmonics of the seed at 260 nm.
Taken from Ref. [37].

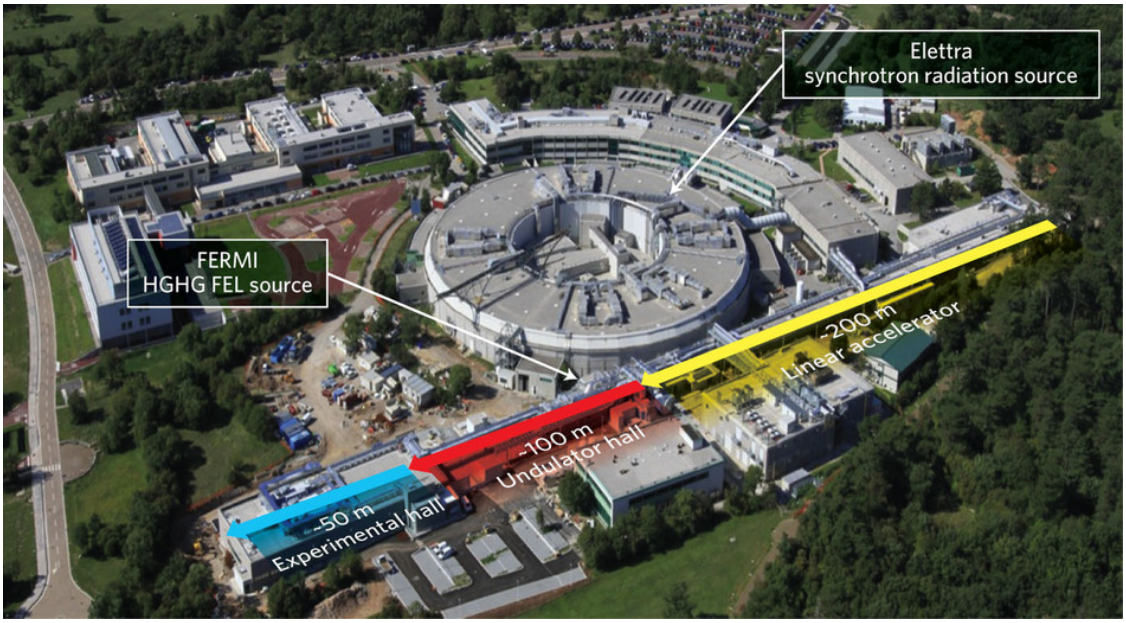

Figure 1.11: FERMI and Elettra facilities in Trieste.
Taken from Ref. [40].

1.2.1 The LINAC

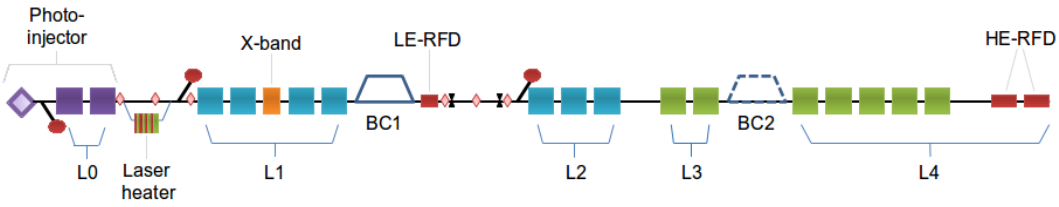

Figure 1.12: The linear accelerator tunnel of FERMI. Different colors denotes different types of accelerators.
Taken from Ref. [41].

A high brightness electron beam is generated by the impact of a UV laser on a copper cathode and pre-accelerated up to $\sim$ 100 MeV in the *photo-injector* itself, that includes two booster cavities (L0) equipped with solenoids for compensation of space charge -induced emittance growth.
In typical working conditions, an electron bunch at the exit of the photo-injector may have a duration of approximately 10 ps, a charge up to 1 nC, a slice emittance below 1.2 mm-mrad and an energy spread below 2 keV. The electron bunch repetition rate has been 10 Hz up to now, an upgrade to 50 Hz being planned for the near future.

The *main LINAC* comprises four stages (L1 to L4) of normal-conducting travelling-

wave accelerating structures working at a radio frequency of 3 GHz (S-band), that bring the electron beam to a final energy of $\sim$ 1.2 GeV for FEL-1 operation and $\sim$ 1.5 GeV for FEL-2 operation.

For higher peak currents to be reached, two *bunch compressors* - located at $\sim$ 320 MeV (BC1) and $\sim$ 670 MeV (BC2) - squeeze the electron bunch length by first inducing a correlation between the energy and the longitudinal position of the electrons (through off-crest acceleration) and then guiding electrons with different energies along different paths (through a magnetic chicane) so that electrons in the tail of the bunch almost catch up with those at the front.
Two main bunch configurations have been envisaged in the conceptual design stage: a 0.8 nC "medium length" bunch (MLB) - preferable for FEL-1 - yielding a peak current of 800 A upon compression from 9 ps to 700 fs, and a 1 nC "long" bunch (LB) - preferable for FEL-2 (for accommodating two seed laser pulses one next to the other within a same bunch) - yielding a peak current of 500 A upon compression from 11 ps to 1.4 ps. Commissioning activities, however, mainly concentrated on shorter (2.8 ps), lower current (500 pC) beams and a single stage of compression.

Actually, the spatial displacement Δz undergone by an electron in a bunch compressor is not simply a linear function of its energy separation ΔE from the reference energy E_0, rather: $\Delta z = R_{56}\frac{\Delta E}{E_0} + T_{566}\left(\frac{\Delta E}{E_0}\right)^2 +$ higher order terms. Then, installed half-way between the four sections of L1, an RF cavity working at the fourth harmonic of the main LINAC frequency (*X-band*) de-phased with respect to the other sections has the role of pre-compensating the quadratic chirp component introduced during the bunch compression in order for this process to return a charge density uniform across the bunch.

At high compression factors, micro-bunching instabilities take place: density modulations that - originating from shot noise, longitudinal space charge fields or whichever other source - significantly degrade the beam quality. To suppressed them, a so-called *laser heater* section is placed soon after the photo-injector, made of a short undulator in a weak magnetic chicane where interaction with an external laser causes an energy modulation of the electron beam that, smeared out in the second half of the chicane, does not convert into a spatial modulation but purely results in an increase of the incoherent energy spread.
Besides this, it has demonstrated [42] that, as a consequence of the actual energy spread induced by the laser heater being non-Gaussian, the FEL power at high harmonics is strongly enhanced with respect to the foreseen Gaussian case, allowing a much larger tuning range to be covered with a single HGHG stage.

Four *transfer lines* - one between the gun and the booster cavities, one in the laser heater area, one at the end of the first bunch compressor and one at the end of the LINAC - host quadrupole magnets for transverse beam matching, various

screens for beam profile imaging and spectrometer lines for invasive measurements of the electron beam energy and energy spread. Moreover, three *transverse deflectors* - one after the first bunch compression region (LE-RFD) and two at the end of the LINAC (HE-RFD) - allow, when turned on, bunch length determination and slice parameter measurements (i.e. characterization of parameters pertaining to each longitudinal portion of the electron bunch of the order of the cooperation length).

For high FEL performances, the electrons should have flat current and energy profiles and a low slice energy spread. Indeed, a linear chirp in the bunch energy distribution would mainly results in a shift of the FEL wavelength and a quadratic chirp in an increase of its bandwidth. The time jitter between the electron bunch and the seed laser, in combination with these elements, would then transfer into fluctuations of both the spectrum and the intensity of the output radiation.
Keeping under control the electron longitudinal phase space is - however - a delicate task, since it is affected by many factors: besides the mentioned non-linear chirp coming from the bunch compressor through the second order dispersion term T566, unavoidable contributions come from the accelerating sections (as the sinusoidal shape of the radio frequency field imparts a negative quadratic chirp to the "on-crest" bunch) and longitudinal wakefield effects (causing the beam to lose energy and acquire an energy spread along the bunch).
The deflecting cavity at the end of the LINAC, kicking the electron bunch in the vertical direction, together with a spectrometer bending magnet, energy dispersing the electrons in the horizontal direction, and an imaging screen therefore prove very useful for properly setting the laser heater and X-band parameters as well as the accelerating cavity phases during LINAC optimization. Fig. 1.13 reports few examples taken from Ref. [43] of electron phase spaces and current and energy spread profiles obtained in such way.
If the installation of both the laser heater and the X-band in May 2012 already led to a significant improvement of the machine performances, further steps ahead are going to be undertaken, following for example the experimental demonstration - given in Ref. [44] - of the benefits of ramp shaping the temporal profile of the photo-injector laser intensity.

1.2.2 The undulators

A system of bending magnets - called the "*spreader*" - carries the electron beam from the LINAC to one of the two parallel, 1 m spaced, undulator lines. It is at this point of their trajectory that the electrons join the seed laser pulses.

FEL-1 consists of a single stage made of one 3 m long undulator with a period of 10 cm the "*modulator*" - a *dispersive section* and six 2.4 m long undulators with

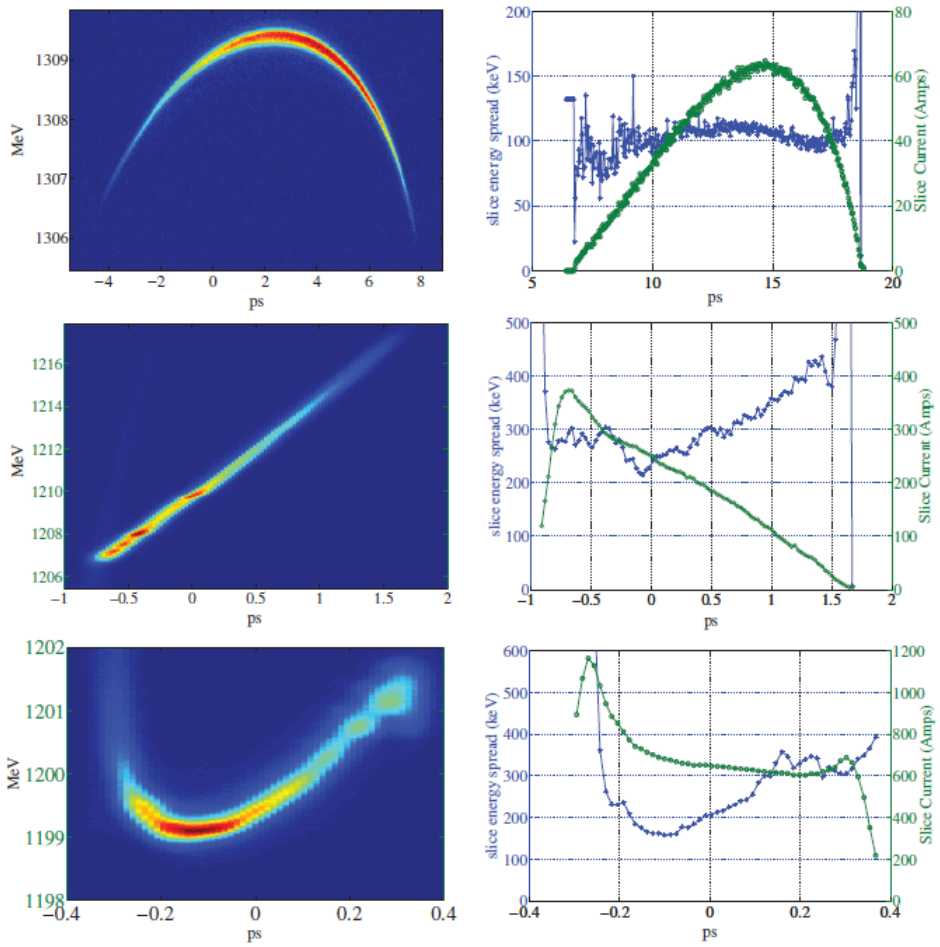

Figure 1.13: Electron beam longitudinal phase space (*left*) and corresponding time-sliced energy spread (*right, blue curve*) and time-sliced current (*right, green curve*) as measured at the end of the LINAC for three exemplifying cases. *Top*: 500 pC uncompressed bunch. The electron charge being distributed on a long bunch, the slice current is low, leading to a low FEL intensity. *Middle*: No laser heater and no X-band, all RF sections on crest. The current has a ramped profile with higher values at the head of the bunch where microbunching instabilities are recognizable as "hot spots". *Bottom*: With laser heater and X-band and all RF sections on crest but the last two which are set +30° off crest. The flatness of the current profile is optimized, allowing to push the compression further and thus reach higher peak currents; the residual quadratic chirp - however - will affect the FEL spectrum, broadening its bandwidth.
Taken from Ref. [43].

a period of 5.5 cm the "*radiators*".
FEL-2 features a first stage - operating in a low gain regime - which mimics FEL-1 except that the radiators are two, followed by a second stage - operating in the

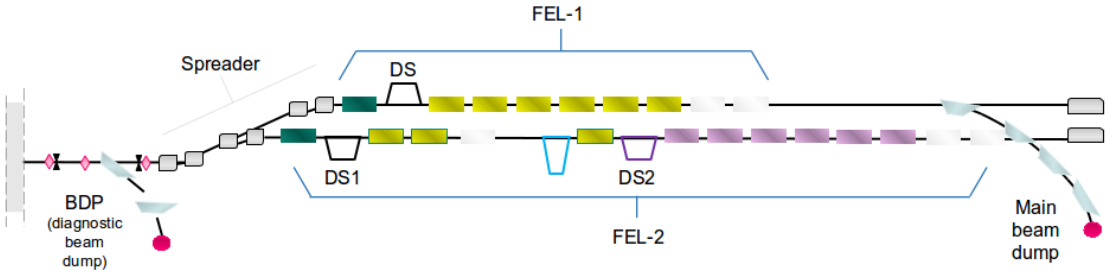

Figure 1.14: The undulator hall of FERMI.
Taken from [41].

high gain regime - with one more modulator, an additional dispersive section and six more radiators, the latter with a lower period of 3.5 cm. A magnetic chicane placed between the two stages delays the electron bunch with respect to the co-propagating FEL pulse and destroys the bunching induced by the first stage.
Whereas the modulators are made by simple planar undulators, the radiators are made by helical undulators of the Apple II type, the most efficient among the insertion devises able to provide full control of the light polarization state.
All undulators have variable gaps (from 220 down to 10.5 mm) in order to guarantee FEL wavelength tunability at constant electron beam energy, as we will better see in the following.

Permanent magnet *phase shifters* installed between every two radiator sections help the electron beam to maintain the right phase relation with respect to the radiation.

The electron beam position is non-invasively measured with sub-micron resolution before entering the modulators and before each radiator module using *cavity beam position monitors*, i.e. exploiting the dipole resonant mode excited by the electrons at the passage through a C-band cavity, whose intensity in the horizontal and vertical polarizations is proportional to the beam offset in the x and y directions.

The spatial overlap between the electron and seed laser beams is adjusted using a steering mirror for the seed laser and checked on two fluorescent screens of cerium-activated yttrium aluminum garnet (chemical formula, $Y_3Al_2O_{12}$, hereafter named "*YAG*") placed before and after the modulators.

Before the modulators, a fast photodiode monitors the time synchronization between the two beams by simultaneously detecting the seed laser and the visible radiation produced by the electrons when crossing the interface of two media with different dielectric constants in a so-called *OTR* screen. Delays shorter than 6 ns can be compensated by a delay line on the seed laser path, whereas longer delays call for an adjustment of the electronic trigger sent to the seed laser.

Final optimization of the seeding process is accomplished by observing the electron beam spectrum on a YAG screen at the main beam dump spectrometer line. Electrons from the portion of the beam that has come in spatial superposition with the seed laser are, in fact, recognizable as a dark area on that screen (Fig. 1.15), because they have moved away from their initial position along the bunch as a result of the interaction.
Using this signature, it is also possible to measure the timing jitter between the two beams, as explained in Ref. [45].

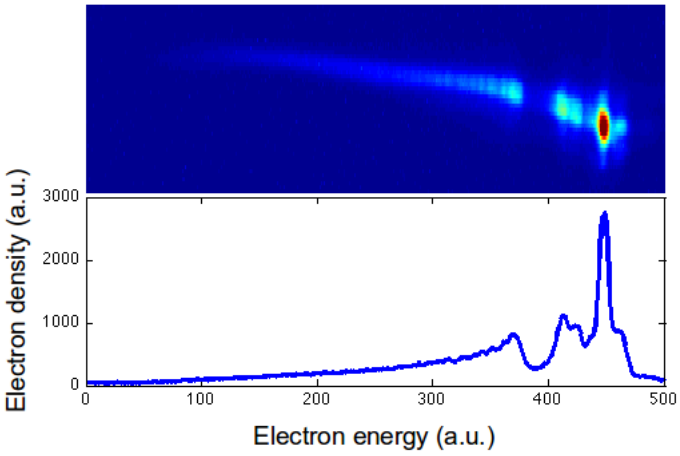

Figure 1.15: Electron beam spectrum at the main beam dump. The zone of charge depletion marks the occurred interaction with the seed laser.
Credits: E. Allaria.

1.2.3 The seed laser

The HGHG process is initiated by the same external laser for both FEL lines. In consideration of the need for a broad tuning in the UV range, this is provided by the the mechanism of optical parametric amplification (OPA) in the infrared followed by a sequence of frequency mixing processes.
As peak powers in excess of 100 MW are required to produce strong enough bunching, the OPA is pumped by the amplified output of a Ti:Sapphire oscillator: the oscillator delivers pulses centered at $\sim$ 780 nm with a Fourier-transform limited duration of 70 fs which are sent to a 10 Hz commercial regenerative amplifier, in-house upgraded by adding a single-pass amplifier stage to raise the maximum output energy from 3.3 to 6.5 mJ.
The OPA is a TOPAS-C from Light Conversion, a two stage optical parametric amplifier of white-light continuum that outputs signal and idler waves spanning continuously from 1150 nm to 2600 nm [46].

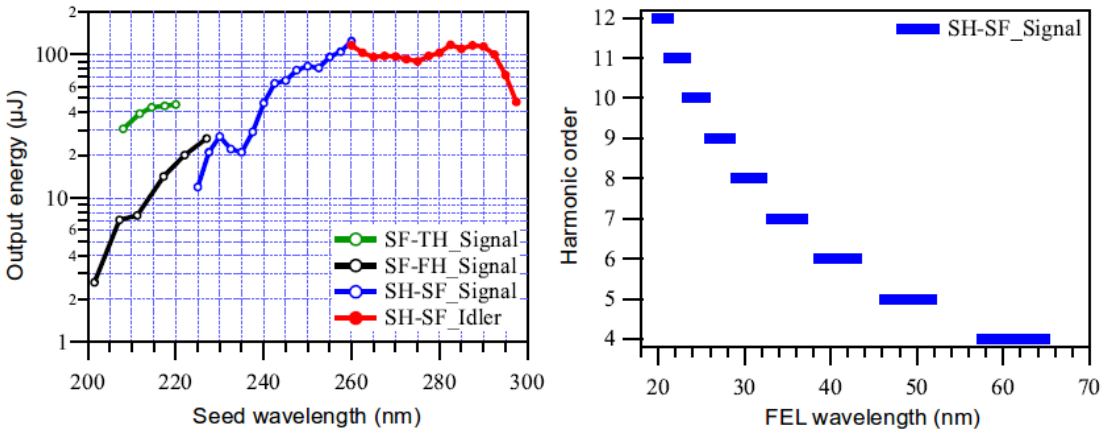

Figure 1.16: *Left*: possible ways of providing seed laser tunability in the 200-300 nm wavelength range. *Right*: FEL wavelength tunability achievable in $4th$ to $12th$ harmonic with a seed given by the second-harmonic of the sum frequency between the pump and the signal waves.
Taken from Ref. [47].

Fig. 1.16 provides an overview of possible up-conversion mechanisms turning UV into EUV light: a combination of sum-frequency generation (SF), second-harmonic (SH), third-harmonic (TH) and fourth-harmonic (FH) generation processes. Combined with the demonstrated capability of FERMI of producing FEL harmonics up to the 12-th, these schemes guarantee operations over a wide portion of the FEL-1 range.
The main working configuration for the experiments up to now conducted has been the one that returns pulses in the 228-262 nm range, with energies between 10 and 100 uJ, relying on the second-harmonic of the sum frequency between the pump and the signal waves (blue curve in Fig. 1.16).
More recently, seeding with the fourth harmonic of the signal giving coverage of the 285-365 nm range has also been successfully tested.
A major part of the earliest commissioning activities, on the other hand, has been done using as a seed the third harmonic of the Ti:Sapphire amplifier output. This possibility always exists for all those applications in which wavelength tunability is not requested while higher energies are desirable that, in this option, come together with better spatial quality and pulse-to-pulse stability. Actually, a small tunability of about 1% around the central wavelength of 261 nm may result from a fine rotation of the angle of the third harmonic crystal, which - in combination with a switch to different FEL harmonics - can still be exploited in a number of cases.

A spectrometer allows to determine the seed laser wavelength shot-by-shot and within an uncertainty of about 0.1 nm.

The pulse length can be determined by cross-correlation of the seed pulse with a portion of the IR pulse extracted from the Ti:Sapphire oscillator: the two pulses overlap in a non-linear crystal and the intensity of the generated sum frequency pulse is recorded as a function of their relative time delay yielding a Gaussian profile whose fwhm is the sum in quadrature of the fwhm durations of the generating pulses.
The seed signal from third harmonic generation has a typical bandwidth of about 0.8 nm fwhm, to which a Fourier-transform limited duration of 120 fs should correspond. In practice, the actual pulse duration is around 200 fs, due to various sources of chirp that, however, can be partially compensated with a grating compressor leading to a final duration of about 140 fs. Regarding the seed signal from the OPA, since it is not compressed at present, it is characterized by an increased time-bandwidth product, which is the higher, the greater is the energy per pulse due to stronger self-phase modulation.

By means of a periscope system with multilayer mirrors conceived to cover the widest range with the smallest losses, the seed laser beam arrives in the undulator hall, where it is focused at the entrance of the modulator to maximize the overlap with the electron bunch at the beginning of their interaction.

Tight synchronization of the seed laser with the electron beam is ensured by the timing distribution system of FERMI, thoroughly described in Ref. [45]. Here, an upper limit of 63 fs rms over 40 s is reported as a timing jitter, based on correlated measurements of the FEL central wavelength fluctuation and the seed laser/electron bunch delay.
Since the whole laser setup of FERMI - comprising, besides the seed laser, also the photo-injector laser, the laser heater and the user laser - needs to be synchronized with the global clock system of the machine, there is a proposal, discussed in Ref. [48], to replace the mode-locked Ti:Sapphire oscillators of the various laser units by a single ultra-fast optical master oscillator (UOMO) - possibly a Er/Yb fibre laser generating sub-picosecond laser at around 1550 nm - that will also provide the clock for RF plants of the facility with sure advantages of simplification in the laser architecture, cost reduction and - most importantly - automatic synchronization.

1.2.4 The user laser

An analogous timing jitter of the order of several tens of fs would also characterize the synchronization between the FEL beam and any external laser a user may want to use to perform pump-probe experiments. Had it not that an alternative strategy has been adopted at FERMI, which consists in using different portions of the same IR pulse generated by the aforementioned Ti:Sapphire amplifier both as a seed for the FEL process and as an external laser to be delivered at the beamlines.

Already, the timing jitter accumulated by the electron bunch in the LINAC - mainly due to noise in the power that feeds the accelerating cavities and to a conversion of energy fluctuations into time fluctuations operated by the bunch compressors - does not count in a seeded scheme. When, in addition, the seed and external laser pulses are derived from the same source, one gets rid of the timing jitter that originates from synchronization errors of both lasers with their reference signal and from the noise affecting the distribution of the reference signals themselves and is are left with the only timing jitter which is acquired during the transport of both beams.

Ref. [49] provides a detailed description of the beam transport, whose optical and mechanical components have been thoughtfully designed to minimize pulse losses and lengthening as well as movements induced by slow temperature gradients and acoustic noise from the environment, and along which a certain number of control points with CCD cameras for beam position diagnostics and actuators for beam steering have been disposed to operate an active beam stabilization down to a few μm level. There reported are also the results of measurements that aimed at evaluating, by recording the intensity fluctuations at the steepest point of various cross-correlation curves, the separate contributions to the timing jitter coming from the 150 m long beam path from the seed laser location to the end-stations optical breadboards - estimated to be $\sim$ 3.2 fs - and that from the OPA (which is part of the only seed laser system) - estimated to be $\sim$ 6.7 fs.

Evaluation of the overall timing jitter between the seed and user lasers has also been conducted at both the DiProI and TIMEX beamlines by measurements of FEL-induced transient reflectivity changes on various semiconductor systems [50]. As I was personally committed to these activities, they will be the subject of a dedicated chapter.

1.2.5 The photon transport and diagnostic system

At the exit of the undulators, while the electrons are deviated by a sequence of bending magnets to a beam dump, the FEL radiation proceeds toward the experimental area passing through the Photon Analysis Delivery and REduction System (PADReS) [51], a section hosting photon diagnostics and beam tailoring optics to characterize and manipulate the photon beam while transporting it to the various end-stations.

The layout of PADReS is shown in Fig. 1.17.
For both FEL lines, there are, in sequence: a shutter, a beam defining aperture (BDA), a beam position monitor (BPM), an intensity monitor (I0M_UH), a differential pumping system, a gas absorber and, on the other side of the wall between the undulator hall and the so-called safety hutch, a second differential pumping system,

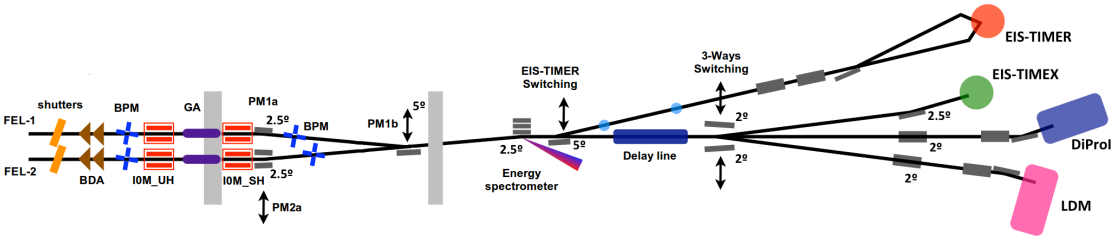

Figure 1.17: Layout of the photon transport and diagnostic system of FERMI.

a second intensity monitor (I0M_SH), a second beam position monitor and, finally, two mirrors for FEL-1 (PM1a and PM1b) and one mirror for FEL-2 (PM2a) that deflect the FEL light toward the energy spectrometer in the experimental hall.
Next, we find an insertable switching mirror to possibly direct the beam to the EIS-TIMER end-station, followed by a beam split and delay-line and by a 3-ways switching chamber, from which three branchlines divert the beam to either the EIS-TIMEX, DiProI or LDM end-stations, each one being served by its own focusing optics.

A concise description of the diagnostic instruments routinely employed in our experiments follows.

Among the mentioned elements, the beam position monitors, the intensity monitors and the energy spectrometer work online providing shot-by-shot characterization of each photon pulse in terms of position, absolute intensity, central wavelength and spectral distribution.

- The *BPMs* consist of four metallic blades each, which intercept the tails of the photon beam in both vertical and horizontal directions.
  Simultaneously recording their drain currents allows to evaluate the centroid of the transverse intensity distribution. Whence the possibility of measuring the relative position of the beam with a spatial resolution better than 2 μm, as well as - combining the information from both BPMs - the angular movement of the beam with an angular resolution better than 1 μrad.

- The *intensity monitors* are ionization chambers, i.e. chambers filled with a rarefied gas (N_2 at about 10^{-5} mbar in the present case) where the incident ionizing radiation creates ion pairs that migrate to electrodes of opposite polarity thus generating a measurable current.
  Almost completely transparent, with no dead times and exploitable in the whole wavelength interval of FERMI within their large dynamic range, they well suit the purposes of a real-time diagnostic tool.
  The ionization currents are read by low-noise picoammeters specifically de-

veloped by the Detectors and Instrumentation Laboratory of Elettra. Their absolute calibration has been made in the early stages of machine commissioning by simultaneously measuring the FEL intensity with a photodiode/YAG detector (PYD) system, also in-house developed and in turn absolutely calibrated at a beamline of Elettra.
Shown in Fig. 1.18 are the so-obtained calibration curves, from which a linear interpolation has been derived at all other wavelengths and which are each, time by time, rescaled by the ratio between the reference and measured in-chamber pressures. No valid arguments have been raised so far explaining the quite surprise fact that a non-linear response occurs at the lowest intensities. Further measurements are devised to extend the present set, especially at coverage of the higher intensities meanwhile reached by the machine.

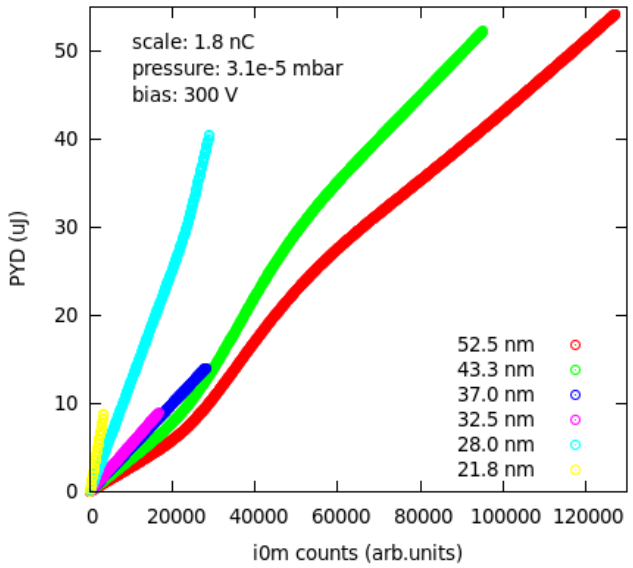

Figure 1.18: Absolute calibration curves for the intensity monitors of FERMI.

- The Pulse-Resolved *Energy Spectrometer*, Transparent and Online, (PRESTO) relies on two variable line spacing (VLS) diffraction gratings: the low energy one, with a groove density of 500 lines/mm and a graphite coating to span in first and second order the 12-90 eV energy range with a resolution between 0.2 and 2.4 meV and the high energy one, with a groove density of 1800 lines/mm and a gold coating to span in first and second order the 40-360 eV energy range with a resolution between 0.3 and 10.6 meV.
  The FEL beam impinges on the grating at a fixed angle of 2.5° and gets deflected by a fixed angle of 4°. While the zeroth diffraction order is directed almost undisturbed toward the beamlines, the chosen diffraction order is focused onto a YAG screen and imaged by a movable CCD detector (Fig. 1.19).

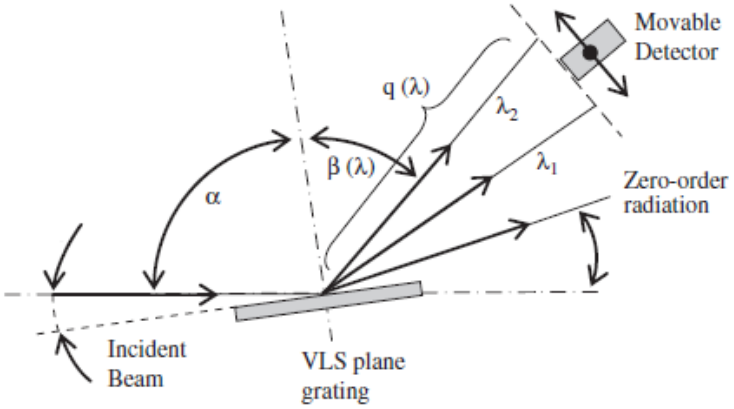

Figure 1.19: Conceptual optical layout of the energy spectrometer of FERMI. Taken from Ref. [52].

The variation of the groove density across the grating surface is such to focus the spectrally dispersed radiation on an almost flat surface so that, when changing the FEL wavelength, it is sufficient to move the detector along the focusing line to have it centered on the energy interval of interest. Such movement is motorized, automated and calibrated according to the following formula:

$$\Delta\lambda = \Delta\text{pix}\cdot\text{Pixel2Micron}[\mu m/pix]\cdot\text{WavelengthSpan}[nm/mm]/1000[\mu m/mm]$$

where Pixel2Micron expresses the correspondence between the CCD pixels and the beam size (in microns) along the axis normal to the focal plane (about 15.4 at focus) and WavelengthSpan expresses the correspondence between the radiation wavelength (in nanometers) and the CCD position (in millimeters) along the focal plane. The measured resolution per pixel $\Delta E/\Delta\text{pix} = (E\ \Delta\lambda)(\lambda\ \Delta\text{pix})$ of the instrument is reported in Fig. 1.20.
Determination of the absolute energy is guaranteed as far as the incoming beam mantains a stable trajectory, which - we experienced - is not as trivial as it can be at a synchrotron.
For single-shot spectrometer acquisitions to carry significant information, an FEL intensity higher than at least 1 μJ is typically required. Of course, integration over multiple shots supplying average information is always possible. Besides characterization of the pulse energy content, the spectrometer may serve two additional purposes.
Firstly, since dispersion and focusing only act on the horizontal plane, a vertical cut of the two-dimensional CCD image provides a shot-to-shot mea-

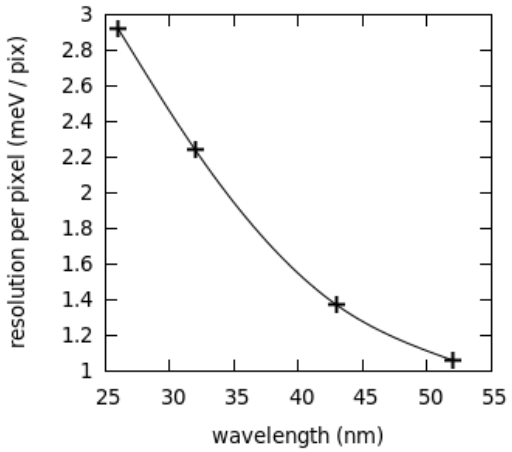

Figure 1.20: Measured resolution of the spectrometer of FERMI.

surement of the beam spatial profile.
Secondly, integration of the averaged horizontal spectrometer profiles works as an additional intensity monitor, particularly useful when the FEL radiation contains more separate wavelengths like in the case of a FEL-2 stage coming together with an unfiltered FEL-1 stage, or the case - later on introduced - of twin pulses.

"Non-online" instruments (in the sense that a change of their settings cannot be controlledly operated within the time between one FEL shot and the successive) include the beam defining aperture, the gas absorber and the delay line.

- The *BDA* is formed by two trunks of pyramid that, moved the one with respect to the other and/or both relative to the ideal longitudinal axis, allow to select the effective beam aperture.
  Its settings are established by motoring the FEL lateral profile on a CCD camera that looks at the FEL-induced fluorescence on a YAG screen placed downstream of the BDA. Two such screens are present along Padres at, respectively, 52.4 and 72.5 m from the radiator exit.

- The *gas absorber* is a 6 meters-long differentially-pumped cell where up to four different gases can be injected - N_2, He or Ne, according to the spectral range in use - at a finely controllable flow until reaching a maximum pressure of about 0.1 mbar. With this system, the FEL intensity can be attenuated continuously over four orders of magnitude. The photon beam characteristics are unchanged, apart for an altered ratio between the first and third harmonic components with respect to the original pulse, which is - however - irrelevant in most cases due to the low percentage (on the order of 1%) of third harmonic

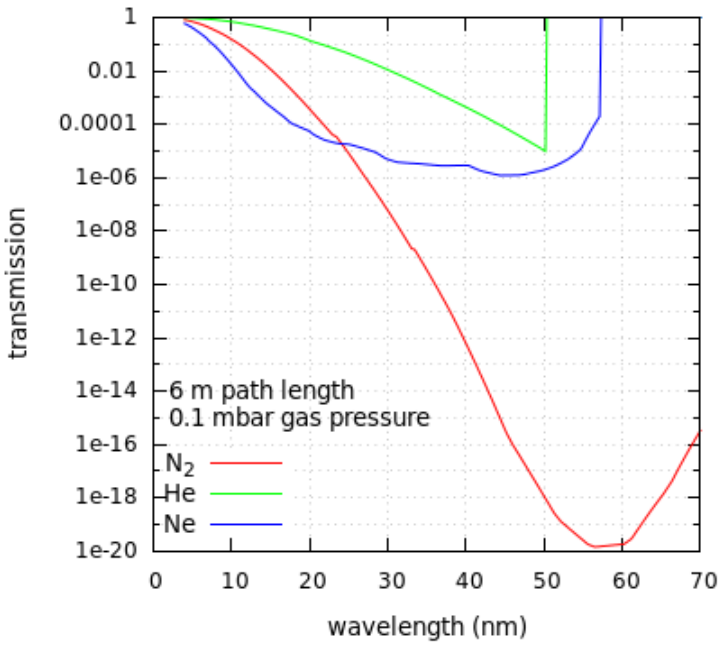

Figure 1.21: Possible attenuation regimes with the gas absorber of FERMI evaluated with the online toolset by CXRO [53].

content. Regarding the reduction of FEL intensity, I here open a parenthesis to say that at least two additional ways of achieving this task have been exploited during our experiments: insertion of solid-state filters (available both along Padres and at the end-station entrance) and reduction of the current feeding the dispersive section.
In the first case, only a discrete step intensity reduction is obviously possible. In the second case, the intensity reduction is accompanied by larger intensity fluctuations. Viceversa, an increase of the dispersive section current above an optimum level leads to an increase of the higher harmonics content and, more tangibly, to the development of non-Gaussian temporal profiles which are manifest in a pronounced deterioration of the spectrum.
Still another way of tailoring the pulse intensity to the experimental needs comes from an adjustment of the seed laser intensity. However, being this operation not without consequences for the successive steps of lasing, we - as beamline operators - do not have a direct control on it.

- Lastly, an *AutoCorrelator/Delay-Creator* (AC/DC) serves the functions of splitting the beam, introducing a controllable delay in the 2 to 30 ps range between the resulting half-beams, and recombining them on the beam transport path (Fig. 1.22).
This tool has been under development at the time where most of the works

presented in this thesis were done. In October 2014, we contributed to the delay line commissioning by performing the first pump-probe experiment with both the pump and the probe given by the high-intensity ultra-short pulses at EUV energies of FERMI.

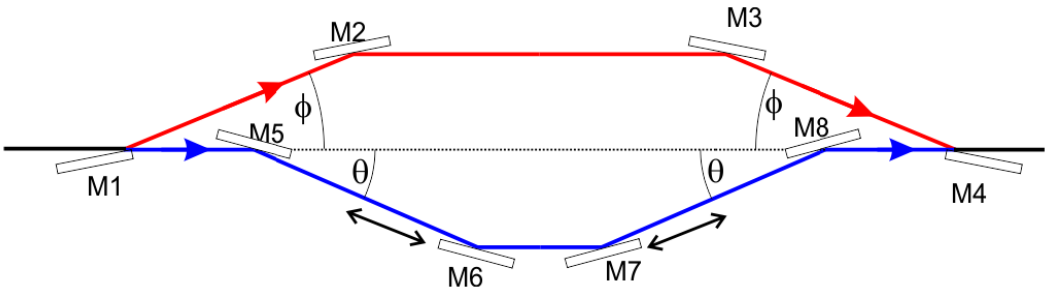

Figure 1.22: The split and delay line of FERMI.
Credits: N. Mahe.

1.2.6 Main measured properties of FEL radiation

With the discussed diagnostics at disposal, the FEL radiation could be characterized in its main properties. Those regarding FEL-1 are briefly commented in the following.

Intensity distribution

A typical intensity distribution looks like the one in Fig. 1.23: intensity fluctuations of the order of 10% which follow a quasi-Gaussian distribution with a longer tail on the low intensity side.
Their origin lies in fluctuations of the electron beam parameters and, to a smaller extent, of the seed laser parameters, which also couple to a timing jitter between the electrons and the seed. As such, they have the potential to be improved as soon as technologies will advance in these respects, a fact that contrasts with the situation for SASE FELs, where intensity fluctuations are inherent to the stochastic nature of the generation process.
All of these parameters - which also determine the level of average intensity that can be reached - highly depend on the varying machine working conditions (especially those regarding the electron beam), making it difficult to give quantitative information of general validity. Roughly speaking, fluctuations even smaller than 10% may characterize the FEL radiation in the configuration that uses the third harmonic at $\sim$ 261 nm as a seed laser, in which cases pulse intensities above 200 μJ can be reached for wavelengths greater than 35 nm. When the OPA is used,

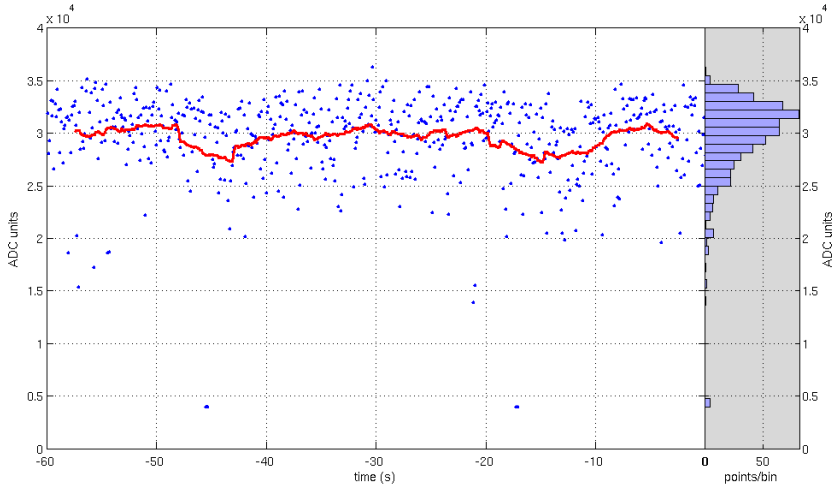

Figure 1.23: Raw data from one of the ionization monitors for 600 successive FEL shots.

instead, fluctuations are typically above 10% and intensities are in the order of 100 μJ per pulse in the 35 - 65 nm wavelength range, while being about a factor 5 less at 20 nm.

Spectral distribution

FEL pulses from FERMI feature a very narrow spectrum and an excellent spectral stability in both wavelength and bandwidth. These characteristics may be clearly appreciated in Fig. 1.24, which refers to FEL-1 radiation at the 8th harmonic of the 260 nm seed laser.
From the plot of panel a), one may see that the FEL spectrum is larger than the seed laser spectrum: $\sigma_{seed} = 4.7$ meV rms at 260 nm; $\sigma_{FEL} = 14$ meV rms at 32.5 nm. Nonetheless, the relative bandwidth of the FEL is smaller than that of the seed laser: $\sigma_{seed}/\lambda_{seed} = 0.098$ %; $\sigma_{FEL}/\lambda_{FEL} = 0.038$ %. The measured bandwidth increase is roughly compatible with the expected shortening of the FEL pulse length at high harmonic numbers with respect to the seeding pulse length [55] [56], thus suggesting close to the Fourier limited time-bandwidth product.
The plot of panel b) shows that, at a photon energy of 38.19 eV with a bandwidth of 22.5 meV rms, phonon energy fluctuations amount to about 1.1 meV rms ($\sim$ 0.003%) and bandwidth fluctuations amount to about $5.9{\cdot}10^{-4}$ rms ($\sim$ 3%).

When seeking to obtain maximum pulse energy by increasing the seed intensity and/or the strength of the dispersive section, a multi-peaked spectral distribution develops.
This fact - which is usually a drawback as it calls for a compromise between power and spectral purity - may be turned into a novel opportunity for two-color pump-probe experiments in the XUV since, combined with a wavelength chirp of the seed

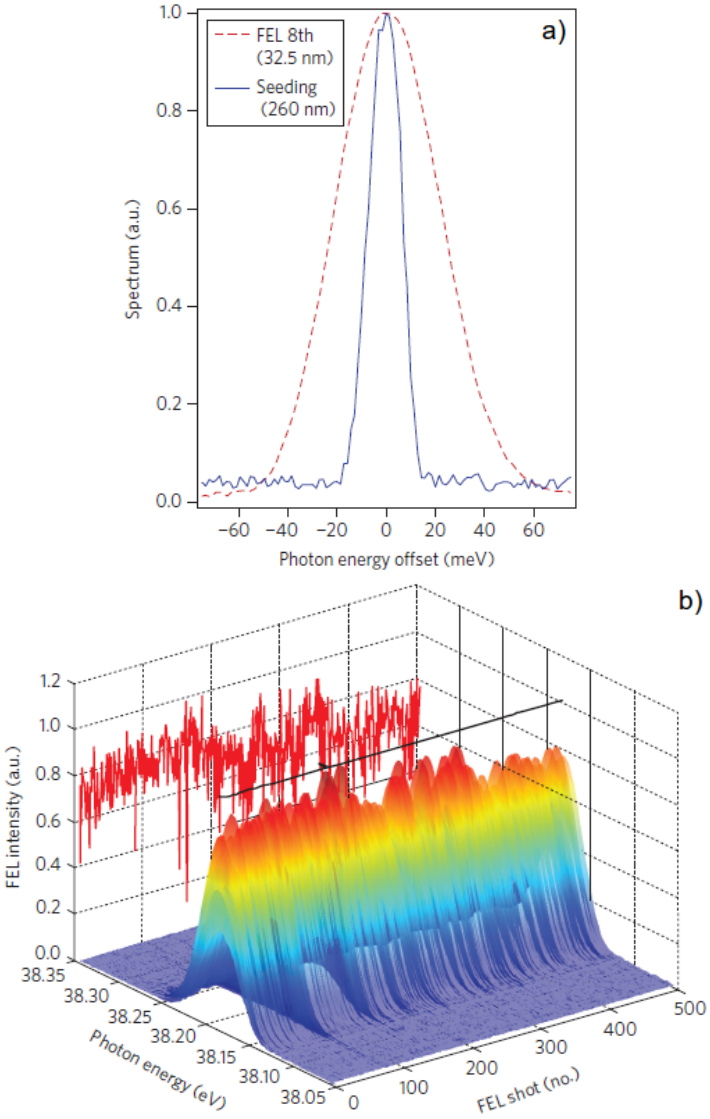

Figure 1.24: *Top*: measured FEL and seed laser spectra. *Bottom*: 500 consecutive FEL spectra.
Taken from Ref. [54].

laser, can be exploited to produce separate radiation pulses. At high seed laser intensities, in fact, the part of the electron beam that has interacted with the center of the seed laser beam acquires an energy spread which is too large to be sustained by the FEL amplification process (a condition referred to as "over-bunching"). The output radiation, only coming from the head and tail of the interacting electrons, will therefore consist of two separate pulses that, in case of significant chirping of the seed laser, will also have different wavelengths (Fig. 1.25).
The maximum achievable temporal split is of several hundred femtoseconds, limited

by the electron bunch length and/or by the possibility of generating long enough seed pulses with significant local power at their tails. The corresponding relative spectral separations are in the order of few percent.

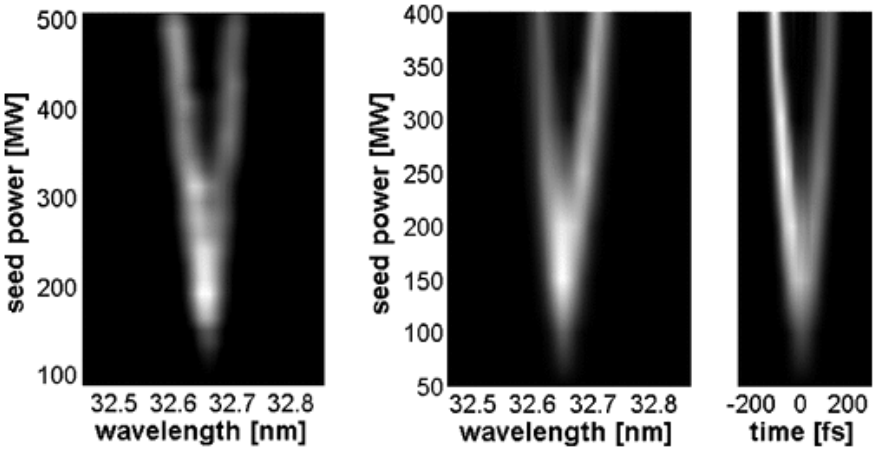

Figure 1.25: Projected spectral and temporal FEL intensities for different seed powers. *Left*: experimental spectral splitting; *center* and *right*: simulated spectral and temporal splitting (using the code Perseo).
Taken from Ref. [57].

An alternative way to this same end is using two independent seed pulses separated in time and with different wavelengths, in which case less constraints exist between the time and wavelength separations (that, anyway, keep being limited by the electron bunch length and FEL gain bandwidth).
Both schemes has received recent experimental confirmation at FERMI [57] [58].

Transverse profile

Very clean TEM00 modes can be generally obtained.
Checking the spatial profile of the unfocused beam on a YAG is, however, recommended. A small undulator mismatch, in fact, is sufficient to produce a "doughnut" transverse mode looking like the one on the right panel of Fig. 1.26.

Pulse length

Estimation of the peak powers and time resolutions achieved during an FEL experiment requires that the pulse duration is known. At present, however, a precise determination of this parameter is lacking.

We therefore based our considerations upon the scaling law $\tau_{FEL} = \tau_{seed}/\sqrt[3]{n}$ theoretically predicted for seeded FELs by Ratner *et al.* [55], where n is the harmonic number and τ_{seed} is the seed laser pulse duration evaluated, as already ex-

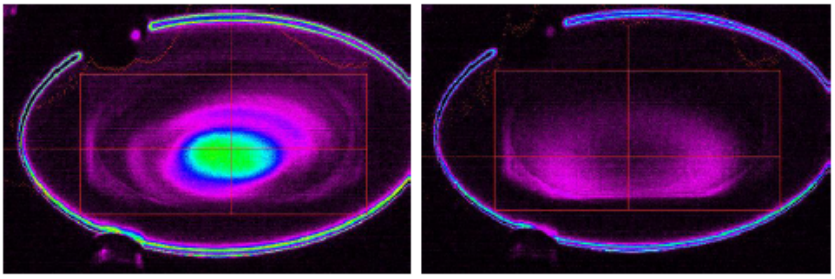

Figure 1.26: Good vs "doughnut" transverse mode on a YAG.

plained, from autocorrelation measurements.
Like reported in Ref. [56], an attempt have been made to validate this relationship based on measurements of the spectral profiles that, fitted to a Gaussian, were used to evaluate the pulse length via the ideal time-bandwidth product of 0.44. No agreement has been found with the above relation assuming the measured seed laser pulse duration, and only partial agreement (at higher wavelengths) supposing a longer pulse length for the seed laser. These results possibly reveal a failure of the assumption of fully coherent pulses with no chirp or phase noise and encourage to invest additional efforts in providing a better control of the seed laser pulse quality.

As soon as the delay-line of FERMI became available, an experiment has been performed at the LDM beamline following the approach successfully attempted at FLASH: the FEL pulses are split into two sub-pulses, of which one is delayed and both are focused on a He target. The pulse duration is then deduced by measuring with a time-of-flight spectrometer the yield of doubly charged helium ions arising from two-photon ionization as a function of the delay between the two half-pulses [59].
The experiment has been carried out with the seed laser prepared in different configurations of energy chirp so as to study which one is best suited to counteract the energy chirp of the electron beam at the origin of spectral broadening, as well as at different harmonics of the seed laser so as to put to a test the aforementioned scaling law.
Moreover, several FEL spectra have been acquired, from which the autocorrelation coherence function $g(\tau) = \dfrac{\langle E^*(t)E(t+\tau)\rangle}{\langle E^*(t)E(t)\rangle}$ and - hence - the longitudinal coherence (its width) can be reconstructed based on the Wiener-Kinchin theorem [60]: $g(\tau) = \left| FT\left[\dfrac{1}{N}\sum_{i=1}^{N} I_i(\omega)\right]\right|$, with FT Fourier transform and $I(\omega)$ energy spectrum.
The results of this long experimental campaign are still under evaluation [61].

Additional parameters

Other FEL parameters that, like the pulse length, cannot be directly accessed with some instrument are the following.

- *Polarization* can be rapidly switched from vertical to horizontal to circular thanks to the APPLE-II type undulators, but then determining the exact degree of polarization represents an experiment itself. The interested reader is addressed to Ref. [62] for an overview of the polarization measurements done at FERMI by three different techniques and a discussion on their possible use as permanent diagnostics.
  In our work, polarization was not a main concern, therefore we prevalently used circularly polarized light as it is the configuration in which the FEL outputs the highest powers due to a better coupling between the electromagnetic field and the electrons [54].

- A Hartmann sensor is at disposal for measurements of the light *wavefront*. Fractioning the incoming beam into smaller beams by a pinhole array and detecting, at a given distance from it, the deviation of the various spots from a reference set of positions, it allows to derive the local wavefront gradient whence, with appropriate algorithms, the whole wavefront can be reconstructed.
  Although not directly interested in the wavefront information, we used this instrument downstream of the TIMEX chamber as a feedback to optimize the quality of FEL focusing. Knowledge of the beam intensity and wavefront, in fact, can be exploited to calculate parameters like the beam width and divergence, the waist diameter and the waist position [63].

- The *transverse or spatial coherence* can be measured with a classical Young's experiment, a set of double slits with different spacings being placed along the beam transport together with a YAG and a CCD, 8.5 m after, for the detection of the interference fringes on the transverse plane.

- *The longitudinal or temporal coherence* can be measured by splitting the beam, recombining the two half-beams and recording the generated interference fringes as a function of the time delay imparted to one of the half-beams with respect to the other. Preliminary measurements of this kind have been done during the AC/DC commissioning with participation from the TIMEX team.

Chapter 2

The EIS-TIMEX end-station

Although few experimental campaigns have also been carried out at the DIPROI beamline, a detailed description of the only EIS-TIMEX beamline is presented in this thesis, as it provided the setup for the major part of the reported experiments and, not secondly, because the author took an active part in its development.

An essential layout of the TIMEX end-station is sketched in Fig.2.1.

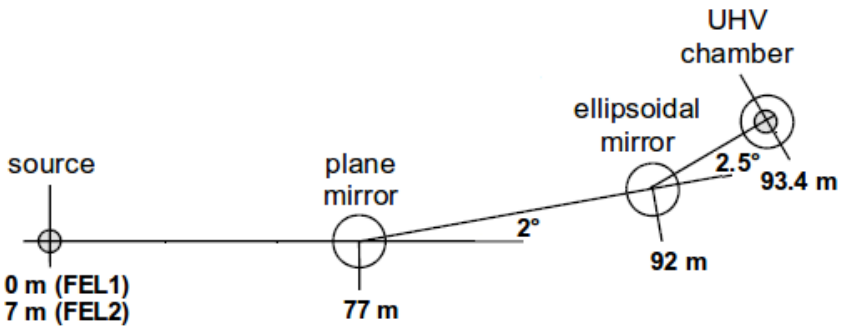

Figure 2.1: Sketch of the EIS-TIMEX end-station.

It basically consists of a plane mirror (400 mm long, at 2° incidence angle, in Au-coated fused silica), an ellipsoidal mirror (450 mm long, at 2.5° incidence angle, in Au-coated fused silica) and a high-vacuum chamber hosting the sample and diagnostics of various kinds.

2.1 Beamline equipment

2.1.1 Focusing optics

The plane mirror is located inside the already-mentioned 3-ways switching chamber; 15 m downstream of it, the ellipsoidal mirror focuses the radiation at the center of the TIMEX chamber, 1.4 m apart.

The source beam can be considered to have its waist at the position of the last undulator, which differs of 7 m for the FEL-1 and FEL-2 lines. Placing the ellipsoidal mirror at 85 m from the beam waist of FEL-2 corresponds to the choice of providing optimized photon fluxes when operating with this light.
Under ideal conditions, the focal spot has a Gaussian distribution with size given by the source size times the optics demagnification factor, in turn given by the focal length to source distance ratio. Considering a source size of about 290 μm fwhm for FEL-1 and of about 140 μm fwhm for FEL-2, this simple estimate yields a focal spot of about 4.4 μm fwhm for FEL-1 and of about 2.3 μm fwhm for FEL-2.
An indication of the real focusing capabilities for FEL-1 can be inferred from Fig.s 2.2 and 2.3.

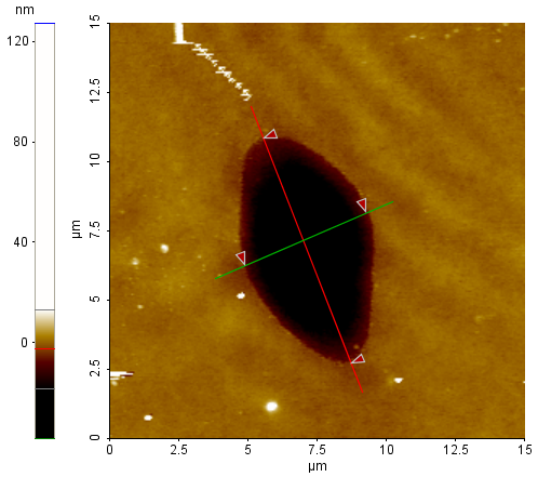

Figure 2.2: Imprint of a single FEL-1 pulse at the best focus in the TIMEX chamber on a PMMA, as visualized *ex situ* by an atomic force microscope.
Credits: C. Svetina.

The first one is a single-shot ablation imprint of the FEL at the best focus on a PMMA sample imaged on an atomic force microscope. The crater contour corresponds to the portion of the beam at a peak fluence above the ablation threshold. Collecting and analyzing this kind of images for various fluences gives a good method to deduce - along the prescriptions of Ref. [64] - a value for the effective area by which normalizing the incoming pulse energy, whose validity is not lim-

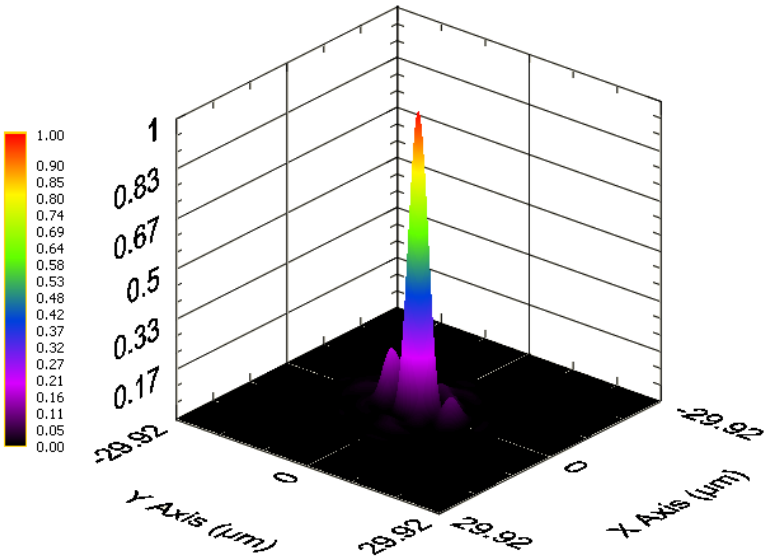

Figure 2.3: Reconstruction of the measured FEL-1 spot at the best focus in the TIMEX chamber.
Credits: L. Raimondi.

ited to ideal Gaussian pulses but that unfortunately yields this information only *a posteriori*. We therefore most often rely on the wavefront sensor mentioned in chapter 1 that, mounted at the back of the TIMEX chamber, with the help of some algorithms allows us to reconstruct the beam profile (like in Fig. 2.3) almost in real-time, thus providing precious guidance for a fine optimization of the ellipsoidal mirror positioning during the operations of beam alignment.

In short time, the plane mirror will be replaced by an active optics with 15 piezoelectric actuators glued on the rear face of its substrate that, by application of an appropriate voltage, allow to modify the mirror profile so as to obtain a desired beam shape at focus. The results of ray-tracing simulations and metrology measurements on prototypes have been reported in Refs. [65] and [66].
From the last paper, I borrow the three images of Fig.2.4, representative of a focal spot featuring - respectively - a Gaussian distribution, a double-peaked distribution and a flat-top distribution, obtained - the first one - from a flat mirror profile and - the last two - from Lorentzian-like mirror profiles with different parameters. The main purpose behind this project is to gain control over the spatial distribution of the energy density deposited on the sample but applications can be, of course, diverse. Non-negligible beam tails would, for example, make it possible a direct measurement of the sample temperature raising with an infrared pyrometer, following the lines described in Ref.[67].

As shown in Fig. 2.5, the overall beam transport transmittance (until after the

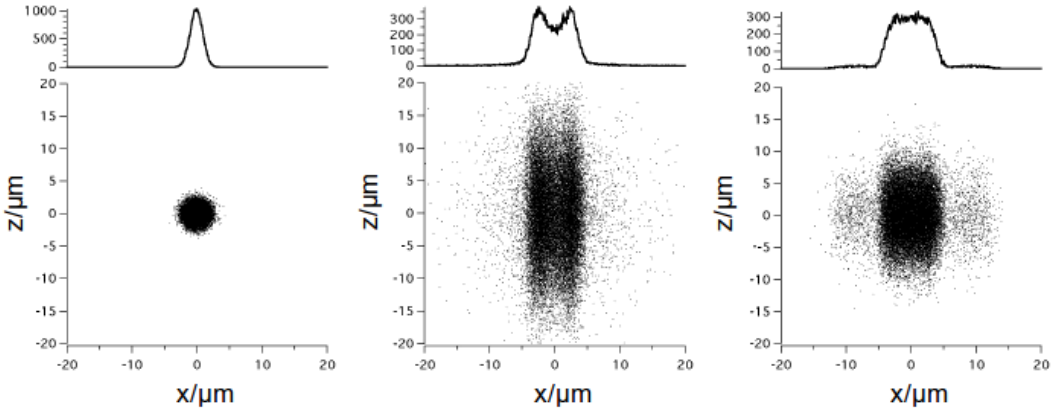

Figure 2.4: Ray-tracing results of the expected spots at focus with corresponding mirror profiles for a wavelength of 5 nm and a divergence of 7.5 μrad. From *left* to *right*: Gaussian, double-peaked and flat-top distributions.
Taken from Ref.[66].

ellipsoidal mirror) is in the order of 65-70 % for circularly polarized radiation in a wide wavelength range, quite substantially smaller only below 7 nm and above 70 nm. The vertical polarization has considerably higher transport efficiency than the horizontal one in the whole energy interval under consideration, with the larger differences occurring at lower energies.

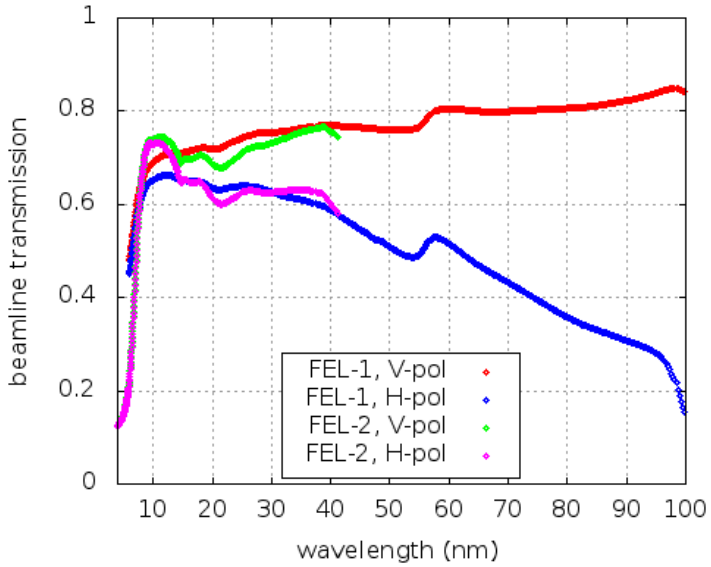

Figure 2.5: Beamline transmission up to (and included) the ellipsoidal mirror.

The main TIMEX chamber, illustrated in Fig. 2.6, has a cylindrical shape with an internal diameter of 500 mm and is kept at a vacuum level of $\sim 10^{-8}$ mbar. It

includes the equipment listed in the following sections.

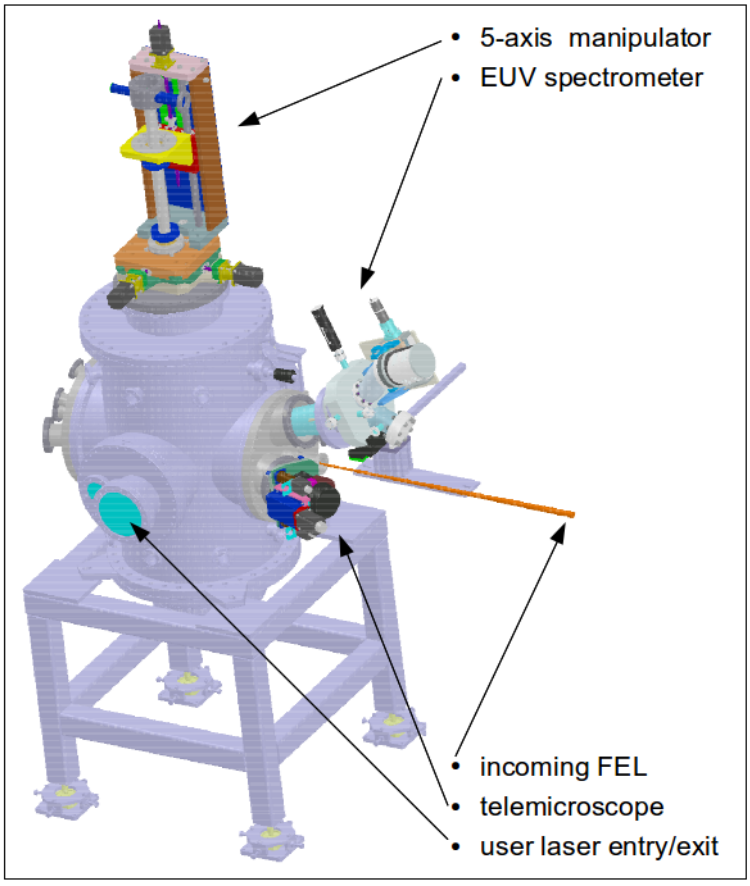

Figure 2.6: External view of the main TIMEX chamber.

2.1.2 Sample holder

Few samples, together with fundamental beam imaging diagnostics - like YAG, phosphor and diamond screens - can be mounted on a vertical manipulator (Fig.2.7). Rapid and precise positioning of the sample/screen under the beam is obtained by motorized movements along the optical axis x, the horizontal axis y, the vertical axis z[1], the polar angle ϕ and the azimuthal angle θ.

2.1.3 Telemicroscope

While two GigaEthernet cameras from Axis Communications provide a wide view on the inside of the chamber, close visual inspection of the sample/radiation

[1]Unpleasantly, the convention is different from that in use by the machine physicists to refer at the FEL coordinates of motion.

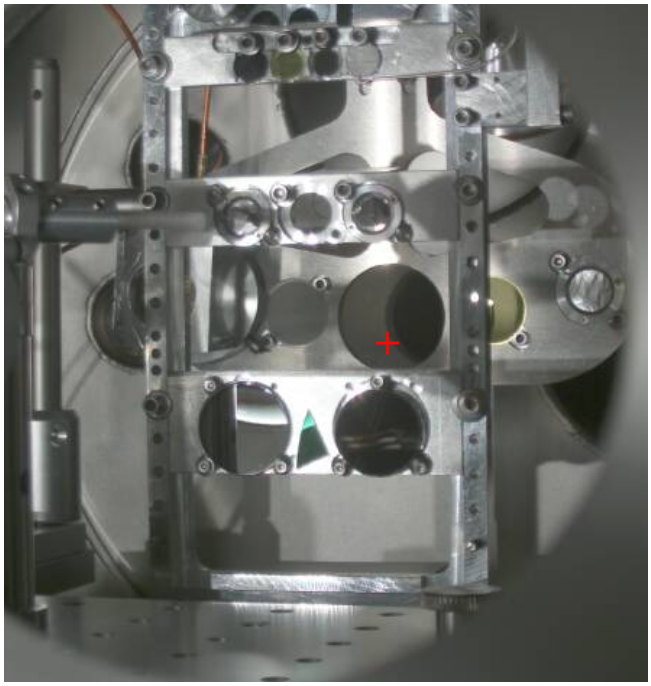

Figure 2.7: View of the vertical manipulator hosting various samples and diagnostic screens from inside the main TIMEX chamber.

interaction region is allowed by a long distance microscope from Questar whose objective is placed at 35 cm from the chamber center at an angle of about 20° with respect to the direction of the incoming light. It serves a number of purposes, namely: combined with a fluorescent screen, to determine the beam focal plane and estimate *in situ* the spot size; when also working with the user laser, to spatially superimpose the two beams; to precisely position the sample under the beam (both transversally and at the desired focal depth) and monitor its damage level upon more or less prolonged radiation exposure; and, based on the visualized damage crater, even to provide a feedback for focal plane adjustment to the algorithm that manages the sample movement in a serpentine path, as it will be better explained later.

The telemicroscope has a resolution better than 10 μm, a focal depth of few tens of μm and a lateral field of view of about 600 μm. If the point to be observed lies outside of them, it can be moved on motorized translators in the three directions, one parallel ("zoom") and the other two orthogonal ("tilt x" and "tilt y") to the telemicroscope main axis. During the preliminary phase of each experiment, we are used to move the sample manipulator at few positions along the FEL propagation axis and, for each one of them, find the corresponding positions of the three telemicroscope axes for which the same point of the sample surface is imaged at focus on the same central portion of the telemicroscope observation window.

A plot of the coordinates "zoom", "tilt x" and "tilt y" against the x coordinate (like the one in Fig.2.8), then provides a calibration that, once implemented in the control system, allows to "lock" the telemicroscope so as it moves rigidly with the sample. This makes easy and quick the evaluation of the caustic curve, on which basis it may be decided to slightly revise the beam focusing through pitch, roll and yaw movements of the ellipsoidal mirror and/or the upstream optics. Viceversa, if we keep the telemicroscope fixed and move the manipulator along x, samples of different thicknesses can be accurately positioned all at the same focal plane by simply observing when their surface is seen at focus on the telemicroscope.

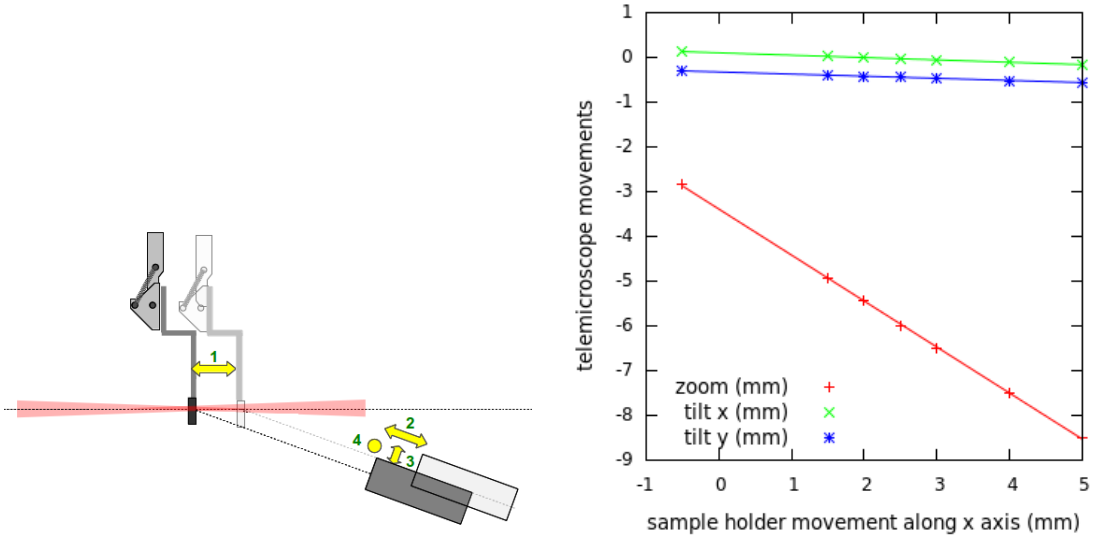

Figure 2.8: When the telemicroscope (*left image, bottom right*) is "locked" to the sample holder (*left image, top left*), a movement along the x coordinate (1) also produces a movement of the coordinates "zoom" (2), "tilt x" (3) and "tilt y" (4), according to the calibration on the *right image*.

2.1.4 Detectors

The beamline disposes of a set of photon detectors to be placed in transmission and reflection geometries.

The mostly used are Si p-n junction photodiodes from IRD Inc. Both the AXUV and SXUV models fully cover the spectral range of our interest. The one or the other is chosen depending on the expected flux level at the detector, the first one featuring a higher responsivity and the second one, on the contrary, a higher radiation hardness. Their wide dynamic ranges can be further extended by use of an amplifier (in cases of low signal), or by application of a reverse bias (in cases of high signal).

The pulse energy is in principle determinable as $E_{ph} \cdot N_{ph} = E_{ph} \cdot Q/QE$ where

E_{ph} denotes the photon energy, $Q = \int V(t)dt/R$ is the measured electron charge - obtained by time integrating the voltage signal $V(t)$ output from the photodiode and dividing by the equivalent resistance R (including the internal resistance of the detector and the load resistance from the circuit) and QE represents the quantum efficiency, i.e. the ratio between the number of photo-generated carriers and the number of incident photons (the ratio QE/E_{ph} takes the name of responsivity).

The producer supplies data sheets for the energy-dependent quantum efficiency which, however, are derived from measurements with CW radiation. It is not unlikely that the photodiode response to (yet unfocused) FEL light is altered by the short duration of the pulses. For this reason, we have tested the response of these photodiodes to laser light with longer wavelength (800 nm) but comparable pulse duration ($\sim$ 100 fs). The obtained nVs vs μJ calibration curves (Fig.2.9, panel a) have been rescaled from the IR laser wavelength to the FEL one under the assumption that the quantum efficiency, although altered in its absolute value, preserves its energy dependence as reported by the producer, and then compared with the nVs vs μJ calibration curves recorded at TIMEX (Fig. 2.9, panel b). If we trust the incident pulse energy as measured, in the first case, by a power meter and, in the second case, by the gas ionization monitor of the FERMI beam transport system, from the comparison reported in panel c of Fig.2.9, we must conclude that the photodiode response is significantly different from what expected.
Bolometers from Fortech HTS GmbH have also been tested which, directly sensitive to the radiation-induced temperature variation, are expected to have a linear and wavelength-independent response in their μJ to mJ operational range. Laboratory laser measurements roughly confirmed both expectations (800 nm and 400 nm were the only wavelengths that could be measured with high enough signal levels). But those calibrations, when applied to the signals detected at TIMEX, would predict unreasonably high FEL intensities, analogously to the photodiode case. Moreover, these detectors have shown a significantly higher signal-to-noise ratio and a larger non-uniformity across the surface with respect to the photodiodes, which were therefore preferred.
Measurements with an ultra-fast laser light source being not a viable solution to absolutely calibrate the detectors responses, we have chosen to rely on a cross-calibration with the ionization monitor from Padres. Since this calibration is subject to small variations from time to time according to the beam pointing, the fine transport optics settings, the detector positioning as well as the seed contribution (that one may want to suppress with appropriate filters or not), we have adopted the strategy of recording one such calibration curve prior to any measurement.

While following this safer procedure, we have also pursued other directions. The following additional diagnostics have, in fact, been developed and commissioned:

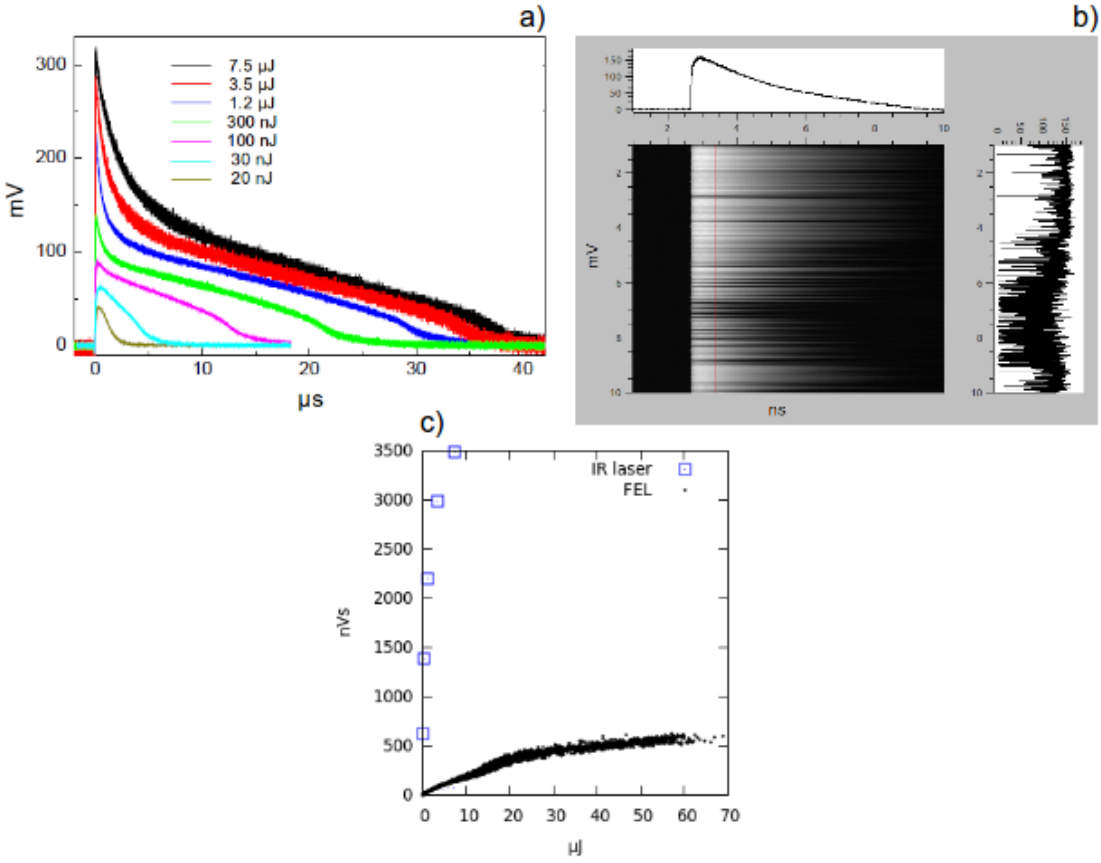

Figure 2.9: SXUV photodiode response curves to: *panel a)* light from an ultra-fast optical laser (pulse energy measured with a power meter), *panel b)* light from FEL-1 at 34.5 nm (pulse energy measured by a gas ionization monitor several meters upstream). *Panel c):* plots of the time integrated output voltage signal against the input pulse energy for the two cases of the a) and b) panels.

- custom scintillator detectors obtained by coupling an Al-coated YAG fluorescence screen to a photodiode with enhanced responsivity in the visible (UVG model from IRD Inc.). The fluorescence screen operates as an EUV to VIS optical transducer that stretches the pulse duration from $\sim$ 100 fs to a few hundreds ns reducing problems of non-linearity and damage risks; the 100 nm thick Al layer deposited on it stops the seed laser radiation.
  Of a similar type is the photodiode with which the gas ionization monitors have been calibrated.

- CCD cameras from Basler looking at the fluorescence signal produced by the FEL on a YAG screen. They have a high dynamic range, are robust and insensitive to beam pointing fluctuations. But we generally still prefer the photodiodes because, for a same level of accuracy, great care must be taken to

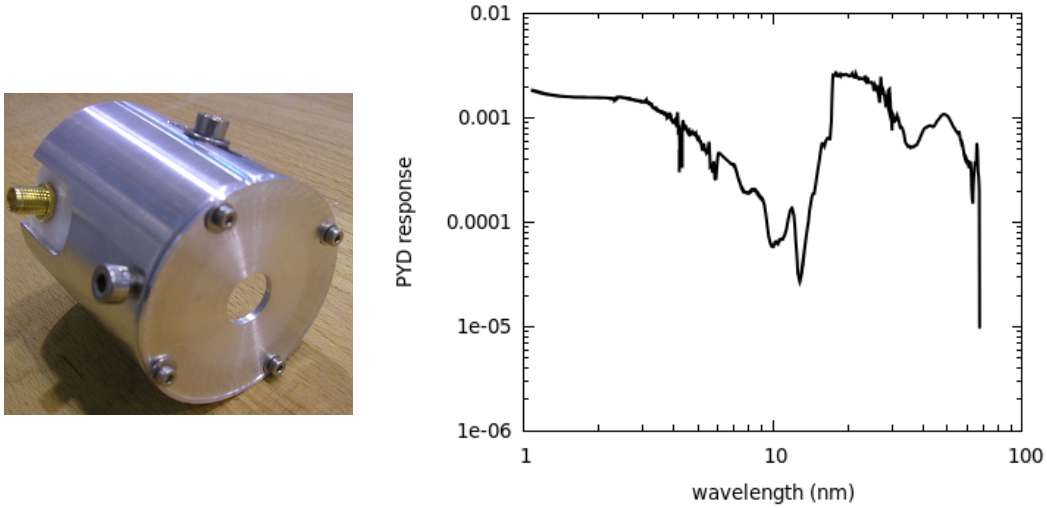

Figure 2.10: In-house developed scintillator for the detection of transmitted and/or reflected FEL intensity. On the *right*, dependence of the instrument response (in arb. units) upon the wavelength of incoming (synchrotron) light.

avoid influence from the environmental light and the seed laser. They cannot be used at all in pump-probe experiments with the user laser because dazzled from its light that, even if not directed to the detector, is diffused all around and counted all along the ms integration time.

- a metallic grid made by 3 mm - spaced, 50 μm - thick Cu wires to be placed at the entrance of the TIMEX chamber. Hit by the primary FEL beam (which gets negligibly attenuated, it generated a photocurrent proportional to the number of incident photons.

- similarly, when the ellipsoidal mirror is hit by the FEL beam some electrons are photoemitted and brought away from a properly distanced cathode. Collecting the resulting drain current from the mirror surface provides an additional monitor for the FEL intensity.

Efforts have been undertaken to associate the outputs from these devices with absolute values of the incoming or transmitted/reflected FEL intensity. With this purpose, campaigns were dedicated to characterize the response of these custom instruments at the BEAR beamline of ELETTRA. Selected results are shown in the graphs of Fig. 2.10 and 2.11.

The signals from all these detectors are read out by high-speed digitizers of the following kinds:

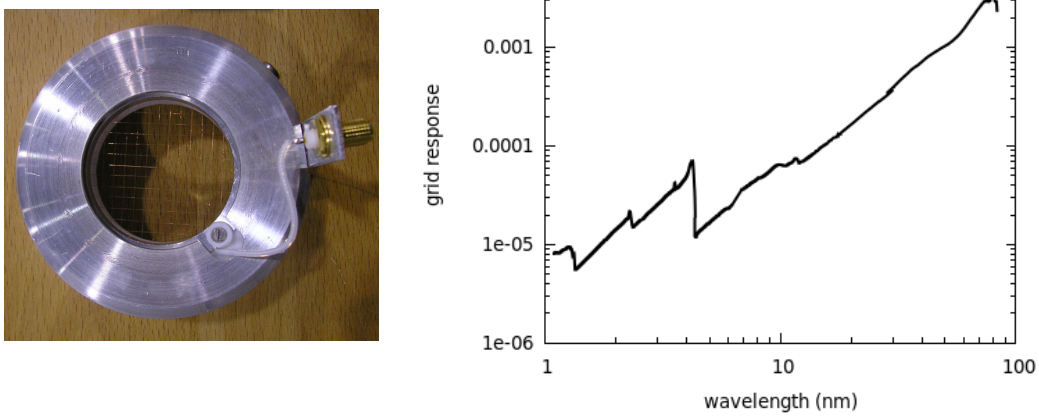

Figure 2.11: In-house developed metallic grid for the detection of incoming FEL intensity. On the *right*, dependence of the instrument response (in arb. units) upon the wavelength of incoming (synchrotron) light.

- AH401B, a 4-channel picoammeter developed by Sincrotrone Trieste for low current measurements (from 50pA with a resolution of 50 aA up to 1.8μA with a resolution of 1.8 pA). The input stage works as a charge integrator over a selectable (from 1 ms to 1 s at steps of 100 s) time window. Raw values from the coupled 20-bit resolution ADC converter can be turned into current values by the formula $I = FSR * (raw\_value - 4096)/(2^{20}\, T)$, with FSR the selected full scale range and T the selected integration time.
  These same devices are those which are used to read the currents outputs from the ionization chambers and the beam position monitors along the FEL beam transport. We have used them successfully in early measurements, but they have been dismissed as we have witnessed to a bistable response that still remains a puzzling issue to be solved.

- V1720, an 8-channel digitizer from CAEN that, similarly to a digital oscilloscope, outputs a digitized waveform, with a 12 bit resolution and a 250 MS/s sampling rate. Despite the higher amounts of occupied memory (which has not to be regarded as a minor point when an entire experiment is run acquiring single-shots data at 10 Hz!), we generally prefer to record the whole pulse profile to recognize possible features of malfunctioning (readout rates are, in any case, such to guarantee dead-timeless acquisitions and real-time signal processing).

2.1.5 Spectrometer

On request, an EUV spectrometer can be made available, to be positioned either on the FEL axis or in reflectance/fluorescence geometries.
Realized in the framework of an In-Kind Project for the EuroFEL consortium leaded by CNR-IFN Padova, its compact and flexible design is conceived for portability at various end-stations [68].

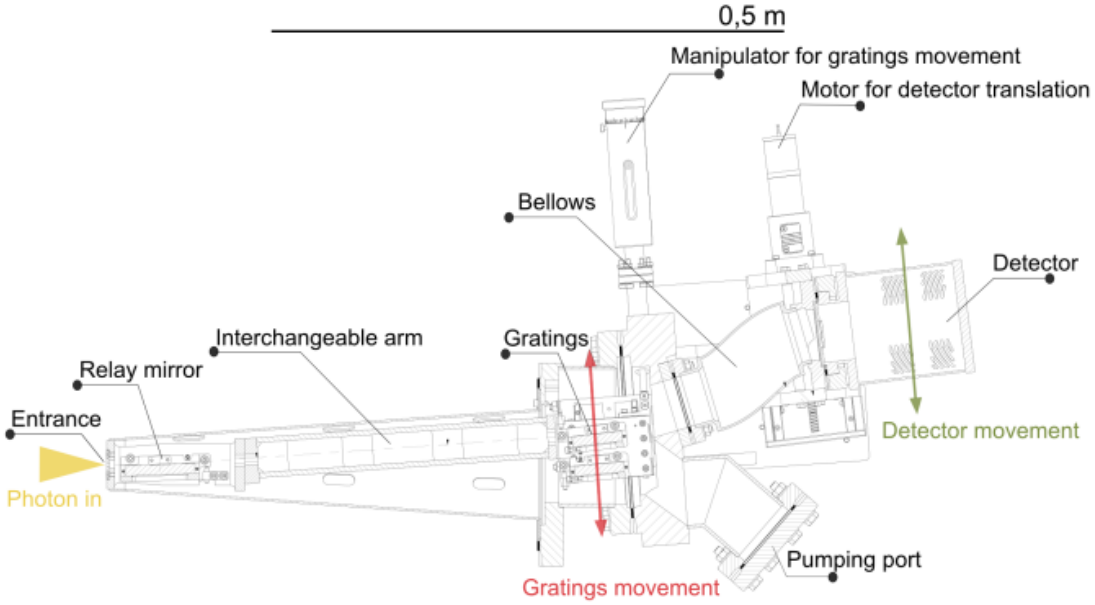

Figure 2.12: Drawing of the spectrometer developed by CNR-IFN Padova for single-shot X-ray emission-spectroscopy (XES).

The instrument uses two interchangeable grazing-incidence gratings of spherical shape and variable line spacing and an EUV-enhanced CCD camera movable along the nearly-flat focal curve. It allows to cover the wide energy range from 25 to 800 eV with high spectral resolution (better than 0.2% in the whole interval) and large acceptance angles ($10 \cdot 17$ mrad^2 in the interval from 30 to 250 eV and $5 \cdot 17$ mrad^2 in the at 250-800 eV).
Different input sections, with/without an entrance slit and with/without an additional relay mirror can be installed to best serve the experimental needs. The TIMEX end-station has hosted the prototype shown in Fig. 2.12, featuring no entrance slit and one grazing-incidence cylindrical mirror between the source and the grating. It was mounted at an angle of 18° with respect to the FEL axis to collect the light reflected from a Si sample shined at an angle of 9°.
As reported in Ref. [68], single-shot spectra have been collected at various harmonics of the 323.7 nm seed laser (down to the 27-th in a superradiant cascade configuration providing a calibration for the instrument and - more importantly -

demonstrating its high sensitivity to low photon fluxes as well as its capabilities as a diagnostic tool complementary to the already available PADRES spectrometer, with respect to which it features a lower resolution but a much wider spectral window.
We are currently working on technical solutions to accommodate the instrument at a 90° angle relative to the incoming beam in order to acquire, with the best signal-to-noise ratio, weak fluorescence signals (yields of few hundreds photons per pulse expected for solid samples at FEL-1 energies) and thus open the way for single-shot EUV emission spectroscopy of materials under transient extreme conditions.

2.1.6 Alternative focusing optics

Preliminary commissioning activities were carried out with an unfinished focusing ellipsoidal mirror. On January 2012, one year after the deadline foreseen for its completion, the manufacturer (SESO) declared not to be able to fulfill the specification of 1 μrad rms slope error. While committing the job to another company (Zeiss), we had to rustle up a new setup. From March 2012 until October 2013, the beamline was therefore operated with a plane mirror hosted in the chamber that was originally devoted to the ellipsoidal mirror and a spherical mirror directly placed inside the main TIMEX chamber.

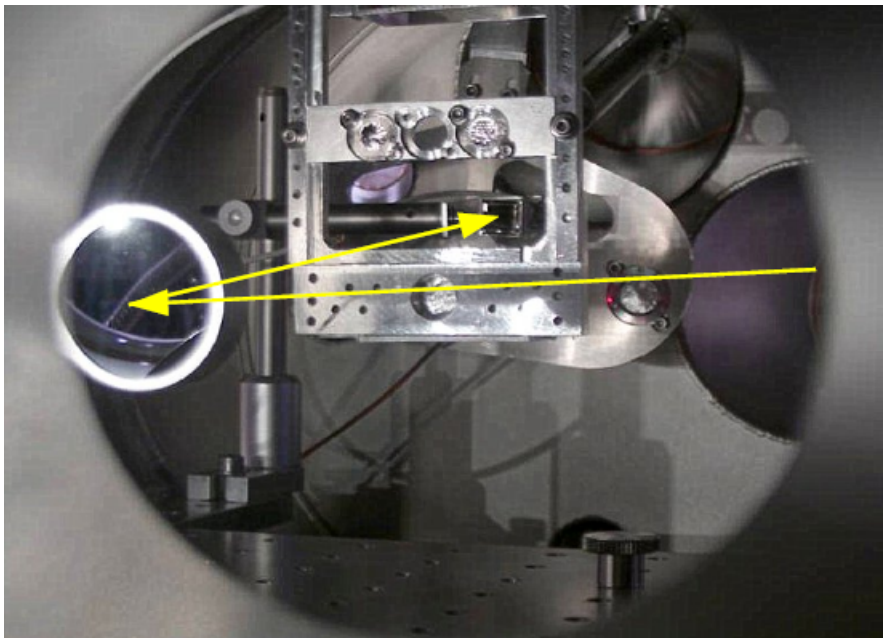

Figure 2.13: Temporary (/alternative) setup with focusing optics internal to the TIMEX chamber.

Accommodating both the ellipsoidal mirror and the plane mirror on the same cham-

ber, we are now able to switch relatively easily between the "external focusing setup" and the "internal focusing setup". For the last configuration, several spherical mirrors are at disposal, with a diameter of 1.5 inch, a focal length of 200 mm and an either single or multilayer coating deposited on a Si substrate of roughness less than 0.2 nm rms. The main drawback of this alternative setup is the considerable loss of flux available at the sample position due to a combination of two factors, namely:

- the *lower reflectivity*, due to the near-normal incidence geometry.

  To have an idea, consider that, at the chosen incidence angle of 3° and at a typical wavelength of 40 nm, reflectivities are around 10.5 % and 16 % for single layers of, respectively, Au and Pt coatings (see Fig. 2.14, top panel). Multilayer coatings can yield enhanced reflectivities but only within restricted energy intervals. Thus, for example, a Mg/SiC multilayer can be a good choice to work at 30 nm where it yields a reflectivity of $\sim$ 40 %, whereas an Al/Mo/B_4C multilayer can be a good choice to work at 21 nm where it yields a reflectivity of $\sim$ 50 %. In ref. [69], a detailed characterization of the multilayer mirror specifically conceived to perform on TIMEX an absorption spectroscopy experiment at the $L_{2,3}$ edge of Si is reported: a twofold Mo/Y structure (i.e. two periodic stacks with same materials but different parameters one on top of the other) whose throughputs have been tested under both synchrotron and FEL irradiation demonstrating the desired efficiency (greater than 0.1 over 12.15-12.65 nm spectral range with a reflectance peak of about 45% at 12.35 nm (see Fig. 2.14, bottom panel)) and resistance to light damage. The effects induced by the phase shape of the multilayer coating on the FEL pulse, investigated both theoretically and from an experimental point of view via total electron yield (TEY) measurements, turned out as negligible. Likewise, the relative delay between the arrival times at the sample of the rays impinging on the spherical mirror at its center and those impinging at its border was found non-influential (lower than 1 fs).

- the *larger spot size*.

  A ray tracing simulation (performed with Shadow) for an FEL at 40 nm wavelength and 50 μrad divergence predicts a quite pronounced astigmatism even at a near-normal incidence angle of 3° (Fig. 2.15). Therefore, moving along the optical axis, the beam passes from being mainly elongated in the horizontal direction to being mainly elongated in the horizontal direction; at the least confusion focus - occurring at about 0.41 mm from the nominal focal distance - the spot is asymmetric with fwhm dimensions of 13 μm x

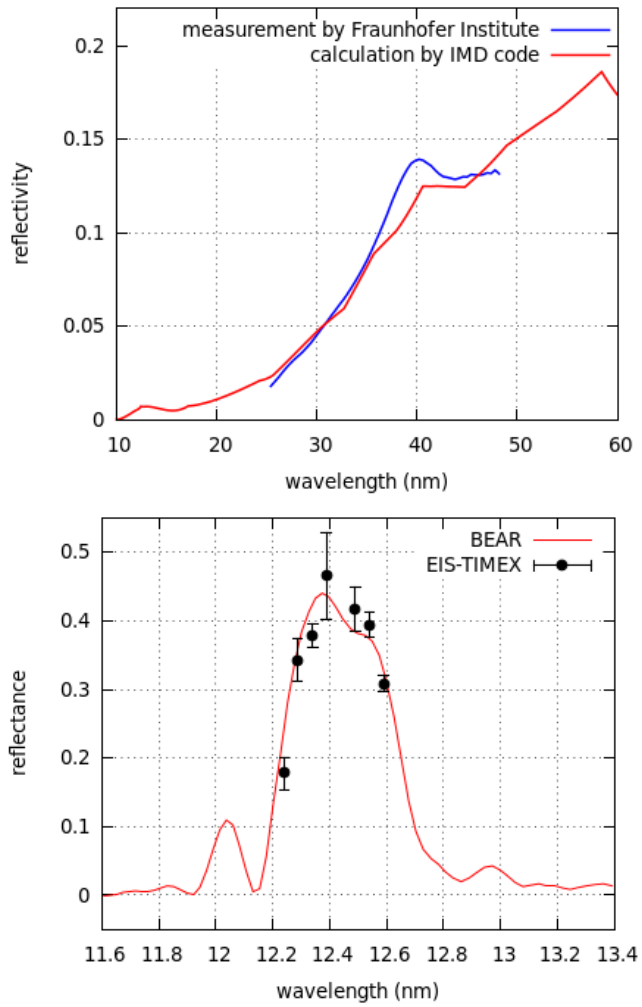

Figure 2.14: *Top*: reflectivity of a 10 nm Pt layer with roughness of 0.2 nm on a Si substrate with similar roughness as calculated with the code IMD [70] (*red curve*) and measured by the producer (Fraunhofer Institute) (*blue curve*). *Bottom*: reflectivity of a tailor-made Mo/Y periodic stack as measured at the BEAR beamline of ELETTRA (*red curve*) and on TIMEX (*black points*). The incidence angle is 3°.

4 μm. These expectations are confirmed by FEL permanent imprints on a YAG crystal, as shown on panel c) of Fig. 2.15.

2.1.7 Optical breadboard

In July 2013, with the completion of the user laser transport to the experimental hall, the TIMEX beamline was subject to a major upgrade: the installation of an optical setup for combined laser / FEL pump-probe experiments.
The user laser comes up with pulse durations of 100-120 fs and intensities between

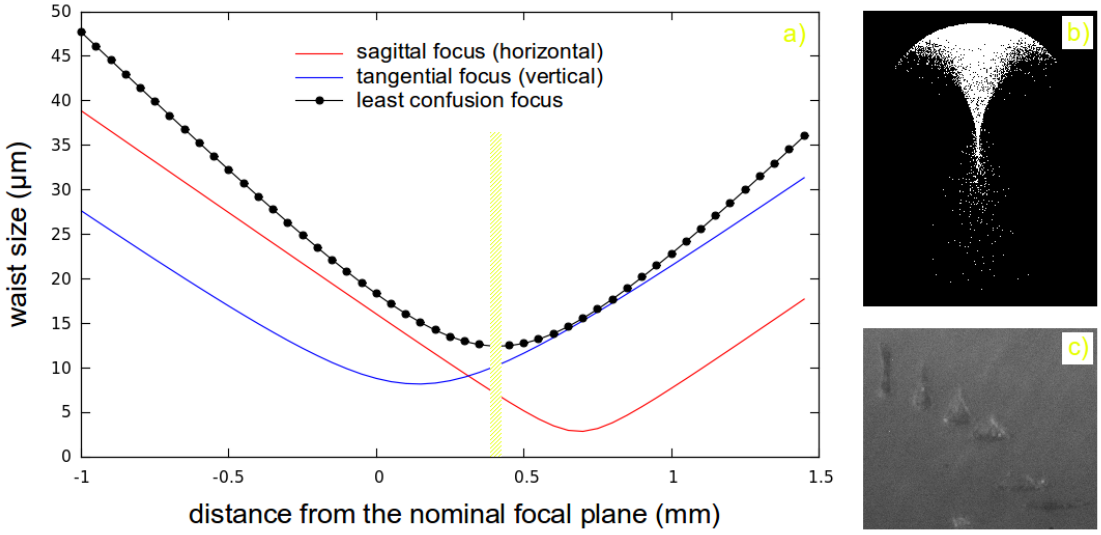

Figure 2.15: *a*): ray tracing simulation of a light beam at 40 nm wavelength focused by a spherical mirror at 3° angle of incidence; *b*) expected beam dimensions at the best focus; *c*) ablation imprints on a YAG crystal at various focal distances across the best focus.
Credits: E. Principi.

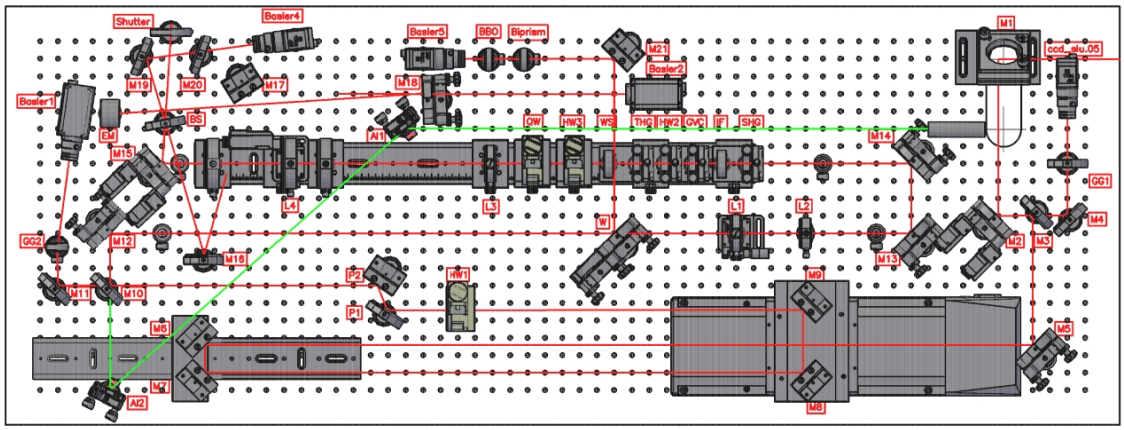

Figure 2.16: Top view of the TIMEX optical breadboard.
Credits: G. Curdi.

100 and 500 μJ, as measured by an autocorrelator and a power meter respectively. Within our optical setup, we can manage the attenuation level, the polarization status, as well as select between the fundamental radiation at 780 nm and its second (390 nm) and third (260 nm) harmonics. In the last two cases, the available intensity will be - by necessity - smaller and the pulse length may be slightly altered, despite the use of compensator crystals.
A motorized delay line allows to adjust the time delay relative to the FEL within

a range of -1 to + 1 ns. Translation of a focusing optics permits to obtain a spot size variable between 30 and 200 μm fwhm.
If fluorescence YAG screens are found to overestimate the spot size of the FEL (as we will better see), even more critical is their use with the optical laser which gives rise to a huge diffusion. To estimate the laser footprint at the sample position we therefore rely on another method: while the main part of the laser beam enters the vacuum camera, a small fraction of it goes through an identical path (of the same length, with the same optical elements) ending with a CCD camera that thus plays the role of "a virtual sample". Furthermore, on-line processing of the image acquired by this CCD provides the signal for a feedback loop that acts on the high precision piezo-driven tip-tilt mounts of the focusing mirror. Such a fine steering of the laser beam trajectory traduces into tangible improvements of both the pointing and timing stabilities, with great benefit for experiments that exploit the spatio-temporal superposition with the FEL beam.
Another CCD camera collects the back-reflected laser light in those pump-probe experiments where the laser acts as a probe.
Regarding the experiments with a laser pump and a FEL probe, they are going to benefit from a revision of the optical setup in the perspective of reaching higher laser fluences at the sample. This should be possible by substituting the focusing optics with one of shorter focal length, to be positioned directly inside the TIMEX chamber.
Figs. 2.16 and 2.17 illustrate in more details the current configurations of, respectively, the external (i.e. in air) and internal (i.e. in vacuum) optical breadboards.

2.2 Data harvesting

2.2.1 The control and acquisition system

As in the whole FERMI, all hardware and software assets are managed within the framework of TANGO, an open source device-oriented controls toolkit under continuous development by a consortium of synchrotron facilities [71].

For each instrument, a device with configurable attributes and operations exists, that continuously updates a circular memory buffer with the acquired data. Tagged with an increasing counter named bunch number, these are exported to the higher level device (FERMIDAQ) having instantiated the acquisition thread from that instrument. The user himself can select the data source devices of its interest, whether they come from the end-station instrumentation or from the machine diagnostic systems, from an all-comprehensive list. The desired information will be organized and stored by the FERMIDAQ in hierarchical data format (HDF5). On

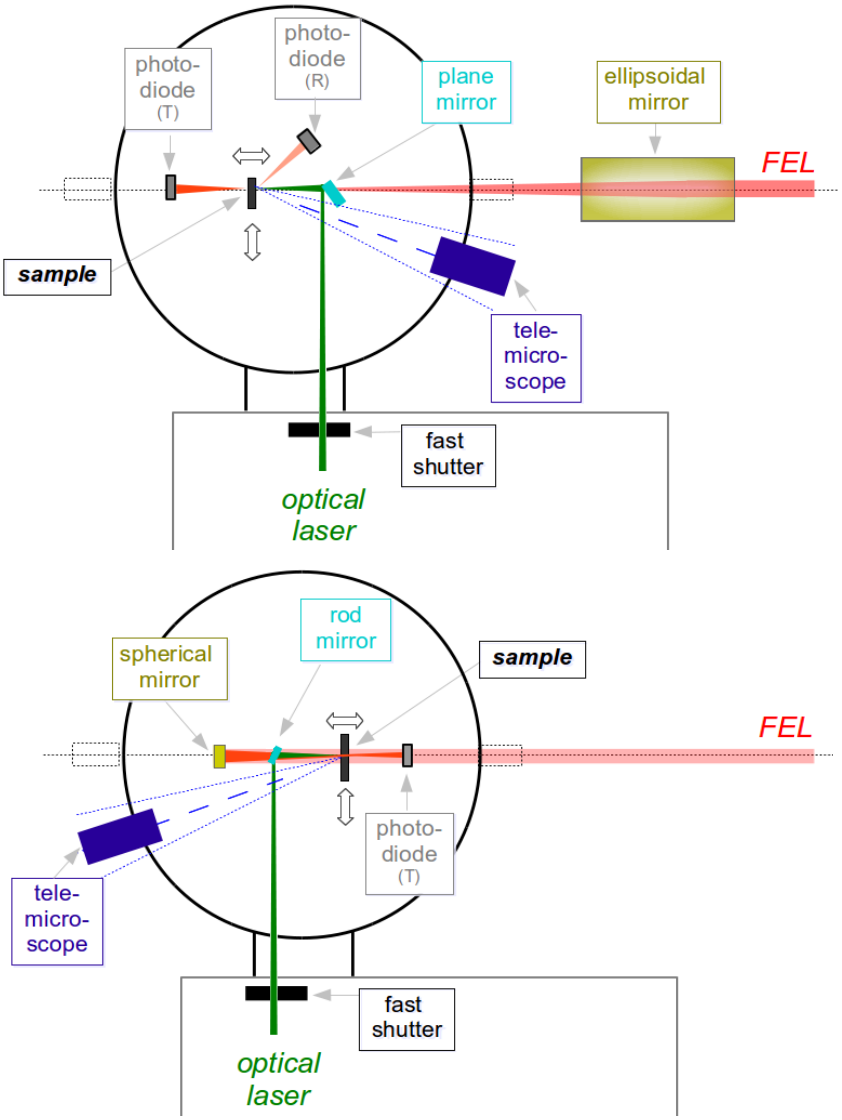

Figure 2.17: Internal top view of the TIMEX chamber equipped for pump-probe experiments with an additional optical laser. Top: configuration with internal-chamber FEL focusing optics; bottom: configuration with external-chamber FEL focusing optics focus.

top of the chain, an EXECUTER device launched by the user runs the one or the other of the available scripts conceived to execute the operation sequences required in the most common experimental situations.

Despite being in its early years of operation, the beamline is in an advanced status of automation, much part of the push for additional sophistications with respect to a synchrotron beamline coming from the fact each light shot is potentially destructive for the sample under investigation. Hence, one may choose if running continuous or N-shots acquisitions and if keeping the sample position fixed or mov-

able along a given serpentine path in the (y,z) plane. For the last case, various algorithms have been developed to compensate (with movements along the focal direction) for possible non-orthogonal positioning of the sample with respect to the incoming FEL beam, thus assuring controlled irradiation conditions. Since sample movement from one position to an adjacent one overall requires more than 0.1 s, the light beams have to be shuttered in between one pulse and the other - an operation that is accomplished by a fast shutter in the optical laser case while being based, in the FEL case, on the de-synchronization between the electron beam and the seed laser beam (obtained by moving a delay line along the path of the last). Procedures exist to launch delay line scans in either continuous or stepped modes with both the delay line of TIMEX - on the optical laser path - and the one of Padres - on the FEL path. Enabling the pump-probe option, maximum flexibility is left in the choice of the number of FEL and laser pulses before and after a time-zero pump-probe event; therefore, for example, one may choose to probe the sample with the desired accuracy both before and after a given number of pump shots (whichever are the pump and the probe among the FEL and the optical laser).

2.2.2 Data reduction

The most salient aspect of the data reduction is that concerning the rescaling of the signal detector counts to yield absolute intensity values.
We have already hinted to the fact that, if i0 denotes the upstream FEL intensity measured by the ionization monitor in the safety hutch and i1 denotes the downstream FEL intensity measured at TIMEX by a time by time different detector, the i1 vs i0 curve recorded with no samples in between does not solely depend on the detector type but also on a number of additional factors.

Some of these factors are related to the settings of the photon transport line. From Fig. 2.18, it can be seen how keeping more or less open the beam defining slits placed downstream of both the i0 and the i1 instruments affects the i1 vs i0 calibration in a non-trivial manner.

Other factors may reside in the characteristics of the FEL emission itself. Do not forget, indeed, that - although FERMI, as a seeded facility, offers greater stability than other SASE-based facilities - fluctuations in the beam parameters among successive pulses always exist, therefore often calling for the need to treat the experimental data on a statistical basis.
Fig. 2.19 shows that FEL shots with slightly different spectral features populate separate regions of the i1 vs i0 curve. This fact was recognized by sorting the horizontal spectrometer profiles on the basis of the number of peaks, average peak position and average peak width through appropriately developed algorithms.
We still have to clarify whether it is the wavelength content itself that matters for

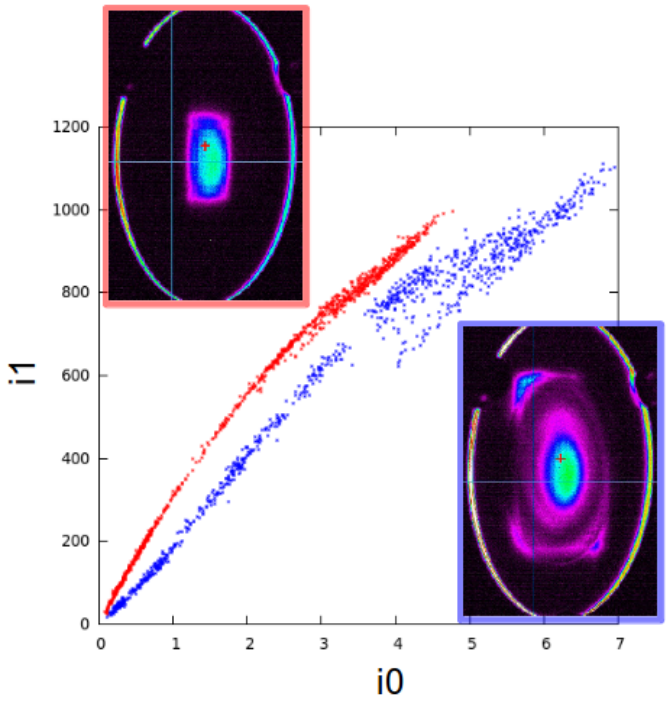

Figure 2.18: Dependence of the calibration curves on the settings of the beam defining aperture. It is good practice to exclude the off-axis radiation.

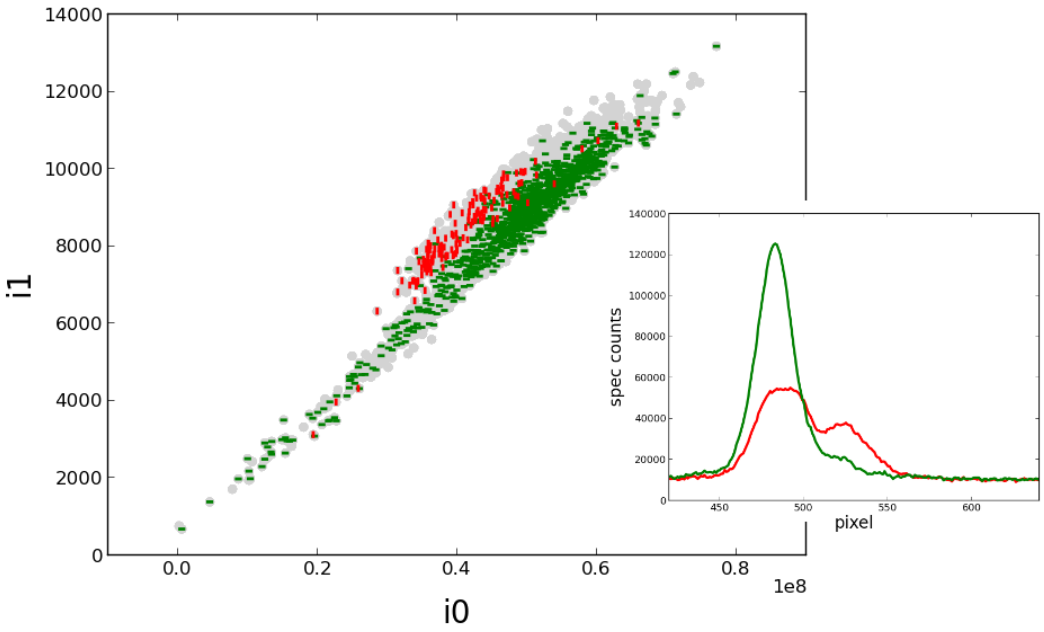

Figure 2.19: Dependence of the calibration curves on the beam spectral profile. Filtering algorithms may be used to "clean" the data, of course at the expense of statistics. In *gray* the raw data, in *green* shots with a singly-peaked spectrum, in *red* shots with a spectrum whose fwhm exceeds a certain threshold.

the detector response or if, rather, spectral changes are just markers of instabilities in the machine operative conditions that alter different properties of the pulse (its trajectory for example). The key to figure it out will be to correlate measurements at the end-stations, not only with the output of the PADRES diagnostics, but also with the many parameters coming from upstream instrumentation in the accelerator and undulator sections of FERMI.
As a general remark, bear in mind that, if filtering algorithms may succeed in reducing the dispersion of the calibration curves (and thus the error bars), they of course do so discarding a considerable amount of points, which is definitely inconvenient in the single-shot mode of operation imposed by the sample damage.

In consideration of all these aspects, the i1 vs i0 calibrations may deviate substantially from linear curves. Depending on how they looked like, in the data analysis for the experiments reported in this thesis, we have either chosen to go for a polynomial fit - as in the case of the upper curve of Fig. 2.20 - or for a binning - as in the case of the bottom curve of the same figure.
In both the shown cases the wide intensity interval was covered, besides by the natural FEL fluctuations, by varying the gas cell pressure. The latter, combined with a bistable response of either the i0 or the i1 monitor for that particular situation, is at the origin of the fractal-like (more hardly manageable) shape highlighted by the inset of Fig. 2.20.

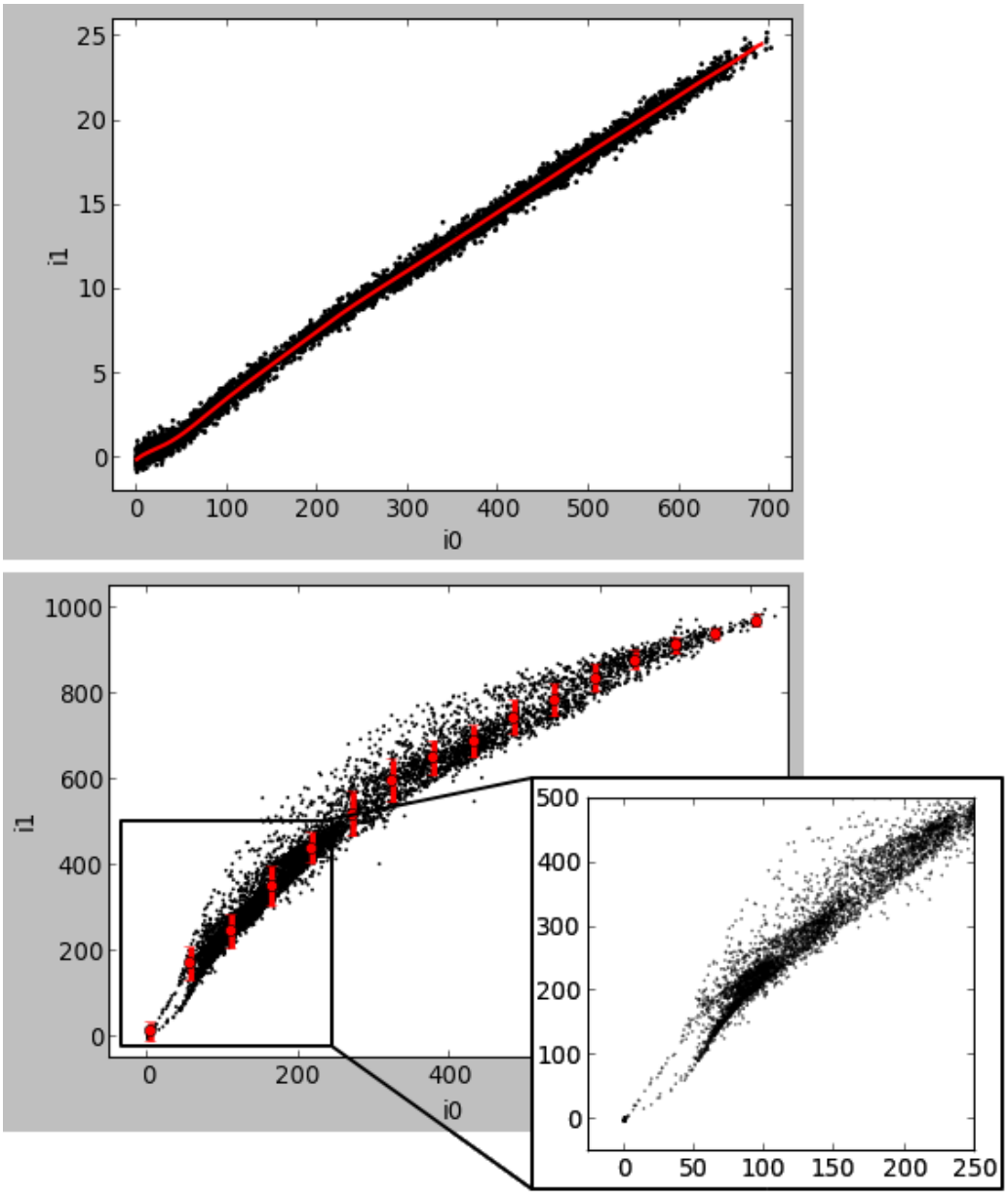

Figure 2.20: Two examples of calibration curves. On the y axis, the time integrated voltage signal from *top*: an IRD UVG20S photodiode looking at an FEL-illuminated Al-coated YAG screen and *bottom:* an IRD SXUV100 photodiode directly hit by the FEL beam. Units are pC for the i0 and nVs for the i1.

Part II

Second part

In this section, I report on the early investigations carried out at the TIMEX end-station, where metallic systems were excited into transient states of extreme conditions by a single FERMI FEL pulse and, by the very same pulse, characterized through their EUV reflectance and/or absorbance.
I refer to this class of measurements as "self-reflection and self-transmission experiments", reserving the phrase "pump-probe experiments" to that class of measurements where two different pulses take on the distinct roles of pumping and probing. Even in this basic approach where the system dynamics could not be followed beyond the roughly 100 fs long pulse duration, full exploitation of the outstanding properties of FERMI as a tunable source of short and intense EUV pulses have led to original and interesting results. Precious information like the average free electron density and temperature or the average ion charge could be derived by resorting to a simple setup and a simplified yet meaningful interpretive perspective on the obtained novel data.

Chapter 3

FEL self-reflection and self-transmission experiments

Titanium samples were the object of the first self-reflectance and self-transmission measurements, which were conducted - respectively - near its plasma frequency (17.7 eV) and $M_{2,3}$ absorption edge (32.6 eV).
Self-transmission measurements were then conducted on aluminum in the energy region of free-free absorption (37 eV) and on magnesium near its $L_{2,3}$ absorption edge (49.7 eV).
The following sections are devoted to their presentation and discussion.

3.1 Ultra-fast high-energy-density near plasma frequency reflectance spectroscopic study of Ti

The idea behind this experiment was to determine the key parameters connoting a dense plasma of Ti by exploiting (along the lines that will be illustrated in a short while) a "plasma mirror effect" - i.e. the reflectivity enhancement which is expected to occur following intense FEL excitation just above the plasmon resonance.

Diagnosing the conditions of temperature, density and ionization of a photo-generated plasma state is the first step towards its comprehension. Thus far, the most established way to do so resorts to the technique of X-ray Thomson scattering, which have been masterfully reviewed by Glenzer and Redmer in Ref. [72].
Depending on the probe energy and scattering geometry which determine the exchanged momentum between a photon and an electron ($k = 4\pi \sin(\theta/2)/\lambda$), the scattering spectrum gives access to electron density fluctuations on different length scales ($\approx 1/k$). Therefore, if a dimensionless scattering parameter $\alpha = \dfrac{1}{k\lambda_s}$ with λ_s screening length (the Debye length for a classical plasma or the Thomas-Fermi

length for a fully degenerate plasma [73]) is introduced, single-particle motion is probed under the condition $\alpha < 1$, whereas the condition $\alpha > 1$ corresponds to probing a collective regime.
In the latter case, the scattering spectrum features an elastic Rayleigh peak due to scattering from ion acoustic waves (essentially from weakly and tightly bound electrons) and a couple of red- and blue-shifted inelastic peaks due to scattering from electronic plasma waves (essentially from free electrons). From the ratio between the intensities of the blue-shifted to red-shifted peaks, given by the Bose-Einstein factor $e^{\hbar\omega/k_B T_e}$, the free electron temperature T_e can be determined, whichever the electronic distribution is provided the plasma has reached thermodynamic equilibrium. Furthermore, the free electron density n_e can be determined from the spectral shift of the plasmon peaks with respect to the elastic one, which - in a first approximation - is quantifiable via the Bohm-Gross dispersion relation as $\omega_p^2 + \frac{3k_B T_e}{m_e}k^2$, n_e entering the definition of the plasma frequency ω_p.

This same shift in ω_p upon photo-excitation ascribable to a change in n_e is also expected to lead to an increase in the XUV reflectivity.
What happens at high enough intensities when the created plasma reaches an electron density exceeding the critical one $n_c = \frac{\epsilon_0 m_e}{e^2}\omega^2$ is indeed that the remaining part of the incident pulse become screened by a strongly increased target reflectivity. Sometimes known as self-induced plasma shuttering, such effect is at the base of a recognized method to improve pulse contrast, i.e. the ratio of the peak intensity to the intensity of pre-pulses and/or pedestals which are unfavorable for many applications, like for example high-order harmonic generation from a solid surface [74, 75].

These considerations suggested us to map out FEL-induced reflectivity variations in that low energy side of the EUV spectrum which, dominated by plasma resonances, may provide access to the most relevant plasma parameters of so-excited Ti.

3.1.1 Experimental details and results

The experimental setup was the one employing the alternative focusing optics, that is, a spherical mirror (substrate: Si, coating: 10 nm of Pt, roughness: < 0.2 nm rms, diameter: 30 mm, focal length: 200 mm, incidence angle: 3°) directly placed inside the TIMEX chamber and able to provide a focal spot of area $\sigma^2 \approx 100\ \mu\text{m}^2$. The sample was a 100 nm thick layer of Ti deposited on a Si substrate and passivated with 3 nm of TiO_2.
The reflected beam was detected by a system consisting of a 0.5 mm thick YAG crystal coated with 100 nm of Al on the FEL side and coupled to an UVG20S

photodiode on the opposite side.

Reflectivity data have been collected as a function of both photon energy and fluence. The photon energy was varied in discrete steps by changing the seed laser wavelength while keeping fixed the harmonic number, while the pulse intensity was varied continuously thanks to the gas attenuator. At all the explored photon energies $\hbar\omega$ = 18.9, 19.1, 19.4, 19.7, 20.0 and 20.3 eV we could rely on a pulse intensity in the 1-300 μJ range. The corresponding maximum fluence at the sample position was of approximately 25 J/cm^2, once proper account is taken of the beamline transmission, the focusing mirror reflectivity and the TiO_2 passivation layer transmission (which we have evaluated to take on values of about 52-56 %, 15-20 % and 73 %, respectively, in the investigated photon energy interval) as well as of the focal spot dimensions.

In reflection geometry it was not possible to obtain a calibration curve by correlating - in absence of any sample - the simultaneous signals from the Padres ionization monitor (recording the incoming intensity I_0) and our detector (recording the reflected intensity I_R). Thus, in order to get rid of the diagnosed non-linear relationship between these two signals, for each FEL wavelength employed in the experiment we have taken multiple-shots reflectivity measurements in the whole available intensity range with the sample moved 3 mm away from the plane of best focus so as to deduce a curve I_R^{defoc} vs I_0^{defoc} by which normalizing the corresponding I_R vs I_0 curve relative to the single-shot measurements at best focus.
What we could get was, therefore, the relative reflectivity: $\frac{R(F)}{R(0)} = \frac{I_R/I_0}{I_R^{defoc}/I_0^{defoc}}$, with the ratio between I_R/I_0 and I_R^{defoc}/I_0^{defoc} to be intended as a ratio over I_0 and I_0^{defoc} bins of equal photodiode counts.

As a check, we have - in turn - normalized the I_R^{defoc} vs I_0^{defoc} curve to the I_R^{NS} vs I_0^{NS} curve recorded without the sample, in transmission geometry and with a similar but different detector, obtaining the trend shown in Fig.3.1.
Although it may not represent the actual unpumped reflectivity of the sample, its flatness as a function of fluence assures us of the fact that no artifacts from the ionization monitor are affecting our findings.

The dependence upon fluence of the relative reflectivity is reported for three representative photon energies in Fig.3.2, where each filled circle corresponds to a single-shot measurement (i.e. - we remind - taken on a fresh portion of the sample) and its error bar has been calculated from on the standard deviation of the normalizing out of best focus multiple-shots measurement.
A very clear raise is noticeable, which amounts up to about 40-50 % at the maximum reached fluences.

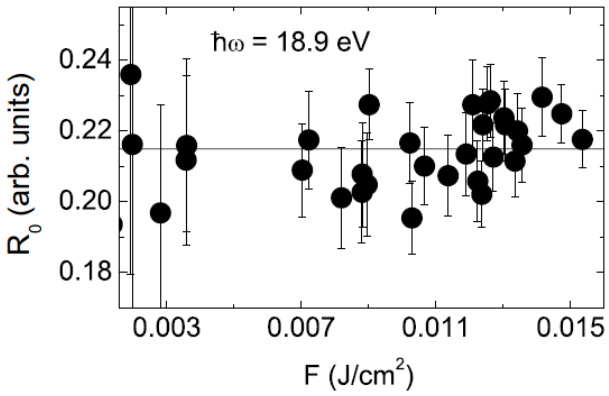

Figure 3.1: Reflectivity measurements at $\hbar\omega = 18.9$ eV as a function of fluence in the low fluence regime realized for the same incoming FEL intensities as in the high fluence regime but with the sample placed 3 mm away from the plane of best focus. For the reasons explained in the text, data points do not represent the reflectivity of the unexcited sample but they are proportional to it.

3.1.2 Analysis and discussion

Let us attempt, now, a quantitative interpretation of these results.

For the present conditions of near normal incidence and sample thickness exceeding the penetration depth of the radiation ($L < 23$ nm), the reflection coefficient can be expressed in terms of the complex dielectric function ϵ as

$$R \approx \left| \frac{\sqrt{\epsilon} - 1}{\sqrt{\epsilon} + 1} \right|^2 . \tag{3.1}$$

In metals, a simple expression for ϵ is provided by the Drude formula:

$$\epsilon = 1 - \frac{\omega_p^2}{\omega^2 + i\omega\gamma}, \tag{3.2}$$

where

$$\omega_p = \sqrt{N_e e^2 / m_e \epsilon_0} \tag{3.3}$$

is the plasma frequency - with n_e, e, m_e and ϵ_0 the free electron density, the elementary charge, the effective electron mass and the vacuum permittivity, respectively - while γ is the inverse lifetime of the plasmon resonance, basically related to the mean electron-phonon collision frequency [76].

In this framework, a variation in R can only be ascribed to a change in either ω_p or γ.

Fig.3.3 illustrates the dependence of the reflectivity on ω_p for three reasonable

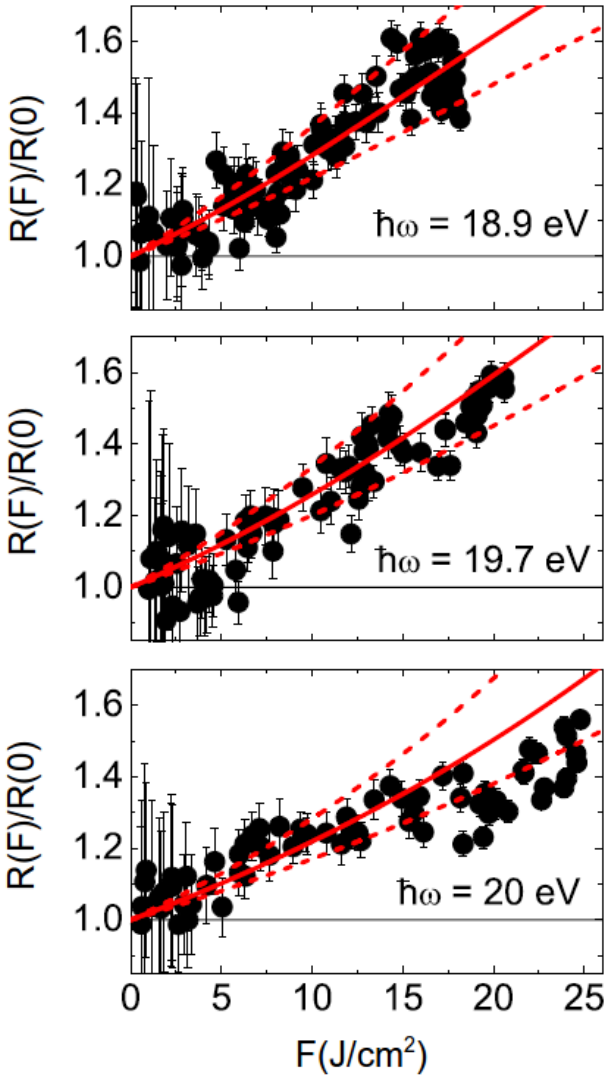

Figure 3.2: Relative reflectivity as a function of fluence for three selected photon energies. *Red full lines* are the model results calculated through Eq.3.6; *red dashed lines* mark the estimated confidence interval.

values of γ [77, 78, 79] at two photon energies ω above the plasma frequency of unexcited Ti $\omega_p(0)$=17.7 eV [80, 81]. We infer from it that, in the photon energy range of choice for this experiment, the sensitivity to on ω_p is more relevant than the one to γ.

That established, in lack of a literature reference for this parameter in Ti, we set $\hbar\gamma = 1.5$ eV in analogy to what found for Al by the authors of Ref. [77], according to which it is $\gamma \approx 0.1 \cdot \omega_p(0)$. Then, neglecting a possible variation of γ with fluence, we claim that the observed increase in reflectivity is due to an increase in

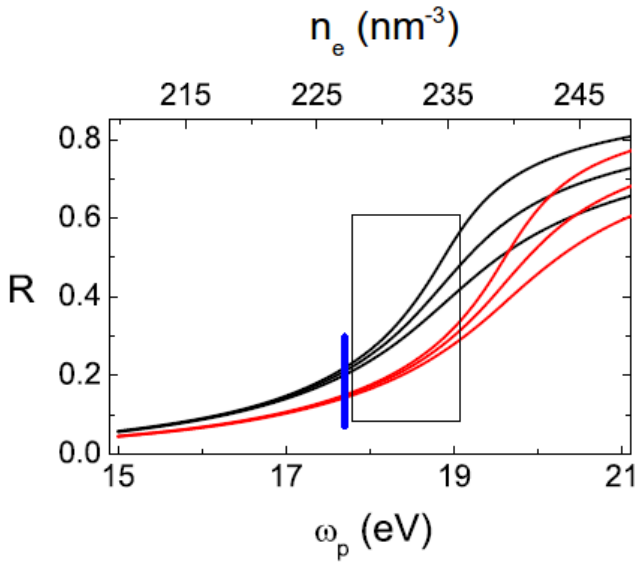

Figure 3.3: Dependence of R on ω_p for $\hbar\gamma = 1$, 1.5 and 2 eV (*higher to lower curves*) at $\hbar\omega = 18.9$ and 20 eV (*black and red lines*), calculated with Eq.s 3.1 and 3.2. The *upper horizontal scale* for n_e is the one corresponding to the bottom horizontal scale for ω_p via Eq.3.3. The *blue vertical segment* indicates the expected plasma frequency of the unexcited sample; the *hatched area* delimits the range of ω_p that we determined to have reached under the high fluence irradiation conditions of the present experiment.

the plasma frequency, in turn due to an increase in the free electron density upon strong illumination.

In order to gain a more quantitative insight, we assume that the increase in n_e is proportional to the energy density $\overline{E}$ deposited into a sample layer of thickness $d < L$ below the metal surface.
In expressing the last quantify, we account for both the temporal and the spatial profiles of the FEL pulse as well as - through a factor $1 - R(F,t,x,y)$ - for the reduction in the amount of energy available for further excitation at a later time caused by the reflectivity raise by that time.
Hence, in formulas:

$$\omega_p^2(F,t,x,y) = \omega_p^2(0)\ \left[1 + A\,\overline{E}(F,t,x,y)\right] \tag{3.4}$$

with A an empirical constant representing the fractional increase in n_e per unit $\overline{E}$ and

$$\overline{E}(F,t,x,y) = \frac{F\sigma^2}{L}\int_{-\infty}^{t} dt'\ S(x,y)\,G(t')\,[1 - R(F,t',x,y)]\,, \tag{3.5}$$

where the normalized time and space intensity distributions $G(t)$ and $S(x,y)$ have

been approximated by Gaussian functions with variances $\sigma_t = 45$ fs ($= \sigma_{seed}/\sqrt[3]{n}$, $\sigma_{seed} = 70\ fs$ and $n = 4$) and $\sigma_x = \sigma_y = 5\ \mu m$.
It is worth to stress that treating $G(t)$ as a well defined function was only possible as a result of the seeded nature of our FEL source (had we had a SASE FEL source, this kind of analysis could not have been carried out!).

Using Eq.s 3.1, 3.2, 3.4 and 3.5, the fluence-, time- and space- dependent reflectivity $R(F,t,x,y)$ can be calculated, whose time and space averages provide a term of comparison for our experimental observable:

$$\frac{R(F)}{R(0)} = \frac{1}{R(0)} \int dx \int dy \int dt\ S(x,y)\ G(t)\ R(F,t,x,y). \tag{3.6}$$

A simultaneous fit of the data to this equation at all the available photon energies has been performed with $\hbar\omega_p(0) = 17.7$ eV and $\hbar\gamma = 1.5$ eV yielding a best value of $7.5 \cdot 10^{12}$ m^3/J for the free parameter A.

The temporal evolutions of $\dfrac{R(F,t)}{R(0)} = \dfrac{1}{R(0)} \int dx \int dy\ S(x,y)\ R(F,t,x,y)$ for two representative photon energies and fluences are displayed in Fig.3.4, along with that of $G(t)$. The fluence evolutions of $R(F)/R(0)$ for three representative

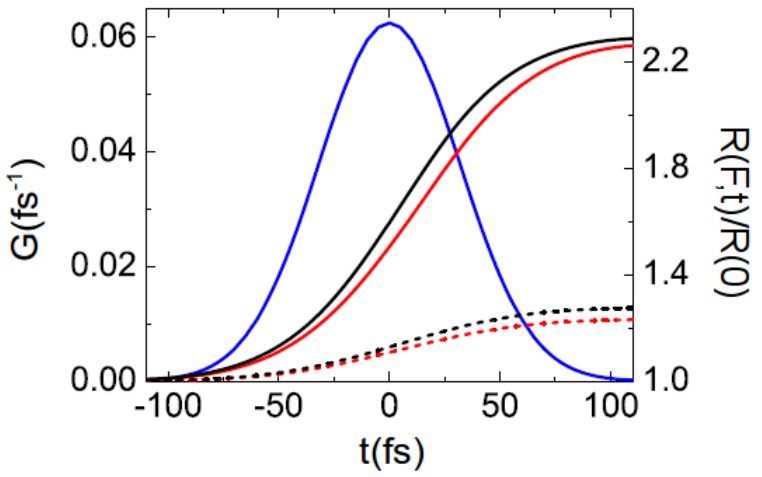

Figure 3.4: Temporal evolutions of the pulse intensity profile (*left scale, blue line*) and of the corresponding relative reflectivity (*right scale*) for the two representative energies 18.9 eV (*black lines*) and 20 eV (*red lines*) and the two representative fluencies 5 J/cm^2 (*dashed lines*) and 20 J/cm^2 (*full lines*).

photon energies are instead shown as red continuous lines in Fig.3.2 along with the corresponding experimental determinations.
They agreement is good and permits to estimate an average increase in the plasma frequency and the free electron density up to ≈ 4 % and 8 %, respectively, at the

highest fluences.
Upper and lower red dashed lines in the same figure correspond to values of A larger and smaller by 25 %, that we regard as the limits of the estimated confidence interval.
Various fitting trials convinced us that - according to the level of accuracy of the experimental data - the results are only marginally affected when the value of $\hbar\gamma$ is chosen in the fairly broad 0.5-2.5 eV range, which basically encompasses all the values encountered in a large class of metals [77, 78, 79].
The range of values for $\omega_p(0)$ that proves compatible with the experimental data within their experimental uncertainty is instead narrower, between 17 and 18 eV, coherently with our model assumptions.

Once $\omega_p^2(F,t,x,y)$ is determined, it is straightforward to compute the corresponding average free electron density or, equivalently, the average ion charge:

$$Z(F) = \frac{Z(0)\,N_e(F)}{N_e(0)} = \frac{Z(0)\,\omega_p^2}{\omega_p^2(0)} = \frac{Z(0)}{\omega_p^2(0)} \int dx \int dy \int dt\, S(x,y)\, G(t)\, \omega_p^2(F,t,x,y), \tag{3.7}$$

where it is $Z(0) = 4$, the number of 3d and 4s electrons which are collectivized in the unexcited sample. Fig.3.5 reports the obtained variation of the average ion charge with fluence. It is indicative that shallower core electrons are ionized and do not recombine within the pulse duration. Indeed, the energy reached during the

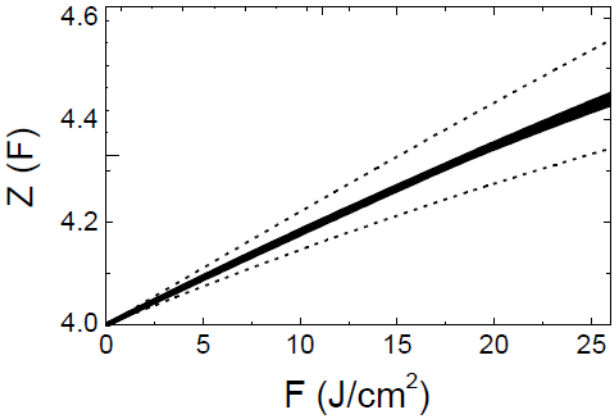

Figure 3.5: Estimated mean ion charge as a function of fluence at the employed photon energies (*full lines*) and corresponding confidence interval (*dashed lines*).

experiment are comparable to the ionization energy E^+ of 99 eV/atom reported in Ref. [82]) for the $Ti^{4+} \rightarrow Ti^{5+}$ process. If we assume that the latter is the leading ionization process, then the data shown in Fig.3.5 tell us that at the highest fluence of ~ 25 J/cm^2 and within the FEL pulse duration of ~ 45 fs, approximately 40 % of Ti atoms result ionized. Such finding is in qualitative agreement with what found

for Al according to Ref. [83], where the onset of FEL-induced saturable absorption due to ionization of almost all the atoms is observed at similar irradiation fluences. Finally, we can attempt an evaluation of the electronic temperature based on the crude assumption that in a moderately excited sample the deposited energy either goes into ionization energy or into electron kinetic energy. Therefore:

$$\overline{E}(F) = \int dx \int dy\, S(x,y)\, \overline{E}(F, t=\infty, x, y) = E^{+}\left[Z(F) - Z(0)\right] + \frac{3}{2} k_B T_e(F) Z(F) \tag{3.8}$$

The electronic temperature estimated in this way is shown in Fig.3.6 as a function of fluence for very low fluences and compared with the ones reported in Ref. [83] for Al. The latter data having been obtained by interpreting soft X-ray emission spectra within a free electron gas assumption, we can speculatively infer a common low-fluence behavior of photo-excited metals in the sub-0.1 ps timescale, which is dictated by the role of free electrons to a much larger extent than by the details of the atomic structure.
In this spirit, a more effective approach to determine the electronic temperature from measurements of the frequency-dependent absorption coefficient of Ti will be proposed in the next paragraph.

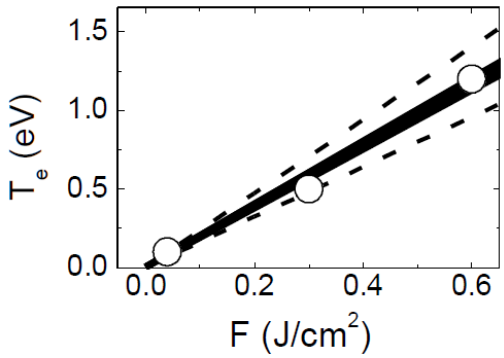

Figure 3.6: Estimated electron temperature as a function of fluence for low fluences at the employed photon energies (*full lines*) and corresponding confidence interval (*dashed lines*). Data are compared with the analogue parameter determined for Al in Ref. [83] (*circles*).

Summarizing, we have experimentally observed an enhancement in the reflectivity of titanium upon irradiation with ultra-short high-fluence EUV pulses tuned above the plasma frequency. These drive the sample into a short-living exotic state that exhibits electronic temperatures typical of plasmas while still retaining a cold atomic lattice. Reflectivity data have been interpreted through a Drude-like analytical model employing a single empiric parameter to account for the increase in

the plasma frequency within a FEL pulse. Despite likely an oversimplification, it is able to reproduce the observed phenomenology, demonstrating to capture the main physical process at its base and allowing us to derive an estimate for the average ion charge in the excited sample.
Our method can, therefore, be regarded as a complementary tool with respect to the one based on the measurement and analysis of the plasmon lineshape in the inelastic scattering spectra of the excited sample, a class of experiments that, although highly informative, rely on the development of sophisticated spectrometers and is limited by low cross-sections in high-Z samples and de-coherence effects at low electron densities [73]. Furthermore, the possibility to operate at lower photon energies than here used (down to ≈12 eV soon feasible at FERMI) will permit to extend our probe to a spectral region where the metallic reflectivity should be increasingly insensitive to plasma frequency variations and acquire instead a strong dependence on the plasmon lifetime, so that information on the electron-electron and electron-phonon interactions could be gained as well.

The work here presented has been published in May 2014 on Scientific Reports [84] with F. Bencivenga as the main author, who conceived the experiment and to whom my acknowledgments are due.

3.2 Ultra-fast high-energy-density near-edge absorption spectroscopy study of Ti

Aim of this experiment was to monitor possible changes of the absorption spectrum of Ti driven by transient modifications of the electronic subsystem occurring upon intense FEL irradiation.

3.2.1 Experimental details and results

FEL focusing was provided by the same spherical mirror employed in the previous experiment.
An UVG20S photodiode sealed in a grounded Al box and coupled to a YAG screen coated with 100 nm of Al on the FEL side was used to detect the FEL light transmitted by the Ti sample in the form of a self-standing foil with nominal thickness $d = 50$ nm, so-chosen to guarantee adequate penetration all throughout the sample depth (the attenuation length for quasi-normal incidence at 32.6 eV being about 42 nm [53]).
As we expect the reflectivity of Ti around 30 eV to be lower than 1% [53], we can derive the absorption coefficient μ or, more conveniently, the absorbance α from measurements of the sample transmission T by means of the Lambert-Beer relation $\mu d = \alpha = \ln(1/T)$.

Transmission spectra at ambient conditions are - of course - known and tabulated but, since an oxide layer always forms on the Ti surface during the even short time in which it is exposed to air when being loaded on its holder, we recorded a more faithful reference spectrum at the synchrotron beamline BEAR. Moreover, having the sample such a small thickness, we expected it to be, not only very fragile, but also to display sizable non-homogeneities (Fig.3.7).

With synchrotron light, we therefore made two survey measurements spanning all the sample at a fixed energy close to the transmission maximum (32 eV). While no differences were recorded with a beam of dimensions 900 μm x 400 μm, small differences were evidenced when the beam size was reduced to 400 μm x 100 μm. In correspondence to each of the three sample positions that resulted in the most diverse transmissions, we then acquired the complete energy scans which are shown as colored points in Fig.3.8. From such measurements, an average curve is deduced as the cubic root of the multiplied three original curves, that is plotted with a black continuous line in Fig.3.8 As it is there visible, the measured transmission is always pretty much lower than the one predicted for a non-oxidized sample (dotted line in Fig.3.8).
Further, it deserves a comment the fact that the transmission, rather than starting to slightly increase with increasing energy soon after the edge (as it usually hap-

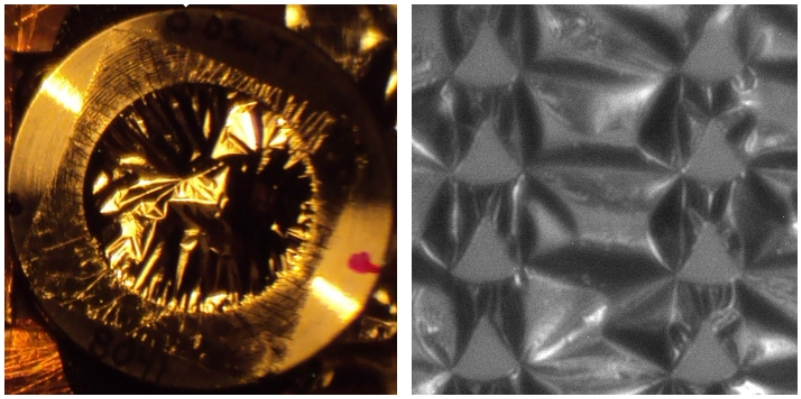

Figure 3.7: Appearance of a 50 nm -thick self-standing Ti foil. *Left*: on its mounting ring of 10 mm diameter. *Right*: as seen through the telemicroscope; each imprint results from the exposure to a single FEL pulse; the triangular spot shape is caused by astigmatism of the spherical focusing mirror.

pens), does indeed the opposite. Such feature is nothing but a Fano resonance that comes from the interference between the direct atomic transition process $[Ar]3d^24s^2 \rightarrow [Ar/3p\text{-hole}]3d^34s^2$ and the autoionization process $[Ar]3d^24s^2 \rightarrow [Ar]3d^14s^2\epsilon f$, as more diffusively explained in Ref. [85].

Let us come now to the measurements taken with FERMI at TIMEX.
In Fig.3.9, the same black continuous line of Fig.3.8 is reported to provide a term of comparison for the hundreds of shots data taken on a same sample position with a severely attenuated FEL light.

The fluence has been kept in this case well below the value of 1 mJ/cm^2 by choosing a spot size of about 120×60 μm^2 and by use of both an Al filter and the gas attenuation chamber, variously attenuated according to the expected sample absorbance in order to have a comparable energy density for every wavelength. The two spectra - the synchrotron one and the attenuated FEL one - are in very good agreement, thus demonstrating that the absorption coefficient of Ti is not modified when the pulse duration is as short as 100 fs provided that the pulse energy is sufficiently low.

Finally, a series of single-shot high-fluence measurements has been carried out at the four photon energies signaled by the vertical arrows in Fig.3.9, namely: E = 23.8 eV (well below the $M_{2,3}$ edge), E = 31.4 and 32 eV (close to the $M_{2,3}$ edge) and E = 34.4 eV (above the $M_{2,3}$ edge).
A fluence interval between 1 and 10 J/cm^2 has been covered by decreasing the FEL spot area at the sample down to ∼100 μm^2, by removing the Al filter along the transport path and by using the gas attenuator as a variable intensity filter.
Single-shot high-fluence results binned in groups of 5 to 15 single-shot experimental

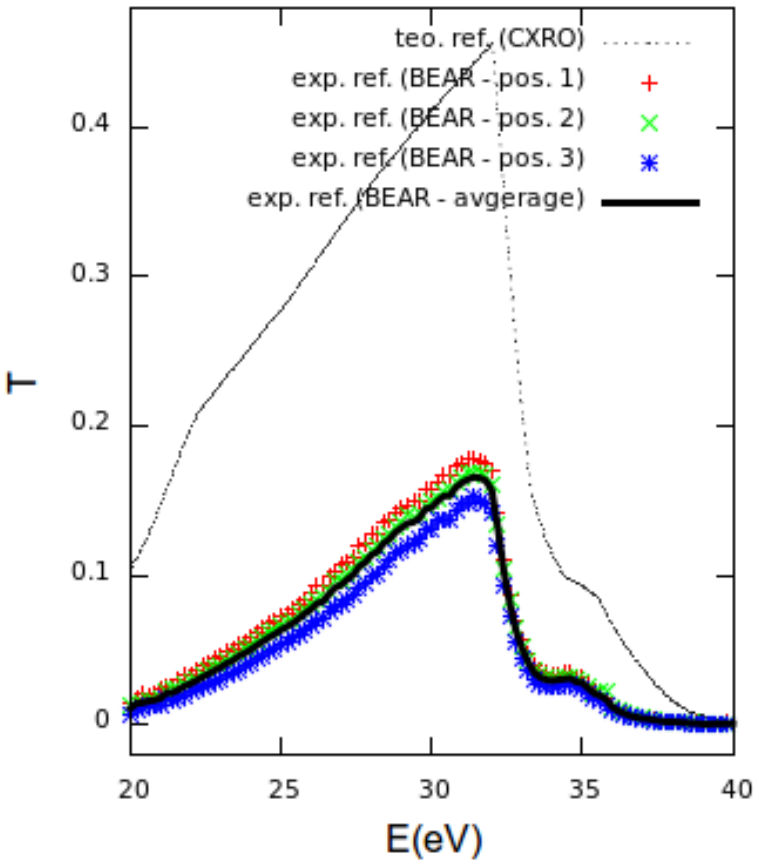

Figure 3.8: Transmission spectrum of Ti in standard conditions as tabulated in the CXRO database (*black dashed line*) and as measured with synchrotron light on three different sample positions with a 400 μm x 100 μm beam(*colored point*, from which the average spectrum shown as a *black continuous line*).

points (filled circles) are represented together with unbinned multiple-shots results collected below the sample degradation threshold (open circles) on a common fluence scale in Fig.3.10. Unfortunately, single-shots measurements are affected by considerable noise due to a combination of factors: poor counting statistics, very low signals (looking at Fig.3.8, one can notice how close to zero the transmission is - especially at the probed photon energy above the edge) and non-uniform foil thickness (as evidenced by the synchrotron measurements at the smallest possible beam size that was nonetheless greater than the FEL beam size for these measurements, thus smearing indeed higher dishomogeneity effects).

Despite these unfortunate circumstances, tangible modifications of the absorption spectrum upon high-intensity irradiation are evident at all of the probed energies.

An increase of absorption with fluence is clearly noticeable just before the $M_{2,3}$

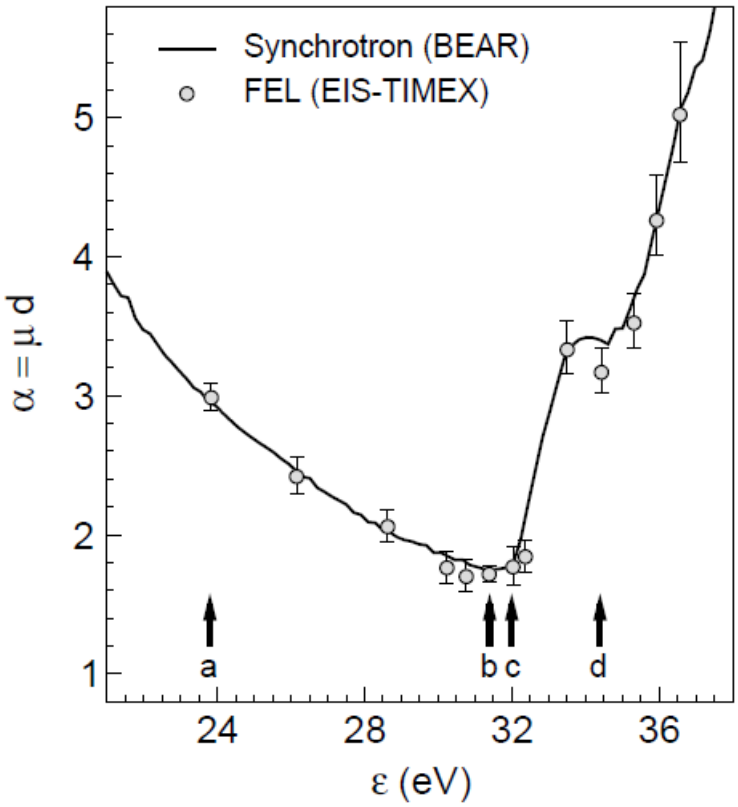

Figure 3.9: Standard absorption spectrum of Ti in the region of the $M_{2,3}$ edge. Data collected at TIMEX with a highly attenuated FEL (*gray points*) are compared with data collected at the BEAR beamline of the Elettra synchrotron (*continuous line*). *Vertical arrows* indicate the photon energies at which high-fluence absorption and reflectivity measurements were taken.

edge (panels b and c of Fig.3.10), where variations amount up to $\approx 25\%$. Even if subject to a greater experimental uncertainty, we can still say that the data at E = 23.8 eV (panel a of Fig.3.10) point out a less-pronounced ($\Delta\mu \approx 10\%$), yet similar trend. At E = 34.4 eV (panel d of Fig.3.10), the experimental points are particularly scattered and a twofold trend seems discernible, i.e. a decrease of absorption at intermediate fluences followed by an increase at higher fluences.

During the same experimental campaign, complementary reflectivity measurements at an angle of incidence of about 6° have been carried out.
The Ti sample was this time in the form of a 100 nm -thick layer, deposited on a Si substrate and passivated with a 3 nm -thick layer of Ti_2O_3 and had a rms roughness of $\simeq$ 1 nm.
The detector was an AVG20S photodiode operating with a bias of 150 V.

We selected the same photon energies as for the absorption measurements. The achieved maximum fluences were instead lower, because an Al filter had to be to

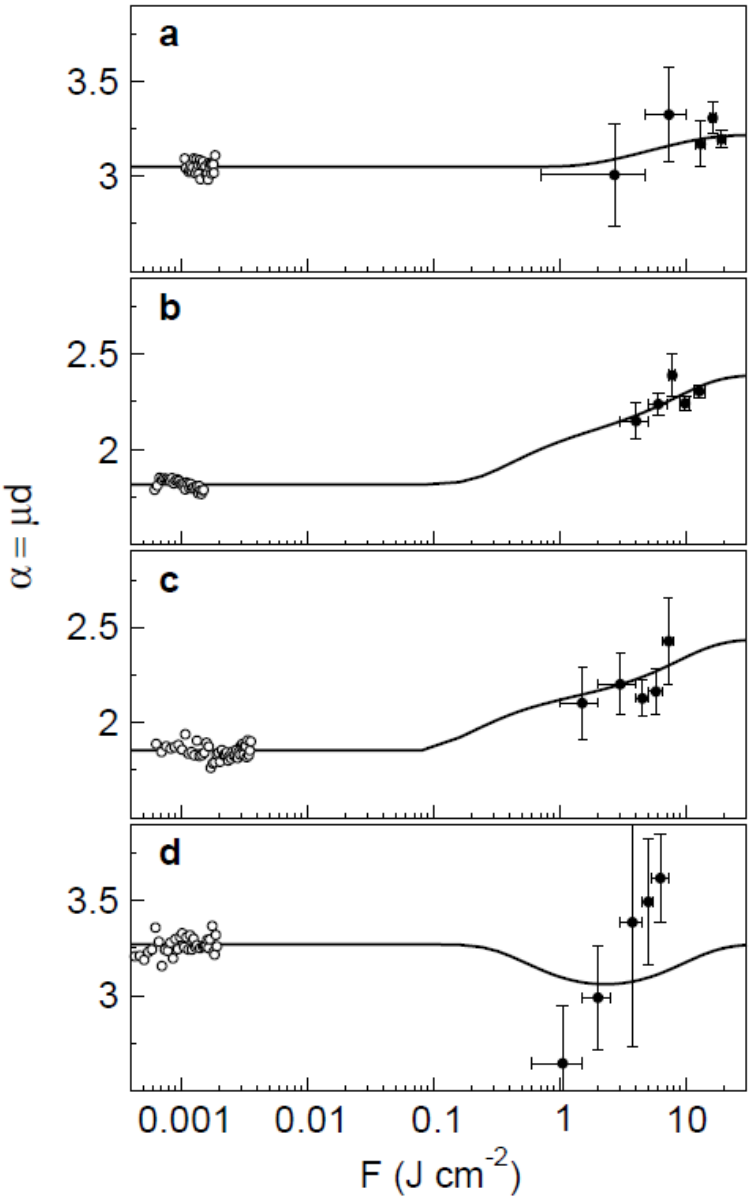

Figure 3.10: Absorbance of Ti as a function of FEL fluence at four selected photon energies across the $M_{2,3}$ edge: (a) 23.8 eV, (b) 31.4 eV, (c) 32.0 eV, (d) 34.4 eV.
Open circles are single-shot experimental data; *filled circles* result from an average of 5 to 15 single-shot experimental data; *solid lines* represent the trend predicted by the model described in the text.

inserted (by necessity before the sample) to block the seed laser light that would have otherwise been read by the EUV-sensitive photodiode.

Results are reported as a function of fluence in Fig.3.11. They are not absolute (so no units are indicated) because, not disposing of a calibration for the detector

placed in reflection, we normalized our measurements of the reflected vs incident intensity by the calibration curve for the detector placed in transmission that - as said - was of a different type.

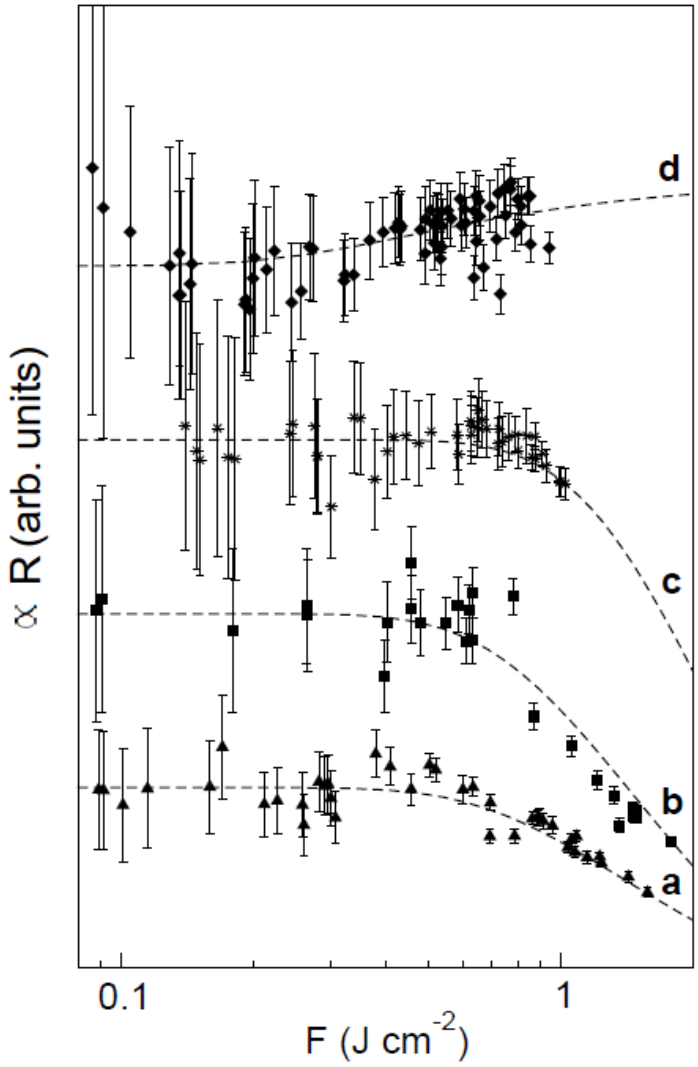

Figure 3.11: Reflectivity of Ti as a function of FEL fluence at the same four selected photon energies of Fig.3.10: (a) 23.8 eV, (b) 31.4 eV, (c) 32.0 eV, (d) 34.4 eV.
Dashed lines are guides for the eye.

An anticorrelated behavior emerges for the reflectance data with respect to the absorbance ones: the three energies below the $M_{2,3}$ edge are again characterized by a common trend, in this case of decreasing reflectivity (curves a,b,c in Fig.3.11) while the energy above the $M_{2,3}$ edge is again characterized by an opposite trend of increasing reflectivity (curve d in Fig.3.11).

3.2.2 Analysis and discussion

A possible interpretation for the illustrated experimental findings is proposed below.

At the moderate EUV photon intensities here achieved, the ponderomotive potential locally exerted by the FEL pulse on the electrons in the target can still be considered negligible.
Following the time-dependent perturbation theory valid within the weak field regime, the absorption coefficient $\mu(E)$ is then proportional to the probability for an electron in the core level i to be promoted to a final state f, as given by Fermi's golden rule:

$$\mu(E) \propto |\langle i| H' |f\rangle|^2 \rho_f(E), \tag{3.9}$$

where H' is the perturbation Hamiltonian representing the electron-photon interaction that drives the transition and ρ_f is the density of available final states [86].

At a pulse energy of 10 μJ, $\sim 2 \cdot 10^{12}$ FEL photons interact, within a volume of $\sim$100 μm^2 x 42 nm, with $\sim 2 \cdot 10^{11}$ Ti atoms. Therefore, an average of approximately 10 photons is delivered to each atom, which may seem a huge number.
However, one should consider two facts: on the one hand, that amount of photons is released on an atom not at once but over a pulse duration of about 100 fs; on the other hand, the 3p core-hole lifetime in Ti - dominated by a super-Coster-Kronig transition (i.e. an Auger process where the initial hole, the jumping electron and the departing electron all come from the same M shell) - is expected to be shorter than 1 fs following Ref. [85].
For these reasons, we hypothesize that, despite the high photon density, the target atoms involved in the photoionization process are at their ground state.

On the basis of these considerations, we assume the matrix element appearing in Eq. 3.9 as invariant upon FEL pulse absorption and consequently ascribe the observed changes in the absorption coefficient to an ultra-fast variation of the density of available final states: $\Delta\mu(E) \propto \Delta\rho_f(E)$.

Moreover, since modifications of the atomic order have to be excluded within the short time window of a FEL pulse, it is convenient to decouple the ionic subsystem from the electronic one.
We may then treat the former as stationary at room temperature and the latter as an electron gas that, during the first 100 fs of irradiation has thermalized at a certain electron temperature T_e. This assumption does not go without criticism, the electronic thermalization time being not a consolidated datum. Postponing a more diffuse discussion to the final comments, we anticipate our positive evaluation of the plausibility of this hypothesis and thus finally adopt the free electron density of states:

$$DOS(E, T_e) \propto \sqrt{E} \cdot f(E, T_e), \tag{3.10}$$

where

$$f(E,T_e) = \frac{1}{e^{\frac{E-\gamma(T_e)}{k\,T_e}}+1} \tag{3.11}$$

is the Fermi function and

$$\gamma(T_e) \simeq E_F\left[1-\frac{\pi^2}{12}\left(\frac{k\,T_e}{E_F}\right)^2\right] \tag{3.12}$$

is the chemical potential [87].
In principle, the Fermi energy E_F depends - like $E_F \propto n^{2/3}$ - on the density of free electrons n, that in turn increases as an effect of FEL-induced ionization. However - based on the results of the previously presented experiment - we estimate that, within the fluence range pertinent to the current case, n is only subject to an increase of $\approx 5\%$, which fact leads us to neglect the dependence of E_F on n in Eq. 3.12.

Hence, by introducing a scaling factor ξ roughly proportional to the absorption jump at the edge, we can ascertain how changes in the electronic density of states affect the absorption coefficient via the expression:

$$\alpha(E,T_e) = \alpha(E,T_e^0) + \xi\cdot\sqrt{\bar{E}}\cdot\left[f(\bar{E},T_e^0) - f(\bar{E},T_e)\right], \tag{3.13}$$

with $\bar{E} = E + E_F - E_b$, being $E_b = 32.6$ eV the core binding energy and $T_e^0 = 0.025$ eV the initial electron temperature.

A simultaneous fit of the datasets of Fig.3.10 through the model function of Eq.3.13 provides a realistic assessment for the parameters $E_F = 9.5$ eV, $\xi = 0.2$ $\mathrm{eV}^{-1/2}$ and $T_e(\mathrm{eV})/F(\mathrm{J/cm^2}) = 2.0$. Our estimate for E_F agrees, in fact, with the band structure calculations of Ref. [89], according to which it is $E_F = 9.1$ eV, while our estimate for T_e confirms the same linear trend with fluence also evidenced by the analysis on the above referred experiment.
Such analytical curves are reported as solid lines along with the corresponding experimental points in Fig.3.10, which highlights a substantial agreement between them: the rise of absorption before the edge is well reproduced and the occurrence of a relative minimum of absorption above the edge is also accounted for, despite the less quantitative agreement at this energy.

Extended all across the $M_{2,3}$ edge spectral region, the changes of $\mu(E)$ with the electron temperature as predicted by Eq.s 3.11, 3.12 and 3.13 are illustrated in panel c of Fig.3.12, evidencing a drastic attenuation of the absorption jump. The densities of states for the Ti free electron gas at the same selected electron temperatures $T_e = 0.025$, 0.5, 2.0 and 5.0 eV are traced in panel b and compared with the room temperature photoemission data that, taken from Ref. [88], are reported

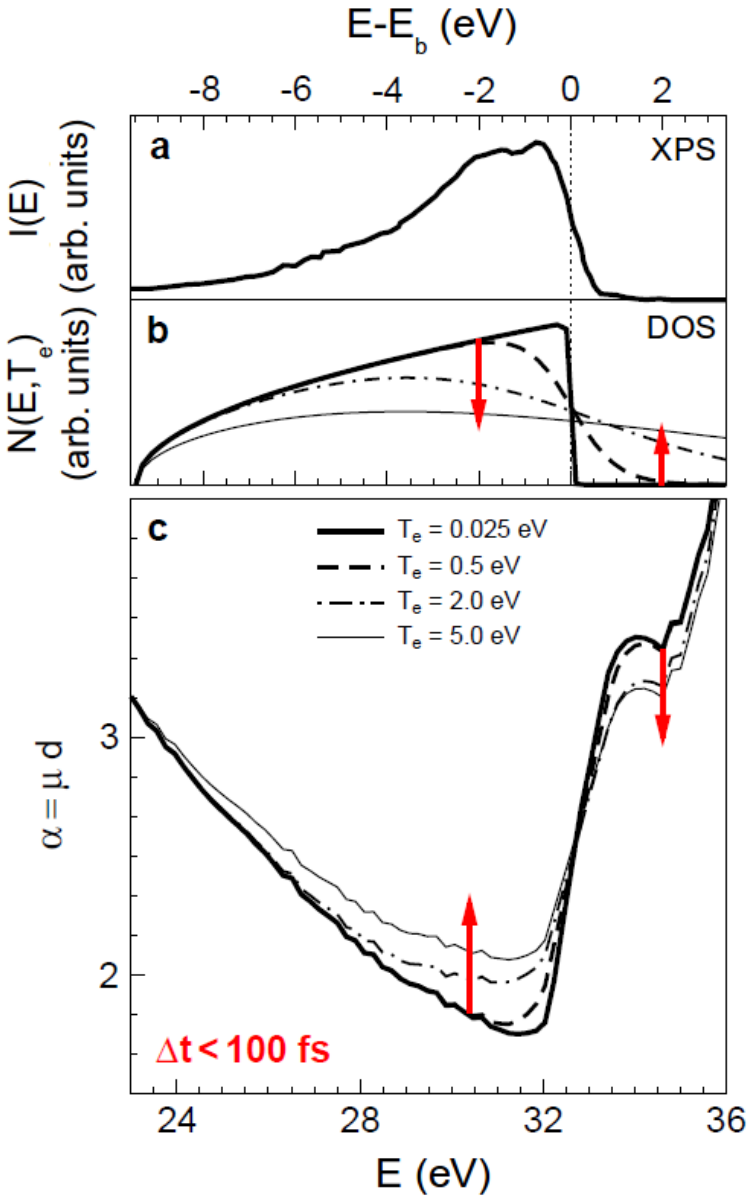

Figure 3.12: *Panel a)* Valence band photoemission spectrum of Ti at standard conditions taken from Ref. [88].
Panel b) Valence band density of states of FEL-excited Ti at different electronic temperatures as predicted by Eq.3.10.
Panel c) Ultra-fast modification of the absorption spectrum of Ti in the region of the $M_{2,3}$ edge as predicted by Eq.3.13.
The *vertical dotted line* marks the Fermi level at room temperature; the *red arrows* indicate the direction of increasing electronic temperature.

in panel c of the same figure.

In conclusion, we have evidenced that, under irradiation by ∼100 fs long EUV light pulses, the electronic population around the Fermi level in titanium exhibits a considerable rearrangement, which is manifest in an altered opacity and reflectivity of the sample during the pulse duration itself. Furthermore, the significant agreement between the experimental data and an analytical model foreseeing a cold ion lattice and a hot free electron gas may suggest that thermalization within the electronic subsystem has occurred on an even shorter timescale than accessible in the current probing conditions.

Very few studies have until now addressed the relaxation dynamics of photo-excited materials on timescales smaller than few hundreds fs.

Of great interest is the one authored by Medvedev *et al.* [90], who investigated by Monte Carlo simulations the electron dynamics in Al irradiated by intense 10-fs pulses at 92 eV. Obtained non-equilibrium distributions consisted of: a delta-like peak at 30 eV due to photoemitted L-shell electrons which only appears during the excitation pulse, a bump at 73 eV due to Auger electrons from the decay of L-shell holes which has a known lifetime of 40 fs, a main bath of low-energy electrons that are distributed according to an only slightly perturbed Fermi function and a high-energy tail arising from the photoabsorption of free electrons and scattering events that take a long time to equilibrate with the rest of the electronic population so that, at a fluence of 5 J/cm^2, the whole distribution reaches a Fermi shape after ≈400 fs.
The authors then used these findings to explain why, under analogue conditions, electronic temperatures of ∼40 eV were deduced from the bremsstrahlung spectra reported in Ref. [91] while electronic temperatures of ∼1 eV were deduced from the radiative decay spectra reported in Ref. [92]: the two spectra reflect, respectively, the minority hot part of the electron distribution and the prevailing colder one.
In analogy with the latter, our absorption spectroscopy experiment probes the majority electrons with energies near the Fermi level within which thermalization is very rapidly established.

Another work that certainly deserves our attention is a recent one by Mueller and Rethfeld [93], where the transient electron distributions in Al, Au and Ni metals during and after excitation by 800 nm 10 fs -long pulses are determined by deriving appropriate Boltzmann collision integrals with the specific purpose of establishing when the concept of a temperature can be applied. They found out that the electronic thermalization time strongly decreases with fluence, spanning from $\lesssim$1 ps to ∼10 fs at about 0.6 mJ/cm^2. With our one order of magnitude longer pulses, we reached up to 4 orders of magnitude higher fluences than this, which should validate our hypothesis of a thermalized electron system.
What may go against it is that they also evidenced a dependence of the electronic

thermalization time of the kind $\tau \propto \kappa^{3.6}$ on the screening parameter κ and of the $\tau \propto [DOS(E \approx \mu)]^{-3}$, two quantities that we are not able to trace in their possible dependence on the electron temperature for our case.

In effect, a theoretical study appeared (just few months before the time of writing) [94], in which Bévillon and co-authors report density functional theory calculations aimed at ascertaining the effects of a thermal activation energy $\sim K_B T_e$ around the Fermi energy with T_e between 10^{-2} to 10^5 K (and T_i the cold ion temperature), on a number of material properties for Al, Ni, Cu, Au, Ti and W. In particular, they showed that the density of states of titanium expands and shifts toward higher energies with increasing electronic temperatures (Fig.3.13), a change that is accompanied by an increase of the number of d electrons and an increase of the Hartree energy. Explained by an evolution of the electron-ion effective potential that results from a variation of the electronic screening generated by a change of the electronic occupation of the localized d block, these modifications have consequences on the electronic chemical potential (which lowers for Ti), number of free electrons per atoms (which increases), electronic heat capacity (which increases) and electronic pressure (which increases).

These new findings weaken the hypothesis at the bases of our simple model and

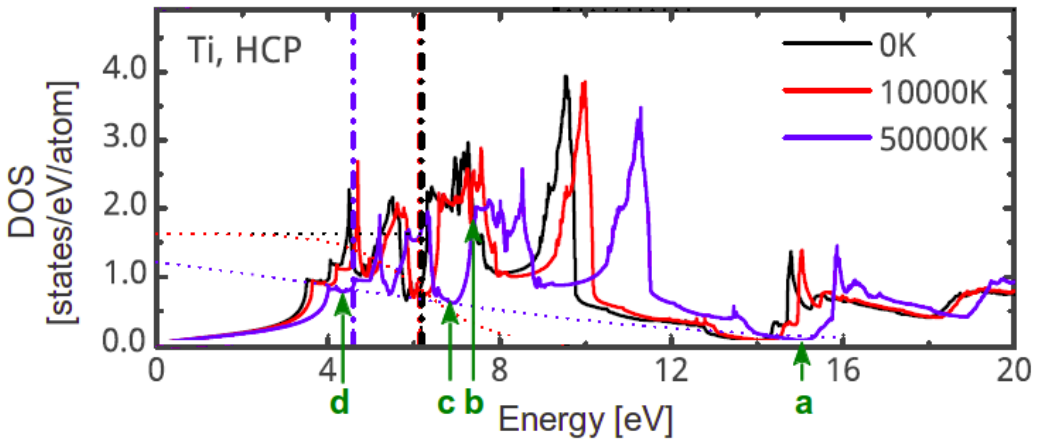

Figure 3.13: Density of electronic states (*solid line*) and associated Fermi-Dirac distribution function (*dotted lines*) and electronic chemical potential (*dashed line*) for three values of the electronic temperature. *Green arrows* mark the energies at which our high-fluence measurements were taken (Fig.s 3.9, 3.10, 3.11).
Taken from Ref. [94].

call for a replacement of Eq.3.10 with the real temperature-dependent DOS. We will certainly try to implement this modification.
Meanwhile, we offer the reader a comparison by drawing arrows on the density of states at 50000 K taken from Ref.[94] in correspondence to the energies that were

probed in our high-fluence experiment (their unperturbed chemical potential level at 6.2 eV is made to correspond to the nominal position 32.6 eV of the Ti M2, 3 edge). Based on that results, the DOS should be substantially smaller at 32.0 eV leading to a considerable absorption increase (consistently with what we found), moderately lower at 34.4 eV and 23.8 eV (which matches which our absorption measurements for fluences greater than 3 J/cm^2), and practically unchanged at 31.4 eV (which is not the case depicted by our findings). Of course, a precise comparison should also include an adequate relation between fluence and electronic temperature.

While aware of the possible oversimplifications behind our approach to the analysis, we point out how moving away from an equilibrium scenario suddenly complicates things up to a point where new paradigms must emerge from detailed theoretical investigations - as exactly demonstrated by the work that, fresh of publication, we have just presented.
Our efforts were, on the other hand, intended to be primarily directed at the experimental observation of the discussed phenomena. From this point of view, we cannot not stress the novelty of our experimental data which provide the first example of ultra-fast near-edge absorption spectroscopy with a sub-femtosecond temporal resolution.

Previous attempts were mainly based on table-top setups where, in the interaction of an ultra-fast laser with a solid target, X-ray pulses are produced which have typical durations of few picoseconds. One such example is the work by Mancić *et al.* [95] on aluminum brought into a warm dense matter state by heating with a laser-accelerated multi-MeV proton beam and probed near the K edge with ∼4 ps -long laser-produced X-ray pulses.
An alternative could be using long synchrotron pulses coupled to streak cameras with, again, time resolutions of few picoseconds. One such example is the work by Cho [96] on copper brought into a warm dense matter state by heating with a femtosecond optical laser and probed near the L_2 and L_3 edges by dispersing the 70 ps -long pulses from the ALS synchrotron onto a 2 ps -resolved streak camera.
In both cases a smearing of the absorption edge has been observed which is, however, related to the temperature reached by the overall sample after electron-ion equilibration.

We have here demonstrated that, thanks to the short and tunable EUV pulses of FERMI, it is now possible to take snapshots of the electronic structure with an unprecedented temporal resolution, that allows to study - not only fully equilibrated warm dense matter states (yet of the uppermost importance) - but also exotic systems of highly non-equilibrium conditions driven by suddenly raising electron temperatures in excess of 10 eV.

3.3 Interplay of electron heating and saturable absorption in the ultra-fast EUV transmission of Al

The higher the pulse intensity, the larger is the fraction of atoms that get excited by its photons and, the shorter the pulse length, the most probable is that they have insufficient time to decay back to their ground state. Ultimately, the photon-absorbing level will be depleted and the absorption bleached.
This phenomenon is well-known for visible and near-infrared radiation, so much so that saturable absorbers find extensive application as cavity components in ultra-fast lasers based on passive mode locking and Q switching [97].
Realizing the intensity conditions for induced transparency to be manifest at shorter wavelengths - where excited core holes have shorter lifetimes - has become possible only with the advent of free electron lasers.

FLASH (the FEL in Hamburg) led the way with the first experimental demonstration of such effect in aluminum irradiated at a soft X-ray photon energy of 92 eV (above the $L_2, 3$ edge) by 15 fs -long pulses with high intensities of 10^{16} W/cm^2 (fluences up to $\sim$200 J/cm^2) [83].
Saturable absorption has then been observed at SACLA: in tin at a EUV photon energy of 24 eV (on the N_5 edge) by $<$100 fs -long pulses with moderate intensities of 10^{14} W/cm^2 (fluences up to $\sim$6 J/cm^2) [98] and very recently (in October 2014) in iron at a hard X-ray photon energy of 7130 eV (just above the K edge) by 7 fs -long pulses with extreme intensities of 10^{20} W/cm^2 (fluences up to $\sim$670000 J/cm^2) [99].

For the experiment on Al described by Nagler *et al.* [83], the scenario is as follows: a 92 eV photon ionizes one electron from the 2p core level lying at 73 eV; due to the consequently reduced screening, that 2p core level shifts to 93 eV; since the core hole recombines by Auger decay with a lifetime of 40 fs (which is longer than the pulse duration of 15 fs), the trailing part of an FEL pulse will then experience a decreased absorption at intensities where a large fraction of Al atoms have already been singly ionized by its leading part.

In this framework, we have tried to give our contribution by providing new experimental data for isochorically heated Al at 23.7, 33.5 and 37.5 eV photon energies, falling in that - experimentally unexplored - spectral range between the plasmon frequency (15 eV) and the L-edge (73 eV) where neither collective electronic excitations nor bound state ionization can occur but only valence band ionization.

Vinko and coauthors followed two approaches to theoretically evaluate the free-free absorption cross-section of warm dense Al [100]: i) a semi-analytical model where the electron dielectric function is derived within a random phase approxima-

tion comprehensive of exciton contributions and where the electron-ion interaction potential as well as the ion-ion structure factor are given tentatively adequate forms for the warm dense plasma regime (a one-component plasma structure factor with dynamical screening and a local pseudopotential with correct short and long range limiting forms) assuming, however, thermodynamic equilibrium at the same temperature for both electron and ion subsystems; ii) molecular dynamic simulations within the finite-temperature density functional theory (using the VASP code to calculate the electronic structure and the Kubo-Greenwood formula to calculate the optical properties).

Interestingly, both calculations predict a positive peak in the absorption coefficient at a temperature around 10 eV, which is more pronounced at lower (with respect to higher) energies and, as shown in Fig. 3.14, when the electron subsystem is in thermal equilibrium with the ion one (with respect to when the electron subsystem is hot while the ion one is cold). The authors explain that, in fact, both the electrons are contributing to it - via plasmon thermal broadening - and the ions - via thermal broadening of the peaks in the ionion structure factor enabling a larger range of k-vectors to contribute to the absorption. This behavior is in sharp con-

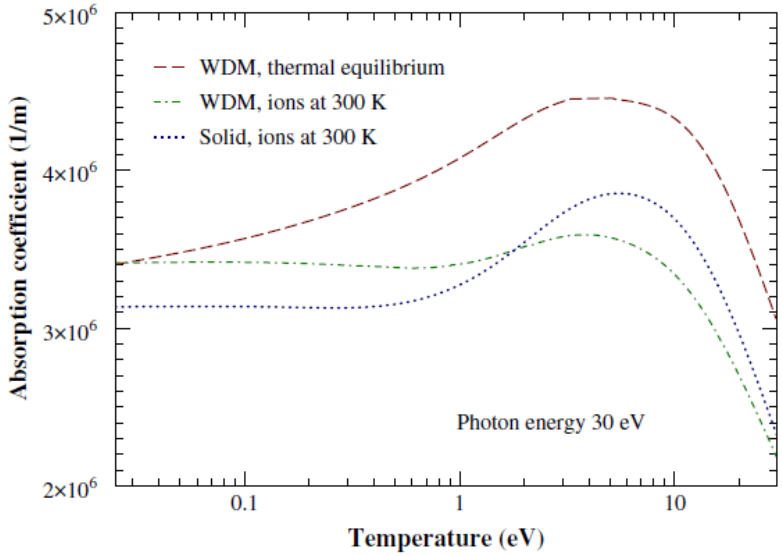

Figure 3.14: Absorption coefficient at 30 eV versus temperature for warm dense Al in thermal equilibrium (*red*), warm dense Al with ions at room temperature (*green*) and solid Al with ions at room temperature (*blue*) as computed by the authors of Ref. [100] from which the image is taken.

trast with what predicted by the standard inverse bremsstrahlung model of plasma physics where the absorption coefficient is found to scale as $T^{-3/2}$, and also in disagreement with the findings of Iglesias [101]. Based on a Drude model where the electron-ion collision frequency is obtained from an inverse bremsstrahlung all-order

formula corrected for degeneracy and many-body screening effects, the latter predicts a larger and monotonic increase of the absorption coefficient with increasing temperature below 10 eV, that is attributed to a combination of increased availability of final states due to a reduced electron degeneracy and increased electron-ion interaction due to a reduced screening length.

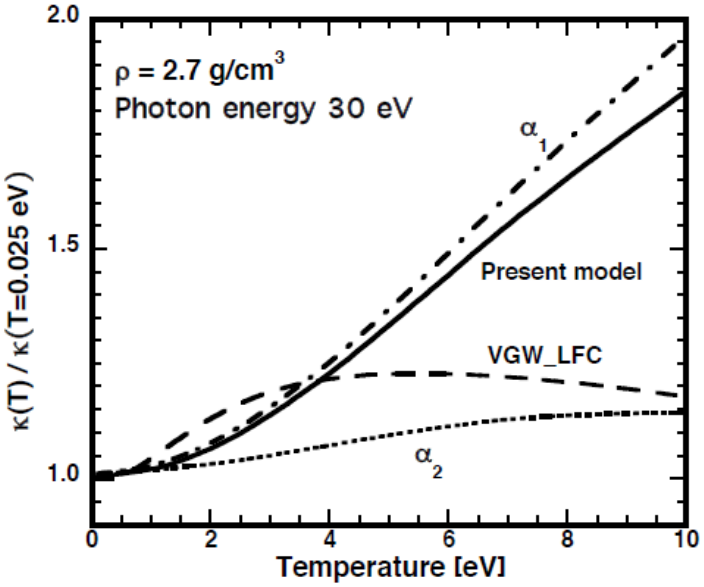

Figure 3.15: Absorption coefficient at 30 eV versus temperature for warm dense Al as evaluated by the author of Ref. [101] (*solid line*). In both α_1 and α_2 dispersion and multiple collisions are neglected but, while α_1 is all-order in the electron-ion interaction, α_2 makes the Born approximation. For comparison, *VGW LCF* shows the different behavior deduced from the authors of Ref. [100] (here on a linear temperature scale). Each calculation is normalized to the respective value at a temperature of 0.025 eV.
Taken from [101].

There is therefore a great need for experimental data that could set the benchmark for (up to now diverging) theoretical approaches.

3.3.1 Experimental details and results

Measurements being part of a same campaign in early 2012, the setup was again the one in use for the previously illustrated experiment on titanium: focusing provided by the spherical platinum-coated silicon mirror at quasi-normal incidence and detection provided by the (100 nm)Al/(0.5 mm)YAG/UVG20S PYD. Samples were unsupported 100 nm -thick Al foils.
Photon energies of 23.7, 33.3 and 37 eV were explored, at which FERMI could reach maximum energies per pulse of about 300 μJ, 180 μJ and 130 μJ. Due mainly to

the limited efficiency of the temporary focusing optics, those energies per pulse translated into highest fluences at the sample of about 20 J/cm^2, 13 J/cm^2 and 10 J/cm^2. Attenuation over three decades below those values was obtained by exploiting the natural intensity fluctuations of the FEL pulses, possibly in combination with the use of a gas absorber at variable pressure and/or solid-state filters.

The whole set of data is presented in Fig. 3.16.
As it is standard at TIMEX, each point is a single-shot on a fresh sample portion. The spread of the data at a given fluence is due to thickness fluctuations, as well as to counting statistics. The detector sensitivity was adequate, except for the fluence range below 5 J/cm^2 at the lowest photon energy of 23.7 eV where, the sample being highly absorbing, we could not get reliable measurements. A statistically significant

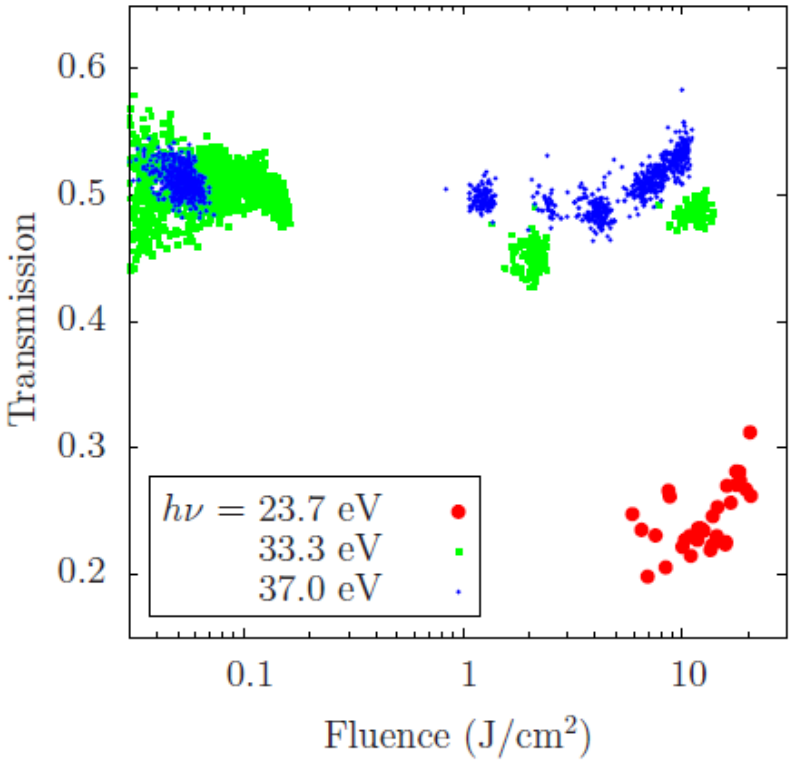

Figure 3.16: Single-shot transmission data of FEL-1 pulses across a thin Al foil as a function of the estimated fluence for the three photon energies 23.7 eV (*red circles*), 33.3 eV (*green squares*) and 37.0 eV (*blue circles*).

variation of the Al transmission with increasing FEL fluence is observable at all three photon energies, featured by an initial decrease at intermediate fluences and a following increase at higher fluences.
I will show in the following how we could reproduce the observed non-monotonic trend based on a simplified three-channel model accounting for both saturation and electron heating effects.

3.3.2 Analysis and discussion

The exponential attenuation of light in an absorbing medium - as expressed by the familiar Lambert-Bear law - only holds in a low-intensity regime where each photon absorption event is independent and involves atoms in the same ground state.

Steady-state solutions $\overline{N_1}$ and $\overline{N_2}$ to the rate equations of a two-level system undergoing the processes of absorption, stimulated emission and spontaneous emission can be easily derived (following for example Ref. [2]), then yielding:

$$d\phi(z) = -\alpha(\omega)\,\phi(z)\,dz = -\sigma(\omega)\left(\overline{N_2} - \overline{N_1}\right)\phi(z)\,dz = -\frac{\alpha_0(\omega)}{1+\phi/\phi_{sat}}\phi(z)\,dz \quad (3.14)$$

with $\alpha_0(\omega) = \sigma(\omega)\,N$ the usual absorption coefficient to which $\alpha(\omega)$ reduces when the fluence ϕ is small compared to the saturation fluence $\phi_{sat} = \dfrac{h\nu\,\Delta t}{2\sigma(\omega)\,\tau}$. This model envisages an equilibrium condition that is indeed valid only when the pulse duration Δt is much longer than the excited state lifetime τ. Such may be the case of deep core excitations, which usually have few fs -long relaxations times.
For pulses with a duration well below the excite state lifetime - like in optical transitions where recombination rates can even be in the order of ms - one may resort to the Frantz-Nodvik equation:

$$\phi(z) = \phi_{sat}\ln\left[1 + e^{-\alpha_0 z}\left(e^{\frac{\phi(0)}{\phi_{sat}}} - 1\right)\right] \quad (3.15)$$

with $\phi_{sat} = \dfrac{h\nu}{2\sigma}$; well known to laser physicists as it the same that expresses the saturated gain of a light beam propagating through the inverted medium of an amplifier [102].
Applied to the experimental data of Nagler *et al.* [83], both models predict much smaller values of the saturation fluence, as visible in Fig. 3.17. The basic reason is that for this case the number of excited states cannot be considered constant in time, neither with respect to the excitation process (as in Eq. 3.14) nor with respect to the relaxation process (as in Eq. 3.15).

In a recent paper [103], Hatada and Di Cicco showed that they were able to reproduce those data with a phenomenological model contemplating three channels: a ground state $|1\rangle$ and an excited state $|2\rangle$ involved in the absorption and stimulated emission processes, and a relaxed state $|3\rangle$ of intermediate energy, virtually representing the ensemble of all possible states reached by the decay of the state $|2\rangle$ and in turn decaying into the state $|1\rangle$.
The occupation numbers N_1, N_2 and N_3 of these states were allowed to vary ac-

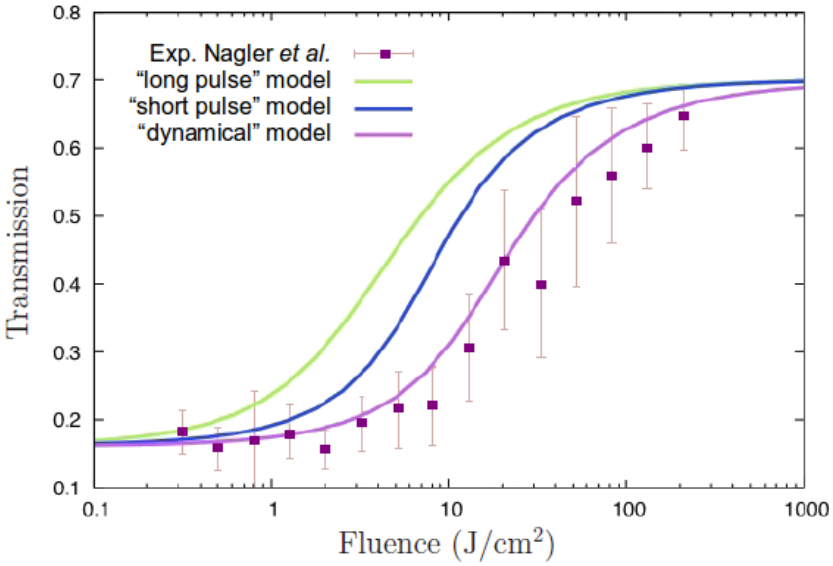

Figure 3.17: Transmission of a 53 nm -thick Al foil as a function of incoming fluence for 15 fs-long FEL pulses at 92 eV. Experimental data from Ref. [83] are confronted with the three models discussed in the text.
Credits: K. Hatada.

cording to the set of rate equations

$$\begin{aligned}
\frac{dN_1(z,t)}{dt} &= \frac{g(z,t)I(z,t)}{h\nu} + \frac{N_2(z,t)}{\tau_{21}} + \frac{N_3(z,t)}{\tau_{31}} \\
\frac{dN_2(z,t)}{dt} &= -\frac{g(z,t)I(z,t)}{h\nu} - \frac{N_2(z,t)}{\tau_{21}} - \frac{N_2(z,t)}{\tau_{23}} \\
\frac{dN_3(z,t)}{dt} &= \frac{1}{\tau_{23}}N_2(z,t) - \frac{1}{\tau_{31}}N_3(z,t)
\end{aligned} \tag{3.16}$$

subject to the sum-rule constraint

$$N = N_1(z,t) + N_2(z,t) + N_3(z,t) \tag{3.17}$$

and coupled with the transport equation of the light field

$$\frac{dI(z,t)}{dz} + \frac{1}{c}\frac{dI(z,t)}{dt} = \alpha(z,t)I(z,t) \tag{3.18}$$

where

$$\alpha(z,t) = \sigma(T)\left[N_2(z,t) - N_1(z,t)\right] \tag{3.19}$$

denotes a generalized absorption coefficient which depends on time and space,

through the occupation numbers of the ground and excited states, as well as, through the absorption cross-section, on the photon energy and, possibly on temperature.
A temperature dependence has been introduced for the absorption cross-section in the attempt to account for the decreased transmission that we observed in our measurements at intermediate fluences. To this purpose, we have calculated the energy deposited on a sample slice of thickness Δz and valence electron density n_e as $\Delta E = \dfrac{\Delta F}{n_e\,\Delta z}$ and made it correspond to a temperature variation via the Maxwell-Boltzmann approximation $\Delta E = \dfrac{3}{2}k_B\Delta T$, thus obtaining

$$\Delta T_e = \frac{2\,\Delta F}{3k_B n_e \Delta z} \tag{3.20}$$

With this relationship between fluence and temperature, we could then use for $\sigma(T)$ the calculations results from Ref. [100] that - reported in Fig. 3.14 - were discussed above.
Regarding the relaxation times that appear in the rate equations, we can assert the following. On the one side, the decay time from the upper to the intermediate state is extremely short, namely: $\tau_{23} \sim 1$ fs from the inelastic mean free path in Al of an electron with 20 eV kinetic energy. On the other side, since we are dealing with valence band excitations, the lifetimes of the upper and intermediate states can be considered longer than the pulse duration of about 100 fs, as suggested by the already quoted Monte Carlo simulations of Ref. [90]. The chosen values were $\tau_{21} = \tau_{31} = 500$ fs, but we have verified that the simulated transmission vs fluence curve is only very slightly affected if these parameters take on different values in the range 0.2-1 ps.

Finally, Eq.s 3.16, 3.17, 3.18, 3.19 and 3.20 have been solved numerically using discretized grids with Δt = 0.4 as and Δz = 1.2 nm. The result for a photon energy of 37.0 eV is shown as a black line in Fig. 3.18 where it is compared with the corresponding experimental data (blue points) and the results of two other calculations, the one only including the saturation effect (gray curve), which clearly fails to reproduce the initial transmission decrease and the one only including electron heating (red curve), which in the contrary overestimates that decrease.

As a further result of the calculation, we represent in Fig. 3.19 - on both logarithmic (main plot) and linear scales (inset) - the estimated electron temperature throughout the film as a function of the incoming fluence for all the three EUV photon energies. Upper and lower bounds of the curves correspond to the minimum and maximum temperatures reached respectively at the rear and front sides of the sample.

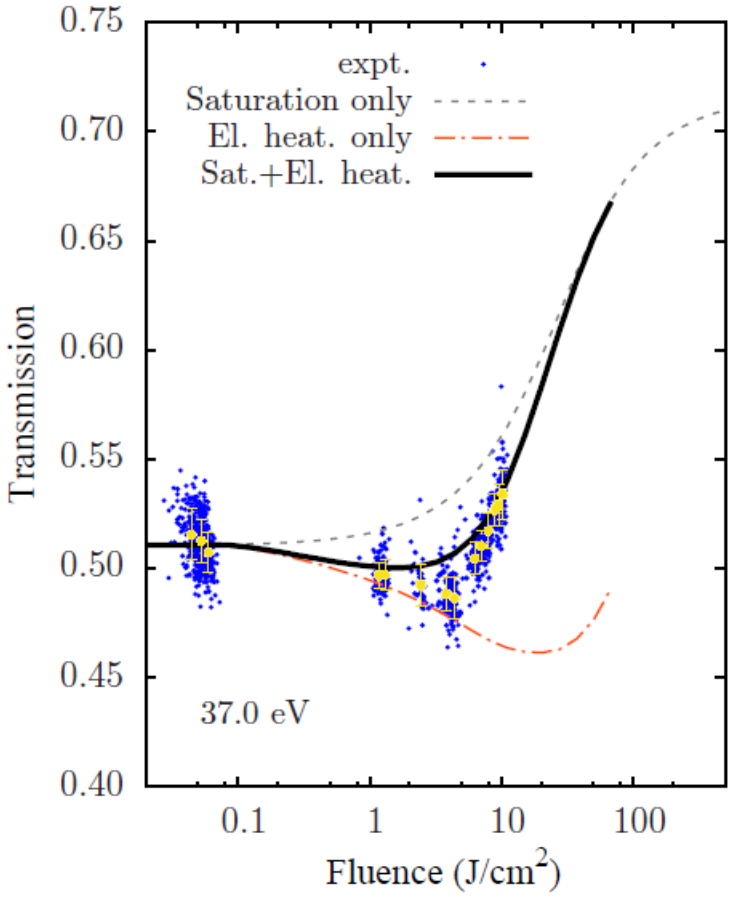

Figure 3.18: Transmission vs fluence data at 37.0 eV photon energy compared with different calculations: the *gray curve* results from considering the dependence of the absorption coefficient on the ground and excited states occupations, the *gray curve* results from considering the dependence of the absorption coefficient on temperature, the *black curve* results from considering both effects.

Electron temperatures in excess of 1 eV are obtained for fluences greater than $\sim$ 3 J/cm^2. The highest temperature is reached for 37.0 eV photons amounts to $\sim$ 7 eV.
Up to about 10 J/cm^2, the electron temperature is linear with fluence and its spread across the 100 nm -thick sample is around 15 %. At greater fluences, saturable absorption limits the deposited energy and at the same time provides a quasi-uniform bulk heating.

To summarize, we have provided novel experiment data for the EUV transmission of Al at solid density and temperatures up to $\sim$ 7 eV. We have also proposed a simple - yet effective - way to model them, in which the FEL pulses are let dynamically interact with the target as they propagate through it: Absorption, stimulated

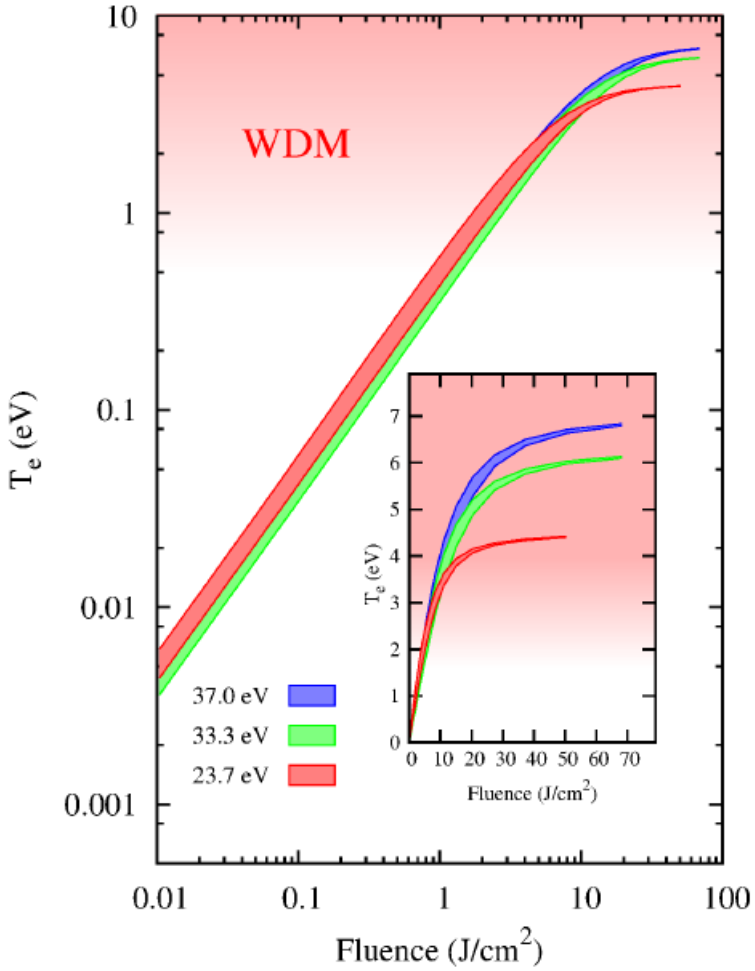

Figure 3.19: Estimated electron temperature as a function of incoming fluence at different photon energies (curves enclose maximal and minimal temperatures through the 100 nm -thick Al film for a given fluence).

emission and decay occur inside the sample, that result in a transmission decreasing exponentially with the thickness at low fluences but more linearly at higher fluences; in addition, the positive bump in the absorption coefficient at intermediate fluences predicted in Ref. [100] seems to find confirmation in the measured non-monotonic transmission trend, which is nicely reproduced only when saturation is made to interplay with this effect.

This work has been accepted for publication in Physical Review B, Rapid Communications. My acknowledgments go to A. Di Cicco, the principal investigator and to K. Hatada, the author of the model computational code.

3.4 Ultra-fast saturation spectroscopy of the Mg $L_{II,III}$ edge

Last in this class of investigations in which a same FEL pulse acts as both a pump and a probe, I present a self-absorption experiment conducted on magnesium samples.
Like for the case of Ti, we want to exploit the photon energy tunability across an absorption edge, here the $L_{II,III}$ one. Contrarily to that situation, however, the photo-absorption process is now characterized by a core-hole lifetime which lasts longer than the exciting pulse length. Similarly to the Al case, this circumstance translates in the showing up of saturation effects, that we now aim to study in a joint manner both below and above the threshold for an inner-shell ionization.

3.4.1 Experimental details and results

The experiment under discussion has been carried out in a definitely more advanced stage of commissioning with respect to the previous ones.
If, on the one side, this implies that part of the analysis is still ongoing at the time of writing, on the other side, it also implies that the acquired data boast a superior quality.
Indeed, the machine was optimized keeping a watchful eye on the energy spectrum so as to have a good energy resolution guaranteed and, together, near- transform limited Gaussian pulses, whose duration we thus confidently estimate to be of 65 ($= 150/\sqrt[3]{12}$) fs fwhm.
The employed setup was, finally, the one with the finished ellipsoidal focusing mirror, whose higher efficiency ($\sim$ 99% reflectivity, $\sim$ 5 μm σ spot size) allowed to reach fluences in excess of 50 J/cm^2. Regarding the detection of the transmitted light, it again relied on the same instrument in use for the previously illustrated experiments.

Transmission measurements have been collected at several photon energies around 50 eV as a function of the incoming FEL fluence for two Mg samples with thicknesses of, respectively, 50 and 141 nm, each capped with Al on both sides.
The complete set of data is shown in Fig. 3.20. With increasing light intensity, a drastic transmission increase is observed at all photon energies and for both samples.
The onset of nonlinear saturable absorption is better catched from a representation in logarithmic scale for the abscissa, as given in Fig. 3.21 for the three energies of 48.8, 49.6 and 50.2 eV. Besides their averages, also shown in this figure are the raw data points which result from single-shots measurements of the transmitted light with no further treatment beyond the normalization to the detector calibration

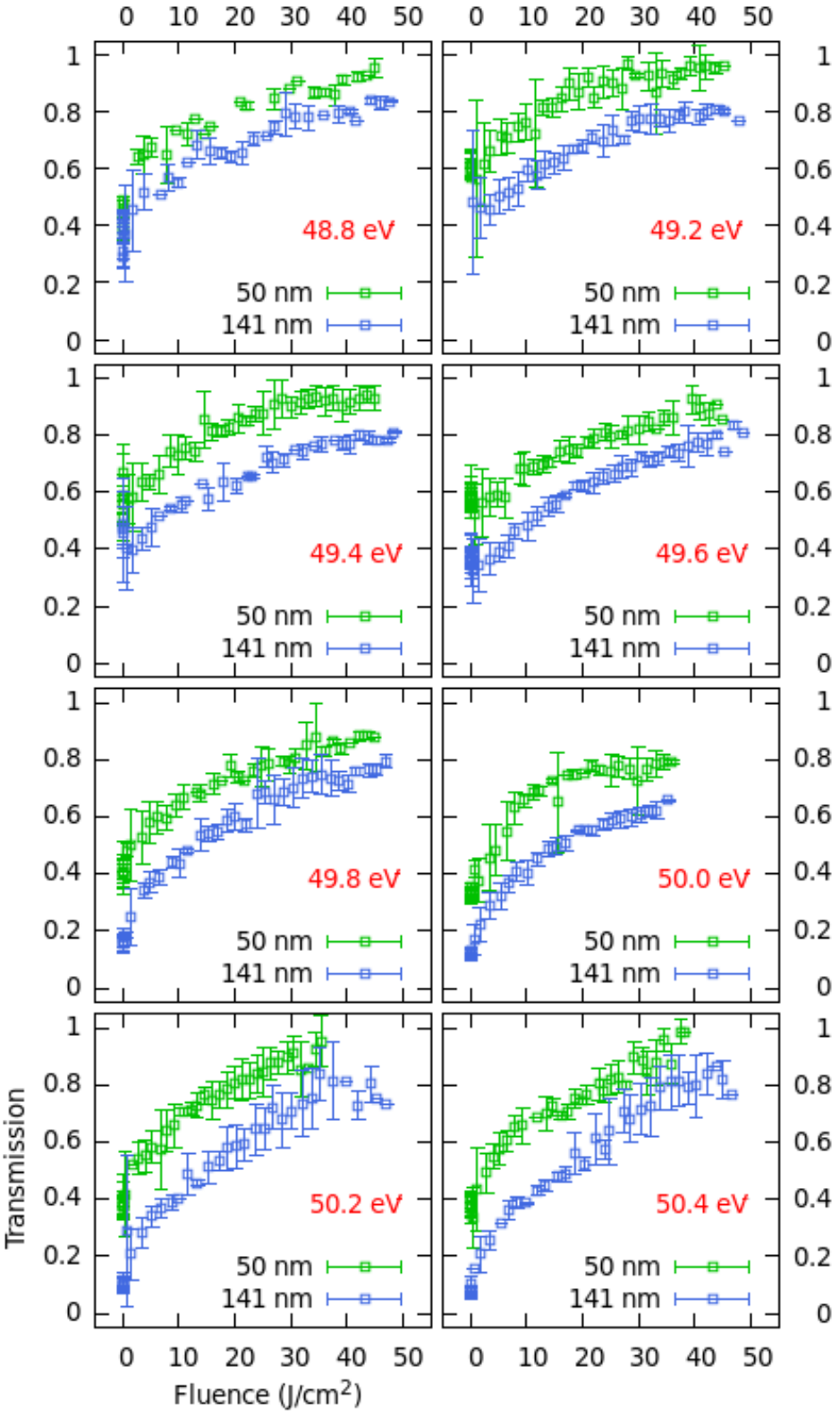

Figure 3.20: Fluence dependence of transmission for Mg samples of two thicknesses (green and blue labels) capped between two Al layers with a nominal thickness of 37.6 nm each at different photon energies (red labels) accross the Mg $L_{II,III}$ absorption edge.

against the ionization chamber recording the incident light. An abrupt change is

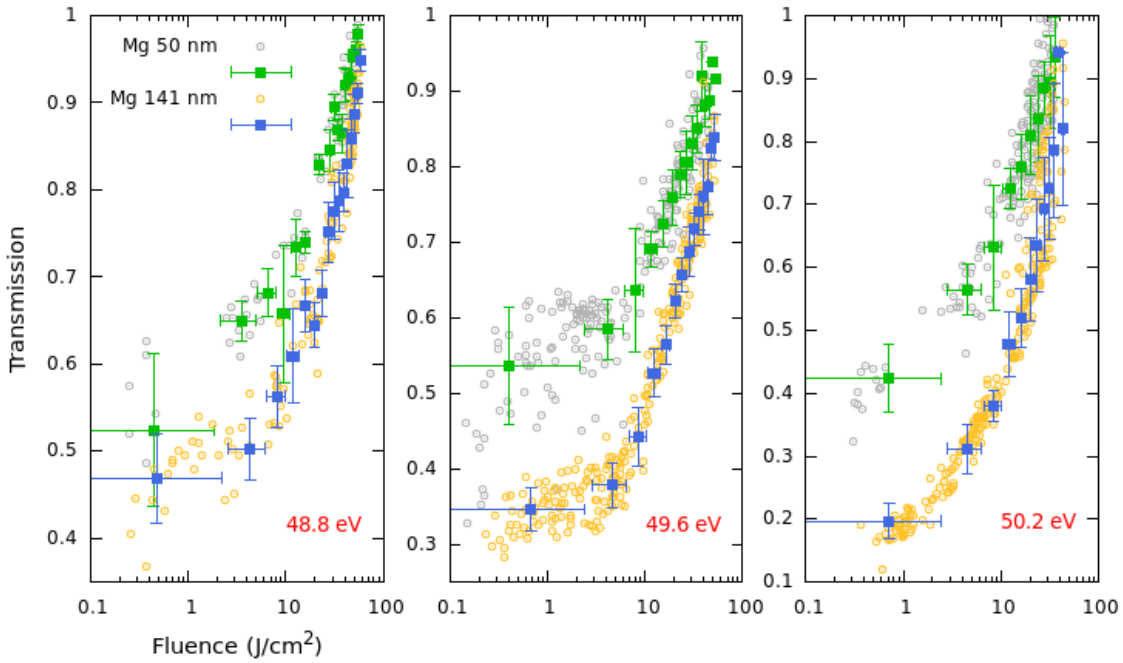

Figure 3.21: Same data of Fig. 3.20 shown for three selected energies (below, on and above the Mg $L_{II,III}$ absorption edge) in a logarithmic fluence scale. Circles represent single-shots data; filled squares give their average and error bars their one standard deviation.

seen to occur around 5 J/cm^2 at 49.6 eV, an energy which falls on the initial raising part of the absorption edge. Although more data extending to lower fluences would be needed to ascertain these conclusions, it seems that at 48.8 eV - below the edge - an onset appears around 6 J/cm^2, whereas at 50.2 eV - above the edge - this is located around 1 J/cm^2.

Independently from the starting transmission level (higher below the edge, lower above the edge), at all energies the transmission attains almost the same level, of about 0.8 for the thicker sample and exceeding 0.9 for the thinner one. This reveals, beyond an overall reduced opacity, a strong suppression of the absorption edge feature, as Fig. 3.22 clearly shows. Here, absorption data at the fluences of 10 and 50 J/cm^2 are compared with measurements at a very low fluence of 0.02 J/cm^2 (about 20 times smaller than the estimated damage level) obtained by moving the sample several mm before the FEL best focus. Using the CXRO database [53] as a reference for the "static" absorption coeffients of the various species, one finds that the lowest fluence spectra are best reproduced if the two samples are considered as consisting of: 50 nm of Mg, 32 nm of Al and 8 nm of Al_2O_3 the first one (Fig. 3.22, left) and 141 nm of Mg, 28 nm of Al and 14 nm of Al_2O_3 the second one (Fig. 3.22, right). An analogous treatment can be applied to the higher fluences

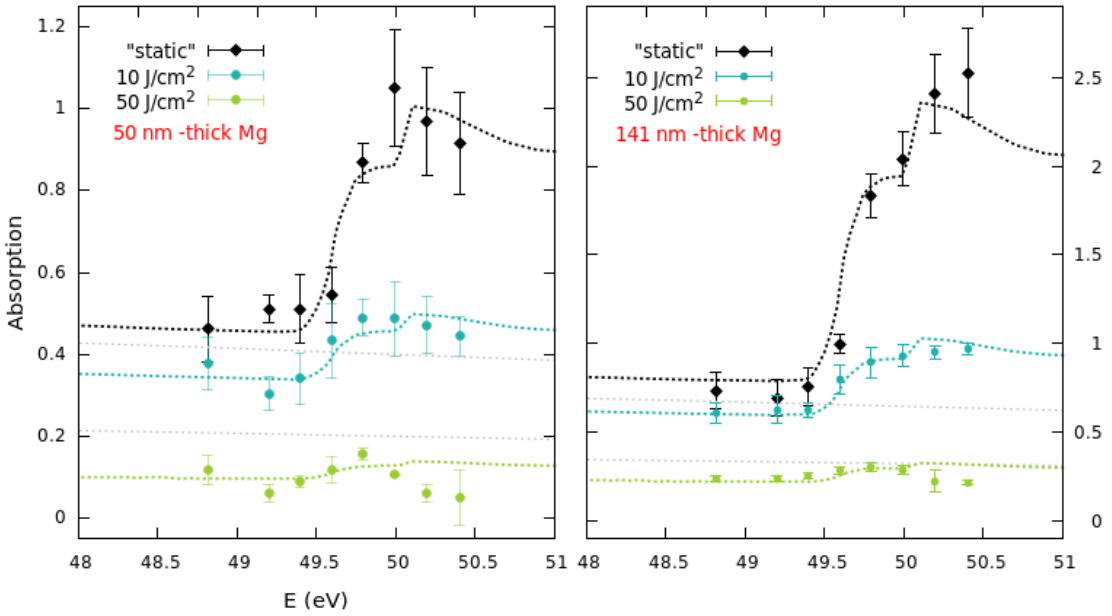

Figure 3.22: Fluence-driven modifications of the absorption spectra of the two Al-Mg-Al stacks at the Mg $L_{II,III}$ edge. Colored points are taken from the data of Fig. 3.22, black points each come from an average over 500 shots taken on a same sample position, several mm apart from the FEL best focus. Dashed lines represent the absorption of "equivalent" layers of Mg, Al and Al_2O_3 atoms, with thicknesses as quoted in text.

spectra. The results - shown as the coloured dashed lines in Fig. 3.22 - indicate Al_2O_3-Al-Mg-Al-Al_2O_3 layers with the following thicknesses: 1.75, 1.75, 15, 5 and 15 nm for the thinner sample at 10 J/cm^2; 0, 0, 4, 2 and 3 nm for the same sample at 50 J/cm^2; 4.5, 10, 40, 7.25 and 15 nm for the thicker sample at 10 J/cm^2; 0, 0, 10, 4.5 and 8 for the same sample at 50 J/cm^2. Such numbers should by intended as "equivalent" thicknesses from which to deduce - under the assumption that each unexcited element do not contribute anymore to the absorption - the number of ionized Mg atoms. These easily seen to be in the amount of 30 % / 28 % at 10 J/cm^2 and 8 % / 7 % at 50 J/cm^2 for the thinner / thicker stacks.
Even if certainly not rigorous, this procedure allows at least to judge that the aluminum capping layers and their oxides are playing a role as well. In fact, completely depleted Mg layers would correspond to the upper gray dashed lines in both panels of Fig. 3.22, while completely depleted Mg layers and rear Al and Al_2O_3 layers would correspond to the lower gray dashed lines in that figure. Both cases, if compared to the measured spectra at the highest fluence, overestimate the absorption and lack the residual features from the Mg $L_{II,III}$ edge that instead, although small, are still present.

3.4.2 Analysis and discussion

Further analysis are currently underway.

First, we want to ascertain the thickness of the oxidized layers.
To do so, we plan to exploit a combination of X-ray photoemission spectroscopy and Ar sputtering: the Al_2O_3 layer thickness will be then given by the time required for the disappearance of the O 1s peak in the XPS spectrum times the sputtering rate - determined in turn from the time required for the disappearance of the Al 2p peak and the nominal thickness of the Al layer.

Second, with the results of these additional measurements, we have in mind to implement the following analytical modelization, which develops along the lines pursued to analyze the fluence-dependent self-reflection measurements on Ti.
The absorption coefficient of each element i in the stack decreases with increasing fluence of a factor which we assume proportional to the fraction of ionized atoms over the total illuminated atoms N^i, a fraction espressed by the ratio between the deposited energy E_d^i and the ionization energy E_{ion}^{i*}:

$$\mu^i(F,t) = \mu_0^i \left[1 - \frac{E_d^i(F,t)}{N^i\, E_{ion}^{i*}}\right]. \tag{3.21}$$

In a self-consistent manner, the energy deposited into each layer of thickness d^i is in turn determined by that fluence- but also time- dependent absorption coefficient, so as to properly take into account the fact that ionization processes reduce the number of atoms available for further absorption at later times within the same pulse:

$$E_d^i(F,t) = \int_0^t \left[1 - e^{-\mu^i(F,t')\, d^i}\right] G^i(t')\, dt', \tag{3.22}$$

where we define

$$G^i(t') = \begin{cases} g(t') & i = 1 \\ e^{-\mu^{i-1}(F,t')\, d^i} G^{i-1}(t') & i = 2,3,4,5 \end{cases} \tag{3.23}$$

$g(t')$ being the Gaussian temporal profile of area equal to the pulse energy E_{in} and the index i denoting - in the order - the first Al, the first Al_2O_3, the Mg, the second Al and the second Al_2O_3 layers.
Further, we suggest that, while ionization processes involving aluminum and aluminum oxide atoms may be described by a single value of ionization energy, two different values of this variable are needed to describe ionization processes involving magnesium atoms, which encompass a low-absorption regime below the edge

energy E_b and a high-absorption one above it:

$$E_{ion}^{i*} = \begin{cases} E_{ion}^{i} & i = 1, 2, 4, 5 \\ \dfrac{E_{ion}^{i}}{1 + \Theta(E_b^i - E)A^i} & i = 3 \end{cases} \tag{3.24}$$

where Θ is the Heaviside function and A^i is a parameter whose value we aim at determining by fitting the ensemble of experimental data to the expression

$$T(F) = \frac{1}{I_{in}} \int_{-\infty}^{\infty} \prod_{i=1}^{5} e^{-\mu^i(F,t)\, d^i} G^i(t)\, dt. \tag{3.25}$$

Such kind of analysis has been preliminarily done on an older dataset (referring to a sample similar to the thicker one of the two before described), taken at fewer photon energies and lower pulse intensities with respect to the measurements here presented, but by all means compatible with them. Taking from Ref. [104] E_{ion}^{*} = 53.31 eV/atom for Al and E_{ion}^{*} = 22.67 eV/atom for Mg at below-threshold energies, application of a genetic fitting algorithm has rendered: an oxide layer thickness of 7 nm per side, an ionization energy of 2700 eV/particle for Al_2O_3 and an A parameter of 0.46, leading to an ionization energy of 42±2 eV/atom for Mg in the solid-density plasma state that is created at above-threshold energies.
For the reader to fully appreciate this result, it may be the case to better stress its significance.

The ionization energy is usually understood as the minimum amount of energy required to remove an electron from an isolated atom. When the same atom is embedded in a condensed medium, the electrons are increasingly attracted towards neighboring ions. As pictorially depicted in Fig. 3.23, this is at the origin of the so-called "ionization potential depression" (IPD) that, when greater than the ionization potential itself, is responsible for the so-called "pressure ionization" or "continuum lowering" [105].
So, for example: according to the NIST database [106], the first ionization energy for atomic Mg is 7.65 eV/atom, whereas, as reported in Ref. [104], the first ionization energy for solid Mg is 22.67 eV/atom. The latter in fact corresponds, not more to the $Mg \rightarrow Mg^{1+}$ ionization process, but to the $Mg^{2+} \rightarrow Mg^{3+}$ one (that would require an energy of 80.14 eV/atom in an isolated Mg atom) because the two 3s valence electrons in metallic Mg already belong to the continuum.
Isochoric heating by intense light beams opens the possibly to experimentally quantify the IPD in warm/hot dense plasmas, thus putting to a test current models whose results find extensive application in determining properties like charge state distributions, opacities, equations of state and transport equations within many

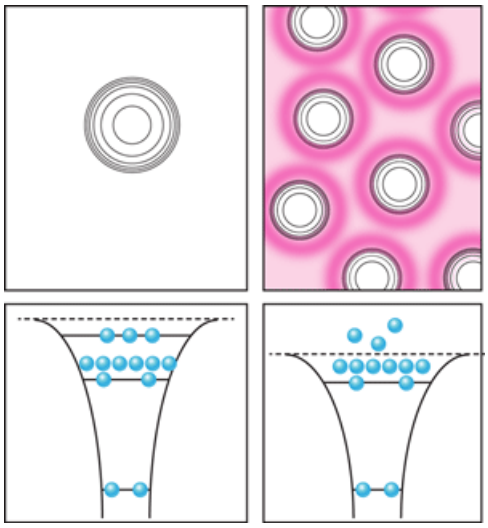

Figure 3.23: Simplified representation of the ionization potential depression from a vacuum (*left*) to a dense plasma environment (*right*). *Top:* black circles represent the electron energy levels, outer red circles represent the extent over which the ion charge is neutralized in an ion sphere model; *bottom:* the dotted lines represent the energy of the continuum.
Taken from Ref. [105].

simulation codes for astrophysics and inertial confinement fusion research.
Ref. [107] reports on a pioneering experiment performed by Vinko *et al.* where 80 fs -long X-ray pulses from the LCLS free electron laser with peak intensities exceeding 10^{17} W/cm^2 have been used to both create solid-density Al plasmas at temperatures up to 180 eV and probe them via detection of K-α emission spectra as a function of photon energy. As the latter is increased in the 1560-1830 eV range, an increasing number of fluorescence lines appears associated with transitions where the K-shell hole generated upon photoionization is filled by L-shell electrons with an increasing number of L-shell holes. A measure of the K-edge position for different charge states is thus provided, whose comparison with the predictions of two possible models of IPD is reported by Ciricosta *et al.* in Ref. [108]. Surprisingly, better agreement is found with the model of Ecker and Kröll [109] rather than with the most widely used model of Stewart and Pyatt [110], which fact - according to the authors - calls for a reconsideration of many standard codes modeling atomic kinetics in dense plasmas.
The Ecker and Kröll model evaluates the ionization potential depression as $IPD = \frac{z\,e^2}{4\pi\epsilon_0 R_{EK}}$ where the average radius of a neutral sphere containing an ion with charge z is given by $\frac{4}{3}\pi R_{EK}^3 = \frac{1}{n_i + n_e}$. The reason why this simplistic picture should capture an actually more complicated scenario is not clear and the agree-

ment with the experimental data does not provide a meaningful inside in itself. That experiment has therefore renewed the interest to undertake a further step in theoretical modeling which could be based on more founded grounds than the average atom approach, an effort documented by a series of very recent publications on the subject [111, 112, 113].

Coming back to our experiment, the value of 42±2 eV/atom for the ionization energy of singly-ionized magnesium that we have deduced from an analysis of FEL self-absorption measurements at above $L_{II,III}$ edge energies well compares to the one of 44 eV/atom predicted by the Ecker and Kröll model.
Moreover, it is interesting to note that a realistic estimation of the analogue experimental value for aluminum may be obtained by simply rescaling the denominator in Eq. 3.24 for the different material densities, namely: $A_{Al} = (A_{Mg} - 1)\frac{\rho_{Al}}{\rho_{Mg}} + 1 = 0.84$. Whence, considering a first ionization energy of 53.31 eV/atom for the solid state (Al^{3+}) [104], the value of 64±3 eV/atom is obtained for the singly-ionized state (Al^{4+}), which is very close to the one of 67±7/atom determined experimentally by Ciricosta *et al.* [108].
Both these results provide encouraging support to our approach of deducing first ionization energies from near-edge absorption spectroscopy in a regime of intensities where saturable absorption effects are sizable.

As said, works are ongoing to refine the anticipated results on the basis of a more recent and complete set of data. The leading role of R. Mincigrucci, who is taking care of the analysis, is particularly acknowledged.

Part III

Third part

Subject of this third part of the thesis are experiments which exploit the pump-probe technique: the excitation and subsequent relaxation dynamics initiated by an intense pump pulse on insulating or semiconductor samples have been monitored by recording the reflected and/or transmitted signals of a weaker probe pulse as a function of the time delay between the two pulses.
Three configurations have been used, which foresee respectively: i) an FEL beam acting as a pump and an IR beam acting as a probe, ii) an IR beam acting as a pump and an FEL beam acting as a probe, iii) pump and probe FEL pulses derived by splitting a beam into two portions and recombining them on the same trajectory after the one has been delayed with respect to the other.
Experiments of the first and second classes have been possible after the FERMI user laser infrastructure making an ultra-fast IR laser available at the end-stations has been completed in Spring 2013. In Fall 2014, we got the chance of using for the first time the FERMI split-and-delay line to perform an experiment of the third class.
The informed reader will agree with the author that all of such investigations are within the first of their kind, standing at the forefront of research with free electron lasers.

Chapter 4

FEL-pump / optical laser-probe experiments

Developed under the push to serve the needs of optical-pump / FEL-probe experiments, FEL-pump / optical laser-probe experiments inaugurate a new class of investigations which further challenge our understanding of FEL-induced material changes, here mirrored in the variations of their optical refractive index.

4.1 Establishing space and time coincidence at FEL facilities

When wishing to realize a pump-probe experiment combining FEL and laser pulses, the first step is to ensure their superposition in both space and time.

Spatial superposition does not raise particular concerns. Simply placing a YAG crystal at the sample position and imaging the FEL-induced fluorescence allows to judge the overlapping between the two beams with sufficient accuracy. The two beams are in fact tailored by the respective focusing optics in such a way that the footprint of the probe beam fall well inside the footprint of the pump beam.
Truthfully, although highly desirable to retrieve information which refer to homogeneous excitation conditions, this constraint is often the object of a compromise. Indeed, a too large focal spot for the pump would limit the energy density deposited on the sample, besides the fact that fewer measurements could be taken per available sample. On the other hand, a too small focal spot for the probe may induce modifications in the sample that uncontrollably sum up with those caused by the pump, in cases where the probe intensity cannot be strongly attenuated without compromising the detectability of the reflected and/or transmitted signals.
Two more comments regard the fact that the laser beam cannot be brought to a

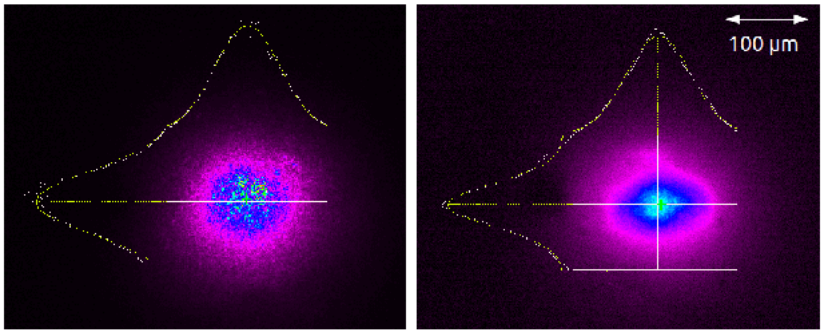

Figure 4.1: User laser (*left*) and FEL (*right*) pulses imaged on a YAG screen at the sample position inside the TIMEX end-station. The FEL beam is here out of best focus, yet it still preserves a good transverse profile. The user laser beam is instead close to the best focus achievable with the current setup (its dimensions are likely overestimated by the YAG fluorescence, as the "virtual focus" camera indicates an indeed smaller spot.)

focal spot as tight as the one that can be realized for the FEL beam (which is always true for reasons imposed by light diffraction) and the fact that its focusing mirror causes the FEL beam not to preserve a nice Gaussian shape away from the plane of best focus (which is a drawback related to the use of an ellipsoidal optics). That pointed out, once the best focusing conditions are realized for both beams, a feedback system will act on the laser beam optics to stabilize its trajectory.

Temporal superposition is usually regarded as a much more critical issue. This is not because it implies complicated operations when running an experiment, but because it is subject to intrinsic limitations: the synchronization of an external laser with the reference RF signal of an FEL source is affected by an error that typically exceeds 100 fs rms, to which further errors add due to thermal drifts and acoustic vibrations.

As it has been already anticipated, FERMI has opted for exploiting different portions of the same IR pulse from a Ti:Sapphire amplifier both as a seed for the FEL process and as an external laser to be delivered at the end-stations. This choice, in combination with a careful design of the laser beam transport in terms of optical and mechanical components as well as active stabilization of the pointing, has truly revealed as a winning strategy. The synchronization error - or *time jitter*, as it is usually called - is so small at FERMI to render unnecessary (for the current pulse durations) a shot-by-shot diagnostics of the relative arrival time between the two pulses and the consequent correction of the acquired data for the actual temporal delay.

What is still needed is to determine the position of the delay line that corresponds to the synchronous arrival of the laser and FEL pulses at the sample, the so-called *time zero*, once prior to any pump-probe experiment after the spatial superposition

has been optimized. This is accomplished in two steps.
First, a coarse indication (to a sub-50 ps level) comes from detecting the photoemission signals generated by the impact of the two light pulses on a specially designed copper antenna, connected via a high bandwidth coaxial cable to a fast oscilloscope.
Only then, we can go for a more precise determination (to a sub-10 fs level) by measuring the laser light reflected by some FEL-excited sample while scanning the laser delay line. The selected sample is usually a semiconductor whose optical reflectivity undergoes a very abrupt change when an EUV/X-ray pulse causes a certain number of electrons to be transfered from bound core and valence states to free states in the conduction band, abrupt change whose occurrence thus marks the desired time zero.

The latter technique, pioneered at the free electron laser FLASH [114], has become a standard in the last few years.
In Ref. [115], the concept of *spatial encoding* of the time delay coordinate is exploited: by using an orthogonal geometry between the EUV FEL and the IR laser pulses and imaging on a two-dimensional detector the IR light reflected by a GaAs sample, the temporal evolution of the reflectivity change can be retrieved on a shot-to-shot basis from the signal modulation along the spatial coordinate. The method was used to measure the time jitter of FLASH: 500 fs rms over 5 minutes.
In Ref. [116], the concept of *spectral encoding* of the time delay coordinate is exploited: a continuum pulse (i.e. a short duration pulse with a large bandwidth in the visible/IR obtained by focusing the main IR pulse on a crystal, here sapphire) is frequency chirped (so that different frequency components arrive on the sample at different times) and its fraction transmitted through a Si_3N_4 sample is frequency dispersed and imaged on a two-dimensional detector, thus yielding a shot-to-shot information. With this method, the time jitter of LCLS was measured: $\sim$ 180 fs rms.
As recently reported in Ref. [117], both types of arrival time monitors (with spatial and spectral encoding) have been installed in a transmission geometry just before the sample interaction region at a beamline of LCLS: their simultaneous use makes the arrival time known with an accuracy of 6.4 fs rms; as a result, the oscillations in the FEL signal scattered by a laser-excited Bi sample (related to the well-known phenomenon of induced coherent optical phonons) - indistinguishable in the raw data - emerge from them after the pump-probe delay values are corrected for the actual measured ones.

At FERMI, transient optical responses of FEL-irradiated materials are now routinely collected at both the TIMEX and DIPROI end-stations in the starting phase of every pump-probe experiment. Measurements specifically aimed at char-

acterizing the temporal synchronization capabilities at our FEL are presented in the paper "Towards jitter-free pump-probe measurements at seeded free electron laser facilities" by Danailov *et al.* [50].
An example from TIMEX is shown in Fig. 4.2. The top panel represents the relative variation in the reflectivity of 780 nm pulses ($\sim$ 130 fs fwhm duration, < 5 mJ/cm^2 fluence) from a Si_3N_4 sample pumped by FEL pulses at 18.8 nm (< 80 fs fwhm duration, ≈ 20 mJ/cm^2 fluence). A geometry with the laser beam near-collinear to the FEL beam and both almost orthogonal to the sample surface is adopted to maximize the temporal resolution. Like in the previously cited cases, the drop occurs on a timescale perfectly compatible with the cross-correlation width of the two pulses, indicating that the electronic modifications responsible for it occur on an even shorter timescale (and therefore represent a suitable diagnostics of the pump-probe coincidence). Unlike in the previously cited cases, however, those displayed are raw data: no corrections have been applied to the relative arrival times, nor filters have been introduced to mitigate the effects of the natural intensity fluctuations.
With the delay fixed at the middle of the steepest reflectivity change, a few thousand shots were acquired. The fluctuations in the transient reflectivity were then converted into time fluctuations on the basis of the slope provided by the complete time scan (Fig. 4.2, panel b)). These resulted to be distributed according to a Gaussian of about 5.9 fs rms (Fig. 4.2, panel c)).
Analogous measurements from DIPROI (for which the final part of the laser beam transport is differently isolated) yielded a jitter level of about 9.8 fs rms, whereas a shift of the time zero of only 65 fs was found during a 24 hours long monitoring. For both the end-stations, drifts were negligible over tens of minutes. Moreover, the implementation of a higher bandwidth beam pointing stabilization feedback promises to further push closer the goal of jitter-free pump-probe measurements at FERMI.

4.2 Transient optical response of FEL-irradiated Si_3N_4 films

Having collected for temporal synchronization purposes a certain number of curves like the one in Fig. 4.2 a), we noticed that they were displaying a qualitative different behavior under slightly diverse experimental conditions. Intrigued by the possibility of learning more about a kind of dynamics which is substantially unexplored in these terms, the joint TIMEX and DIPROI teams decided to devote an experimental campaign to the systematic investigation of the transient optical response of FEL-excited Si_3N_4 samples with different thicknesses and substrates

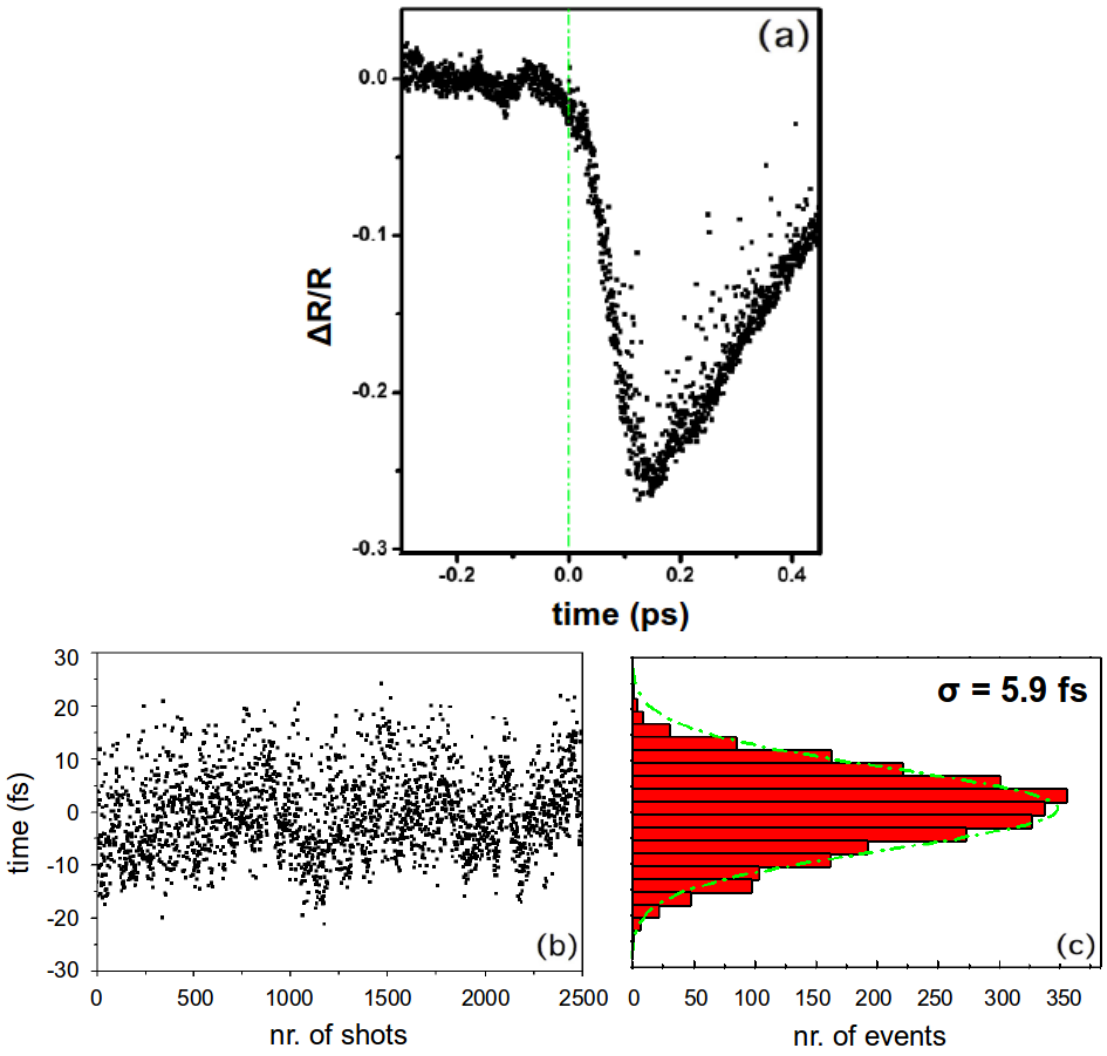

Figure 4.2: Evaluation of the time jitter affecting pump-probe measurements at TIMEX by means of the transient optical reflectivity curve of a FEL-pumped Si_3N_4 sample.

as a function of the pump energy and intensity and of the probe polarization. Explained below is how we rationalized the obtained results.

4.2.1 Experimental details and results

The measurements were performed at the DIPROI end-station, where FEL pump pulses with a duration of 80 fs impinge on the sample at normal incidence while laser probe pulses with a duration of 120 fs arrive on it at an angle of $\sim 45^o$.
Samples were crystalline Si_3N_4 films with a thickness ranging from 70 to 2060 nm, either free-standing or deposited on a 200 μm Si substrate. Si_3N_4 demonstrated

a high resistance to FEL exposure, thus avoiding the need for sample movement after each shot. Furthermore, the large (> 4.5 eV) bandgap of this material likely made it unresponsive to excitations from probe photons at 1.6 eV.
The transient optical response is explored up to 5 ps after the FEL pulse arrival (the origin of the time axis having been arbitrarily fixed at the onset of any detectable variation) with a temporal resolution dictated by the non-collinear geometry which causes a delay mismatch of about 300 fs between opposite sides of the probe transverse profile.

In the investigated ranges of 8-35 mJ/cm^2 for the pump pulse intensity and 29.0-48.4 eV for the pump photon energy, the same mechanisms seem at play. As it is shown in Fig. 4.3 for a 70 nm thick window, the relative reflectivity change in p-polarization shows an initial drop occurring on the same timescale of our resolution, followed by a rise occurring on a slightly slower timescale of ≈ 700 fs. Almost linearly, the drop makes deeper and the level reached upon recovery (always higher than the starting one) gets higher with a raising FEL intensity. Upon increasing FEL energy - instead - while the drop almost stays constant, the level reached upon recovery (still always higher than the starting one) does not follow a monotonous trend. This may be attributed to the nitrogen 2s resonance which leads to an increase after 37.3 eV of an otherwise monotonously decreasing absorption cross-section.

Major differences in the transient optical reflectivities and transmissions were observed under equal pumping conditions as a function of the sample thickness and type of substrate, as well as of the probe polarization.
This circumstance led us to hypothesize the intervention of interferometric phenomena. Indeed, when confronted with hard x-rays, soft x-rays have a shorter penetration depth, that may give rise to the aforementioned effects when smaller than the sample thickness (and both smaller than the observation depth). Resorting to the phenomenological model illustrated below, we demonstrated that this is actually the case.

4.2.2 Analysis and discussion

Let us consider the case of a 70 nm -thick Si_3N_4 sample pumped by 35 mJ/cm^2 FEL pulses at 48.4 eV for which the time dependences of both reflectivity and transmission in both p- and s- polarizations were measured. They are shown in Fig. 4.4: reflectivity with red points, transmission with green points, p-polarization in panel a), s-polarization in panel b).
In a first approximation, the target can be thought as composed of two slabs: the top excited one - of thickness d_{ex}, characterized by a time dependent refractive index $\widetilde{n}_{ex}(\mathrm{t}) = n_{ex}(\mathrm{t})$ - $i\ k_{ex}(\mathrm{t})$ - and the bottom unperturbed one - of thickness d-

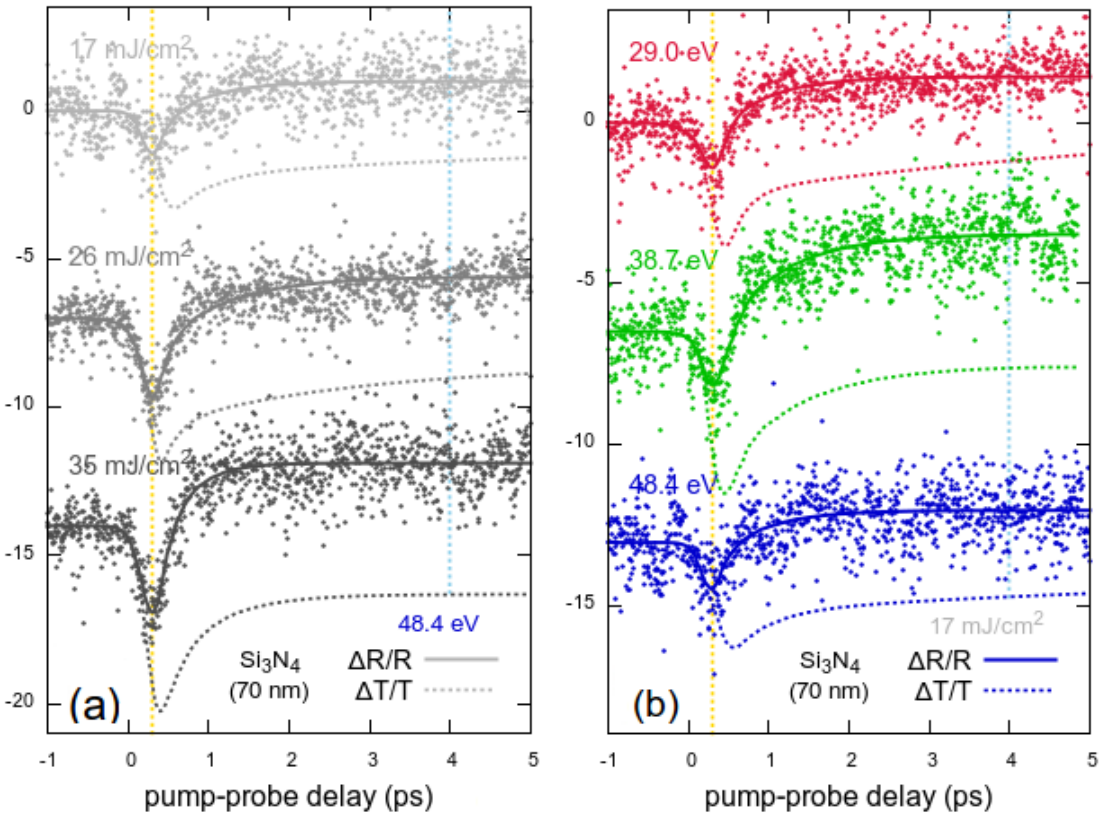

Figure 4.3: Relative variation of the optical properties of a FEL-pumped 70 nm -thick Si_3N_4 film probed by p-polarized light at 1.6 eV energy and < 5 mJ/cm^2 intensity. *Panel a):* dependence on the pump intensity at 48.4 eV pump energy; *panel b):* dependence on the pump energy at 17 mJ/cm^2 pump intensity. *Points* are experimental reflectivity data, *full lines* of the same color represent a fit to the experimental reflectivity data, *dashed lines* of the same color represent a fit to the experimental transmission data collected simultaneously to the reflectivity ones.

d_{ex}, characterized by a time independent refractive index $\widetilde{n} = n$ - $i\ k$, like sketched in panel c) of Fig. 4.4.
We therefore did the following.

First, we fitted the experimental data to a piecewise function - consisting of a negative exponential at early time delays and a couple of positive exponentials at later time delays - convolved with a Gaussian.

Second, using the four fitting functions, we deduced - for each delay point in the experimental mesh - the real and imaginary components of $\widetilde{n}_{ex}(t)$ by numerically solving the equation for the propagation of an electromagnetic wave through a bilayer system.

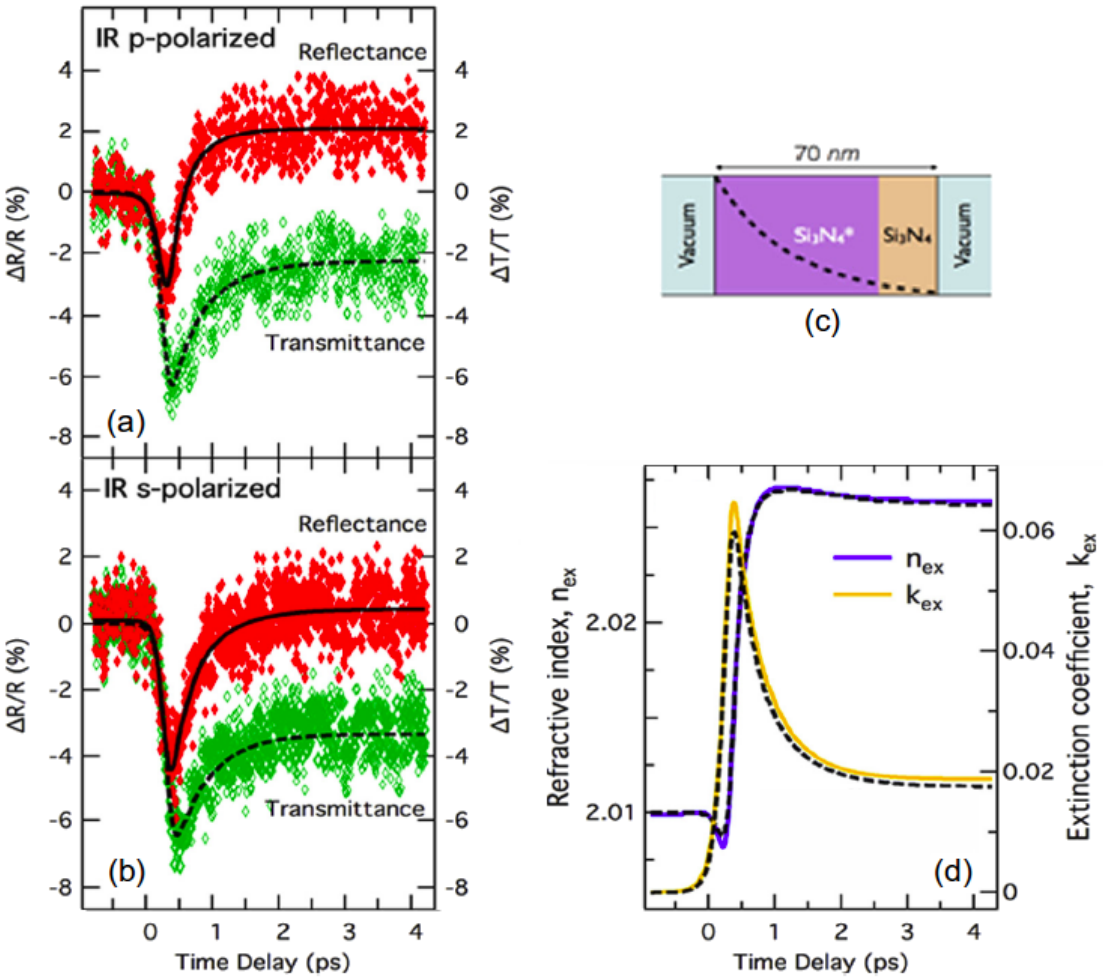

Figure 4.4: Transient optical response of a 70 nm -thick Si_3N_4 film after irradiation by 35 mJ/cm^2 FEL pulses at 48.4 eV. *Red* and *green dots* represent the measured relative reflectivity and transmission variations, shown in *panel a)* for a p-polarized optical probe and in *panel b)* for a s-polarized optical probe as a function of the pump-probe delay. From a fit of these experimental data - treating the sample as a bilayer system (Si_3N_4* | Si_3N_4), like depicted in *panel c)* - inversion of the Fresnel equations results in the temporal evolutions of the real and imaginary parts of the refractive index within the excited topmost layer (Si_3N_4*) that are shown as *violet* and *yellow lines* in *panel d)*. *Dashed lines* in the same panel come from a similar procedure where, however, the sample is treated as a system of many layers across which the excitation decays exponentially and the resulting $n_{ex}(t)$ and $k_{ex}(t)$ values are then averaged along the sample thickness. *Black lines* in *panels a)* and *b)* are self-consistent calculations from the complex refractive index back to the observable optical properties.

This is easily obtained via the transfer-matrix method [118], according to which the transmitted (E^+) and reflected (E^-) field amplitudes at the two sides of an interface j are related one another by a matching matrix accounting for continuity boundary conditions -

$$\begin{pmatrix} E_j^+ \\ E_j^- \end{pmatrix} = \frac{1}{t_j} \begin{pmatrix} 1 & r_j \\ r_j & 1 \end{pmatrix} \begin{pmatrix} E_{j+1}^+ \\ E_{j+1}^- \end{pmatrix} \tag{4.1}$$

with r_j and t_j the elementary reflection and transmission coefficients given by the well-known Fresnel formulas - whereas the transmitted (E^+) and reflected (E^-) field amplitudes at the two sides of a layer j are related one another by a propagation matrix accounting for both phase shift and absorption -

$$\begin{pmatrix} E_j'^+ \\ E_j'^- \end{pmatrix} = \begin{pmatrix} e^{i\phi_j} & 0 \\ 0 & e^{-i\phi_j} \end{pmatrix} \begin{pmatrix} E_j^+ \\ E_j^- \end{pmatrix} \tag{4.2}$$

being $\phi_j = \frac{2\pi}{\lambda} \widetilde{n_j} d_j \cos\theta_j$ with λ the field wavelength, $\widetilde{n_j}$ the layer complex refractive index, d_j the layer thickness and θ_j the propagation angle.
The results are displayed as the violet and yellow lines in panel d) of Fig. 4.4.

Third, the resulting temporal evolution for the complex refractive index was used to predict transient changes in the optical properties of samples with different thicknesses and/or substrate subject to the same FEL irradiation conditions.
Full and dotted black lines in Fig. 4.4 a) and b) are the result of this procedure applied to the same 70 nm -thick Si_3N_4 film from which $n_{ex}(t)$ and $k_{ex}(t)$ were derived. Their perfect accordance with the experimental data thus provides a positive self-consistency check.
Applied to a Si_3N_4 film with a greater thickness of 2060 nm and to a Si_3N_4 film of the same thickness but deposited on the optically opaque Si substrate, those same $n_{ex}(t)$ and $k_{ex}(t)$ curves were found to yield transient reflectivity and transmission curves that reproduce very nicely the respective experimental data, as demonstrated in Fig. 4.5.
The reader can here observe the different trends that we were mentioning: a FEL-induced reflectivity drop followed by a recovery to a new value above the equilibrium one may for example turn into a more or less pronounced reflectivity enhancement followed by a recovery to a new value below the equilibrium one due to the presence of a back reflecting interface, be it either an opaque back reflecting substrate or the unperturbed rear portion of the sample itself.

The collected data were compatible with an excited slab of 54 nm thickness,

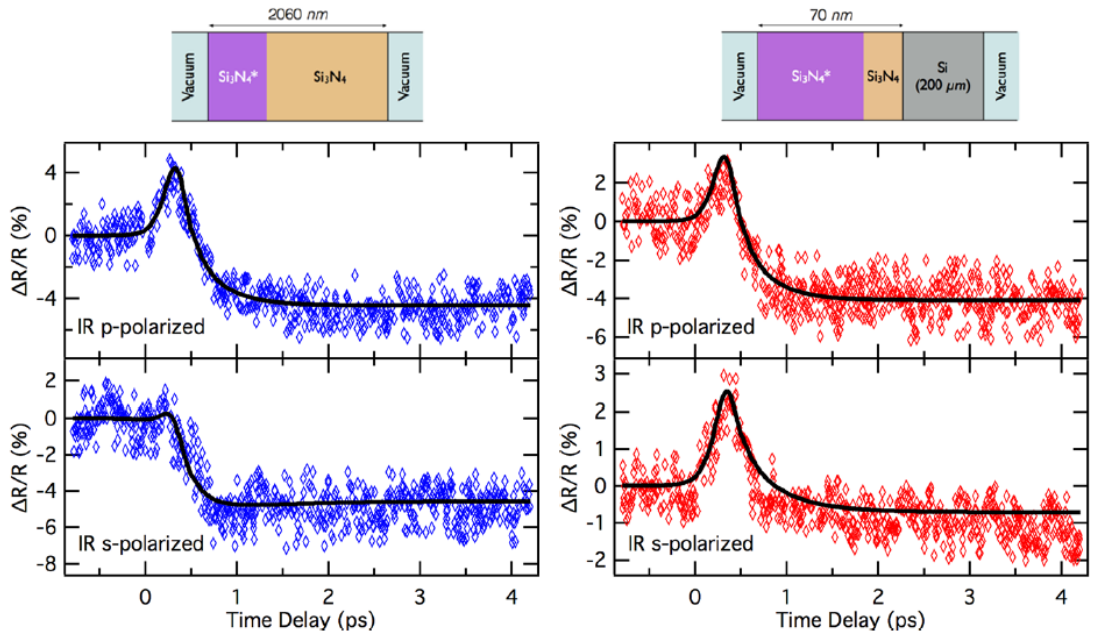

Figure 4.5: Time dependent relative changes in the reflectivity of a 2060 nm -thick Si_3N_4 film (*left panels*) and a 70 nm -thick Si_3N_4 film on a Si substrate (*right panels*) measured with p-polarized (*top panels*) and s-polarized (*bottom panels*) probe light following irradiation by mJ/cm^2 FEL pulses at 48.4 eV. *Colored points* are experimental data; *black lines* are predictions of the wave propagation model for a bilayer or trilayer system with the topmost layer having - on average - the refractive index and extinction coefficient displayed in panel d) of Fig. 4.4.

in reasonable agreement with the attenuation length for 48.4 eV photons which equals 36 nm [53]) for a perfect Si_3N_4 crystal but may be expected higher for the amorphous material.
A more realistic description would consider an exponential decay of the FEL excitation along the sample thickness, rather than a sharp boundary. This has been done with the result that, once averaged over the whole sample depth, the complex refractive index does not differ significantly from the one so far discussed, especially at pump-probe delays longer than a few hundred fs. The comparison is offered in panel d) of Fig. 4.4 where these new values are represented by the dashed lines.

The results presented in this section have been published on Applied Physics Letters [119]. A particular thank goes to F. Casolari who implemented the code for the analysis.
A few further considerations follow.

Having remarked the role of interferometric effects in this class of experiments where EUV / soft x-ray pulses are used to pump samples that have a thicknesses greater than their penetration depth and are transparent to their optical / IR probes is a warning against misinterpretation of the data.
On the other hand, it also contains the suggestion of exploiting these effects to enhance the output signal by properly tailoring the sample thickness - much like demonstrated for other optical techniques such as Raman scattering [120] and Kerr spectroscopy [121]. As proven in Fig. 4.6, a maximum relative reflectivity change

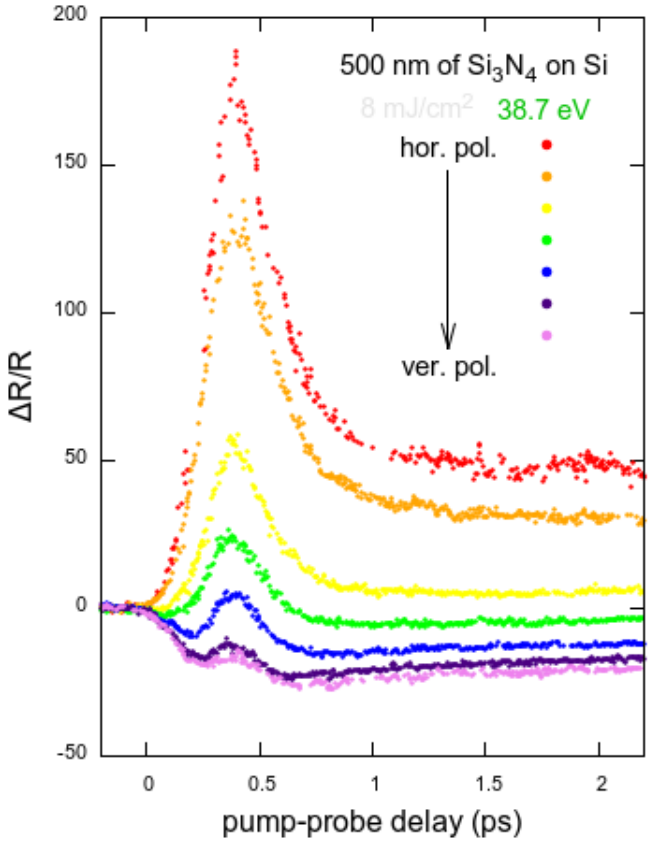

Figure 4.6: Relative reflectivity variation in a 500 nm -thick Si_3N_4 sample irradiated at time zero by FEL pulses with a fluence of 8 mJ/cm^2 and an energy of 38.7 eV, displaying an interferential increase upon tuning of the probe polarization.

of about 200% was measured in the particular case of 8 mJ/cm^2 pump pulses at 38.7 eV and a $\approx$ 500 nm -thick Si_3N_4 sample. Such an augmented signal may, for example, turn useful to improve the accuracy of timing diagnostics relaying on these FEL-pump / optical laser-probe experiments.

We here note that EUV FELs benefit from some additional advantages with respect to X-ray FELs in this regard.

The same shorter penetration depth that is responsible for the showing up of the discussed interferential phenomena is, in fact, also responsible for the creation of a higher density of free carriers, which ensures better transient signal levels.
At the same time, the density of free carriers takes a shorter time to increase, thus guaranteeing a better temporal resolution.

This concept is illustrated in Ref. [122], that is worth a few words as it is one of the very few attempts to treat the subject from a theoretical point of view. Here, a Monte Carlo model is applied to study the electron kinetics in an insulator (SiO_2) irradiated by a fs X-ray pulse. The following processes are included in an event-by-event simulation: photoionization of deep shell electrons, elastic scattering with atoms and inelastic scattering with other electrons from the valence band or deep shells to the conduction band (i.e. impact ionization), Auger decay of core holes and electron-hole recombination. As a result, the transient distribution functions of electrons and holes, their densities and energies are derived and the corresponding change in the optical properties of a probe visible pulse calculated with a Drude model where all these quantities enter the expressions for the plasma frequencies and the mean scattering frequencies.
An initial rapid decrease of the optical transmission is predicted corresponding to an increase of the free electron density, followed by a recovery which appears to mainly proceed via recombination of self-trapped excitons [123, 124]. Shortening the pump pulse duration speeds up the production of primary photoelectrons, but this is insufficient to shorten the time scale for the free electron density increase in cases of high photon energies, when a cascade of secondary electrons is produced.
In order for the free electron density to follow the time integral of the pump pulse profile, each photon must yield one electron only, which is what happens when its energy equals what in a previous publication from the same main author is called the effective energy gap [125]. The last is defined as $E_{EEG} =< E_e > + E_g + < E_h > \simeq \frac{1}{2} \cdot (E_g + E_e^{min} + |E_h^{min}|)$ with E_g band gap, E_e energy of the ionized electrons and E_h energy of the holes, and it is better approximated by $E_{EEG} \approx 2\, E_g$ rather than by $E_{EEG} \approx E_g$ (as it is, instead, commonly assumed).

In commenting similar X-ray pump / optical probe experiments, the authors of Ref. [126] drew their attention to the fact that - while in Si_3N_4 the reflectivity recovers monotonically from the low reflectivity side after the initial drop - in GaAs it overshoots the equilibrium value before approaching it from the high reflectivity side.
They attributed this difference to the fact that the 800 nm probe pulses are nearly resonant with the band gap in GaAs, thus making manifest in this case effects of band structure modifications.

Substantially the same conclusion is echoed by Durbin that, discussing the same

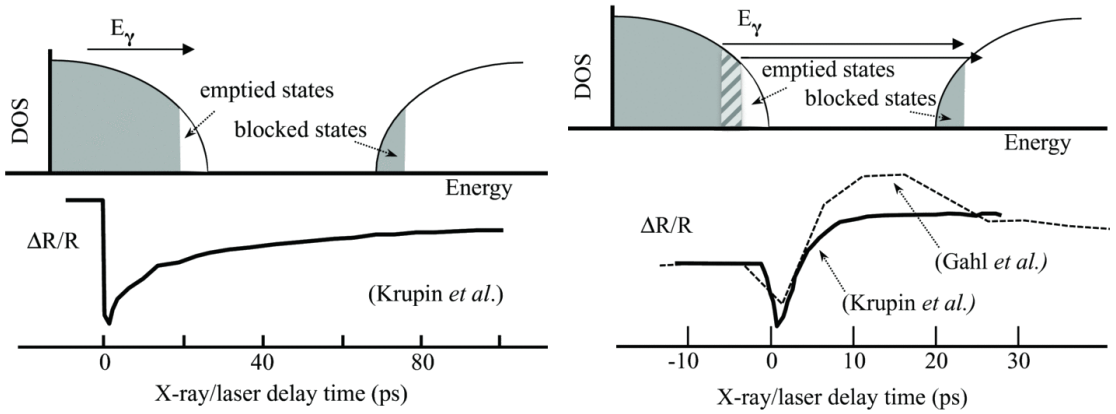

Figure 4.7: X-ray pumped insulating Si_3N_4 (*left*) and semiconducting GaAs (*right*). At the *top*, the density of states (in *gray* the occupied ones); at the *bottom*, the corresponding optical reflectivities.
Taken from Ref. [127].

kind of data in Ref. [127] outlined a picture where band filling cannot account alone for all of the experimental evidences. As depicted in Fig. 4.7, X-ray absorption promotes valence electrons into the conduction band, where they fill the lowest energy states following thermalization to a common electron temperature. This should cause probe photons with an energy smaller than the band gap (like in the case of Si_3N_4) to experience an enhanced absorption (due to the promotion into the hole states of deeper valence electrons) and - conversely - probe photons with an energy greater than the band gap (like in the case of GaAs) to experience a depressed absorption (due to a reduced number of occupied valence band states that can couple to empty conduction band states).
It appears, however, that this stage of decreased absorption (and therefore increased reflectivity) is preceded by an initial transient of sharply reduced reflectivity that could be possibly explained by a band gap narrowing induced by the not-yet thermalized population of highly excited carriers. While such an effect has been predicted for optically pumped GaAs [128], its extension to X-ray pumped GaAs is not straightforward, as the presence of deep core holes is not taken into account.

Concluding, time has certainly come for the class of experiments here discussed to receive attention from a more than mere technological perspective and be exploited, in conjunction with novel theories, to answer specific questions on the ultra-fast dynamics of materials following femtosecond X-ray and EUV excitation.

Chapter 5

Optical laser-pump / FEL-probe experiments

In the experiments described in this and the remaining chapter, the illustrated pump-probe capabilities of FERMI are exploited together with a more targeted use of the selectivity proper of its EUV pulses when tuned for core-level spectroscopies. The underlying aim is to investigate the laser-induced melting of covalently bonded semiconductors by monitoring the dynamics of the electronic subsystem with both energy and time resolution.

5.1 Ultrafast melting by optical femtosecond lasers: an introduction

Ultrashort laser pulses may cause transformations of materials along pathways that are inaccessible under thermodynamic conditions. With a pump-probe technique it is possible to trace the evolution of the laser irradiated material, which - in general terms - proceeds through the fundamental steps of laser energy deposition into the electrons and its subsequent transfer from these to the lattice.

Upon excitation with laser pulses of longer than roughly a few ps duration, the energy transfer from the electrons to the lattice occurs within the pulse duration itself. In this case, the electrons and the lattice are in equilibrium and "usual" thermodynamic considerations apply: beyond the melting point - the temperature at which the Gibbs free energy of the solid equals that of the liquid - a series of thermodynamic instabilities occurs, that provide as many qualitative criteria for identifying the onset of the phase transformation.
The most known of these is Lindemann's criterion, according to which the lattice starts to disorder when enough energy is provided for the average amplitude

of the thermal oscillations of the ions around their equilibrium positions to exceed about 10 % of the nearest neighbor distance. At temperatures higher than this, the squared amplitude of vibrations no more remains proportional to the temperature because a shift of the equilibrium atomic positions by thermal expansion confers vibrations a sizeable non-harmonic character.
Close to the melting threshold, the phase transition usually starts at the free surface where no energy has to be spent to overcome tension forces at the solid-liquid interface and proceeds into the bulk in relative long times, the upper limit for the melt front velocity being determined by the speed of sound. Under conditions of strong superheating, however, homogeneous (i.e. bulk) nucleation also becomes a possible thermal pathway for melting, characterized by a timescale that - according to Ref. [129] - is dominated by the electron-lattice equilibration rather than by the nucleation kinetics.

When the excitation laser pulses have a duration roughly shorter than a few ps, it is legitimate to ask whether melting can still be regarded as a truly thermodynamic phase change - that is, starting from and ending into well-defined thermodynamic states - or whether, on the contrary, hot electrons can affect the cold lattice before electron-phonon collisions can operate the energy equilibration among them. To date, numerous experimental and theoretical findings support the hypothesis that melting occurs in strongly excited semiconductors as a non-thermal transition: when a significant fraction of electrons is excited from bonding states in the valence band to anti-bonding states in the conduction band, the ions start experiencing an augmented repulsive potential that causes the lattice to deform while still cold [130].

This scenario has been envisaged from the first time by Stampli and Bennemann [131], who used a tight-binding model to analyze the effects of a dense electron-hole plasma on the stability of the diamond structure of the group IV semiconductors Si Ge and C. They found that the elastic shear constant becomes negative and the frequency of the transverse-acoustic phonons (roughly proportional to the square root of the latter) becomes imaginary if more than 9% of the valence electrons get excited into the conduction band. Correspondingly, atom displacements take on an exponential rather than oscillatory time behavior, in which case the lattice may need roughly 200-300 fs to melt.
More recently, Recoules and coauthors [132] reported on their density functional perturbation theory calculations of the phonon spectrum of three representative materials as a function of the electronic temperature. While confirming the same picture of bond softening for silicon, they further showed that the opposite behavior is displayed by metallic samples, which exhibit an increase of the Debye temperature (and hence of the melting temperature). The effect is small for aluminum

but much more pronounced in gold, the different responses being ascribable to a different influence of the electronic temperature on the electronic density of states of the two materials (as already discussed in chapter 4 commenting the FEL self-transmission experiment on Ti): negligible in the case of the free-electron-like metal Al, such influence is instead considerable in the case of the noble metal Au where the bonding is participated by localized electrons whose excitation ultimately gives rise to an increased ion-ion potential.
We leave aside the discussion about a class of systems - comprising Bi, Sb, As, Te [133, 134] - for which a yet diverse phenomenology has been evidenced: the Peierls mechanism stabilizing their distorted structures becoming less effective under intense electronic excitation, a displacive force launches large amplitude coherent optical phonons while driving the crystal to disorder on a sub-vibrational timescale.

Coming back to semiconductors, the most studied materials among them have been probably silicon [135, 136, 137, 138, 139] and gallium arsenide [136, 140, 141, 142, 143] - that are characterized, at room temperature, by the diamond and the (similar) zincblende lattice structures, respectively.
From an experimental point of view, for long time the most exploited technique has been time-resolved pump-probe optical reflectivity [135, 136, 142, 137, 138] - possibly at two angles of incidence and with broadband continuum pulses to retrieve the energy-dependent dielectric function [141, 143]). In more recent years, a growing community has start developing time-resolved pump-probe X-ray [144] and electron [145] diffraction, which have the benefit of being directly sensitive to the lattice structure changes.

The amount of experimental data is considerable, still their interpretation is not universally accepted. Gamaly [146], for example, raises a long series of concerns regarding in particular the explanation of diffraction experiments and, more in general, offers an insight on femtosecond-excited solids that goes against the prevailing view.
He in fact comments that the drop in the diffraction peak intensity observed with both X-ray and electron probes are ascribable to the shift in the equilibrium atomic positions which results from the spatially inhomogeneous profile of the absorbed energy density, exponentially decaying with depth in the skin layer. He stresses how this same shift and the anharmonic character of the atomic vibrations close to the melting threshold are both elements that invalidate the use of the classical Debye-Waller factor for estimating the lattice temperature rise after laser irradiation. Stating that the electronic and lattice subsystems establish an internal equilibrium within 10-20 fs, he developed a thermodynamic description of each subsystem from which he deduced that the entropy rise associated to an even strong electronic excitation is insufficient to account for the degree of lattice disordering emerged

in several experiments. This finding, together with the consideration that point defects are only expected to form on much longer timescales because proportional to the concentration of atoms belonging to the high-energy tail of the Maxwell distribution, led him to conclude that overheating of the lattice due to the high density of deposited energy is the sole responsible for ultra-fast melting. The latter is therefore judged as of pure thermal nature. Such conclusion reconciles with the observed short melting times once proper account is taken of the temperature dependence of the electron-phonon energy exchange time, as better detailed in Ref. [147].
Indeed, the electron-phonon energy exchange rate is roughly proportional to ratio of the electron heat capacity over the electron-photon coupling [148]. Numerous works by now exist showing that both these quantities - treated as constants within standard two temperature models - strongly depends, instead, on the electronic temperature. The first-principles electronic structure calculations of Ref. [25], for example, demonstrated that this dependence is even opposite in sign among the various investigated metals and, as expectable, reveals at increasing electronic temperatures an increasing sensitivity to the details of the electronic structure.

All these considerations should have given the reader at least a flavor of how complex the time-resolved dynamical study of yet the simplest phase transition in yet the most known materials can be.
Trying to keep the discussion in simple terms, I conclude proposing - rather than the approach suggested in Ref. [149] of looking at the thermal and non-thermal regimes as separated by a distinct line at about 10^{-12}s - the approach followed in Ref. [150]. The authors of the latter work identified a simple condition for the onset of melting in laser-irradiated Si, where thermal and non-thermal processes jointly contribute through, respectively, the first and second terms on the right-hand side of the following equation: $\rho\, C_L\, (T_m - T_0) = \rho\, C_L\, (T - T_0) + n\, \widetilde{E_g}$. Here, the lattice temperature T and the electron-hole plasma density n are computed within a two-temperature model; T_0 denotes the starting temperature, T_m the melting temperature, C_L the lattice specific heat and $\widetilde{E_g}$ a renormalized energy gap (both the last two quantities could possibly be generalized to account for their T and n dependences). The melting time is so observed to be a strongly decreasing function of the incident fluence: for below- or near-threshold fluences, the above condition is satisfied a few ps after the pulse arrival receiving a dominant contribution from the "thermal" term $\rho\, C_L\, (T - T_0)$ whereas, for higher fluences, it can be satisfied during the laser pulse thanks in this case to the prevailing contribution from the "non-thermal" term $n\, \widetilde{E_g}$.

Besides the one of understanding the fundamental mechanisms that regulate the

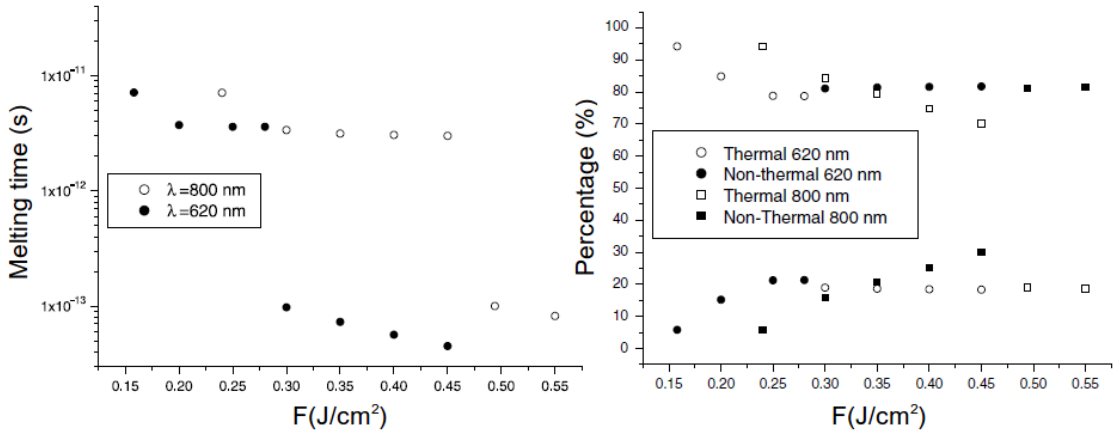

Figure 5.1: *Left:* simulated melting time in Si as a function of the incident laser fluence (100 fs pulse duration); *right: relative contributions of thermal and non-thermal processes to the ultra-fast laser melting of Si.*
Taken from Ref. [150].

electron-lattice interaction on very short timescales, a further reason for pursuing this kind of studies lies in the possibility to gain access to states of matter which cannot be explored by other experimental means.

An example in this sense is provided by the melting of carbon, which is notoriously hard to achieve experimentally for at least two reasons: the required melting temperature beyond $\approx$ 4000 K exceeds that of any containment vessel and, furthermore, slow adiabatic heating of the solid ends up in the sublimation to the vapor. Impulsive heating at nearly constant volume, on the contrary, results in a high enough pressure to temporarily generate the liquid state (Fig. 5.2).

Conducting pump-probe reflectivity measurements with femtosecond light pulses, Reitze *et al.* [152] were the first to observe pyrolytic graphite and diamond undergoing melting within $\sim$ 1 ps. The so-obtained (common) liquid state was characterized by a visible reflectance higher than the one of the starting solid and - as indicated by a Drude fit to reflectivity data at a few probe energies - by a surprisingly low conductivity, that connotes the carbon melt as having poor metallic properties.

What further makes interesting these investigations, is the possible existence - much debated in the literature - of liquid-liquid phase transitions in carbon. Indeed, as carbon can give rise to different solid phases, characterized by different densities and different types of bonding with either sp, sp^2 or sp^3 hybridization character, it is intriguing to find out if the liquid can exhibit a similar kind of poly(a)morphism. Femtosecond optical pump / picosecond X-ray probe absorption spectroscopy measurements at the carbon K-edge performed by Johnson *et al.* at a synchrotron slicing source [153] evidenced different spectral features in the liquid state according to whether the original solid was diamond or amorphous carbon with a smaller density

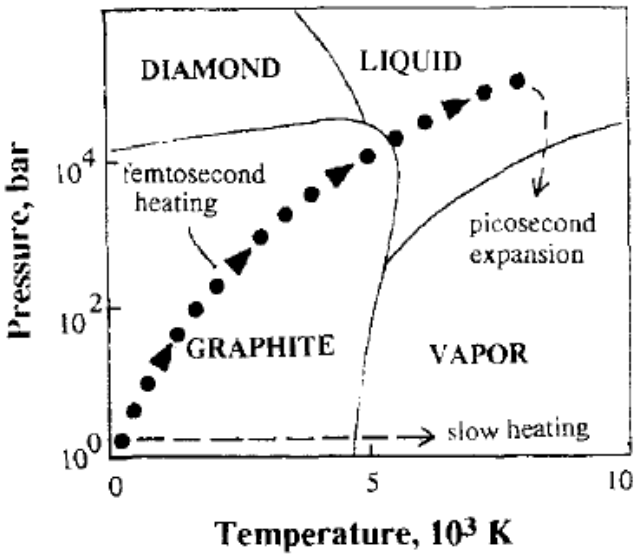

Figure 5.2: Equilibrium phase diagram of carbon in pressure and temperature regimes accessible in pulsed laser heating experiments. Slow pulsed heating leads to little change in sample pressure, since thermal expansion can occur during the pulse. Femtosecond heating creates substantial internal pressure, allowing temporary access to the liquid phase.
Taken from Ref. [151].

and whether the sample was or not tamped with LiF foils to prevent expansion, an indication that the link between density and local atomic coordination is retained upon melting.
However, theoretical evidences exist both in support of a continuous variation of the liquid properties with density [154] and of the existence of a veritable first-order phase transition, possibly ending in a critical point [155]. Importantly, such a transition has been proposed as the key to explain the many anomalies displayed by all those systems that - like the most famous case of water - become denser upon melting. These for example comprise silicon and germanium, where the latter behavior basically descends from the fact that their stable phases at ambient conditions possess an open (i.e. scarcely space-efficient) tetrahedral structure stabilized by strongly orientation-dependent bonds. Notwithstanding the profound implications it would have, no direct experimental verification has yet been accomplished since the conjectured liquidliquid phase transition would lie in the so-called "no man's land", under conditions in which the undercooled liquid rapidly transforms into the stable crystal phase (Fig. 5.3).

Ultrafast experiments provide a unique opportunity to gain an insight into this elusive regime. One can expect rapid and strong irradiation to abruptly break the covalent bonds of the diamond lattice causing structural disorder and, only at a

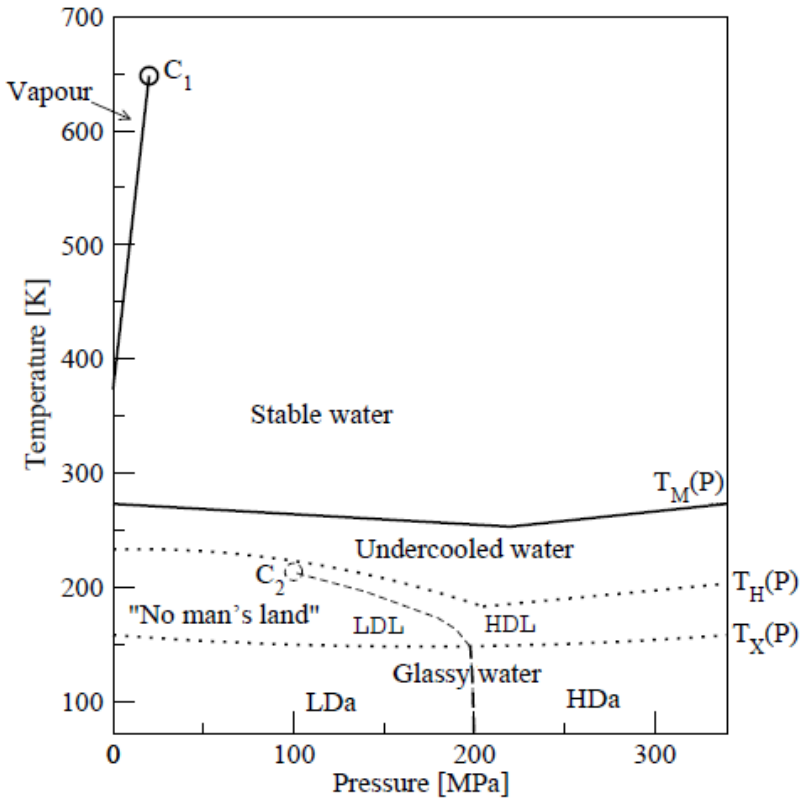

Figure 5.3: Water phase diagram. Below the melting line (T_M) all represented phases are metastable (ice-I is the stable phase up to the pressure of the melting line minimum). Upon quenching water below T_X, glassy water is obtained in its two forms, high density amorphous (HDa) and low density amorphous (LDa); when slowly heating the glass above T_X and when undercooling water below T_H, the system rapidly crystallizes into ice. The region between the two dotted lines is therefore usually called "no man's land"; there, a low density liquid (LDL) - high density liquid (HDL) coexistence line ending in a second critical point (C2) has been hypothesized.
Taken from Ref. [156].

later stage, an alteration of the average density.
This approach has been pursued in a very recent theoretical work [157], where the application of a hybrid Monte Carlo - tight binding molecular dynamics model has revealed a two-step transition taking place in diamond irradiated with 10 fs pulses at 10 keV: by $\sim$ 170 fs a state with a graphite-like structure but a diamond-like density is formed, which turns into a truly graphite state with an increased interlayer distance after $\sim$ 235 fs. The initial transformation is non-thermal, as proved by the fact that the lattice temperature is seen to increase only in conjunction with the subsequent volume relaxation. An electron-hole plasma density of $\sim$ 1.5% is needed to trigger the process, which is then qualified as a first-order solid-solid

phase transition.
Experimentally, a robust indication for the occurrence of a first-order liquid-liquid phase transition in Si has come from Beye *et al.* [158], who performed femtosecond soft X-ray emission spectroscopy at the L-edge of the optically-excited crystalline sample. Comparison of the density of occupied electronic states retrieved from such measurements with existing calculations for the crystalline, low-density-liquid and high-density liquid phases of Si (Fig. 5.4) strongly suggested that the sample evolves first into the LDL state - semimetallic, with a partially closed gap - and subsequently from this into the HDL state - metallic, with a completely close gap. A plateau between 2 and 4 ps both in the measured position of the valence band edge (indicative of the band gap closure) and in the measured ratio between the intensities of the two most prominent peaks in the valence band DOS (indicative of the loss of long-range order) was recognized as a further fingerprint of the intervened first order LDL-HDL phase transition.

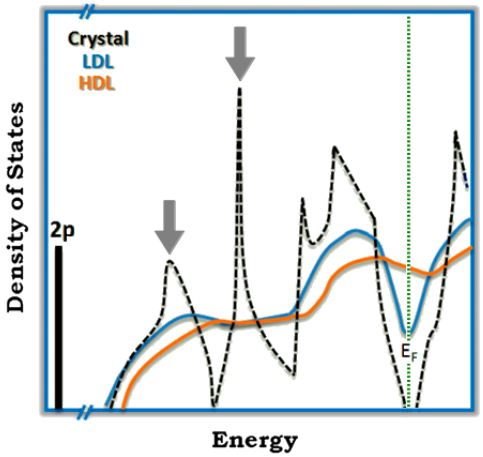

Figure 5.4: Electronic density of states for Si in its crystalline (semiconducting, *dashed black line*), low-density liquid (semimetallic, *blue line*) and high-density liquid (metallic, *red line*) phases.
Taken from Ref. [159].

5.2 Ultrafast dynamics of laser-excited Ge probed by FEL absorption spectroscopy at the $M_{4,5}$ edge

Within this context, we proposed to investigate the electron dynamics following ultra-fast laser heating of germanium by means of time-resolved EUV absorption spectroscopy at the M edge.

A germanium sample was chosen because its M edge falls in an energy range where previous commissioning activities [47] allowed us to test both the tunability of FERMI and the response of the detectors for the transmitted FEL light. We expected, however, close similarities with silicon, both materials being characterized by a diamond-like lattice structure and an indirect-bandgap electronic structure.
Tracking the evolution of the absorption spectrum, on the other hand, could yield a complementary picture with respect to the one gained through a time-resolved emission spectrum, since the former technique is sensitive to the occupied density of states whereas the latter technique is sensitive to the unoccupied density of states.
Lastly, we could rely on a significantly better temporal resolution compared to the experiment of Ref. [158], where this was limited to about 1 ps due to a jitter issue.

5.2.1 Experimental details and results

The Ge sample was in the form of a self-standing foil of 80 nm thickness, thin enough to result in a good signal-to-noise ratio all over the measured energy interval, yet thick enough to result in a well-contrasted absorption jump.
Transmittance data were collected, from which the absorbance was obtained by the usual relation A(E) = - ln[T(E)] that holds for negligible reflectance.
The static absorption spectrum was first measured at the synchrotron beamline BEAR, reading the dotted curve in Fig. 5.5. Reported as an inset in the same figure - its first derivative shows a maximum at (29.55±0.01) eV, that well compares to the tabulated values of 29.2 and 29.8 eV for the M_4 and M_5 edges respectively [53] and that we will consider as our reference for the edge energy.
Black points on Fig. 5.5 represent the corresponding data taken at TIMEX and resulting from approximately 1000 strongly-attenuated FEL pulses hitting a same portion of the sample. The error bars mainly reflect the not-always ideal correlation between the intensity read by the upstream ionization monitor and the intensity that actually reached the sample.
The overall agreement with the synchrotron spectrum is quite satisfactory. The largest discrepancies are observed at pre-edge energies and could be due to slightly different degrees of oxidation between the samples in use in the two cases.

A pump beam was then introduced. The latter was provided by the user laser of FERMI operated at its fundamental photon energy of 1.6 eV. Those pulses were compressed to a duration of $\sim$ 90 fs fwhm and impinged on the sample at an angle of about 10° to the surface normal with vertical polarization.
On the other hand, the FEL pulses impinged on the sample at near-normal incidence with circular right polarization. For the FEL photon energy to span the requested range from 26 to 34 eV, the seed laser OPA was operated at a few wavelengths between 315 and 334 nm and the FEL1 undulators were set for frequency

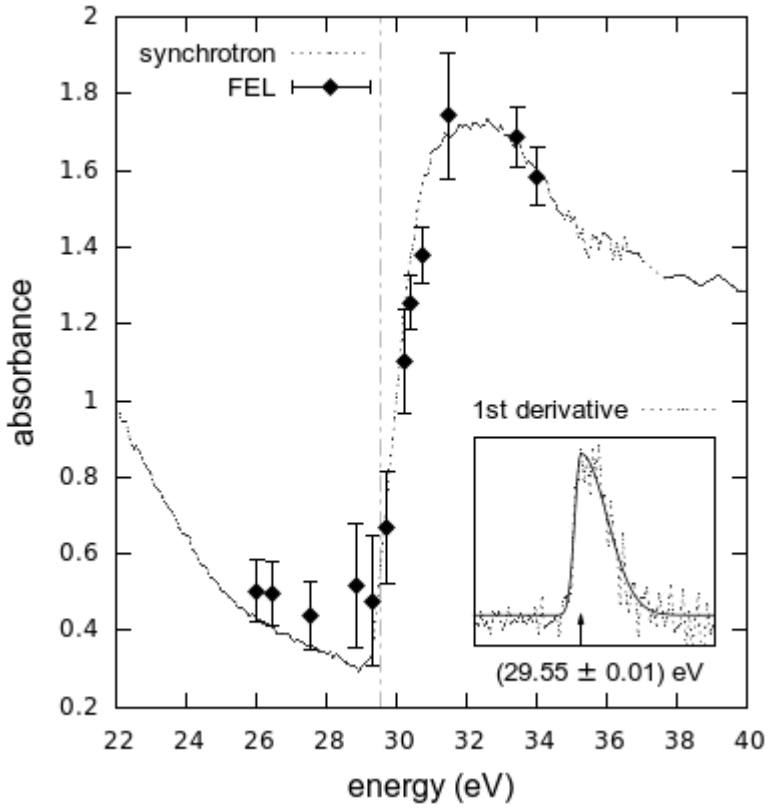

Figure 5.5: Static absorption spectrum of a 80 nm - thick Ge foil. The *dotted line* is the measurement from a synchrotron beamline, the *black points* are the measurement from TIMEX with a greatly attenuated FEL beam.

upconversion either to the 7^{th}, 8^{th} or 9^{th} harmonic. Scaling of the estimated duration of $\sim$ 150 fs for the seed pulses with the cubic root of the harmonic number yields a duration of $\sim$ 72 to $\sim$ 78 fs for the FEL pulses. Further considering the small mismatch between the beams incidence angles puts an upper limit of about 120 fs for the convolution between the pump and probe pulses and - therefore - for the temporal resolution of our time-resolved measurements.
The temporal superposition was established by recording the FEL-induced changes in the IR reflectivity of a Si_3N_4 slab.
The spatial superposition was repetitively checked during the experiment by raising the FEL intensity and looking at the damage craters produced on the sample by both beams.
While the probe spot - evaluated from the fluorescence emission of a frosted YAG placed at the sample position - had a waist diameter of $\approx 30\ \mu m$, the pump spot - evaluated by imaging the "virtual focus", as explained in chapter 3 - had a waist diameter of $\approx 100\ \mu m$.

The incident pump fluence was derived from this estimate for the focus dimensions and the estimate for the IR pulse energy which comes from rescaling by the expected loss of ~ 3 % the reading of the power meter placed just before the beam enters the TIMEX chamber. The uncertainty on those values is such that the incident pump fluence could actually be a factor 2 smaller or greater than the stated one. Nonetheless, its relative variations between the one and the other measure stay meaningful.
Even the less intense pump pulse in this experiment caused a strong permanent damage to the sample (Fig. 5.6).

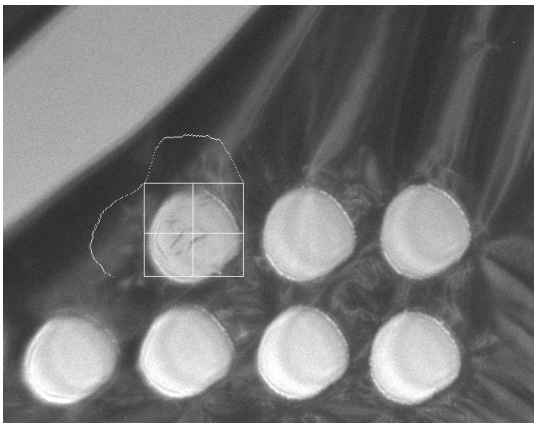

Figure 5.6: Damage craters caused on the sample surface by IR laser pumping below 1 J/cm^2, as imaged by the TIMEX telemicroscope. The mechanical stress upon pulsed irradiation is so high that it is not infrequent for the foil to explode, especially in the vicinity of its sustaining frame.

Measurements have been taken scanning the pump-probe delay over several picoseconds at a few pump fluences and at a few probe energies.
For each time step, 5 to 10 pump-probe shots were collected on consecutive sample positions, of which the reported data represent an average.
At each sample position, the pump-probe shot was preceded by 3 to 5 shots of the only probe, to serve as a measure of the local unperturbed absorption by which normalizing the "dynamic" absorption.
Strikingly different behaviors were observed to take place within diverse spectral regions: a fast, reversible, fluence-dependent increase of absorption before the edge and a slower, irreversible, less fluence-dependent increase of absorption across the edge.
Let us better detail and comment these interesting observations.

5.2.2 Analysis and discussion

In Fig. 5.7, the relative variation of the absorbance at an energy of 27.6 eV is shown for the three pump fluences of about 60, 245 and 985 mJ/cm^2 as a function of the pump-probe delay.

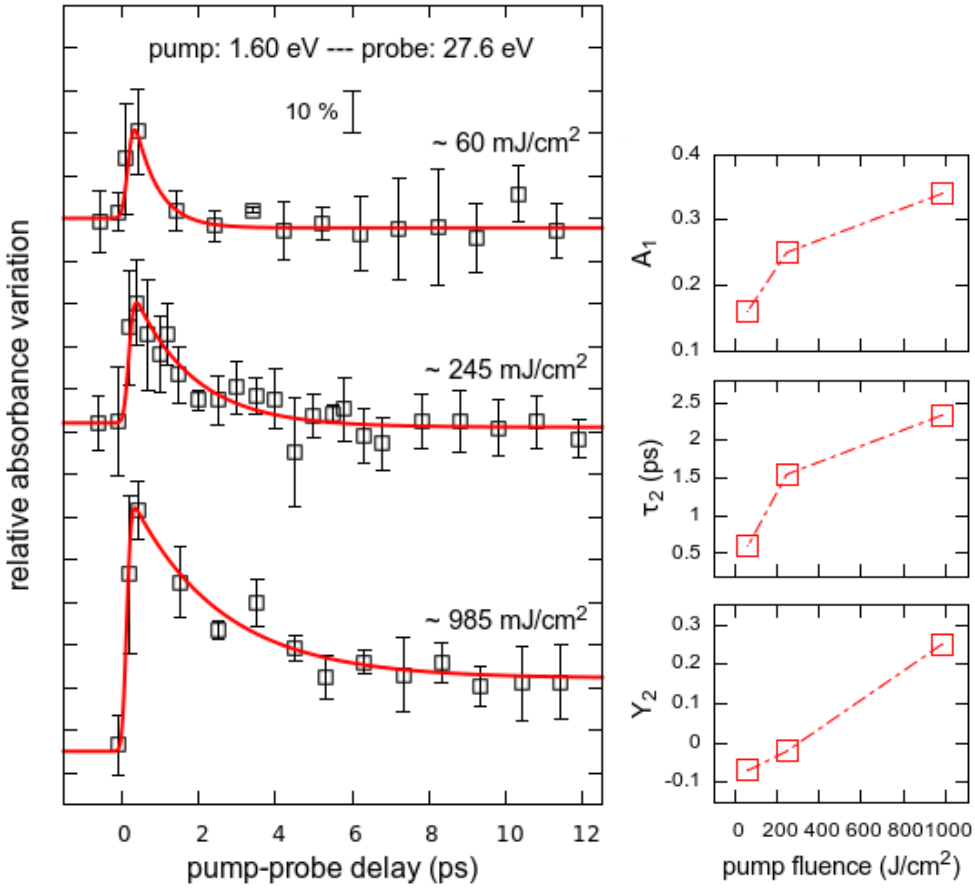

Figure 5.7: *Left:* temporal evolution of the relative change in the absorbance at 27.6 eV of a 80 nm -thick germanium foil excited by intense ultra-fast 1.6 eV pulses at three different fluences. *Right:* corresponding amplitudes of its initial sudden raise, time constants of its subsequent exponential decay and attained asymptotic values as a function of the incident pump fluence.

The absorption is seen to increase on the same timescale of our resolution and to subsequently decay on a few ps timescale.
Red lines in the figure are the result of a fit of the experimental data to the function:

$$f_1(t) = \int_{\infty}^{\infty} A_1 \left[1 + erf\left(\frac{t-\tau}{\tau_1}\right)\right] \cdot \left[Y_2 + A_2 \cdot exp\left(-\frac{t-\tau}{\tau_2}\right)\right] \cdot \frac{1}{\sqrt{2\pi}\,\sigma_G}\, exp\left(-\frac{\tau^2}{2\,\sigma_G^2}\right) d\tau \tag{5.1}$$

with $\sigma_G = 120fs/(2\sqrt{2\log 2})$.
As clearly highlighted by the trends of the fitting parameters A_1, τ_2 and Y_2 on the right panel of the figure, the higher is the pump fluence, the higher is the induced maximum change, the slower the recovery and the higher the level attained by the end of the 12 ps observation window.

We believe that such temporal evolution of the absorption changes mirrors the temporal evolution of the electronic temperature as the laser energy is first absorbed and then redistributed through particle collisions.
For the sake of comprehension, a sketch of the electronic band structure of germanium as taken from Ref. [160] is offered in Fig. 5.8.

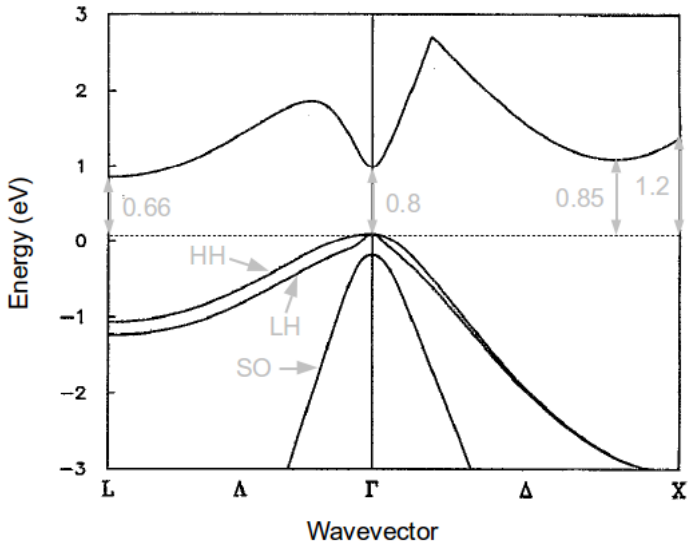

Figure 5.8: Electronic band structure of Ge.
Taken from Ref. [160].

Electron-hole pairs are photo-generated by direct transitions near the Γ point of the Brillouin zone which, however, does not represent the conduction band minimum. Previous works on femtosecond optically excited Ge pointed out that, Γ intra-valley scattering being forbidden [161], the dominant energy relaxation mechanism is provided by inter-valley scattering via optical deformation potential: electrons rapidly scatter out of the Γ valley, mainly to the X valleys and ultimately to the L valleys, where the conduction band has its minimum; meanwhile, both light holes and split-off holes quickly scatter to the heavy hole band, which has a much greater density of states [160].
Absorbance measurements do not dispose of the needed momentum selectivity to afford the detailed picture that those theoretical calculations have drawn, yet they are energy-selective: with our EUV probe at 27.6 eV - corresponding to $\sim$ 2 eV below the steepest point of the "static" absorption edge - we have monitored how

the electronic states in the valence band are filled back after their prompt emptying upon laser excitation. Since inter-valley scattering occurs with the intervention of phonons, electron cooling to the lattice proceeds as well along with electron thermalization.
Notably, while the initial state is fully recovered within very few ps at the two lowest fluences, at the highest fluence a temporary steady state is reached with a higher than initial absorption. Assuming a smearing width of $\approx k_B T$ for the Fermi function, we can argue that - in order for absorption changes to persist at an energy of ~ 2 eV below the Fermi level - the equilibrium temperature reached by the thermalized electrons and ions ~ 6 ps after the excitation should exceed ≈ 4 eV, which connotes this state as "warm dense matter".

In Fig. 5.9 it is shown how, at a fixed pump fluence of about 45 mJ/cm^2, the relative absorbance variations at the three probe energies of 29.7, 30.2 and 30.4 eV evolve in time.
The absorption is observed to exponentially increase with a time constant in the 1.2 - 2 ps range. The overall change is the more pronounced the more the probe energy gets closer to the absorption edge from the high energy side, being as large as the 70% at 0.15 eV above the edge. Those are the numbers retrieved by fitting the experimental data to the function:

$$f_2(t) = \int_{\infty}^{\infty} \left\{ [(t-\tau) < 0] \cdot 0 + [(t-\tau) > 0] \cdot \left[Y_1 + A_1 \cdot exp\left(-\frac{t-\tau}{\tau_1} \right) \right] \right\} \cdot \frac{1}{\sqrt{2\pi}\,\sigma_G}\, exp\left(-\frac{\tau^2}{2\,\sigma_G^2} \right) d\tau. \tag{5.2}$$

The fact that no recovery takes place over several picoseconds implies that at these probe energies we are witnessing structural, rather than electronic, modifications.
The curves of Fig. 5.9 are compatible with a shift of the absorption edge toward lower energies, that we suggest may be due to a collapse of the bandgap as the sample undergoes a transition to a liquid phase with metallic character.
The fact per se that the absorption is subject to such huge increments at energies were the equilibrium density of states is really tiny (as visible in Fig. 5.10) should signify that the density of states has significantly grown in the excited state.
Both Ref.s [163] and [164], indeed, reported K-edge XANES spectra of molten germanium displaying a red shift of, respectively, 1.3-1.4 eV and 0.8 eV with respect to the solid. Such feature comes in addition to an increase of the white line, related to an increased density of states near the Fermi level, and a smoothing on its high energy side, related to an augmented degree of disorder.

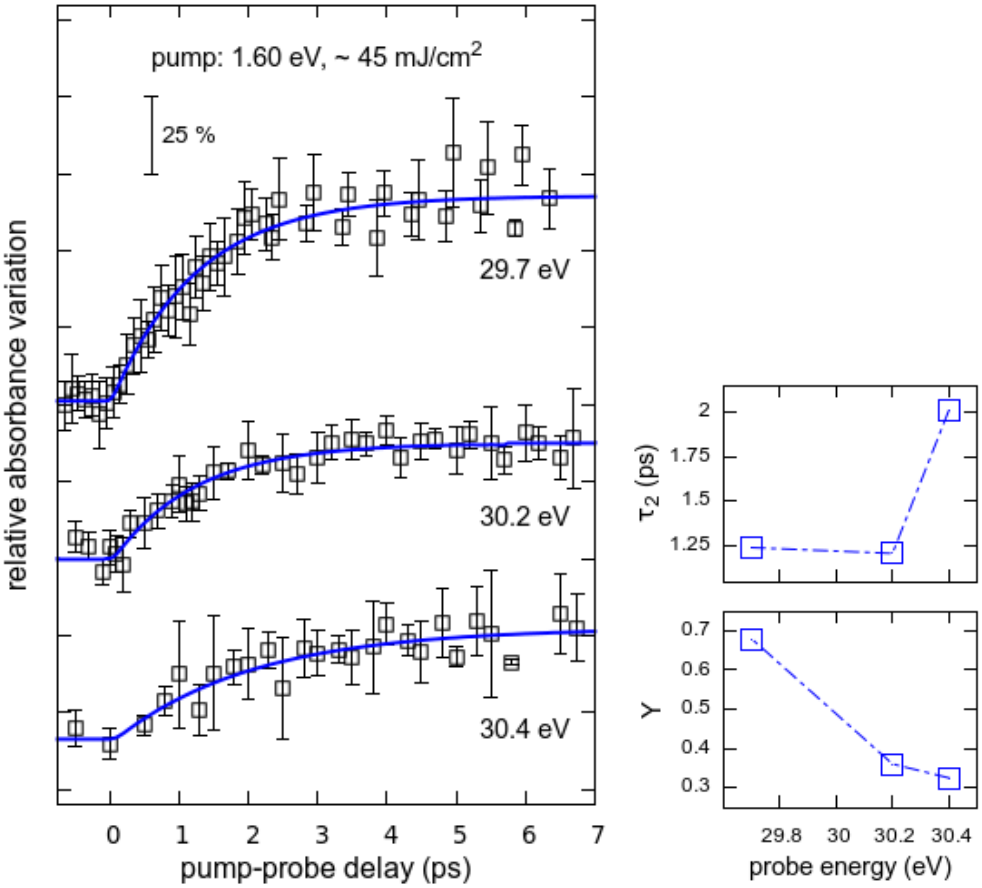

Figure 5.9: *Left:* temporal evolution of the relative change in the absorbance at 29.7, 30.2 and 30.4 eV of a 80 nm -thick germanium foil excited by intense ultrafast 1.6 eV pulses at a fluence of about 45 mJ/cm^2. *Right:* corresponding time constants of its raise and attained asymptotic values as a function of the probe energy.

We cannot ascertain the latter effects at the probe energies of the present experiment, but we can add an important piece of information: the temporal dynamics through which the melting transition develops.
In this regard, we cannot avoid a confront with what are - to our knowledge - the only works aimed at such time-resolved investigations on germanium, namely, the x-ray diffraction studies of Ref.s [165], [166] and [167]. The authors of the latter paper, in particular, reported on pump-probe measurements where a Ge sample was excited by 800 nm laser pulses and the angular-integrated diffraction of 4.5 keV pulses (of unknown duration) from a laser-produced plasma was recorded as a function of the temporal delay between the two pulses. At a pump fluence of 35 mJ/cm^2 (below the melting threshold), they observed the diffraction signal dropping of the

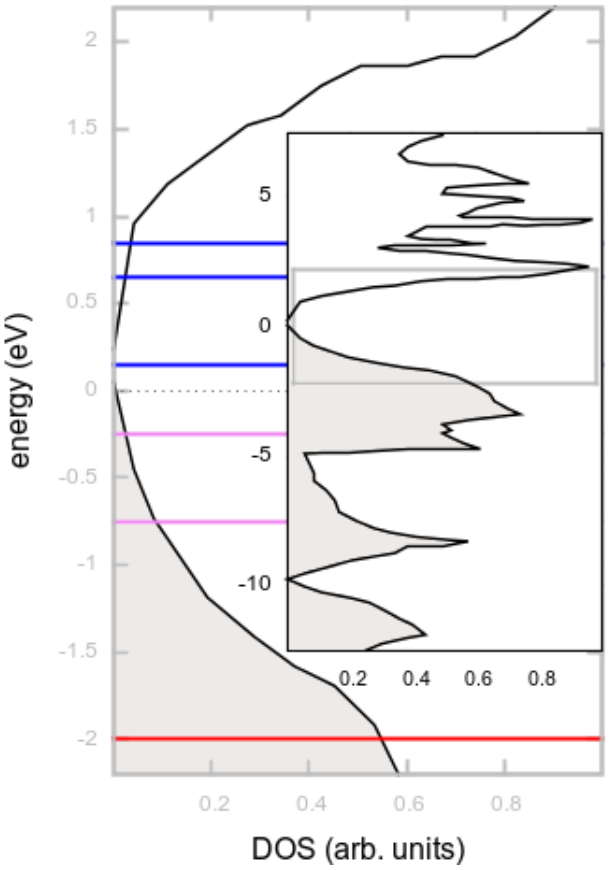

Figure 5.10: Density of states of germanium as taken from Ref. [162] (*black curves*). The horizontal lines indicate the probe energies at which the experimental data in Fig.s 5.7 (*red*), 5.9 (*blue*) and 5.11 (*violet*) were collected.

7% with a time-constant of 1.1 ps, that was identified as the electron-photon relaxation time. At a pump fluence of 200 to 400 mJ/cm^2 (above the melting threshold), they instead measured an initial 25% drop taking place in $\approx$ 300 fs - that was attributed to the melting of an equal percentage of material on the topmost layer - and a subsequent lower-rate decrease over tens of ps - that was ascribed to the propagation of the solid-liquid interface deep within the sample.
For the rapidity of the displayed dynamics, our data better compares with the ones of Ref. [167] that refer to sub- melting fluences, despite we estimate that they refer to an above- melting fluence. The sample should indeed absorb the 65% of the 45 mJ/cm^2 incoming fluence [70]. On the other hand, the expression $F = (\Delta H\, \rho\, V)\, /\, A = \Delta H\, \rho\, d$ (with ΔH = 36.94 kJ/mol enthalpy of fusion, ρ = 5.323 g/cm^3 density and d = 80 nm thickness) yields a melting threshold of $\sim$ 22 mJ/cm^2.
The latter evaluation assumes that the whole sample gets homogeneously excited

by the laser pulse, which we believe to be the case in light of a pump penetration depth of approximately 200 nm. Moreover, this hypothesis is strengthened by the conclusions of Ref. [168] that the large increase of the ambipolar diffusion coefficient at high carrier densities in Ge is responsible for a fast redistribution of the energy of not-yet-thermalized electrons into the bulk.

There is a last set of data from our experiment that further enriches the scenario. These - shown in Fig. 5.11 - refer to the same pump fluence of the data in Fig. 5.9 but to the different probe energies of 28.8 and 29.3 eV, which fall just below the absorption edge (rather than just above as in the previous case).

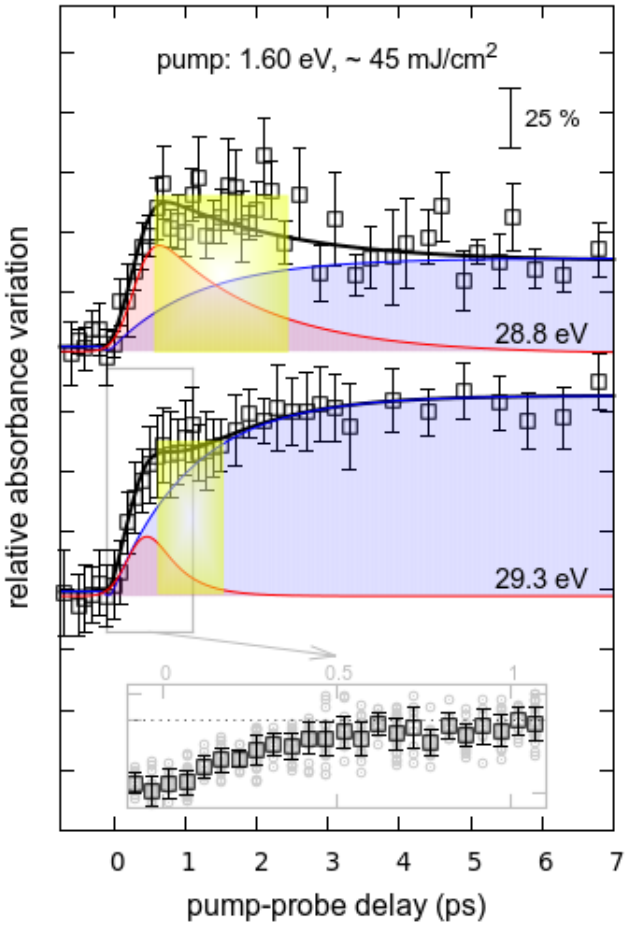

Figure 5.11: Temporal evolution of the relative change in the absorbance at 28.8 and 29.3 eV of a 80 nm -thick germanium foil excited by intense ultra-fast 1.6 eV pulses at a fluence of about 45 mJ/cm^2. The *bottom inset* shows a zoom of the first 1 ps region with the raw data (in *gray*) and a finer binning than shown above (in *black*).

At both these energies there is a first rise in absorption, which is then followed - at

29.3 eV - by a small further increase and - at 28.8 eV - by a more pronounced and slower decrease. The black curves in Fig. 5.11 represent an attempt of modeling the data with a function which is the sum of the functions 5.1 and 5.2 used to model the data well below (red curves) and slightly above (blue curves) the Ge M edge, following the idea that both effects may show up combined at these intermediate energies.
Such functional form is roughly able to reproduce the experimental trend. What is less convincing - however - is that, while the blue components have time constants of 1.1-1.2 ps similarly to the curves of Fig. 5.9, the red components - that were yielding an instantaneous rise in the curves of Fig. 5.7 - should be assigned slower time constants of 0.3 ps to fit the data.
Another tempting hypothesis is to give credit to the plateaus between the end of the initial absorption rise, at $\approx$ 0.5 ps, and the start of the subsequent increase / decrease, at $\approx$ 1.5 ps / 2.5 ps, for 29.3 eV / 28.8 eV. This could mean that, like observed by the authors of Ref. [158] in the case of Si, femtosecond laser -excited Ge undergoes a first transition to a low density liquid state and, subsequently, a second transition to a high density liquid state. In this case one should wonder why the same effect does not also manifest at the energies of 29.7, 30.2 and 30.4 eV, which also fall on the rising part of the static absorption edge. Since we do not have at disposal neither experimental data on a fine energy mesh nor theoretical calculations of the density of states for those putative liquid phases of Ge, this just remains a speculative thought for now.
The picture that for sure we can draw is the one sketched in Fig. 5.12, where the equilibrium M edge of Ge is shown together with representative points at 0.5, 1 and 5 ps after the excitation with a 1.6 eV laser pulse at $\sim$ 45 mJ/cm^2. A shift in time to lower energies is evident, that appears greater on the low-energy tail. This feature recalls the shift-and-broadening behavior with increasing temperature reported in Ref. [169] for resistively heated Si.

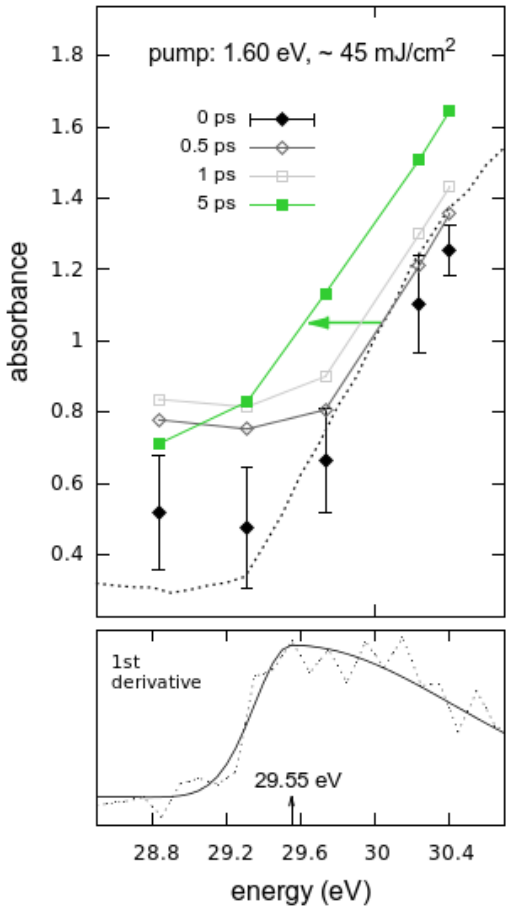

Figure 5.12: Shift and broadening of the Ge absorption edge upon irradiation with femtosecond pulses at 1.6 eV for an incident fluence of $\sim$ 45 mJ/cm^2. Representative points at 0.5, 1 and 5 ps delay times are extracted from Fig.s 5.9 and 5.11.

Chapter 6

FEL-pump / FEL-probe experiments

In this brief last chapter, I present, through an example, a further class of experiments feasible at the TIMEX beamline that - as already hinted at - only the recent installation of a split-and-delay line in the FERMI experimental hall has made possible: FEL-pump / FEL-probe experiments.

6.1 Ultra-fast dynamics of FEL-excited Si probed by FEL absorption spectroscopy at the $L_{2,3}$ edge

Even if most of the efforts turned out to be spent in managing technical tasks, we were motivated by the same scientific goals that had animated our previous study on Ge. The L absorption edge of Si being accessible in the operative configuration that will be illustrated in a while, we aimed at investigating the response of FEL-excited Si through what has been the technique of preference in this thesis: ultra-fast time-resolved absorption spectroscopy at a selected absorption resonance.

6.1.1 Experimental details and results

The experimental setup was arranged as schematically depicted in Fig. 6.1 and briefly described in the following.
The second FEL line of FERMI (FEL-2) has been exploited, run in the standard "fresh bunch" injection mode.
The pump pulses (represented in green in Fig. 6.1) were provided by the FEL

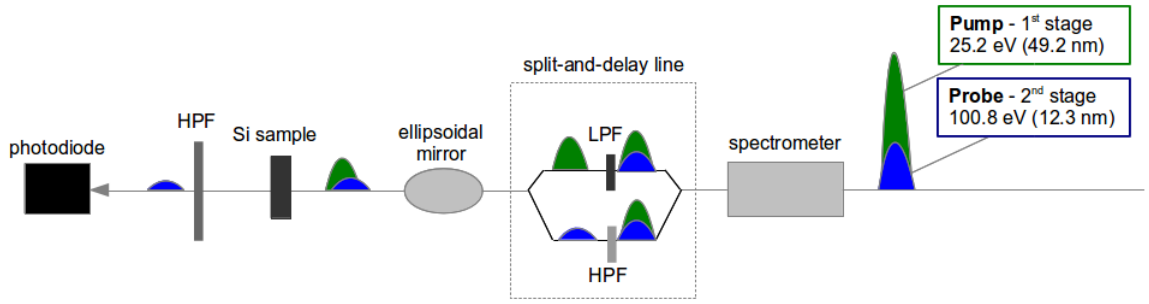

Figure 6.1: Schematic setup for a two-color pump-probe experiment on Si with FEL pulses from FERMI.
Credits: E. Principi.

emission from the first stage of FEL-2 - tuned at the 5^{th}-harmonic of the seed laser -, while the probe pulses (represented in blue in Fig. 6.1) were provided by the FEL emission from the second stage of FEL-2 - tuned at the 4^{th}-harmonic of the first stage FEL emission. In the starting configuration for this experiment, the seed laser was set at 246 nm, thus resulting in a first stage emission at 49.2 nm (25.2 eV) and a second stage emission at 12.3 nm (100.8 eV).
While the former energy is suitable to well-homogeneously excite the 150 nm -thick Si sample, the latter energy falls just above the 99.42 and 99.82 eV binding energies of $2p_{3/2}$ and $2p_{1/2}$ electrons in Si. Tuning the OPA output wavelength around 246 nm, several energies across this absorption edge can be scanned with preserved harmonic settings for the undulators.
The so-obtained two-color FEL beam is divided into two one-color sub-beams, delayed the one with respect to the other and then recombined on a common trajectory within the split-and-delay line AC/DC (Fig. 1.22 in chapter 1). In one of its branches, a low-pass 400 nm -thick Al filter has been positioned, in order to have the only long-wavelength pump component transmitted, while, in the other branch, a high-pass 300 nm -thick parylene filter has been positioned, in order to have the only short-wavelength probe component transmitted.
The spectrometer before AC/DC was aligned for detecting radiation around 12.3 nm, so that the area under the measured spectral profile could be taken as a reference for the incoming probe intensity.
The probe intensity transmitted by the sample was read by a photodiode, in front of which a 200 nm -thick Zr filter has been put to block the residual pump light.
Since neither the spectrometer nor the photodiode yielded absolute energy values (nor homogeneous physical quantities), measurements were taken without the sample to serve as a calibration from which evaluating the sample transmission.

One of the main advantages of this scheme is that no temporal jitter exist at all between the pump and the probe pulses and that both are shorter than what achievable with the OPA-derived user laser. Indeed, a $\sim$ 150 fs -long seed laser pulse is turned in our case into a pump pulse of $\approx 150/\sqrt[3]{5} \simeq 88$ fs length and a probe pulse of $\approx 88/\sqrt[3]{4} \simeq 55$ fs length, yielding a cross-correlation with of ≈ 100 fs.
Pumping with FEL pulses also ensures stronger focusing conditions than pumping with the IR laser.
On the other hand, this scheme has the drawback that less freedom is left to play with the relative spot sizes and pulse intensities between pump and probe pulses. In this experiment a major constraint indeed came from the fact that the second FEL stage is intrinsically more tightly focused than the first one, which made hard optimizing at the same time for maximum pump fluence and minimum probe-induced effects.
We handled this problem by splitting the FEL beam into two greatly unequal parts (clearly in favor of the pump portion) and detuning the last one-two undulators of the second stage (so that the radiation used as a probe is let to skip the final steps of amplification).
An order of magnitude estimate of the pump pulse intensity can be given by scaling the ionization monitor reading of 15 to 30 μJ by the numerous losses occurring along the transport.
Normalizing the resulting average of ≈ 7 μJ per pulse by the ≈ 20 x 30 μm^2 pump focal area, an incoming pump fluence of roughly 40 mJ/cm^2 is obtained, of which about the 70 % is actually absorbed along the 150 nm thickness.
As the split-and-delay line was not yet fully commissioned, the spatial superposition between the two beams was checked and corrected by acting on the internal optics of AC/DC at each measured pump-probe delay (Fig. 6.2).
The zero of the delay scale was established once at the beginning of the experiment by looking for the appearance of interference fringes on a YAG screen at the sample position (Fig. 6.3).

The experimental campaign produced the data which are reported in Fig. 6.5 as a plot of the relative absorbance variation vs the pump-probe delay.
Before entering a discussion on their significance, let us point out why error bars have been assigned that seem oversized with respect to the actually nice trend traced by the data. A comparison with analogous plots from the previous experiment on Ge shows that error bars are indeed comparable - when not smaller - in the current case; just those previous effects were stronger and thus less affected by uncertainties, that rarely stay below 10% in this class of measurements.
The main source of uncertainty was however different among the mentioned two

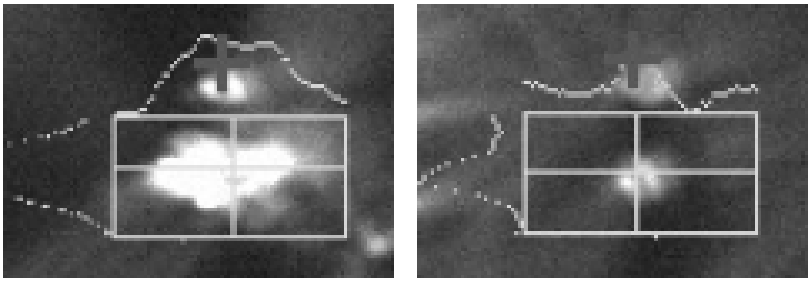

Figure 6.2: *Left*: post-shot imprint left on the sample by a single FEL pulse from the upper branch of the split-and-delay line. *Right*: post-shot imprint left on the sample by multiple FEL pulses from the lower branch of the split-and-delay line with the high-pass filter removed. The fixed white rectangle on the CCD provides a stable reference for the spatial alignment of the two sub-beams.

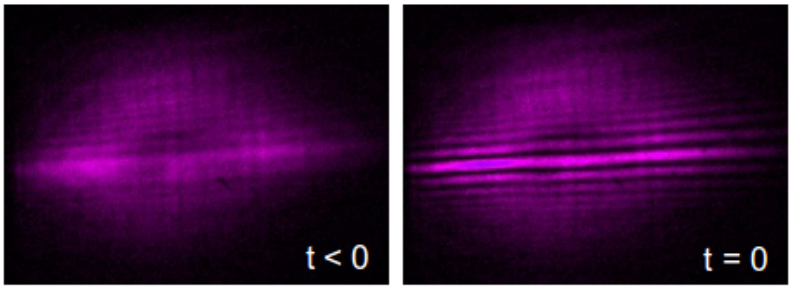

Figure 6.3: *Right:* interference fringes signaling the longitudinal superposition of the pump and probe beams imaged on a YAG screen. The weaker features visible on the *left* image, which is relative to delayed pump and probe beams, generate instead from interference effects at the cutted beam edges.

experiments. As said, each delay point in Fig.s 5.7, 5.9 and 5.11 was an average over a maximum of 10 pump-probe shots. Here, each delay point in Fig. 6.5 is an average over hundreds of pump-probe shots.
The different strategy was obliged by the need to compensate with a heavier statistics the inaccurate knowledge of the incoming probe intensity. The spectrometer in fact monitored the intensity of all the radiation at 12.3 nm. The probe beam was obtained as a given fraction of the latter which should have been constant in principle but in practice was not, because the FEL has some lateral jitter that traduces into a shot-by-shot fluctuation of the relative percentage of radiation between the upper and lower branches of the split-and-delay line. This is what we have inferred from the observation of the very scattered plots of spectrometer vs photodiode counts in the absence of the sample (Fig. 6.4) and what ultimately

prevented us from acquiring a fine mesh of time steps and at least a few different wavelengths.

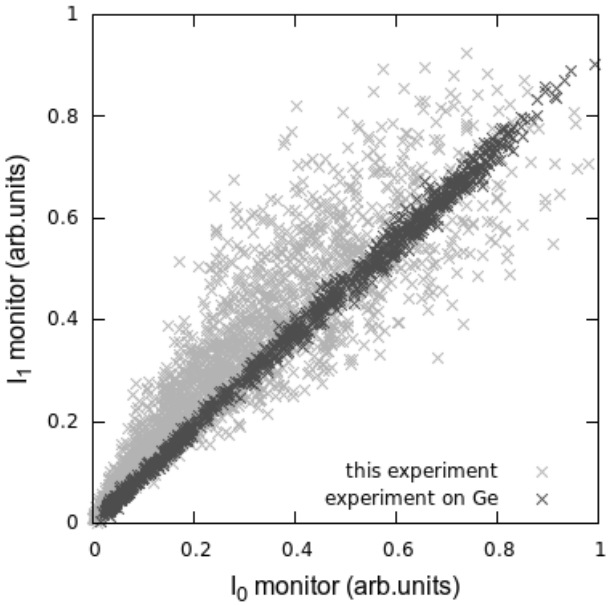

Figure 6.4: Curves showing the correlation between the upstream (I_0) and downstream (I_1) measured probe pulse intensities. *Dark* points are from the experiment on Ge presented in the previous section, with I_0 provided by a ionization monitor along the beam transport and I_1 provided by a photodiode inside the TIMEX chamber. *Light* points are from the experiment on Si presented in this section, with I_0 provided by a spectrometer along the beam transport and I_1 provided by another photodiode inside the TIMEX chamber. All values are normalized to a 0-1 scale for comparison. The latter dataset shows a larger dispersion, due to an instability in the pointing of the FEL beam trajectory which reflects into a instability of the probe fraction selected by the beamsplitting mirror of the split-and-delay line.

6.1.2 Analysis and discussion

Having clarified this point, we can come back to Fig. 6.5 and comment this - despite all - beautiful result.
The excitation of Si with a FEL pulse of roughly 40 mJ/cm^2 produces a steep drop of the absorption at 100.8 eV: a slightly less than 15% decrease which is completed within an overall duration of 300 fs and shows no signs of recovery for the first 2 ps.
Since the energy of 100.8 eV corresponds to $\sim$ 1.2 eV above the $L_{2,3}$ edge, it is natural to compare this response with the one displayed by Ge at energies slightly

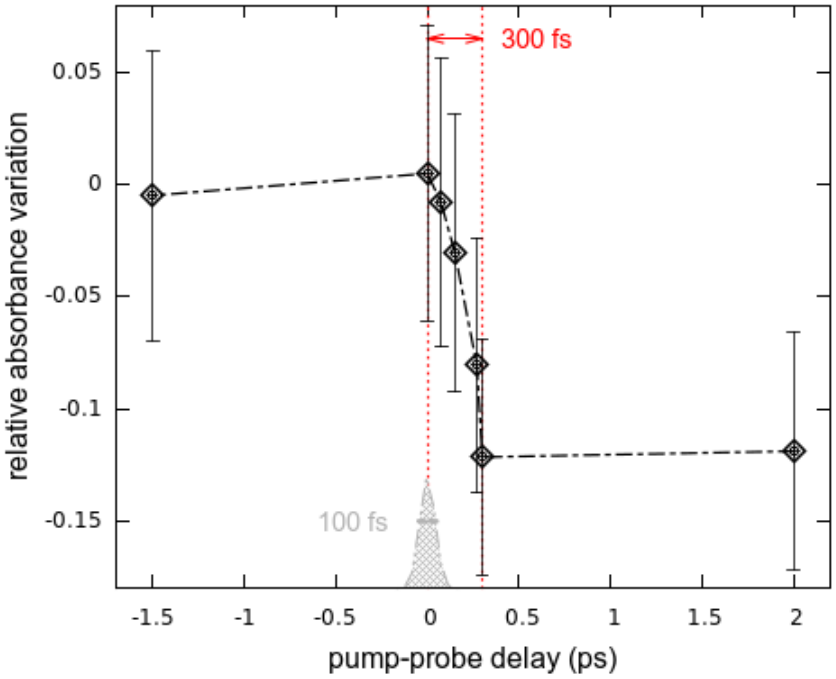

Figure 6.5: Time-resolved relative variation of the absorbance at 100.8 eV for a Si sample excited by a short and intense FEL pulse.

above the $M_{4,5}$ edge, namely with the curves in Fig. 5.9. In the latter case, the absorption was seen to change, not only slowly, but in the opposite direction, a behavior that we interpreted as a shift of the $M_{4,5}$ edge to lower energies, in analogy with what observed for the K edge in static measurements of molten germanium and in agreement with the intuitive picture that, upon transition to the metallic liquid, the bandgap closes making accessible for the core electron unoccupied states at a lower energy.

The work of Ref. [170] provided guidance to a further understanding of our observations. The authors of that paper measured absorption spectra of laser-melted silicon at both the L_1 and $L_{2,3}$ edges. With a resolution of 70 ps, they showed that, 100 ps after laser excitation at 700 mJ/cm^2, the L_1 edge has undergone a shift to lower energies, whereas the $L_2, 3$ edge has undergone a 50 % reduction, like reported on the left panel of Fig. 6.6. They also proposed molecular dynamics simulations from which it is evident how the aforementioned differences mirror the different modifications upon melting of the unoccupied density of states with s and p symmetries.

In this light, all of the discussed results are reconciled and offer us the opportunity to stress the richness of information that core level spectroscopies own.

We therefore look with great excitement at the preliminary data here presented

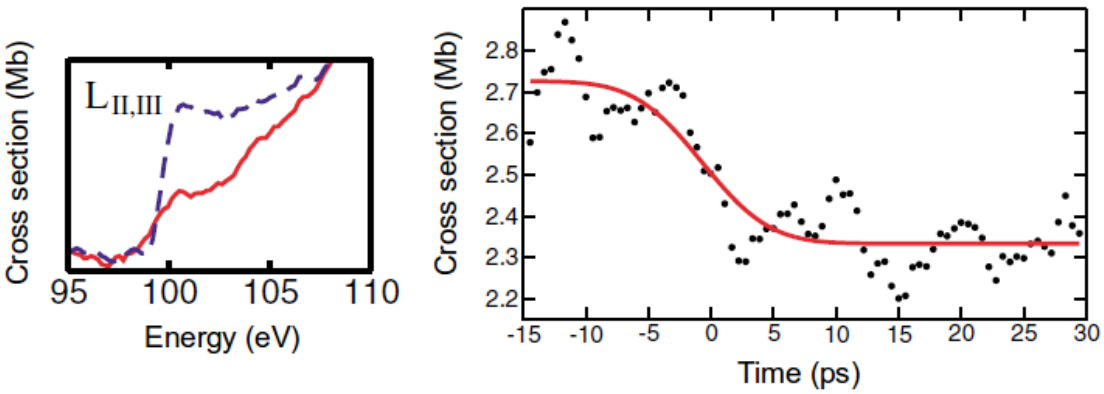

Figure 6.6: Absorption of a thin Si foil before (*blue*) and 100 ps after (*red*) laser excitation as determined by the authors of Ref. [170]. *Left*: XANES $L_{2,3}$ spectra measured with a time resolution of 70 ps and averaged over 100 shots. *Right*: temporal evolution with an improved temporal resolution of 5 ps of the absorption immediately above the $L_{2,3}$ edge, integrated over 5 eV for reasons of low counting and averaged over 100 shots. Note that the latter data measured a drop of the same magnitude as the one we measured ($\sim$ 13%).

that - although improvable in a number of aspects - mark a major step forward in the direction of exploiting these techniques in combination with a femtosecond time resolved pump-probe approach: Fig. 6.5 is indeed the time- and energy- resolved version of Fig. 6.6 (right panel), disclosing the temporal dynamics of melting thought its absorption fingerprint.

Conclusions

Free electron lasers are fourth-generation synchrotron sources which extend to the extreme ultraviolet and X-ray spectral ranges the capability of now conventional high-power ultrafast optical lasers to produce coherent high-brilliance pulses of femtosecond time duration.
Light pulses of the kind they provide can deeply penetrate solid-density matter driving it into transient states of extreme excitation, whose dynamical electronic properties can be studied within a pump-probe scheme by probe pulses either from the free electron laser itself or from a synchronized optical laser. Complementary views are offered in the two cases, as visible and infrared photon energies match the energies of extended valence states, whereas EUV and X-ray photon energies match the energies of localized core states.

This thesis reported on the early investigations carried out at the TIMEX end-station of the free electron laser FERMI in Trieste.

Characterization of the exotic states swiftly reached by FEL-excited metallic samples has been addressed through single-shot measurements of their EUV reflectance and absorbance.
In particular, we have provided the first demonstration of EUV absorption near edge spectroscopy at high energy densities and with sub- 100 fs time resolution. The combination of these features is only possible at FEL sources, but makes FERMI truly unique when further considering that here it comes without a need for monochromatization thanks to its seeded nature which makes the delivered pulses almost Fourier-transform limited in bandwidth.
Results obtained on Ti have been shown, where the dependence on irradiation fluence of the transient absorbance and reflectance for selected wavelengths across the $M_{2,3}$ absorption edge and near the plasma frequency respectively has revealed an ultrafast modification of the electronic structure compatible with a single FEL pulse having turned within about 100 fs room-temperature solid-density Ti into a hot free electron gas coexisting in highly non-equilibrium conditions with a cold ion lattice. An interpretive perspective has been proposed that - based on simplified, yet reasonable, Drude-like models - allowed to gain information on the average free electron temperature and density and the average ionization state of the generated

dense plasma.
Then, ultra-fast high-energy-density self-transmission measurements on Al at a few photon energies between the plasma frequency and the $L_{2,3}$ absorption edge have been presented, evidencing for the first time a non-monotonic trend of the EUV transmission as a function of fluence, that have been seen to be interpretable - within a three-channel model - as resulting from an interplay between saturation effects and absorption cross-section variations due to electron heating.
The description of an analogue experiment conducted on an Al-Mg-Al has followed, where the higher fluence conditions in the meanwhile become at reach have allowed to induce almost full sample transparency over an entire energy region across the Mg $L_{2,3}$ absorption edge. An analytical model has been formulated, that permitted to tentatively deduce from the data an estimate for the first ionization energy of warm dense Mg.

The responses of insulator and semiconductor samples to FEL and laser excitations - from the initial non-equilibrium stage through the subsequent equilibration dynamics to possible phase transformations - has been explored through pump-probe experiments. Here, FEL pulses have been exploited in combination with pulses from the same infrared laser that serves to initiate the FEL emission process, which ensures a natural synchronization between the two radiation sources, - again - a unique feature of seeded FELs.
Measurements of transient optical reflectivity on FEL-pumped Si_3N_4 samples have been illustrated, that have served as a demonstration of the nearly jitter-free pump-probe capabilities of FERMI, thus far unbeaten among FEL facilities. Moreover, discussing the results of a systematic study of the optical response of Si_3N_4 to FEL irradiation for different pump wavelengths and intensities, probe polarizations, sample thicknesses and types of substrate in both reflection and transmission simultaneously, we have pointed out the role of interference effects that are at play due to the different penetration depths of the EUV FEL and infrared laser pulses.
Transient EUV transmissions were collected for Ge at its $M_{4,5}$ edge within a laser pump / FEL probe configuration and for Si at its $L_{2,3}$ edge within a FEL pump / FEL probe configuration, yielding a time and energy -resolved view on femtosecond pulse -induced melting of semiconductors. We have shown that, while able to follow the excitation and de-excitation dynamics of the electronic population in the valence band through below- absorption edge data, we can infer dynamical structural information through on- absorption edge data, in which we have recognized the fingerprint of a partial band gap closure associated with the transition to a liquid state of increased metallic character.

Bibliography

[1] W.L. Kruer. *The Physics of Laser Plasma Interactions*. Frontiers in physics. Westview, 2003.

[2] Peter W. Milonni and Joseph H. Eberly. *Laser physics*. Wiley, 2010.

[3] G Margaritondo, Y. Hwu, and G. Tromba. Synchrotron light: From basics to coherence and coherence-related applications. In S. Mobilio and G. Vlaic, editors, *Synchrotron Radiation: Foundamantals, Methodologies and Applications*, pages 25–53. 2003.

[4] Eric Vauthey. Introduction to nonlinear optical spectroscopic techniques for investigating ultrafast processes. [Online; accessed 04-January-2015].

[5] Michele Kimble. *Femtochemistry VII: Fundamental Ultrafast Processes in Chemistry, Physics, and Biology*. Elsevier Science, 2006.

[6] R Paul Drake. *High-Energy-Density Physics: Fundamentals, Inertial Fusion, and Experimental Astrophysics*. Springer Science and Business Media. Springer, 2006.

[7] Ursula Keller. Recent developments in compact ultrafast lasers. *Nature*, 424:831–838, October 2003.

[8] Opton Laser International. Mode-locking. [Online; accessed 21-August-2014].

[9] D. Strickland and Mourou G. Compression of amplified chirped optical pulses. *Optics Communications*, 55:447–449, October 1985.

[10] Thomas Brabec and Ferenc Krausz. Intense few-cycle laser fields: Frontiers of nonlinear optics. *Rev. Mod. Phys.*, 72:545–591, Apr 2000.

[11] A. McPherson, G. Gibson, H. Jara, U. Johann, T. S. Luk, I. A. McIntyre, K. Boyer, and C. K. Rhodes. Studies of multiphoton production of vacuum-ultraviolet radiation in the rare gases. *J. Opt. Soc. Am. B*, 4(4):595–601, Apr 1987.

[12] P. B. Corkum. Plasma perspective on strong field multiphoton ionization. *Phys. Rev. Lett.*, 71:1994–1997, Sep 1993.

[13] HarMoDyn. High harmonic generation. [Online; accessed 24-August-2014].

[14] R. L. Carman, C. K. Rhodes, and R. F. Benjamin. Observation of harmonics in the visible and ultraviolet created in co_2-laser-produced plasmas. *Phys. Rev. A*, 24:2649–2663, Nov 1981.

[15] F Qur, C Thaury, H George, J P Geindre, E Lefebvre, G Bonnaud, P Monot, and Ph Martin. High-order harmonic generation using plasma mirrors. *Plasma Physics and Controlled Fusion*, 50(12):124007, 2008.

[16] Antonin Borot, Arnaud Malvache, Xiaowei Chen, Aurélie Jullien, Jean-Paul Geindre, Patrick Audebert, Gérard Mourou, Fabien Quéré, and Rodrigo Lopez-Martens. Attosecond control of collective electron motion in plasmas. *Nature Physics*, 8(5):416–421, March 2012.

[17] S. V. Bulanov, N. M. Naumova, and F. Pegoraro. Interaction of an ultrashort, relativistically strong laser pulse with an overdense plasma. *Physics of Plasmas*, 1(3):745, 1994.

[18] T. Baeva, S. Gordienko, and a. Pukhov. Theory of high-order harmonic generation in relativistic laser interaction with overdense plasma. *Physical Review E*, 74(4):046404, October 2006.

[19] A. C. Thompson and D. Vaughan, editors. *X-ray Data Booklet*. Lawrence Berkeley National Laboratory, University of California, second edition, January 2001.

[20] A. A. Zholents and M. S. Zolotorev. Femtosecond x-ray pulses of synchrotron radiation. *Phys. Rev. Lett.*, 76:912–915, Feb 1996.

[21] S. Khan. Femtoslicing in storage rings. In *Proceedings of 2005 Particle Accelerator Conference*, Knoxville, Tennessee, 2005.

[22] J. P. Colombier, P. Combis, E. Audouard, and R. Stoian. Transient optical response of ultrafast nonequilibrium excited metals: Effects of electron-electron contribution to collisional absorption. *Phys. Rev. E*, 77:036409, Mar 2008.

[23] B.D. Patterson. Resource letter on stimulated inelastic x-ray scattering at an xfel. [Online; accessed 05-January-2015].

[24] S. I. Anisimov, B. L. Kapeliovich, and T. L. Perel'Man. Electron emission from metal surfaces exposed to ultrashort laser pulses. *Soviet Journal of Experimental and Theoretical Physics*, 39:375–377, August 1974.

[25] Zhibin Lin, Leonid V. Zhigilei, and Vittorio Celli. Electron-phonon coupling and electron heat capacity of metals under conditions of strong electron-phonon nonequilibrium. *Phys. Rev. B*, 77:075133, Feb 2008.

[26] S. Toleikis, T. Bornath, T. Döppner, S. Düsterer, R. R. Fäustlin, E. Förster, C. Fortmann, S. H. Glenzer, S. Göde, G. Gregori, R. Irsig, T. Laarmann, H. J. Lee, B. Li, K.-H. Meiwes-Broer, J. Mithen, B. Nagler, A. Przystawik, P. Radcliffe, H. Redlin, R. Redmer, H. Reinholz, G. Röpke, F. Tavella, R. Thiele, J. Tiggesbäumker, I. Uschmann, S. M. Vinko, T. Whitcher, U. Zastrau, B. Ziaja, and T. Tschentscher. Probing near-solid density plasmas using soft x-ray scattering. *Journal of Physics B Atomic Molecular Physics*, 43(19):194017, October 2010.

[27] Z. Huang and K. J. Kim. Review of X-ray free-electron laser theory. *Phys. Rev. ST Accel. Beams*, 10(3):034801, March 2007.

[28] Peter Schmüser, Martin Dohlus, and Jörg Rossbach. *Ultraviolet and Soft X-Ray Free-Electron Lasers*. Springer Tracts in Modern Physics. Springer, 1 edition, 2008.

[29] The European X-Ray Free-Electron Laser. Technical design report - part v, 2007. [Online; accessed 30-September-2014].

[30] J. Amann, W. Berg, V. Blank, F. J. Decker, Y. Ding, P. Emma, Y. Feng, J. Frisch, D. Fritz, J. Hastings, Z. Huang, J. Krzywinski, R. Lindberg, H. Loos, A. Lutman, H. D. Nuhn, D. Ratner, J. Rzepiela, D. Shu, Shvyd'koYu, S. Spampinati, S. Stoupin, S. Terentyev, E. Trakhtenberg, D. Walz, J. Welch, J. Wu, A. Zholents, and D. Zhu. Demonstration of self-seeding in a hard-X-ray free-electron laser. *Nat. Phot.*, 6(10):693–698, October 2012.

[31] S. Reiche. Overview of seeding methods for FELs. In *Proceedings of OPAC2013*, Shanghai, China, 2013.

[32] E. Hemsing, M. Dunning, C. Hast, T.O. Raubenheimer, S. Weathersby, and D. Xiang. Highly coherent vacuum ultraviolet radiation at the 15th harmonic with echo-enabled harmonic generation technique. *Phys. Rev. ST Accel. Beams*, 17(7):070702, July 2014.

[33] P. Emma, K. Bane, M. Cornacchia, Z. Huang, H. Schlarb, G. Stupakov, and D. Walz. Femtosecond and Subfemtosecond X-Ray Pulses from a Self-Amplified Spontaneous-Emission-Based Free-Electron Laser. *Phys. Rev. Lett.*, 92(7):074801, February 2004.

[34] E. Saldin, E. Schneidmiller, and M. Yurkov. Self-amplified spontaneous emission FEL with energy-chirped electron beam and its application for generation of attosecond X-ray pulses. *Phys. Rev. ST Accel. Beams*, 9(5):050702, May 2006.

[35] L. Giannessi, a. Bacci, M. Bellaveglia, F. Briquez, M. Castellano, E. Chiadroni, a. Cianchi, F. Ciocci, M. E. Couprie, L. Cultrera, G. Dattoli, D. Filippetto, M. Del Franco, G. Di Pirro, M. Ferrario, L. Ficcadenti, F. Frassetto, a. Gallo, G. Gatti, M. Labat, G. Marcus, M. Moreno, a. Mostacci, E. Pace, a. Petralia, V. Petrillo, L. Poletto, M. Quattromini, J. V. Rau, C. Ronsivalle, J. Rosenzweig, a. R. Rossi, V. Rossi Albertini, E. Sabia, M. Serluca, S. Spampinati, I. Spassovsky, B. Spataro, V. Surrenti, C. Vaccarezza, and C. Vicario. Self-Amplified Spontaneous Emission Free-Electron Laser with an Energy-Chirped Electron Beam and Undulator Tapering. *Phys. Rev. Lett.*, 106(14):144801, April 2011.

[36] C.J. Bocchetta et al. FERMI@elettra conceptual design report, 2007.

[37] FERMI Commissioning Team. FERMI beam parameters. [Online; accessed 01-October-2014].

[38] M Svandrlik, E Allaria, F Bencivenga, C Callegari, F Capotondi, D Castronovo, P Cinquegrana, I Cudin, M Dal Forno, M B Danailov, G D Auria, R De Monte, G De Ninno, A Demidovich, S Di Mitri, B Diviacco, A Fabris, R Fabris, W M Fawley, M Ferianis, E Ferrari, P Finetti, L Froehlich, P Furlan Radivo, G Gaio, L Giannessi, M Kiskinova, G Loda, M Lonza, N Mahne, C Masciovecchio, F Parmigiani, G Penco, O Plekan, M Predonzani, E Principi, L Raimondi, F Rossi, L Rumiz, C Scafuri, C Serpico, P Sigalotti, S Spampinati, C Spezzani, L Sturari, C Svetina, M Trovo, A Vascotto, M Veronese, R Visintini, D Zangrando, M Zangrando, Elettra Sincrotrone Trieste, B Mahieu, C E A Dsm, Drecam Spam, and P Craievich. FERMI seeded FEL progress report. In *Proceedings of IPAC2013*, pages 1182–1184, Shanghai, China, 2013.

[39] F. Bencivenga, R. Cucini, F. Capotondi, A. Battistoni, R. Mincigrucci, E. Giangrisostomi, A. Gessini, M. Manfredda, I. P. Nikolov, E. Pedersoli, E. Principi, C. Svetina, F. Casolari, M. Danailov, Kiskinova M., and C. Masciovec-

chio. Four wave mixing experiments with extreme ultraviolet transient gratings. *submitted*.

[40] Toru Hara. Free-electron lasers: Fully coherent soft X-rays at FERMI. *Nat Photon*, 7(11):852–854, November 2013.

[41] S. Di Mitri, M. Cornacchia, C. Scafuri, and M. Sjöström. Electron beam optics and trajectory control in the fermi free electron laser delivery system. *Phys. Rev. ST Accel. Beams*, 15:012802, Jan 2012.

[42] E. Ferrari, E. Allaria, W. Fawley, L. Giannessi, Z. Huang, G. Penco, and S. Spampinati. Impact of non-gaussian electron energy heating upon the performance of a seeded free-electron laser. *Phys. Rev. Lett.*, 112:114802, Mar 2014.

[43] G Penco, E Allaria, P Craievich, G De Ninno, S Di Mitri, W B Fawley, E Ferrari, L Giannessi, C Spezzani, M Trov, Sincrotrone Trieste, S Spampinati, and Menlo Park. Time-sliced emittance and energy spread measurements at Fermi@Elettra. In *Proceedings of FEL2012*, pages 417–420, Nara,Japan, 2012.

[44] G. Penco, M. Danailov, a. Demidovich, E. Allaria, G. De Ninno, S. Di Mitri, W.M. Fawley, E. Ferrari, L. Giannessi, and M. Trovó. Experimental Demonstration of Electron Longitudinal-Phase-Space Linearization by Shaping the Photoinjector Laser Pulse. *Physical Review Letters*, 112(4):044801, January 2014.

[45] P. Sigalotti, P. Cinquegrana, A. Demidovich, R. Ivanov, I. Nikolov, G. Kurdi, and M.B. Danailov. Ultrafast laser synchronization at the FERMI@Elettra FEL. In *Society of Photo-Optical Instrumentation Engineers (SPIE) Conference Series*, volume 8778 of *Society of Photo-Optical Instrumentation Engineers (SPIE) Conference Series*, May 2013.

[46] *Design and first experience with the FERMI seed laser*, 2011.

[47] E Allaria, A Battistoni, F Bencivenga, R Borghes, C Callegari, F Capotondi, D Castronovo, P Cinquegrana, D Cocco, M Coreno, P Craievich, R Cucini, F D'Amico, M B Danailov, A Demidovich, G De Ninno, A Di Cicco, S Di Fonzo, M Di Fraia, S Di Mitri, B Diviacco, W M Fawley, E Ferrari, A Filipponi, L Froehlich, A Gessini, E Giangrisostomi, L Giannessi, D Giuressi, C Grazioli, R Gunnella, R Ivanov, B Mahieu, N Mahne, C Masciovecchio, I P Nikolov, G Passos, E Pedersoli, G Penco, E Principi, L Raimondi, R Sergo,

P Sigalotti, C Spezzani, C Svetina, M Trov, and M Zangrando. Tunability experiments at the FERMI@Elettra free-electron laser. *New Journal of Physics*, 14(11):113009, 2012.

[48] M.B. Danailov, F.O. Ilday, and F.X. Kaertner. Integrated Design of Laser Systems for a FEL User Facility. *eConf*, C0508213:THPP018, 2005.

[49] P. Cinquegrana, S. Cleva, A. Demidovich, G. Gaio, R. Ivanov, G. Kurdi, I. Nikolov, P. Sigalotti, and M. B. Danailov. Optical beam transport to a remote location for low jitter pump-probe experiments with a free electron laser. *Phys. Rev. ST Accel. Beams*, 17:040702, Apr 2014.

[50] Miltcho B. Danailov, Filippo Bencivenga, Flavio Capotondi, Francesco Casolari, Paolo Cinquegrana, Alexander Demidovich, Erika Giangrisostomi, Maya P. Kiskinova, Gabor Kurdi, Michele Manfredda, Claudio Masciovecchio, Riccardo Mincigrucci, Ivaylo P. Nikolov, Emanuele Pedersoli, Emiliano Principi, and Paolo Sigalotti. Towards jitter-free pump-probe measurements at seeded free electron laser facilities. *Opt. Express*, 22(11):12869–12879, Jun 2014.

[51] M. Zangrando, A. Abrami, D. Bacescu, I. Cudin, C. Fava, F. Frassetto, A. Galimberti, R. Godnig, D. Giuressi, L. Poletto, L. Rumiz, R. Sergo, C. Svetina, and D. Cocco. The photon analysis, delivery, and reduction system at the FERMI@Elettra free electron laser user facility. *Review of Scientific Instruments*, 80(11):–, 2009.

[52] Fabio Frassetto, Daniele Cocco, Marco Zangrando, and Luca Poletto. On-line spectrometer for FEL radiation at FERMI@Elettra. *Nuclear Instruments and Methods in Physics Research Section A: Accelerators, Spectrometers, Detectors and Associated Equipment*, 593(1-2):129–131, August 2008.

[53] B.L. Henke, E.M. Gullikson, and J.C. Davis. X-ray interactions: Photoabsorption, Scattering, Transmission, and Reflection at E = 50-30000 eV, Z = 1-92. *Atomic Data and Nuclear Data Tables*, 54(2):181 – 342, 1993.

[54] E. Allaria, Roberto Appio, L. Badano, W. A. Barletta, S. Bassanese, S. G. Biedron, A. Borga, E. Busetto, D. Castronovo, P. Cinquegrana, S. Cleva, D. Cocco, M. Cornacchia, P. Craievich, I. Cudin, G. D'Auria, M. Dal Forno, M. B. Danailov, R. De Monte, G. De Ninno, P. Delgiusto, A. Demidovich, S. Di Mitri, B. Diviacco, A. Fabris, R. Fabris, W. Fawley, M. Ferianis, E. Ferrari, S. Ferry, L. Froehlich, P. Furlan, G. Gaio, F. Gelmetti, L. Giannessi, M. Giannini, R. Gobessi, R. Ivanov, E. Karantzoulis, M. Lonza,

A. Lutman, B. Mahieu, M. Milloch, S. V. Milton, M. Musardo, I. Nikolov, S. Noe, F. Parmigiani, G. Penco, M. Petronio, L. Pivetta, M. Predonzani, F. Rossi, L. Rumiz, A. Salom, C. Scafuri, C. Serpico, P. Sigalotti, S. Spampinati, C. Spezzani, M. Svandrlik, C. Svetina, S. Tazzari, M. Trovo, R. Umer, A. Vascotto, M. Veronese, R. Visintini, M. Zaccaria, D. Zangrando, and M. Zangrando. Highly coherent and stable pulses from the FERMI seeded free-electron laser in the extreme ultraviolet. 6(10):699–704, 2012.

[55] D. Ratner, A. Fry, G. Stupakov, and W. White. Laser phase errors in seeded free electron lasers. *Phys. Rev. ST Accel. Beams*, 15:030702, Mar 2012.

[56] Enrico Allaria, Miltcho B Danailov, William M Fawley, Luca Giannessi, Elettra-sincrotrone Trieste S C A, Enea C R Frascati, Frascati Roma, and Eugenio Ferrari. Measurements of the FEL bandwidth scaling with harmonic number in a HGHG FEL. In *FEL2014*, pages 1–4, Basel, Switzerland, 2014.

[57] Giovanni De Ninno, Benoît Mahieu, Enrico Allaria, Luca Giannessi, and Simone Spampinati. Chirped seeded free-electron lasers: Self-standing light sources for two-color pump-probe experiments. *Phys. Rev. Lett.*, 110:064801, Feb 2013.

[58] E Allaria, F Bencivenga, R Borghes, F Capotondi, D Castronovo, P Charalambous, P Cinquegrana, MB Danailov, G De Ninno, A Demidovich, et al. Two-colour pump–probe experiments with a twin-pulse-seed extreme ultraviolet free-electron laser. *Nature communications*, 4, 2013.

[59] R. Mitzner, A. A. Sorokin, B. Siemer, S. Roling, M. Rutkowski, H. Zacharias, M. Neeb, T. Noll, F. Siewert, W. Eberhardt, M. Richter, P. Juranic, K. Tiedtke, and J. Feldhaus. Direct autocorrelation of soft-x-ray free-electron-laser pulses by time-resolved two-photon double ionization of he. *Phys. Rev. A*, 80:025402, Aug 2009.

[60] W. F. Schlotter, F. Sorgenfrei, T. Beeck, M. Beye, S. Gieschen, H. Meyer, M. Nagasono, A. Föhlisch, and W. Wurth. Longitudinal coherence measurements of an extreme-ultraviolet free-electron laser. *Opt. Lett.*, 35(3):372–374, Feb 2010.

[61] G. De Ninno. Private communication, 2014.

[62] P. Finetti, E. Allaria, B. Diviacco, C. Callegari, B. Mahieu, J. Viefhaus, M. Zangrando, G. De Ninno, G. Lambert, E. Ferrari, J. Buck, M. Ilchen, B. Vodungbo, N. Mahne, C. Svetina, C. Spezzani, S. Di Mitri, G. Penco, M. Trovo, W. M. Fawley, P. Rebernik, D. Gauthier, C. Grazioli, M. Coreno,

B. Ressel, A. Kivimki, T. Mazza, L. Glaser, F. Scholz, J. Seltmann, P. Gessler, J. Grnert, A. De Fanis, M. Meyer, A. Knie, S. P. Moeller, L. Raimondi, F. Capotondi, E. Pedersoli, O. Plekan, M. Danailov, A. Demidovich, I. Nikolov, A. Abrami, J. Gautier, J. Lning, P. Zeitoun, and L. Giannessi. Polarization measurement of free electron laser pulses in the vuv generated by the variable polarization source fermi. volume 9210, pages 92100K–92100K–12, 2014.

[63] Bernhard Flöter, Pavle Jurani, Svea Kapitzki, Barbara Keitel, Klaus Mann, Elke Plönjes, Bernd Schäfer, and Kai Tiedtke. Euv hartmann sensor for wavefront measurements at the free-electron laser in hamburg. *New Journal of Physics*, 12(8):083015, 2010.

[64] J. Chalupský, J. Krzywinski, L. Juha, V. Hájková, J. Cihelka, T. Burian, L. Vyšín, J. Gaudin, A. Gleeson, M. Jurek, A. R. Khorsand, D. Klinger, H. Wabnitz, R. Sobierajski, M. Störmer, K. Tiedtke, and S. Toleikis. Spot size characterization of focused non-gaussian x-ray laser beams. *Opt. Express*, 18(26):27836–27845, Dec 2010.

[65] C. Svetina, G. Sostero, R. Sergo, R. Borghes, C. Callegari, F. DAmico, F. Bencivenga, C. Masciovecchio, a. Di Cicco, and D. Cocco. A beam-shaping system for TIMEX beamline. *Nuclear Instruments and Methods in Physics Research Section A: Accelerators, Spectrometers, Detectors and Associated Equipment*, 635(1):S12–S15, April 2011.

[66] Andrea Di Cicco, Filippo Bencivenga, Andrea Battistoni, Daniele Cocco, Riccardo Cucini, Francesco D'Amico, Silvia Di Fonzo, Adriano Filipponi, Alessandro Gessini, Erika Giangrisostomi, Roberto Gunnella, Claudio Masciovecchio, Emiliano Principi, and Cristian Svetina. Probing matter under extreme conditions at fermi@elettra: the timex beamline. volume 8077, pages 807704–807704–10, 2011.

[67] E. Principi, R. Cucini, A. Filipponi, A. Gessini, F. Bencivenga, F. D'Amico, A. Di Cicco, and C. Masciovecchio. Determination of the ion temperature in a stainless steel slab exposed to intense ultrashort laser pulses. *Phys. Rev. Lett.*, 109:025005, Jul 2012.

[68] F. Frassetto, P. Miotti, C. Callegari, M. de Simone, P. Finetti, E. Giangrisostomi, C. Grazioli, F. Iesari, A. Kivimki, R. Mincigrucci, E. Principi, S. Stagira, A. Di Cicco, M. Coreno, and L. Poletto. Spectrometer for single-shot x-ray emission and photon diagnostics. volume 9210, pages 92100E–92100E–10, 2014.

[69] Corso A. J., Zuppella P, Principi E, Giangrisostomi E, Bencivenga F, Gessini A, Zuccon S, Masciovecchio C, Giglia A, Nannarone S, and Pelizzo M G. A broadband multilayer optics for ultrafast euv absorption spectroscopy with free electron laser radiation. *in preparation*.

[70] David L. Windt. IMDSoftware for modeling the optical properties of multilayer films. *Computers in Physics*, 12, 1998.

[71] Computing Division ALBA. Tango control system open source collaboration, 2014. [Online; accessed 27-September-2014].

[72] Siegfried H. Glenzer and Ronald Redmer. X-ray thomson scattering in high energy density plasmas. *Rev. Mod. Phys.*, 81:1625–1663, Dec 2009.

[73] G. Gregori, R. Tommasini, O. L. Landen, R. W. Lee, and S. H. Glenzer. Limits on collective x-ray scattering imposed by coherence. *EPL (Europhysics Letters)*, 74(4):637, 2006.

[74] Henry C. Kapteyn, Abraham Szoke, Roger W. Falcone, and Margaret M. Murnane. Prepulse energy suppression for high-energy ultrashort pulses using self-induced plasma shuttering. *Opt. Lett.*, 16(7):490–492, Apr 1991.

[75] C. Thaury, F. Quere, J. P. Geindre, A. Levy, T. Ceccotti, P. Monot, M. Bougeard, F. Reau, P. d/'Oliveira, P. Audebert, R. Marjoribanks, and Ph Martin. Plasma mirrors for ultrahigh-intensity optics. *Nat Phys*, 3(6):424–429, June 2007.

[76] F. Wooten. *Optical Properties of Solids*. Academic Press, New York, 1972.

[77] Kikuo Ujihara. Reflectivity of metals at high temperatures. *Journal of Applied Physics*, 43(5):2376–2383, 1972.

[78] Kurt Sturm and Luiz E. Oliveira. Wave-vector-dependent plasmon linewidth in the alkali metals. *Phys. Rev. B*, 24:3054–3062, Sep 1981.

[79] C. H. Chen, D. C. Joy, H. S. Chen, and J. J. Hauser. Observation of anomalous plasmon linewidth in the icosahedral Al-Mn quasicrystals. *Phys. Rev. Lett.*, 57:743–746, Aug 1986.

[80] J L Robins and J B Swan. Characteristic electron energy loss spectra of the transition metals, Ti to Cu. *Proceedings of the Physical Society*, 76(6):857, 1960.

[81] P. Bracconi and R. Lsser. Investigation of titanium and titanium hydride by AES and EELS. *Applied Surface Science*, 28(3):204–214, 1987.

[82] A.M. James and M.P. Lord. *Macmillan's Chemical and Physical Data*. Macmillan, London, 1992.

[83] Bob Nagler, Ulf Zastrau, Roland R. Fäustlin, Sam M. Vinko, Thomas Whitcher, A. J. Nelson, Ryszard Sobierajski, Jacek Krzywinski, Jaromir Chalupsky, Elsa Abreu, Saša Bajt, Thomas Bornath, Tomas Burian, Henry Chapman, Jaroslav Cihelka, Tilo Döppner, Stefan Düsterer, Thomas Dzelzainis, Marta Fajardo, Eckhart Förster, Carsten Fortmann, Eric Galtier, Siegfried H. Glenzer, Sebastian Göde, Gianluca Gregori, Vera Hajkova, Phil Heimann, Libor Juha, Marek Jurek, Fida Y. Khattak, Ali Reza Khorsand, Dorota Klinger, Michaela Kozlova, Tim Laarmann, Hae Ja Lee, Richard W. Lee, Karl-Heinz Meiwes-Broer, Pascal Mercere, William J. Murphy, Andreas Przystawik, Ronald Redmer, Heidi Reinholz, David Riley, Gerd Röpke, Frank Rosmej, Karel Saksl, Romain Schott, Robert Thiele, Josef Tiggesbäumker, Sven Toleikis, Thomas Tschentscher, Ingo Uschmann, Hubert J. Vollmer, and Justin S. Wark. Turning solid aluminium transparent by intense soft X-ray photoionization. *Nature Physics*, 5(9):693–696, July 2009.

[84] F Bencivenga, E Principi, E Giangrisostomi, R Cucini, a Battistoni, F D'Amico, a Di Cicco, S Di Fonzo, a Filipponi, a Gessini, R Gunnella, M Marsi, L Properzi, M Saito, and C Masciovecchio. Reflectivity enhancement in titanium by ultrafast XUV irradiation. *Scientific reports*, 4(1):4952, January 2014.

[85] L. C. Davis. Photoemission from transition metals and their compounds. *Journal of Applied Physics*, 59(6):R25–R64, 1986.

[86] B.H. Bransden and C.J. Joachain. *Physics of Atoms and Molecules*, volume 2nd Ed. New York: Prentice-Hall, 2003.

[87] N.W. Ashcroft and N.D. Mermin. *Solid State Physics*. Saunders College, Philadelphia, 1976.

[88] H. Hchst, P. Steiner, G. Reiter, and S. Hfner. XPS valence bands of Ti, Zr, Nb, Mo and Hf. *Zeitschrift fr Physik B Condensed Matter*, 42(3):199–204, 1981.

[89] O. Jepsen. Electronic structure and magnetic breakdown in titanium. *Phys. Rev. B*, 12:2988–2997, Oct 1975.

[90] N. Medvedev, U. Zastrau, E. Förster, D. O. Gericke, and B. Rethfeld. Short-time electron dynamics in aluminum excited by femtosecond extreme ultraviolet radiation. *Phys. Rev. Lett.*, 107:165003, Oct 2011.

[91] U. Zastrau, C. Fortmann, R. R. Fäustlin, L. F. Cao, T. Döppner, S. Düsterer, S. H. Glenzer, G. Gregori, T. Laarmann, H. J. Lee, A. Przystawik, P. Radcliffe, H. Reinholz, G. Röpke, R. Thiele, J. Tiggesbäumker, N. X. Truong, S. Toleikis, I. Uschmann, A. Wierling, T. Tschentscher, E. Förster, and R. Redmer. Bremsstrahlung and line spectroscopy of warm dense aluminum plasma heated by xuv free-electron-laser radiation. *Phys. Rev. E*, 78:066406, Dec 2008.

[92] S. M. Vinko, U. Zastrau, S. Mazevet, J. Andreasson, S. Bajt, T. Burian, J. Chalupsky, H. N. Chapman, J. Cihelka, D. Doria, T. Döppner, S. Düsterer, T. Dzelzainis, R. R. Fäustlin, C. Fortmann, E. Förster, E. Galtier, S. H. Glenzer, S. Göde, G. Gregori, J. Hajdu, V. Hajkova, P. A. Heimann, R. Irsig, L. Juha, M. Jurek, J. Krzywinski, T. Laarmann, H. J. Lee, R. W. Lee, B. Li, K.-H. Meiwes-Broer, J. P. Mithen, B. Nagler, A. J. Nelson, A. Przystawik, R. Redmer, D. Riley, F. Rosmej, R. Sobierajski, F. Tavella, R. Thiele, J. Tiggesbäumker, S. Toleikis, T. Tschentscher, L. Vysin, T. J. Whitcher, S. White, and J. S. Wark. Electronic structure of an xuv photogenerated solid-density aluminum plasma. *Phys. Rev. Lett.*, 104:225001, Jun 2010.

[93] B. Y. Mueller and B. Rethfeld. Relaxation dynamics in laser-excited metals under nonequilibrium conditions. *Phys. Rev. B*, 87:035139, Jan 2013.

[94] E. Bévillon, J. P. Colombier, V. Recoules, and R. Stoian. Free-electron properties of metals under ultrafast laser-induced electron-phonon nonequilibrium: A first-principles study. *Phys. Rev. B*, 89:115117, Mar 2014.

[95] A. Mančić, A. Lévy, M. Harmand, M. Nakatsutsumi, P. Antici, P. Audebert, P. Combis, S. Fourmaux, S. Mazevet, O. Peyrusse, V. Recoules, P. Renaudin, J. Robiche, F. Dorchies, and J. Fuchs. Picosecond short-range disordering in isochorically heated aluminum at solid density. *Phys. Rev. Lett.*, 104:035002, Jan 2010.

[96] B. I. Cho, K. Engelhorn, A. A. Correa, T. Ogitsu, C. P. Weber, H. J. Lee, J. Feng, P. A. Ni, Y. Ping, A. J. Nelson, D. Prendergast, R. W. Lee, R. W. Falcone, and P. A. Heimann. Electronic structure of warm dense copper studied by ultrafast x-ray absorption spectroscopy. *Phys. Rev. Lett.*, 106:167601, Apr 2011.

[97] Ursula Keller. Recent developments in compact ultrafast lasers. *Nature*, 424(6950):831–838, August 2003.

[98] Hitoki Yoneda, Yuichi Inubushi, Toshihiro Tanaka, Yuta Yamaguchi, Fumiya Sato, Shunsuke Morimoto, Taisuke Kumagai, Mitsuru Nagasono, At-

sushi Higashiya, Makina Yabashi, Tetsuya Ishikawa, Haruhiko Ohashi, Hiroaki Kimura, Hikaru Kitamura, and Ryosuke Kodama. Ultra-fast switching of light by absorption saturation in vacuum ultra-violet region. *Opt. Express*, 17(26):23443–23448, Dec 2009.

[99] Hitoki Yoneda, Yuichi Inubushi, Makina Yabashi, Tetsuo Katayama, Tetsuya Ishikawa, Haruhiko Ohashi, Hirokatsu Yumoto, Kazuto Yamauchi, Hidekazu Mimura, and Hikaru Kitamura. Saturable absorption of intense hard X-rays in iron. *Nature communications*, 5:5080, January 2014.

[100] Sam M. Vinko, Gianluca Gregori, Michael P. Desjarlais, Bob Nagler, Thomas J. Whitcher, Richard W. Lee, Patrick Audebert, and Justin S. Wark. Freefree opacity in warm dense aluminum. *High Energy Density Physics*, 5(3):124 – 131, 2009.

[101] Carlos A. Iglesias. {XUV} absorption by solid-density aluminum. *High Energy Density Physics*, 6(3):311 – 317, 2010.

[102] L.M. Frantz and J.S. Nodvik. Theory of Pulse Propagation in a Laser Amplifier. *Journal of Applied Physics*, 34:2346–2349, August 1963.

[103] Keisuke Hatada and Andrea Di Cicco. Modeling saturable absorption for ultra short x-ray pulses. *Journal of Electron Spectroscopy and Related Phenomena*, 196(0):177 – 180, 2014. Advances in Vacuum Ultraviolet and X-ray Physics, The 38th International Conference on Vacuum Ultraviolet and X-ray Physics (VUVX2013), University of Science and Technology of China.

[104] H.C. Gupta. *Solid state physics*. Vikas Publishing House Pvt Ltd, Delhi, 2001.

[105] Donald Umstadter. Extreme x rays probe extreme matter. *Physics*, 5:88, Aug 2012.

[106] A.Kramida, Yu.Ralchenko, J.Reader, and and NIST ASD Team. NIST Atomic Spectra Database (ver. 5.2), [Online]. Available: `http://physics.nist.gov/asd` [2014, December 2]. National Institute of Standards and Technology, Gaithersburg, MD., 2014.

[107] S. M. Vinko, O. Ciricosta, B. I. Cho, K. Engelhorn, H.-K. Chung, C. R. D. Brown, T. Burian, J. Chalupsky, R. W. Falcone, C. Graves, V. Hajkova, A. Higginbotham, L. Juha, J. Krzywinski, H. J. Lee, M. Messerschmidt, C. D. Murphy, Y. Ping, A. Scherz, W. Schlotter, S. Toleikis, J. J. Turner, L. Vysin, T. Wang, B. Wu, U. Zastrau, D. Zhu, R. W. Lee, P. A. Heimann,

B. Nagler, and J. S. Wark. Creation and diagnosis of a solid-density plasma with an x-ray free-electron laser. *Nature*, 482:59–62, Feb 2012.

[108] O. Ciricosta, S. M. Vinko, H.-K. Chung, B.-I. Cho, C. R. D. Brown, T. Burian, J. Chalupský, K. Engelhorn, R. W. Falcone, C. Graves, V. Hájková, A. Higginbotham, L. Juha, J. Krzywinski, H. J. Lee, M. Messerschmidt, C. D. Murphy, Y. Ping, D. S. Rackstraw, A. Scherz, W. Schlotter, S. Toleikis, J. J. Turner, L. Vysin, T. Wang, B. Wu, U. Zastrau, D. Zhu, R. W. Lee, P. Heimann, B. Nagler, and J. S. Wark. Direct measurements of the ionization potential depression in a dense plasma. *Phys. Rev. Lett.*, 109:065002, Aug 2012.

[109] Ecker G. and Kroll W. Lowering of the ionization energy for a plasma in thermodynamic equilibrium. *Phys. Fluids*, 6:62, 1963.

[110] J.C. Stewart and K.D. Pyatt. Lowering of ionization potentials in plasmas. *Astrophys. J.*, 144:1203, 1966.

[111] B.J.B. Crowley. Continuum lowering a new perspective. *High Energy Density Physics*, 13(0):84 – 102, 2014.

[112] Sang-Kil Son, Robert Thiele, Zoltan Jurek, Beata Ziaja, and Robin Santra. Quantum-mechanical calculation of ionization-potential lowering in dense plasmas. *Phys. Rev. X*, 4:031004, Jul 2014.

[113] S. M. Vinko, O. Ciricosta, and J. S. Wark. Density functional theory calculations of continuum lowering in strongly coupled plasmas. *Nature Communications*, 5(3533), 2014.

[114] Cornelius Gahl, Armin Azima, Martin Beye, Martin Deppe, Kristian Dobrich, Urs Hasslinger, Franz Hennies, Alexej Melnikov, Mitsuru Nagasono, Annette Pietzsch, Martin Wolf, Wilfried Wurth, and Alexander Fohlisch. A femtosecond x-ray / optical cross-correlator. *Nature Photonics*, 2:165–169, 2008.

[115] Theophilos Maltezopoulos, Stefan Cunovic, Marek Wieland, Martin Beye, Armin Azima, Harald Redlin, Maria Krikunova, Roland Kalms, Ulrike Frühling, Filip Budzyn, Wilfried Wurth, Alexander Föhlisch, and Markus Drescher. Single-shot timing measurement of extreme-ultraviolet free-electron laser pulses. *New Journal of Physics*, 10(3):033026, 2008.

[116] Mina R. Bionta, H. T. Lemke, J. P. Cryan, J. M. Glownia, C. Bostedt, M. Cammarata, J.-C. Castagna, Y. Ding, D. M. Fritz, A. R. Fry, J. Krzywinski, M. Messerschmidt, S. Schorb, M. L. Swiggers, and R. N. Coffee. Spectral

encoding of x-ray/optical relative delay. *Opt. Express*, 19(22):21855–21865, Oct 2011.

[117] Harmand M., Coffee R., Bionta M. R., Chollet M., French D., Zhu D., Fritz D. M., Lemke H. T., Medvedev N., Ziaja B., Toleikis S., and Cammarata M. Achieving few-femtosecond time-sorting at hard x-ray free-electron lasers. *Nature Photonics*, 7:215–218, 2013.

[118] S.J. Orfanidis. *Electromagnetic waves and antennas*. Rutgers University Press, 2013.

[119] F. Casolari, F. Bencivenga, F. Capotondi, E. Giangrisostomi, M. Manfredda, R. Mincigrucci, E. Pedersoli, E. Principi, C. Masciovecchio, and M. Kiskinova. Role of multilayer-like interference effects on the transient optical response of si3n4 films pumped with free-electron laser pulses. *Applied Physics Letters*, 104(19):–, 2014.

[120] G. A. N. Connell, R. J. Nemanich, and C. C. Tsai. Interference enhanced raman scattering from very thin absorbing films. *Applied Physics Letters*, 36(1):31–33, 1980.

[121] G. A. N. Connell. Interference enhanced kerr spectroscopy for very thin absorbing films. *Applied Physics Letters*, 40(3):212–214, 1982.

[122] N. Medvedev, B. Ziaja, M. Cammarata, M. Harmand, and S. Toleikis. Electron kinetics in femtosecond x-ray irradiated sio2. *Contributions to Plasma Physics*, 53(4-5):347–354, 2013.

[123] K. Shimakawa, A. Kolobov, and S. R. Elliott. Photoinduced effects and metastability in amorphous semiconductors and insulators. *Advances in Physics*, 44:475–588, November 1995.

[124] P. Martin, S. Guizard, Ph. Daguzan, G. Petite, P. D'Oliveira, P. Meynadier, and M. Perdrix. Subpicosecond study of carrier trapping dynamics in wide-band-gap crystals. *Phys. Rev. B*, 55:5799–5810, Mar 1997.

[125] Medvedev N. and Rethfeld B. Transient dynamics of the electronic subsystem of semiconductors irradiated with an ultrashort vacuum ultraviolet laser pulse. *New Journal of Physics*, 12(7):073037, 2010.

[126] O. Krupin, M. Trigo, W. F. Schlotter, M. Beye, F. Sorgenfrei, J. J. Turner, D. A. Reis, N. Gerken, S. Lee, W. S. Lee, G. Hays, Y. Acremann, B. Abbey, R. Coffee, M. Messerschmidt, S. P. Hau-Riege, G. Lapertot, J. Lüning, P. Heimann, R. Soufli, M. Fernández-Perea, M. Rowen, M. Holmes, S. L.

Molodtsov, A. Föhlisch, and W. Wurth. Temporal cross-correlation of x-ray free electron and optical lasers using soft x-ray pulse induced transient reflectivity. *Opt. Express*, 20(10):11396–11406, May 2012.

[127] Stephen M. Durbin. X-ray induced optical reflectivity. *AIP Advances*, 2(4):–, 2012.

[128] Catalin Spataru, Lorin Benedict, and Steven Louie. *Ab initio* calculation of band-gap renormalization in highly excited gaas. *Phys. Rev. B*, 69:205204, May 2004.

[129] B. Rethfeld, K. Sokolowski-Tinten, D. von der Linde, and S. I. Anisimov. Ultrafast thermal melting of laser-excited solids by homogeneous nucleation. *Phys. Rev. B*, 65:092103, Feb 2002.

[130] S.K. Sundaram and Mazur E. Inducing and probing non-thermal transitions in semiconductors using femtosecond laser pulses. *Nature Materials*, 1(4):217–224, 2002.

[131] P. Stampfli and K. H. Bennemann. Theory for the instability of the diamond structure of si, ge, and c induced by a dense electron-hole plasma. *Phys. Rev. B*, 42:7163–7173, Oct 1990.

[132] V. Recoules, J. Clérouin, G. Zérah, P. M. Anglade, and S. Mazevet. Effect of intense laser irradiation on the lattice stability of semiconductors and metals. *Phys. Rev. Lett.*, 96:055503, Feb 2006.

[133] C. A. D. Roeser, M. Kandyla, A. Mendioroz, and E. Mazur. Optical control of coherent lattice vibrations in tellurium. *Phys. Rev. B*, 70:212302, Dec 2004.

[134] German Sciaini, Maher Harb, Sergei G. Kruglik, Thomas Payer, Christoph T. Hebeisen, Frank-J. Meyer zu Heringdorf, Mariko Yamaguchi, Michael Horn-von Hoegen, Ralph Ernstorfer, and R. J. Dwayne Miller. Electronic acceleration of atomic motions and disordering in bismuth. *Nature*, 458:56–59, 2009.

[135] C. V. Shank, R. Yen, and C. Hirlimann. Time-resolved reflectivity measurements of femtosecond-optical-pulse-induced phase transitions in silicon. *Phys. Rev. Lett.*, 50:454–457, Feb 1983.

[136] K. Sokolowski-Tinten, J. Bialkowski, and D. von der Linde. Ultrafast laser-induced order-disorder transitions in semiconductors. *Phys. Rev. B*, 51:14186–14198, May 1995.

[137] K. Sokolowski-Tinten and D. von der Linde. Generation of dense electron-hole plasmas in silicon. *Phys. Rev. B*, 61:2643–2650, Jan 2000.

[138] A. J. Sabbah and D. M. Riffe. Femtosecond pump-probe reflectivity study of silicon carrier dynamics. *Phys. Rev. B*, 66:165217, Oct 2002.

[139] Maher Harb, Ralph Ernstorfer, Christoph T. Hebeisen, Germán Sciaini, Weina Peng, Thibault Dartigalongue, Mark A. Eriksson, Max G. Lagally, Sergei G. Kruglik, and R. J. Dwayne Miller. Electronically driven structure changes of si captured by femtosecond electron diffraction. *Phys. Rev. Lett.*, 100:155504, Apr 2008.

[140] E. N. Glezer, Y. Siegal, L. Huang, and E. Mazur. Laser-induced band-gap collapse in gaas. *Phys. Rev. B*, 51:6959–6970, Mar 1995.

[141] Li Huang, J. Paul Callan, Eli N. Glezer, and Eric Mazur. Gaas under intense ultrafast excitation: Response of the dielectric function. *Phys. Rev. Lett.*, 80:185–188, Jan 1998.

[142] K. Sokolowski-Tinten, J. Bialkowski, M. Boing, A. Cavalleri, and D. von der Linde. Thermal and nonthermal melting of gallium arsenide after femtosecond laser excitation. *Phys. Rev. B*, 58:R11805–R11808, Nov 1998.

[143] J.Paul Callan, Albert M.-T. Kim, Li Huang, and Eric Mazur. Ultrafast electron and lattice dynamics in semiconductors at high excited carrier densities. *Chemical Physics*, 251(13):167 – 179, 2000.

[144] Klaus Sokolowski-Tinten and Dietrich von der Linde. Ultrafast phase transitions and lattice dynamics probed using laser-produced x-ray pulses. *Journal of Physics: Condensed Matter*, 16(49):R1517, 2004.

[145] Germn Sciaini and R J Dwayne Miller. Femtosecond electron diffraction: heralding the era of atomically resolved dynamics. *Reports on Progress in Physics*, 74(9):096101, 2011.

[146] E.G. Gamaly. The physics of ultra-short laser interaction with solids at non-relativistic intensities. *Physics Reports*, 508(45):91 – 243, 2011.

[147] E G Gamaly and A V Rode. Ultrafast electronic relaxation in superheated bismuth. *New Journal of Physics*, 15(1):013035, 2013.

[148] J. J. Klossika, U. Gratzke, M. Vicanek, and G. Simon. Importance of a finite speed of heat propagation in metals irradiated by femtosecond laser pulses. *Phys. Rev. B*, 54:10277–10279, Oct 1996.

[149] D von der Linde, K Sokolowski-Tinten, and J Bialkowski. Lasersolid interaction in the femtosecond time regime. *Applied Surface Science*, 109110(0):1 – 10, 1997.

[150] D P Korfiatis, K-A Th Thoma, and J C Vardaxoglou. Conditions for femtosecond laser melting of silicon. *Journal of Physics D: Applied Physics*, 40(21):6803, 2007.

[151] M.C. Downer, H. Ahn, D.H. Reitze, and X.Y. Wang. Dielectric function and electrical resistivity of liquid carbon determined by femtosecond spectroscopy. *International Journal of Thermophysics*, 14(3):361–370, 1993.

[152] D. H. Reitze, H. Ahn, and M. C. Downer. Optical properties of liquid carbon measured by femtosecond spectroscopy. *Phys. Rev. B*, 45:2677–2693, Feb 1992.

[153] S. L. Johnson, P. A. Heimann, A. G. MacPhee, A. M. Lindenberg, O. R. Monteiro, Z. Chang, R. W. Lee, and R. W. Falcone. Bonding in liquid carbon studied by time-resolved x-ray absorption spectroscopy. *Phys. Rev. Lett.*, 94:057407, Feb 2005.

[154] Christine J. Wu, James N. Glosli, Giulia Galli, and Francis H. Ree. Liquid-liquid phase transition in elemental carbon: A first-principles investigation. *Phys. Rev. Lett.*, 89:135701, Sep 2002.

[155] James N. Glosli and Francis H. Ree. Liquid-liquid phase transformation in carbon. *Phys. Rev. Lett.*, 82:4659–4662, Jun 1999.

[156] L.M. Ghiringhelli. *On the Nature of Phase Transitions in Covalent Liquids*. PhD thesis, University of Amsterdam, 2005.

[157] N. Medvedev, Tkachenko V., and Ziaja B. Modeling of nonthermal solid-to-solid phase transition in diamond irradiated with femtosecond x-ray fel pulse. *Contrib. Plasma Phys.*, 55(1):12–34, 2015.

[158] Martin Beye, Florian Sorgenfrei, William F. Schlotter, Wilfried Wurth, and Alexander Fhlisch. The liquid-liquid phase transition in silicon revealed by snapshots of valence electrons. *Proceedings of the National Academy of Sciences*, 107(39):16772–16776, 2010.

[159] Srikanth Sastry. Illuminating liquid polymorphism in silicon. *Proceedings of the National Academy of Sciences*, 107(40):17063–17064, 2010.

[160] D. W. Bailey and C. J. Stanton. Calculations of femtosecond differential optical transmission in germanium. *Journal of Applied Physics*, 77(5):2107–2115, 1995.

[161] X. Q. Zhou, H. M. van Driel, and G. Mak. Femtosecond kinetics of photoexcited carriers in germanium. *Phys. Rev. B*, 50:5226–5230, Aug 1994.

[162] Materials Design. Energy band structure of germanium. [Online; accessed 22-December-2014].

[163] C. Li, K. Lu, K. Tamura, S. Hosokawa, and M. Inui. XANES study of the electronic structure of molten germanium. *Journal of Synchrotron Radiation*, 6(3):540–542, May 1999.

[164] A. Filipponi and A. Di Cicco. Short-range order in crystalline, amorphous, liquid, and supercooled germanium probed by x-ray-absorption spectroscopy. *Phys. Rev. B*, 51:12322–12336, May 1995.

[165] C. W. Siders, A. Cavalleri, K. Sokolowski-Tinten, Cs. Tth, T. Guo, M. Kammler, M. Horn von Hoegen, K. R. Wilson, D. von der Linde, and C. P. J. Barty. Detection of nonthermal melting by ultrafast x-ray diffraction. *Science*, 286(5443):1340–1342, 1999.

[166] K. Sokolowski-Tinten, C. Blome, C. Dietrich, A. Tarasevitch, M. Horn von Hoegen, D. von der Linde, A. Cavalleri, J. Squier, and M. Kammler. Femtosecond x-ray measurement of ultrafast melting and large acoustic transients. *Phys. Rev. Lett.*, 87:225701, Nov 2001.

[167] Klaus Sokolowski-Tinten and Dietrich von der Linde. Ultrafast phase transitions and lattice dynamics probed using laser-produced x-ray pulses. *Journal of Physics: Condensed Matter*, 16(49):R1517, 2004.

[168] A. Cavalleri, C. W. Siders, C. Rose-Petruck, R. Jimenez, Cs. Tóth, J. A. Squier, C. P. J. Barty, K. R. Wilson, K. Sokolowski-Tinten, M. Horn von Hoegen, and D. von der Linde. Ultrafast x-ray measurement of laser heating in semiconductors: Parameters determining the melting threshold. *Phys. Rev. B*, 63:193306, Apr 2001.

[169] M Beye, F Hennies, M Deppe, E Suljoti, M Nagasono, W Wurth, and A Fhlisch. Measurement of the predicted asymmetric closing behaviour of the band gap of silicon using x-ray absorption and emission spectroscopy. *New Journal of Physics*, 12(4):043011, 2010.

[170] S. L. Johnson, P. A. Heimann, A. M. Lindenberg, H. O. Jeschke, M. E. Garcia, Z. Chang, R. W. Lee, J. J. Rehr, and R. W. Falcone. Properties of liquid silicon observed by time-resolved x-ray absorption spectroscopy. *Phys. Rev. Lett.*, 91:157403, Oct 2003.

Acknowledgements

I wish to thank my former professor Andrea Di Cicco for having introduced me to the community of FERMI and my Ph.D. advisor Claudio Masciovecchio for having welcomed me into his group: I am very glad for the opportunity you offered me to work in such a highly stimulating context.

A warm thanks goes to my closest collaborator on TIMEX, Emiliano Principi, for the efforts he has put into the development of the beamline and, not less, for his always enthusiastic outlook on our work.

A sincere appreciation is extended to my Ph.D. colleague Riccardo Mincigrucci for his precious contribute to the realization of the most recent experiments on TIMEX.

In acknowledging the help provided by all other members of the EIS group, I express particular gratitude for the valuable teachings and advices of Filippo Bencivenga and Riccardo Cucini and for the ever-present technical assistance of Alessandro Gessini.

For his unceasing generous support, I am very grateful to my officemate Andrea Battistoni with which I had the fortune to share a rich professional and human path.

The completion of this project would not have been possible without the fundamental support of the many people working at FERMI.
A thankful mention goes, therefore, to the machine physicists: Enrico Allaria, Giovanni De Ninno, Simone Di Mitri, Bruno Diviacco, William Fawley, Eugenio Ferrari, Luca Giannessi, Benoit Mahieu, Giuseppe Penco, Simone Spampinati, Carlo Spezzani, Mauro Trovó; to the PADRES group members: Claudio Fava, Simone Gerusina, Riccardo Gobessi, Nicola Mahne, Erik Mazzucco, Lorenzo Raimondi, Luca Rumiz, Cristian Svetina, Marco Zangrando; to the laser group members: Paolo Cinquegrana, Miltcho Danailov, Alexander Demidovich, Nikolov Ivaylo, Gabor Kurdi, Paolo Sigalotti; to the informatics and control staff: Alessandro Abrami, Roberto Borghes, Valentina Chenda, Alessio Curri, Georgios Kourousias, Giulio Gaio, Marco Lonza, Gesner Passos, Roberto Passuello, Lorenzo Pivetta, Milan Prica, Claudio Scafuri, Martin Scarcia; to the electronics staff: Giuseppe Cautero, Dario Giuressi, Rudi Sergo; and to collaborators from the DIPROI beamline: Flavio Capotondi, Francesco Casolari, Maya Kiskinova, Michele Manfredda, Emanuele

Pedersoli.

Thanks to all of those - especially my family - who cheered me up with their words of confidence and encouragement: I owe you a lot.

Trieste, February 2015